IPP-Report

Max-Planck-Institut
für Plasmaphysik

Antonello Zito

Simulating the impact of perpendicular scrape-off layer transport on momentum and power dissipation in magnetic fusion devices

IPP 2019-16
September 2019

POLITECNICO
MILANO 1863

SCHOOL OF INDUSTRIAL AND INFORMATION ENGINEERING
MASTER OF SCIENCE IN NUCLEAR ENGINEERING

Simulating the impact of perpendicular scrape-off layer transport on momentum and power dissipation in magnetic fusion devices

Advisor:
Prof. Matteo Passoni

Co-advisors:
Dr. Marco Wischmeier
Dr. Daniel Carralero

Author:
Antonello Zito

Academic Year 2018-2019

Antonello Zito:
Simulating the impact of perpendicular scrape-off layer transport on momentum and power dissipation in magnetic fusion devices.
| Master of Science in Nuclear Engineering, Politecnico di Milano.
| Research in collaboration with Max-Planck-Institut für Plasmaphysik, Garching, Germany.

This work has been carried out within the framework of the EUROfusion consortium and has received funding through the FuseNet association from the Horizon 2020 research and innovation programme. The views and opinions expressed herein do not necessarily reflect those of the European Commission.

Politecnico di Milano:
www.polimi.it

Max-Planck-Institut für Plasmaphysik:
www.ipp.mpg.de

EUROfusion:
www.euro-fusion.org

If I have seen further
it is only by standing
on the shoulders of giants

Sir Isaac Newton

Contents

Acknowledgements

Part of the journey is the end. Probably, it is even one of the best and exciting parts. Moreover, it also represents an opportunity to stop and look back; and it is just looking back that I recognize that, if this journey has really reached its end, it is only thanks to the people who never left me alone.

First of all I want to thank my supervisor, prof. Matteo Passoni. I am proud to have been a student, a representative and, in general, a member of the nuclear engineering family at the Politecnico di Milano. My gratitude for this will last forever, and I'm sure that, soon or later, we will have the opportunity of work together again.
Then I also want to express my huge gratitude to dr. Marco Wischmeier, for having followed and supported me during the months in Garching, and above all for the trust he placed in me from the first day we met. I am indebted to you, and also to anyone else which, during my work at the Max-Planck-Institut für Plasmaphysik, spent even just a minute for helping me, in particular to dr. Daniel Carralero; the inspiring discussions had together with both of you have strongly contributed in expanding my knowledge and my horizons in such an interesting and challenging research field.

A special and immeasurable thankfulness must be, finally, given to all the people that, during my life and my studies, believed in me, because without you nothing would have been possible, because I would only have been a shadow of the man I am now without the teachings you gave me, the trust you placed in me, and the moments spent together during these years.
Thanks to my whole family, for always supporting me in whatever I did and for always respecting my choices, especially to my parents and to my grandparents. Thanks to all the friends which have endured studying with me during these intense university years, especially to Francesca, Izzu, Gerri and Laura, for never making me feel alone during each step of the long and winding road that brought me up to here. Thanks to all the people which I had the pleasure of living with while I was far from home, since sharing a place with you has been the most important school of life I have ever had. Thanks to all the friends coming from both my two homelands, since I know that you will be always waiting for me, whenever I'll come back.
If it is true that one can see further only by standing on the shoulders of giants, then you are the real giants on whose shoulders I had the honour to climb to discover my way.

Abstract

Facing the problem of particle and power exhaust in magnetic fusion devices is one of the major challenges in nuclear fusion research. The achievement of a highly dissipative regime for the scrape-off layer (SOL) is required to guarantee safe operation for the plasma-facing components of future plant-sized devices, i.e. for enhancing their lifetime by preventing melting and minimizing erosion.

Enhanced perpendicular transport in the SOL plasma, which may occur under reactor-relevant conditions, could represent key element for accessing a highly dissipative regime. Nevertheless, this transport could lead to further problems, such as increased erosion on the main chamber wall materials. Perpendicular transport has been experimentally studied on various currently operating devices, and an extensive database on experimental measurements related to this has been assembled.

The goal of this thesis is to numerically investigate the experimental observations about perpendicular transport in the SOL plasma. The underlying idea is to undertake a "numerical experiment" motivated by an experimental dataset on a single device, to interpret the possible underlying physical mechanisms. This is done in order to explore how the various dissipative processes in the SOL depend on the nature of the perpendicular transport assumptions.

The SOLPS-ITER code package was used to simulate experimental scenarios obtained in the ASDEX Upgrade tokamak. In order to obtain the most accurate fit to the experimental data a series of simulations was performed with different transport assumptions. Once the most realistic simulations were selected an extensive analysis of the results was performed.

The numerical results successfully reproduced the qualitative trends of the experimental measurements. Analyzing these results allowed then to characterize thoroughly the impact of enhanced perpendicular transport on the plasma conditions in the divertor and, consequently, on the processes leading to momentum and power dissipation.

Preface

In the next future, nuclear energy is going to represent an indispensable source of energy for the industrial-scale electric power production. This arises from the need to fulfill the ever increasing energy demand in a clean and and reliable way.

Currently, much research effort is being devoted to demonstrate the feasibility of exploiting *nuclear fusion* processes for electric power production. The goal is to produce, and sustain in a controlled way, a burning fuel made of light nuclei, namely deuterium and tritium. For achieving this goal, such fuel must exist in the physical form of *plasma* [1].

The major difficulty to sustain nuclear fusion processes in a controlled way in a manmade device is the extremely high temperature needed for making the energy production process possible, of the order of hundreds million degrees [1]. In order to make this possible, the achievement of a safe and reliable confinement for the hot burning plasma is mandatory. For this aim, two different confinement strategies are being studied: the *magnetic confinement fusion* and the *inertial confinement fusion*.

In magnetic fusion devices, on whose research this thesis work is dedicated, magnetic fields are exploited to confine the hot burning plasma. The most exploited layout for the construction of such devices consists in closed-chamber systems of toroidal geometry. In particular, the most widely studied configuration is the *tokamak* (which is the russian acronym of *toroidal'naya kamera s magnitnymi katushkami*, i.e. *toroidal chamber with magnetic coils*), in which the magnetic fields are produced by an axial symmetric system of coils and currents [2]. This is precisely the configuration which is used for the major currently existing research devices, and the one which will be used for future plant-sized fusion devices, i.e. *ITER* [3] and *DEMO* [4]. ITER, whose aim is to demonstrate the physical principles of fusion power generation, is currently being built; DEMO, instead, which is expected to demonstrate the feasibility of electric power generation by fusion on large scale, is currently being designed.

A number of physics and engineering problems are expected to affect such next-step devices. This motivates great research effort about these.

One of these concerns the achievement of a complete understanding of the physics of the *exhaust processes* from the burning plasma. These have, indeed, repercussions on the matters of power removal from the plasma and plasma-material interaction. Such a knowledge is mandatory for estimating the intensities of the various dissipation channels in different operating regimes. This motivates in-depth studies about predicting and controlling the particle and heat fluxes leaving the plasma and striking the material surfaces of the device. This is especially important for ITER and DEMO since these devices are expected to operate at higher density and, moreover, at considerably higher heating power compared to the existing devices. This means that, in these devices, much more power will need to be dissipated, so that such fluxes onto the material surfaces will be potentially much larger than in existing devices. This could lead to untolerable particle and heat loads onto the *plasma-facing components (PFC)* constituting the materials of the device, causing undesired effects such as melting and radiation damage [5].

Being able to predict as accurately as possible how the particle and heat fluxes will be distributed onto these components in realistic operating conditions is, then, fundamental. The final goal is to optimize the lifetime of these materials. This requires to find a way for reducing the particle and heat loads striking them to tolerable values also under reactor-relevant conditions, namely large heating power and high density regimes [6].

In principle, the problem of attaining an efficient exhaust can be faced by creating adequate confinement configurations for a fusion plasma, which optimize the plasma-material interaction. In current devices, this is done by implementing the so-called *divertor configuration*. This consists of shaping the magnetic geometry in such a way that the plasma particles leaving the actual confinement region are rapidly removed from the burning plasma region and transported towards opportunely designed material targets. This is possible as, once the particles cross the so-called *separatrix* (i.e. the magnetic surface which delimits the confinement region) they enter a region, called the *scrape-off layer (SOL)*, which is characterized by open magnetic field lines striking these targets [7][8].

The key point for achieving tolerable values for the particle and heat fluxes striking the targets is then intimately related to the scrape-off layer physics. It is necessary to promote processes leading to a strong power dissipation along the SOL, in order to minimize the fraction of the SOL input power which is deposited onto the targets. Related to this, it is also desired to achieve suitable divertor regimes, such as the so-called detached regime, which can be in turn obtained by promoting momentum dissipation processes along the SOL.

The first matter of investigation concerns the *power dissipation* processes. For a fixed magnetic configuration, the area on which the exhausting power is deposited onto the plasma-facing components of the targets is directly proportional to the major radius R of the device [7]. So, a measure of the severity of the resulting *heat loads* onto the targets could be given by the ratio of the total plasma heating power P_{heat} and the major radius R [6].

From simple transport models it is possible to deduce the resulting values for the heat loads onto the targets, assuming magnetic geometry and target inclination as are expected on future devices, if we suppose to neglect any power dissipation process in the plasma. For example, for a device such as DEMO, in which $P_{heat}/R \approx 80 - 100$ MW/m is expected, these could be estimated to be of the order of 100 MW/m^2 [6].

Based on the existing technology, the plasma-facing components of a future fusion reactor will need to be composed of a high-Z material for both divertor targets and main chamber wall. Tungsten is the most likely choice for this, due to its low erosion yield and its very high melting point. For such a material, avoiding any risks of melting sets the maximum steady-state tolerable heat load at about $5 - 10$ MW/m^2 [6][9][10]. Therefore, the just presented estimate of the heat flux density onto the divertor targets without any power dissipation would be far unacceptable. In particular, according to this estimate, the fraction of the total heating power which must be dissipated before arriving onto the targets in DEMO should be about 95%.

Next, *momentum dissipation* processes must be considered as well. In fact, the just discussed limit for the heat flux translates in a maximum tolerable particle flux density onto the divertor targets of about $5 \cdot 10^{23}$ m^{-2}s^{-1} [6]. This would require to operate in a particular divertor regime, called *detached regime*, defined as a strong reduction of the particle flux to targets compared to what expected from simple transport models [7][8].

It can be shown that the incoming particle flux strongly decreases with increasing pressure drop along the SOL [7]. Therefore, enhancing momentum-removing processes along the SOL is a necessary prerequisite for the detachment.

In the design of a next-step fusion device it is then mandatory to understand if such a highly dissipative regime for the SOL plasma is effectively achievable in a stable way for reactor-relevant conditions, namely in a high density regime.

Positive results for this arise from recent experimental studies for high density operations in currently operating midsize devices. Such studies have shown that, when approaching sufficiently high densities, an abrupt enhancement of momentum and power dissipation from the SOL plasma takes place. This was inferred from measuring a strong enhancement of both particles and heat transported to wall of the device and the achievement of a partial detachment [11][12][13]. Such increased dissipation was attributed to an enhanced regime of *perpendicular transport* of plasma particles to the main chamber wall across the SOL, due to non negligible phenomena of convective nature appearing in this regime.

The intermittent formation of fast radially propagating *blob-filaments* in the SOL plasma was pointed as the physical reason for such an increase of transport. These are magnetic-field-aligned structures, considerably denser than the surrounding plasma, seen to be formed near the separatrix from turbulence phenomena taking place at high density [14][15]. After their creation, these structures become electrically polarized, and the resulting induced drift motion moves them radially outwards towards the main chamber wall. This results in a net radial convective motion for the plasma. In L-mode high density plasmas these structures have been in fact been observed. When they are present, the radial density profiles at the outer SOL midplane becomes considerably flattened [11][12][13]: such feature is called a *density shoulder*.

In addition, it could be expected that such radially convecting structures carry also heat with them. This would result in a substantial fraction of the SOL input power being also radially transported to the wall. In fact, by performing an experimental power balance, it was seen that the fraction of the SOL input power which is radially transported up to the wall after the perpendicular transport enhancement was increased up to 20% [16][17].

This could have positive consequences. First of all, the spreading of power deposition onto the wide surfaces of the main chamber wall would reduce the fraction of heating power which arrives onto the divertor targets. Then, pressure drop along the SOL could be increased as well. This could result from both an enhanced plasma-neutral interaction regime and the enhancement of radial momentum transport itself. This would help the achievement of a detached regime.

However, in seeking similar operating conditions, it should be also considered that enhanced particle and heat fluxes would reaching the main chamber wall would increase the plasma-material interaction on it. A quantification of this effect, and its consequences of an eventually enhanced main wall sputtering, is currently unknown.

An accurate predictive basis for the impact of perpendicular transport on momentum and power dissipation is then mandatory, for ensuring that future devices could operate in safe conditions. A complete knowledge of how such processes will drive the particle and power exhaust in these devices will be necessary in view of the design of both main chamber wall and divertor targets for these. This led to the research to which this thesis is devoted.

The mechanisms relevant for the dissipation processes driven by perpendicular transport are intrinsically complex. The experimental estimates of the effects purely due to perpendicular transport are, indeed, still insufficient. Since no first-principle-based theories exist which are capable to predict perpendicular transport processes in the SOL, investigation of this problem requires the use of sophisticated *numerical models* for simulating the SOL plasma. The employment of numerical codes for predicting the impact of transport enhancement on momentum and power dissipation has, indeed, constituted the final goal of this work.

The idea was to perform a simulation work, testing different transport assumptions, in order to obtain simulated plasma conditions compatible with experimental data. In this way, the experimental measurements of those plasma properties related to a change in the perpendicular transport regime could be compared with the simulations results. The aim was to identify and the characterize the momentum and power dissipation channels arising after the transport enhancement. So, it would have been possible to discriminate the losses which are purely due to the transport enhancement and the losses which arise in dependence on other plasma properties.

For performing the simulations the *SOLPS-ITER* [18][19][20] code package was used. This considers a fluid description for the plasma and a kinetic description for the neutral particles. In particular, it consists of the coupling between the 2D multi-fluid plasma transport code *B2.5* [21][22] and the 3D kinetic Monte Carlo neutral transport code *EIRENE* [23].
The modelling work was applied to the *ASDEX Upgrade* tokamak [24]. This is a midsize device currently operating at the Max-Planck-Institüt fur Plasmaphysik in Garching bei München, Germany, where this thesis work was carried out. SOLPS-ITER was used for numerically reproducing the plasma conditions from an ASDEX Upgrade L-mode discharge, extensively analyzed experimentally [16][17], in two situations where enhanced perpendicular transport is absent and present. Such two scenarios were experimentally identified by noting the absence/presence, respectively, of a density shoulder at the outer SOL midplane.
SOLPS-ITER does not contain a physics-based perpendicular transport model. Therefore, realistic simulations could be only obtained by adjusting the anomalous transport coefficients by means of a fitting procedure to the experimental radial plasma profiles, measured at the outer SOL midplane. In this way, the best assumption to be done for reproducing the impact of fast radially propagating blob-filaments structures on the transport properties was found.
An accurate analysis of the results of these simulation was finally performed. The increase of the dissipation processes resulting from the enhancement of perpendicular transport at high density was, then, quantified. This allowed to characterize thoroughly the impact of perpendicular transport on the SOL plasma conditions and then, consequently, on the processes leading to momentum and power dissipation.
The analyses performed on the results definitely provided a deeper understanding of the underlying physical processes, as well as a general view of the potential impact that these could have on the operation of future plant-sized fusion devices.

This manuscript is organized in two parts. The first three chapters constitute a preparatory and complete introduction to the topic considered in this work. In particular, they are aimed to report all the theoretical considerations, as well as the experimental evidences, on the existence of an enhanced perpendicular transport regime in the SOL plasma.

The Chapter 1 constitutes a brief introduction to the topic of nuclear fusion.
First of all, some basic aspects of fusion reactions are described. Then, the physical principles of magnetic plasma confinement are discussed, as well as the operating principles of tokamaks.

In the Chapter 2 the major properties of the boundary of fusion plasmas in divertor configurations are introduced.
First of all a general overview of the scrape-off layer physics is given. Detailed focus is given to the physical features of the SOL plasma which are of interest for this work, i.e. global particles and energy balances, and the main phenomena influencing these, i.e. plasma-material interaction and volumetric processes. A general overview of the different operating regimes for the SOL is then also given.
Then, a simple mathematical model for the transport processes in the SOL is derived, namely the so-called two point-model. Considering such a simplified model has, in fact, allowed to perform several general and qualitative considerations about the simulations results.
At the end of this chapter a first theoretical introduction to the physical processes considered in this work is given: namely, the existence of an enhanced perpendicular transport regime for the SOL plasma driven by radial blob propagation and consequent formation of a density shoulder at the outer SOL midplane. This is followed by a first qualitative discussion of how this could affect the general SOL behavior, in terms of global transport properties and exhaust processes.

In the Chapter 3 the experimental evidences which have supported this work are reported.
First of all some basic features of the ASDEX Upgrade tokamak are introduced. Then, the most relevant diagnostics systems for plasma edge studies, with which the considered measurements were taken, are described.
This is necessary to discuss the considered experiments. These showed that, under particular plasma conditions, an enhanced perpendicular transport regime, as well as the formation of a density shoulder at the outer SOL midplane, was achieved. Moreover, experimental power balances performed on the obtained results confirmed the theoretical prediction of a substantial fraction of the SOL input power being radially transported towards the main chamber wall.

The second part of the manuscript, instead, is aimed to describe the modelling work which was performed for numerically reproducing the plasma conditions and the physical processes to be investigated, and to finally discuss the simulations results.

In the Chapter 4 the numerical tools used for carrying out the simulations are shortly described.
A general overview of the SOLPS-ITER code package is given. After that, the physics of its two major modules, namely the B2.5 program for plasma particles modelling and the EIRENE program for neutrals modelling, is briefly discussed.
The choice of using such a sophisticated code for the modelling work was motivated by the requirement of simulating the experimental plasma conditions as accurately as possible. Primarily, a feature which was expected to be crucial for a correct modelling was considering a full kinetic treatment for the neutral particles. This is, indeed, supported by the experimental evidence of neutrals playing a key role in the considered physical processes.

In the Chapter 5 the work which was performed to achieve realistic simulations of the considered ASDEX Upgrade discharge, presenting enhanced perpendicular transport, is described.
After a brief description of the modelled discharge, a complete report of the simulation activity is given. This consists in describing the computational grid used for the simulations, the atomic/molecular processes activated in EIRENE, and the considered options which were used to declare the desired physical input parameters to the code.
Then, all the steps followed for obtaining the final simulations are described. These consisted in trying to reproduce several experimental features of the considered discharge. In particular, the choice for the most accurate simulation for each scenario was based on matching the experimental radial plasma profiles at the outer SOL midplane. A good comparison between numerical and experimental results in this region is, in fact, possible as this region is sufficiently well covered by reliable diagnostics systems for measuring both electron density and electron temperature.
The setup of the various simulated cases was performed according to a selective procedure and an optimization algorithm. The first one was aimed to allow a self-consistent choice of the position of the separatrix (and consequently the plasma properties corresponding to it) featuring the best agreement between experimental and numerical results. The second one was aimed to select the best assumption for the anomalous transport coefficients to impose for correctly reproducing the radial density profile in the SOL in all the cases.
Once the most realistic simulation for each scenario is selected, a first brief description of the results is given. In addition, some brief considerations about the validity of the achieved results are given, in terms of physical meaningfulness of the assumptions done for simulating enhanced perpendicular transport.

In the Chapter 6, which is the most relevant part of the manuscript, the final simulations for each scenario (without and with enhanced transport) are analyzed and discussed.
The discussion is mainly focused on two aspects. First, the characterization of the radial transport itself at the outer SOL midplane, as well as the link between this and the formation of a density shoulder. Second, the impact of the enhancement of the dissipation channels, following the transition to enhanced transport, on the particle and power exhaust at the targets.
Regarding the first aspect, radial particle and heat fluxes, neutrals profiles and ionization profiles at the outer SOL midplane are analyzed. The simulations have confirmed the experimental evidence of a non negligible amount of power being radially transported to the wall. Moreover, such increased radial heat fluxes in the far SOL are seen to be responsible for the formation of a density shoulder, through sustaining an increased ionization particle source.
Regarding the second aspect, the exhaust processes are analyzed in terms of plasma and neutrals conditions in the divertor region, particles and heat loads profiles onto the outer target and degree of an eventually achieved detachment. A strong reduction of the heat loads onto the outer target and the achievement of a partial detachment were modelled after the transport enhancement, coherently with the experimental results. The reason for the occurrence of the these features is then discussed in more detail through quantitative momentum and power balances in the divertor region applied to the simulated plasma conditions. In this way, the drop of the power reaching the target was seen to occur mainly after the general density increase, rather then after the transport enhancement. Instead, the increased pressure drop leading to the detachment was seen to be directly caused by the transport enhancement. In detail, this was caused by an increased rate of plasma-neutrals interactions and recombination processes; these, in turn, were seen to occur because of a strong cooling down of the divertor region following the large amount of power dissipated at the midplane through radial transport.

Finally, in the Chapter 7, the conclusions of this work are briefly summarized, suggesting a line of future modelling work regarding the considered physical processes. Possible implications of the obtained results for the operation and the design of future devices are also briefly discussed.

The manuscript is completed by some appendices which deepen some aspects related to the performed work.
In the Appendix A some basic concepts of plasma physics, which are useful for a full comprehension of the text, are briefly summarized.
In the Appendix B some further physical aspects related to perpendicular transport processes driven by radial convective motion of blob-filaments are reviewed in more detail, from both a theoretical and experimental point of view.
In the Appendix C the physics of plasma edge modelling in SOLPS-ITER is described in more detail, focusing on the assumptions made and the equations which are solved by the code.

Chapter 1

Magnetic confinement fusion

In this chapter the general topic of magnetic confinement fusion will be briefly presented, and the current state of art of fusion reactors will be discussed. In detail, in the Section 1.1 the nuclear reactions of interest for fusion research and their major properties will be presented. Then, in the Section 1.2 some fundamentals properties of the magnetically confined plasmas will be discussed, in order to present the working principle of magnetic fusion devices.

1.1 Nuclear fusion

Nuclear fusion is a nuclear reaction which involves the aggregation of two light nuclei, resulting in a net release of energy. The advantage of using electric power generation by fusion reactions, which motivates great research efforts by thousands of physicists and engineers all around the world, can be summarized as:

- *Unlimited fuel resources*: the fuel for the most promising fusion reactions are deuterium and tritium, two isotopes of hydrogen. The first one can be naturally found in oceanic water in relevant quantity and can be extracted at low cost; the second one, instead, can be artificially produced from an isotope of lithium, abundantly present in the earth crust.
- *Low environmental impact*: fusion power generation does not produce carbon dioxide or other greenhouse gases; moreover, the radioactive waste produced, although relevant in quantity, are not as dangerous as that produced by fission reactions.
- *High intrinsic safety*: fusion reactors are not at risk of disruptive accidents since, at each time, they need to be continuously refueled.

The energy outcome of fusion reactions is enormous: in terms of joules released per unit of mass of fuel, 10^6 tons of fossil fuel (chemical combustion reactions) equate 0,8 tons of uranium (nuclear fission reactions) or 0,14 tons of deuterium (nuclear fusion reactions) [1].

Differently from the case of nuclear fission, it is not possible to initiate fusion chain reactions by bombardment of a fuel with slow neutrons, since no neutron-induced fusion reactions exist which present another neutron as reaction product. Therefore, a fusion chain reaction is impossible to produce.

However, fusion reactions of light nuclei could be initiated by substituting neutrons with other light nuclei, that is by making two light nuclei collide. In this way, the absence of a chain reaction would be compensated with a continuous refueling of adequate light nuclei in a reactor. Nevertheless, in order to activate such reactions, the two nuclei should be very close one another (at a distance of about one nuclear diameter): at such distance, a very strong electric repulsion exists between them, being both positively charged. The reactions could then take place only if, initially, the nuclei have sufficient energy to overtake the coulomb barrier, i.e. to bring them to a distance small enough to activate the action of the strong nuclear interaction.

The most promising fusion reaction which is intended to be exploited in fusion reactors is the *D-T reaction*; this consists in the interaction between one *deuterium* nucleus and one *tritium* nucleus (i.e. the two heavy isotopes of hydrogen), leading to the reaction

$$D + T \rightarrow \alpha + n + 17{,}6 \text{ MeV} \tag{1.1}$$

The net energy release of 17,6 MeV results from the net increase of mass defect of the reacting system, according to the well-known mass-energy equivalence $\Delta E = \Delta m c^2$. After the reaction between the two nuclei has occurred, energy is released as kinetic energy of the reaction products. In particular, its global energy release is 3,52 MeV per nucleon of fuel, which macroscopically correspond to $338 \cdot 10^6$ MJ per kg of burnt deuterium-tritium fuel [1].
Since it is the easiest fusion reaction to activate, it is the most studied one, even if this would require a continuous tritium refuelling, which does not exist in nature being radioactive with a half-live of 12,26 years. Its applicability, despite the absence of natural tritium resources, depends on the exploitation of the released neutrons; these, in fact, could be used to produce tritium after reacting with a material made of lithium, surrounding the region where fusion reactions occur, through the reactions

$$^6\text{Li} + n_{\text{thermal}} \rightarrow T + \alpha + 4{,}8 \text{ MeV} \tag{1.2}$$

$$^7\text{Li} + n_{\text{fast}} \rightarrow T + \alpha + n - 2{,}5 \text{ MeV} \tag{1.3}$$

Such solution would then provide both neutron absorption and tritium breeding.
So, ideally, from each fusion-produced neutron a new tritium nucleus would be created, making the reactions self-sustained; however, practically some mechanisms of neutron loss would be unavoidable, for which it is required that the material surrounding the region where fusion reaction occur is a neutron-multiplying medium.

The probability that, in a system, deuterium and tritium nuclei interact can be quantified by means of a quantity called *cross section*, and denoted with σ, having the dimensions of a surface. Usually, it is measured in *barns*, with 1 b $= 10^{-28}$ m^2. More details about it can be found in Appendix A.4.1.
The experimentally measured values of some fusion cross sections, in function of the average center-of-mass kinetic energy of the particles, proportional to the temperature of the system as $K = \frac{3}{2}T$, are plotted in the Fig. 1.1.

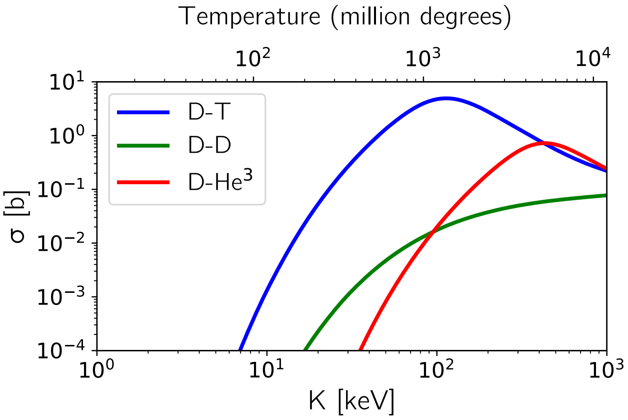

Figure 1.1: Cross sections for some relevant fusion reactions, in function of the center-of-mass kinetic energy of the nuclei. Data taken from [25].

We can note how the D-T reaction has a peak of about 5 b, corresponding to a kinetic energy of the deuterium nuclei of about 120 keV.
However, it must be considered that particles in a system have different velocities, according to their particular velocity distribution, and thus different kinetic energies; therefore a global parameter quantifying the probability of occurrence of fusion reactions in the whole system should take into account such velocity distribution.
Assuming the system in thermodynamic equilibrium, after the many collisions between the travelling nuclei, the populations can be proved to obey a *maxwellian distribution*, described by a distribution function (i.e. density in the phase space) given by [2]

$$f(\boldsymbol{x},\boldsymbol{v},t) = n\left(\frac{m}{2\pi T}\right)^{3/2} e^{-\frac{mv^2}{2T}} \tag{1.4}$$

Here n is the *density* of particles in the system, in m^{-3}, and T is their *temperature*, which here and in the following is expressed in energy units, that is as $T \equiv k_B T_K$, in eV, where $k_B \approx 8{,}617 \cdot 10^{-5}$ eV/K is the *Boltzmann constant* and T_K is the temperature in kelvin. In this way, saying that the system has a temperature (meaning, a thermal energy content) of 1 eV means saying that its classical temperature is about 11600 K.
So, a figure of merit for quantifying the reactivity of a system can be given by integrating the cross section $\sigma(v)$ over all the possible relative velocities between two interacting particles (i.e. over the whole velocity space), taking maxwellian distributions as basis. What we get is the so-called velocity-averaged *rate coefficient* $\langle\sigma v\rangle$, measured in m^3/s. The trend of such coefficient for some fusion reactions, following from the experimental dependencies of the respective cross sections, is plotted in the Fig. 1.2. In particular, for the D-T reaction, $\langle\sigma v\rangle$ has a peak of about $9 \cdot 10^{-22}$ m^3/s at a temperature of about 70 keV.

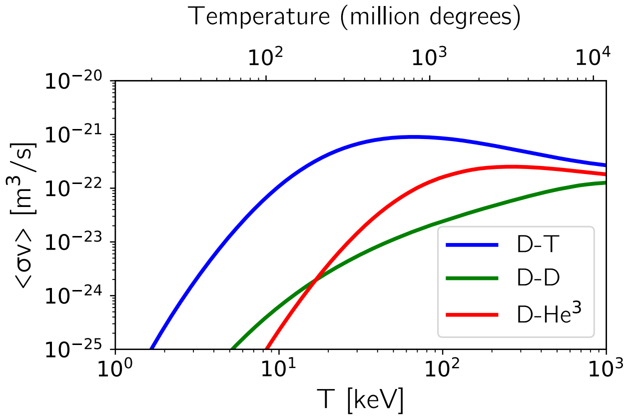

Figure 1.2: Fusion rate coefficients for some relevant fusion reactions, in function of the temperature. Data taken from [25].

We can note that the microscopic kinetic energy required to initiate fusion reactions is in the order of tens of keV, more than 1000 times larger than the usual ionization energy of deuterium and tritium atoms (necessary to tear away one electron from them). Therefore, for a fusion reactor to achieve reactivity, the deuterium/tritium fuel should be heated at such a high temperature to be fully ionized, existing then in form of free electrons and ions [26]. In such a state, the fuel would then be in the in form of *plasma*.

A desirable situation for a future fusion reactor will be one in which the deuterium-tritium plasma is kept at a sufficiently high temperature that the consequent rate of fusion reaction is high enough to provide a positive power balance, i.e. featuring more power produced than power required to maintain the plasma hot.

An even more desirable situation is one in which no external heating is needed at all, which is theoretically possible. In fact, as the fusion reaction rate keeps increasing, the plasma temperature will increase as well, and with these also the rate coefficient (cfr. Fig. 1.2). At some point, the plasma temperature would become sufficiently high the internal heating alone (i.e. provided to the plasma as kinetic energy of the reaction products) will be sufficient to keep the plasma temperature high enough, with no more need of external heating. Such condition, according to which the fusion reactions effectively become self-sustained, is called *ignition*.

The temperature which is necessary to reach such condition will strongly depend on the capability of the plasma to keep the produced heat inside it against the natural *heat transport losses*; this is quantified by its *energy confinement time* τ_E, which has the meaning of the plasma relaxation time for the heat losses, and is a figure of merit of how much the high-temperature plasma is thermally insulated. Another energy loss term which must be taken into account is given by the *radiation losses* by bremsstrahlung emission and line radiation emission.

By performing a simple power balance (cfr. Appendix A.4.2) it can be shown [1] that the condition for the ignition for a D-T plasma can be written as

$$n\tau_E \geq \frac{12}{E_\alpha}\frac{T}{\langle\sigma v\rangle} \tag{1.5}$$

where $E_\alpha = 3{,}5$ MeV is the kinetic energy of the released alpha particles. If this condition is fulfilled, then the energy released by fusion is larger than or equal to the energy lost by heat transport and radiation. Being $\langle\sigma v\rangle$ given in the Fig. 1.2 for the D-T reaction, the right-hand part of (1.5) is a function of the temperature only, with the resulting temperature dependence of the required value of $n\tau_E$ plotted in the Fig. 1.3.

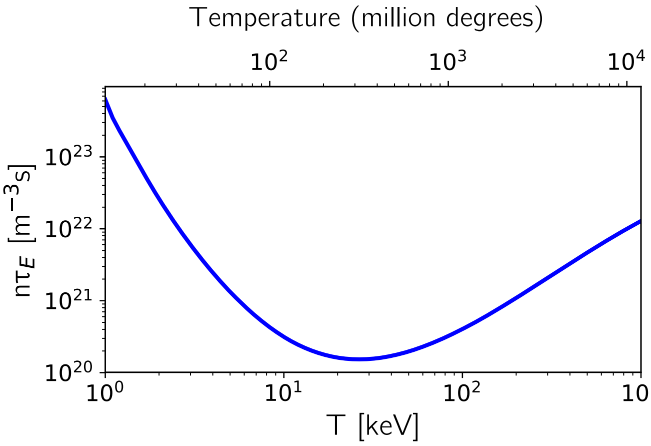

Figure 1.3: The minimum value of $n\tau_E$ which is required to obtain ignition in a D-T plasma, as a function of the plasma temperature. Data taken from [25].

This suggests that the plasma temperature should be kept at about 15 keV, where we find the maximum of fusion output. At this temperature, the ignition condition reads as

$$n\tau_E \geq 1{,}5 \cdot 10^{20} \tag{1.6}$$

with n=[m^{-3}] and τ_E=[s], which is known as *Lawson criterion* [27].

If such criterion cannot be achieved, then some external sources of thermal power need to be used to keep the plasma sufficiently hot.

1.2 Magnetic plasma confinement

We saw that a system which is in the condition to perform fusion reactions must be in the form of plasma; this is a state of matter constituted by charged particles only whose behavior is mainly influenced by long-range forces by external electromagnetic fields, rather than by single-particle interactions (cfr. Appendix A.1.2). The most interesting consequence of this is that a *fusion plasma* can be confined in a given region of space by means of external magnetic fields with adequate configuration, since the motion of the single charged particles will simply follow the magnetic field lines.

1.2.1 Toroidal confinement

The magnetic geometry which is most exploited for this goal is an axially symmetric closed field line geometry with toroidal configuration: as electrons and ions maintain a motion along field lines which close into themselves, they will be confined within a finite torus-shaped volume. In such a geometry, one makes use of an angle φ describing the *toroidal angle* and, at a given toroidal location, of local polar coordinates (θ, r), where θ is the *poloidal angle* and r is the *minor radius*; then, the quantity R_0, which is the distance between the geometric axis of the device and the center of the plasma, is called *major radius.* This is depicted in the Fig. 1.4.

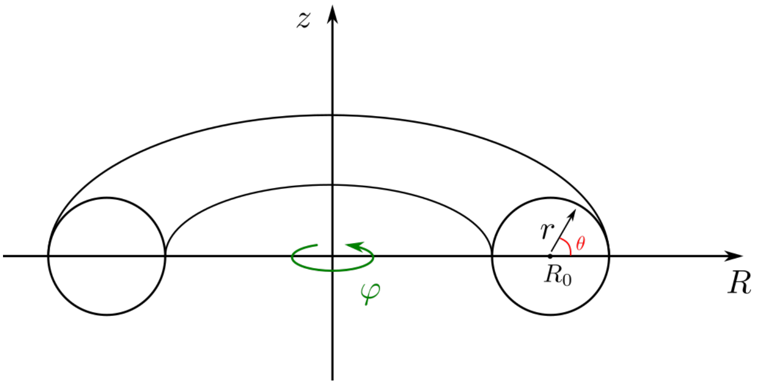

Figure 1.4: Coordinates in toroidal geometry.

In this framework, a first source of confinement can be given by creating a magnetic field characterized by field lines travelling along the toroidal direction, usually called *toroidal field* $\boldsymbol{B}_\varphi$. In a first approximation, charged particles will be confined in the volume of the torus by simply following the field lines which close into themselves each toroidal transit.

A simple toroidal field, however, is not sufficient for an optimum confinement since, in this case, particle drifts would produce fast radial losses of particles, as a consequence of the toroidicity of the geometry. In fact, a purely toroidal field would show a dependence $B_\varphi \propto \frac{1}{R}$ with the major radius: this means that such field would present both a curvature of its field lines and a spatial gradient directed in centripetal direction. Both these features would give rise to a vertical drift of plasma particles (namely, curvature drift and ∇B drift), so that the positive ions would drift to the upper side of the torus and the negative ions to the lower side. This would result in a net charge separation and thus in a vertical downward directed electric field; this would finally yield a net radial plasma drift to the outer side of the torus due to the $\boldsymbol{E} \times \boldsymbol{B}$ drift motion, making the confinement unstable.

A better confinement could be achieved by twisting the field lines by the introduction of an additional field component whose field lines are circles on the poloidal plane, i.e. a *poloidal field* $\boldsymbol{B}_\theta$. So, the resulting total field $\boldsymbol{B}_\varphi + \boldsymbol{B}_\theta$ will have field lines winding helically around the torus, which results in the vertical drift driving the particles to an alternate inward/outward motion; the result is no net vertical charge separation and thus no radial drift, obtaining finally an equilibrium configuration.

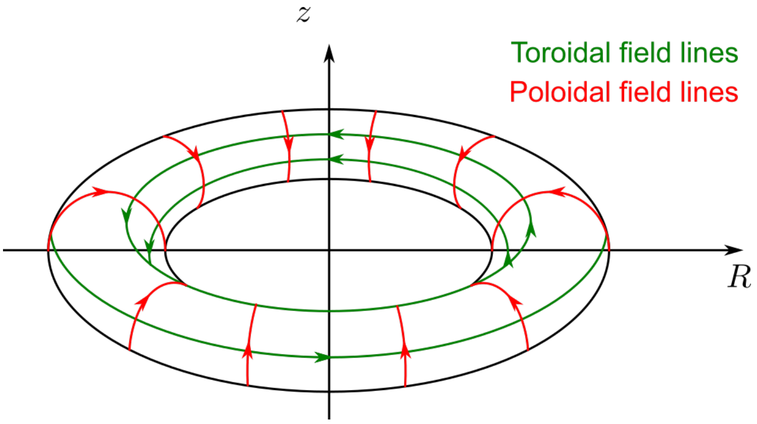

Figure 1.5: Components of the magnetic field in a toroidal configuration.

In such a magnetic geometry, each helical field line will lie on one of a nested set of *magnetic flux surfaces*; these can be described by means of a so-called *magnetic flux function* ψ, defined by $\boldsymbol{B} \cdot \nabla\psi = 0$, so that these surfaces are defined as the contour surfaces where ψ is constant. So, when projected on a poloidal cross section, the motion of plasma particles along the field lines will simply follow the contour of the flux surfaces projected on the poloidal plane.
Force equilibrium for an effective confinement requires that a radially inward directed magnetic force balances the radially outward directed pressure force resulting form the thermal expansion of the plasma (cfr. Appendix A.2.2). Such balance is described by the relation

$$\boldsymbol{J} \times \boldsymbol{B} = \nabla p \tag{1.7}$$

where $\boldsymbol{J}$ is the electric current. In this sense, confining the plasma means to achieve a magnetic configuration which provides toroidally nested surfaces with a maximum pressure at the center (i.e. the innermost flux surface, namely the magnetic axis) and small pressure in the edge region. So, we can say that the particular equilibrium configuration of the magnetic flux surfaces, and thus ultimately the poloidal cross-sectional shape of the plasma, is determined by the balance equation (1.7). From this we can deduce that $\boldsymbol{B} \cdot \nabla p = 0$, meaning that the pressure is constant on each magnetic flux surface; moreover, from the charge conservation $\nabla \cdot \boldsymbol{J} = 0$ we can state that also the current lines lie on the same flux surfaces, just like the magnetic field lines. This situation is schematically shown in the Fig. 1.6.

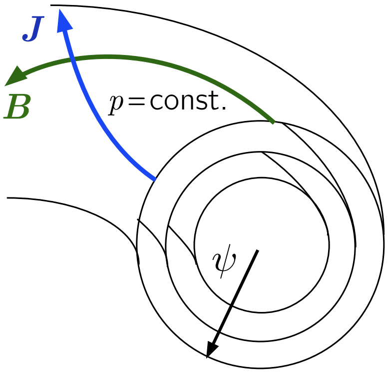

Figure 1.6: Set of toroidally nested magnetic flux surfaces [28].

In order to describe one particular magnetic configuration and to quantify the degree of helicity of the field lines, it is used to define the following parameters.
First, we define the *aspect ratio* a as the fraction

$$a = \frac{R_0}{r} \tag{1.8}$$

with r radial coordinate of the considered field lines with respect to the magnetic axis and R_0 major radius of the torus. If $a \gg 1$, the toroidal flux surfaces could be approximated as cylindrical surfaces. Then, we define the *safety factor* q as the number of toroidal transits for one complete poloidal rotation; in a cylindrical approximation (large aspect ratio $B_\theta / B_\varphi \ll 1$, in which many toroidal transits are needed for completing one poloidal round), this is given by

$$q \approx \frac{rB_\varphi}{R_0 B_\theta} \tag{1.9}$$

If, for a particular flux surface, q is a rational number, then a field line lying on it will close on itself once a poloidal rotation is completed; instead, if q is an irrational number, then a field line will never exactly close on itself, covering rather ergodically the entire flux surface after an infinite number of transits.
Related to this quantity is the local *pitch angle* θ_{pitch}, which quantifies the inclination of a field line with respect to the toroidal direction, as

$$\theta_{pitch} = \frac{B_\theta}{B_\varphi} \approx \frac{B_\theta}{B} \tag{1.10}$$

More detailed concepts about the magnetic equilibrium configuration of toroidally axisymmetric plasmas can be found in the Appendix A.2.3.

1.2.2 The *tokamak* concept

There are different practical approaches for confining a plasma in a toroidal geometry. The most common one, and the one to which the research work of this thesis is devoted, is the *tokamak* [2], with which so far the best confinement properties and the highest temperatures have been achieved.
Here, the toroidal field is produced by currents flowing in an axially symmetric set of magnets surrounding externally the chamber where the plasma is confined, which are called *toroidal field coils*. Then, a central solenoid, acting as the primary circuit of a transformer, is used to produce a time-varying poloidal magnetic flux which induces a toroidal loop voltage, and thus a net current flowing in toroidal direction, called *plasma current* I_p; this, in turn, generates the poloidal field as

$$B_\theta \approx \frac{\mu_0 I_p}{2\pi r} \tag{1.11}$$

This current, besides producing the poloidal field, naturally provides also a heating source for the plasma, by means of the ohmic heating mechanism, due to a finite plasma resistivity R_p, with resulting heating power

$$P_{ohm} = R_p I_p^2 \tag{1.12}$$

In addition, further coils are used to produce a vertical field which allows to create a wide range of plasma shapes and to perform a real-time control of eventual instabilities. Typically, vertically elongated plasmas are produced in this way.

Typical operation of a tokamak discharge starts with the establishment of a large, steady, toroidal field. Next, neutral fuel gas is injected into the chamber in which the plasma is intended to be created. The transformer-induced current starts then to be applied, and the heating source provided from it ionizes the gas taking it to the plasma state; this current is finally ramped up to its maximum value and maintained for the "flat top" portion of the discharge. However, the magnitude of the peak current is such as to induce a poloidal field which is, usually, substantially weaker than the toroidal field (making the large aspect ratio assumption generally valid for tokamaks). During flat top operation, usually, an additional external heating source, in the form of radiofrequency waves or neutral particle beams, is applied to the plasma.
The advantages of such configuration with respect to other toroidal concepts are:

- The large toroidal field, and the correspondingly high safety factor at the plasma edge ($\gtrsim 3$), lead to high values of the energy confinement time τ_E, of the order of tens of ms. So, the good confinement allows the plasma to heat up to high temperatures using a relatively moderate amount of external heating.
- Particular configurations with elongated, non-circular poloidal cross sections are capable of stably confining reactor-grade plasma pressures.

However, the ohmic transformer cannot inductively drive a direct current for an indefinite period of time, for which reason the induced plasma current would result to be alternate. Therefore, for a tokamak to operate in steady state, a large external current drive is also required for sustaining a plasma current which keeps constant at least for the duration of the flat top operation.

In the Fig. 1.7 a schematic design of a tokamak is depicted, in which all the main components are shown.

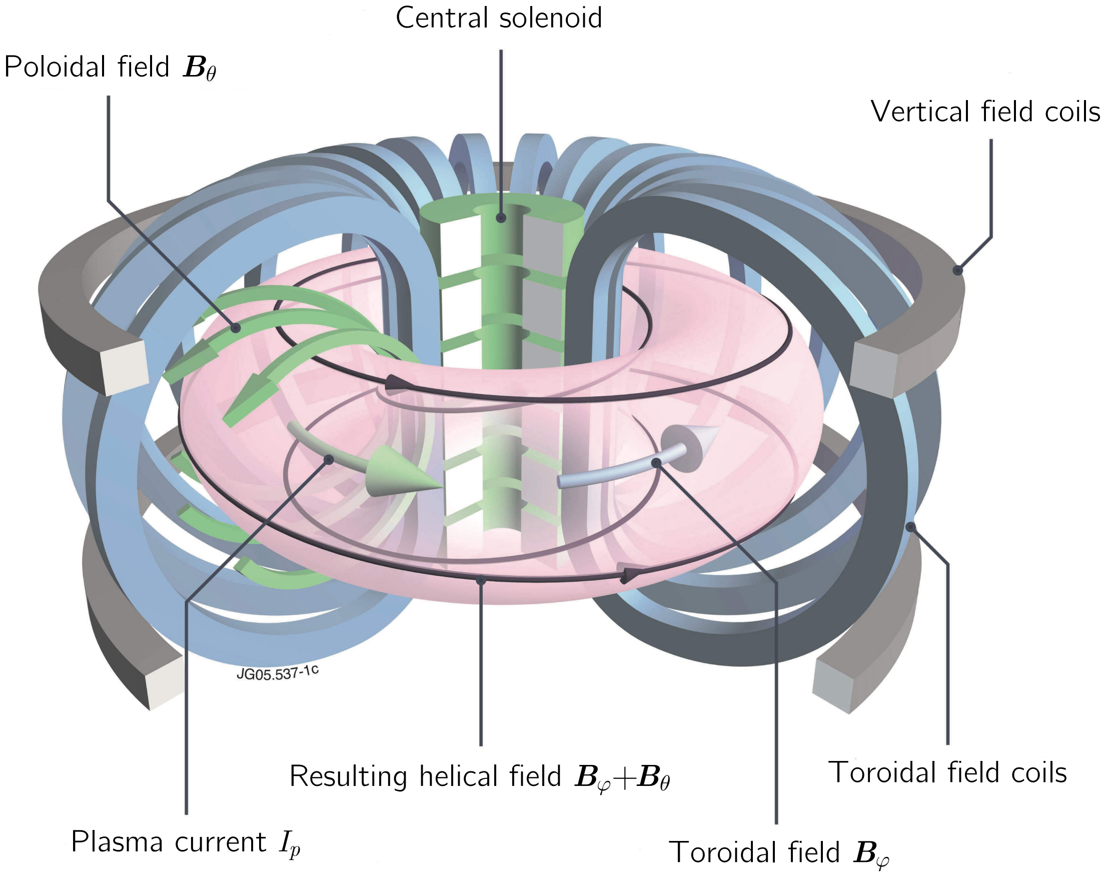

Figure 1.7: Schematic design of a tokamak. Taken from [29].

Chapter 2

Scrape-off layer and divertor physics

In this chapter, the properties of the plasma boundary which are of interest for this thesis will be introduced. First of all, in the Section 2.1 the main characteristics of the divertor tokamak configuration, which is the experimental setup of interest for this work, will be presented; in particular, focus will be given to the global particle and energy balances of this region and on the main physical processes influencing these balances, namely plasma-material interaction and volumetric atomic processes. Then, starting from these fundamental concepts, in the Section 2.2, a simple mathematical model of the plasma boundary will be developed, focusing in particular on the more relevant aspects for its numerical modelling. This will lead to the introduction of several physical characteristics of the plasma in this region, which ultimately yield different operating regimes: an overview of such regimes, together with the resulting differences in the impact on particle and energy balances, will be presented in the Section 2.3. Finally, in the Section 2.4, the physical processes occurring in this region which motivate this work, namely enhanced perpendicular transport driven by radial propagation of blob-filaments and consequent formation of density shoulders, will be introduced.

2.1 Basic aspects of the plasma boundary

The boundary region of tokamak plasmas has a critical importance for both physics and engineering reasons, since it is directly related to the requirements for *particle* and *power exhaust* from the plasma which must be satisfied for a good confinement [7][8].

The major issue consists in the problem of the interaction between the plasma and the solid materials constituting the device: in case of uncontrolled contact with the internal walls of the chamber, severe engineering problems would likely arise due to the resulting exceedingly large *heat loads* on the materials. Realistic values of tolerable loads for steady-state operations should be, indeed, below about $5 - 10$ MW/m^2, in order to prevent melting of the materials [6][9][10]. Another major problem is the eventual *erosion* of these materials, which would lead to a contamination of the plasma with atoms ripped from these due to the plasma-surface interaction [30]: if uncontrolled, these impurities would radiate strongly in the plasma, through bremsstrahlung and line radiation emission, leading to such a strong cooling to prevent a good confinement.

So, the plasma-material interaction should be controlled, avoiding damages to the material surfaces by keeping the maximum heat loads onto these within acceptable engineering limits, and held as far as possible from the confinement region, in order to minimize plasma contamination.

2.1.1 Divertor configuration

The requirements for a safe particle and power exhaust from tokamak plasmas can be achieved with various different techniques. The most promising strategy, and the one which future devices

are likely to be based on, consists in the modification of the magnetic field geometry at the edge of the confinement region by means of an external conductor, placed below the plasma, carrying a current in the same direction as the plasma current [7][8]. As the magnetic geometry, in this way, is somehow "diverted" with respect to a simple toroidal configuration, the resulting one is called *divertor configuration*. The result is a distortion in the poloidal cross section of the magnetic flux surfaces around the plasma edge region; in particular, there will exist a null in the poloidal field, called *X-point*, and the flux surface passing through it will separate an internal region, characterized by closed magnetic field lines, from an outer region, characterized instead by open magnetic field lines; for this reason, such particular flux surface is called *separatrix*.
The region inside the separatrix will be then the actual confinement region for the plasma, since only here plasma particles are confined by following the helical field lines nested around closed flux surfaces; for this reason, it is called the *core plasma*. The region outside the separatrix, characterized by open field lines, is called *scrape-off layer (SOL)*, and constitutes then the actual boundary region of diverted plasmas. Finally, the plasma region inside the separatrix but below the X-point is called *private flux region (PFR)*.
With such configuration, the plasma-material interaction is effectively moved away from the core plasma, being concentrated now on solid plates, placed below the X-point, cutting the flux surfaces in the SOL region, called *divertor targets*. In fact, particles diffusing through the separatrix will just rapidly flow to these targets following the field lines, while still diffusing radially; this will make eventual impurities generated from the plasma-material contact at the targets be concentrated here, away from the confinement region. For this reason, divertor targets must be designed and constructed in such a way to withstand the extremely severe heat loads due to the incoming plasma. The portions of the overall divertor targets which are in direct contact with relevant incoming plasma fluxes are called *plasma-wetted areas*.
Since the ratio of parallel to perpendicular velocity of particles, with respect to the field lines direction, is very high, the region characterized by open field lines striking the solid targets, i.e. the SOL region, still filled with plasma is very thin, of the order of several mm. This definitely makes the plasma-wetted areas quite small in comparison with the total internal surfaces of a device.
The resulting configuration is schematically illustrated in the Fig. 2.1.

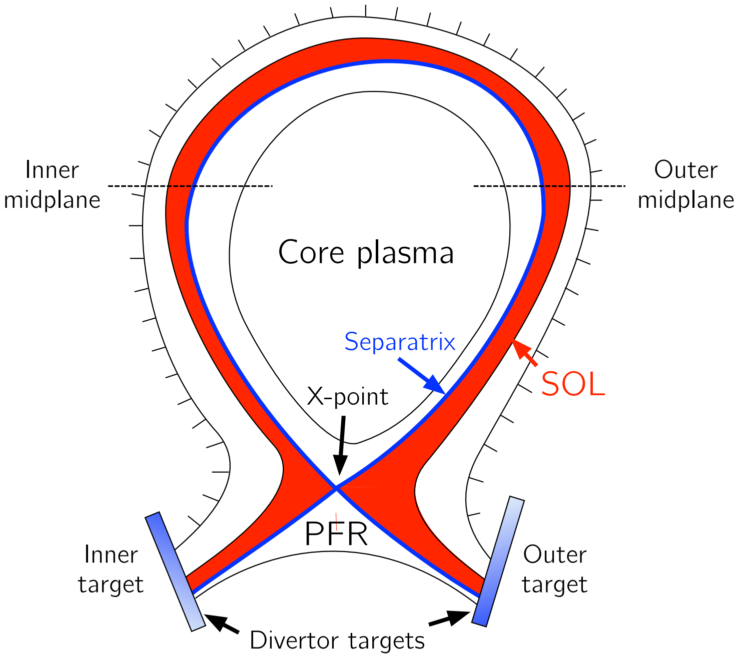

Figure 2.1: Schematic illustration of the scrape-off layer region in a divertor configuration [28].

The main characteristics which give importance to the divertor concept, with respect to other configurations for the plasma boundary, are:

- Achievement of low temperatures in the divertor region, which reduces the impact of the plasma-material interaction on the targets [8].
- Efficient *gas pumping*, through pumps located near the targets, which allows to control the fuel gas density in the chamber and to efficiently remove impurities and ashes from the plasma, in order to avoid fuel dilution and radiation cooling [31].
- Accessibility of an improved confinement regime, namely the so-called *high confinement mode (H-mode)*, in which the confinement of energy and particles in the hot burning plasma can be improved by a factor of 2 with respect to the so-called *low confinement mode (L-mode)* [32].
- Possible achievement of an efficient exhaust regime, consisting in a strong reduction of both particles and heat fluxes onto the targets, in a condition called *detachment* (cfr. Section 2.3.3), reducing then the impact of plasma interaction on target materials [33].

In this framework, we define the *connection length* $L_\parallel$ as half the parallel distance (i.e. along the field lines) between the inner and the outer divertor targets. If the geometry is symmetric, with approximately equal X-point-to-target poloidal distances, this is simply shown to be

$$L_\parallel \approx \pi R_0 q \tag{2.1}$$

with R_0 major radius of the torus and q safety factor in the SOL region (eq. (1.9)).
Another important quantity is the surface area of the separatrix, crossed by particles and heat from the confinement region flowing into the SOL, that is

$$A_\perp = 2\pi R_0 \cdot 2\pi a \cdot \kappa^{1/2} \tag{2.2}$$

with $\kappa \equiv b/a$ plasma elongation, being a, b the horizontal and vertical minor radii of the plasma. Finally, defining δr as the radial distance between two magnetic flux surfaces in the poloidal plane (cfr. Fig. 2.2), such width will be enlarged in proximity to the targets due to the presence of the divertor current; such enlargement can be quantified by means of a quantity called *magnetic flux expansion* f_x, defined as

$$f_x = \frac{\delta r_{\text{target}}}{\delta r_{\text{midplane}}} \approx \frac{(B_\theta/B)_{\text{midplane}}}{(B_\theta/B)_{\text{target}}} \tag{2.3}$$

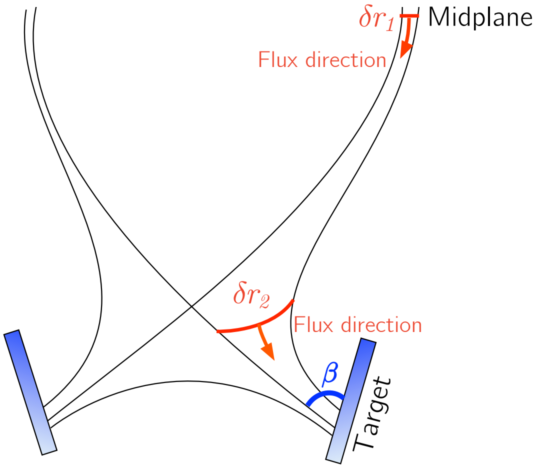

Figure 2.2: Flux expansion near the divertor targets [28].

2.1.2 Plasma-material interactions

In the framework of scrape-off layer studies, critical relevance is given to some physical processes which are peculiar of such region of the plasma because of its vicinity to the material surfaces of the device (both divertor targets and main chamber wall). The most immediate consequence of this is the presence of several kinds of *plasma-material interactions*, occurring when plasma particles are in direct contact with a solid surface [30]. In fact, these surfaces are subject to a continuous flow of charged particles carrying a large fraction of the power exhausted from the core plasma: in this way, their kinetic energy is transferred to the materials, leading to a wide spectrum of consequences.

Major effects arise, in particular, when the ions strike these surfaces, because of their larger mass with respect to the electrons; when this occurs, they can undergo:

- *Absorption*, and consequent trapping in the surface.
- *Reflection* with some fraction of their impact energy, i.e. release as fast ions.
- *Thermal release*, i.e. accommodation in the surface, with subsequent release as thermal ions with velocity dependent on the surface temperature.

Alternatively it can occur that the incident ions, when striking the surface, recombine by ripping off one electron from the surface atoms and are then released again in the plasma in form of neutral atoms. Soon or later, these will be ionized again in the plasma: a steady-state situation in which the rate of loss of charged particles from the plasma equates the rate of re-emission of neutrals constitutes the so-called *fuel recycling*.

Thermal re-emission of incident ions as neutral atoms occurs more usually when the impact energy is low. In particular, if the surfaces are already saturated by implanted ions, then incident ions here undergo surface recombination and re-emission as neutrals with a very high probability.

Another possible consequence can take place if the incident ions are very energetic: in this case, they could transfer momentum to the material and, eventually, erode it, if enough energy is transferred to overcome the surface binding energy E_B necessary to rip off one atom from the material lattice (Fig. 2.3a). This is a threshold process, since enough momentum is transferred only if the incident ion possesses a minimum kinetic energy; the threshold energy E_{th} required to release in this way a surface atom into the plasma can be estimated as [7]

$$E_{th} = \frac{E_B}{\delta(1-\delta)} \tag{2.4}$$

where

$$\delta = 4\,\frac{m_1 m_2}{(m_1+m_2)^2} \tag{2.5}$$

is the maximum energy fraction which can be transferred into a single collision from the incident ion, with mass m_1, to a surface atom, with mass m_2. This phenomenon is known as *physical sputtering*; it is usually quantified by means of a *sputtering yield* Y, defined as the number of surface atoms ejected per impacting ion through such mechanism.

The sputtering yield for monoatomic solids shows a common general behavior for different materials and for light and heavy ions [34]. Colored lines in the Fig. 2.3b represent the physical sputtering yields for incident deuterium ions on different solid materials in function of the impact energy. Peak yields typically take place from hundreds to thousands eV; for even higher impact energies a drop exists, because in this case the impacting ions deposit less energy in the surface layers, since they have enough energy to penetrate deeper into the lattice structure. As can be deduced from the Fig. 2.3b, erosion is minimized for materials with high atomic number Z; in fact, as we can see in eq. (2.4), a large value for E_{th} can be achieved for large values of δ, which in turn is obtained when the mass of the surface atoms is large.

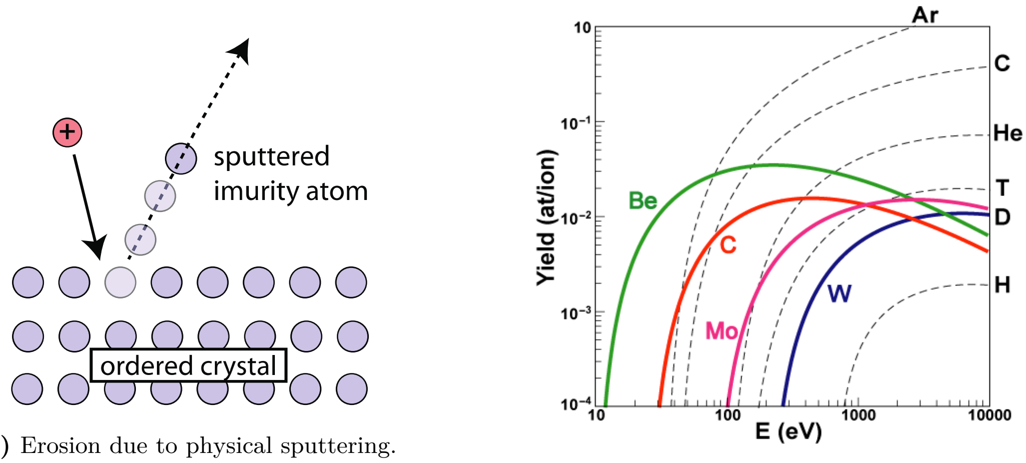

(a) Erosion due to physical sputtering.

(b) Sputtering yields in function of the impact energy.

Figure 2.3: Mechanism of physical sputtering. Taken from [35].

The relevance of this phenomenon is given by the fact that, in this way, the plasma could become contaminated by a number of impurities resulting from the ejection of surface atoms into it. Trying to minimize this phenomenon constitutes one fundamental reason for the employment of divertor configurations for fusion devices, i.e. moving this interaction mainly on targets far from the core plasma; moreover, as such configuration succeeds in achieving a relatively cold plasma in front of the targets, the sputtering yields are minimized in this way as well.
It turns out that the materials for the components of fusion devices which are in direct contact with the plasma, usually referred to as *plasma-facing components*, should be carefully selected, in view of all the possible processes occurring on them. The selection is then performed by weighting requirements for plasma performance (i.e. minimization of erosion and consequent contamination by impurities, which requires low sputtering yields) and engineering constraints (i.e. withstanding of thermal loads, which requires high melting point, thermal conductivity and mechanical resistance) [30]. For future devices, the choice of tungsten seems to be the best compromise since, being a high-Z element, it features a very low sputtering yield, in addition to high melting point and thermal conductivity.

2.1.3 Volumetric processes

A number of different *volumetric atomic processes* occurring in the SOL must be also considered, since they deeply influence its behavior and, definitely, lead to the distinction between operating regimes (cfr. Section 2.3). These primarily occur because of the unavoidable presence of *neutrals* in the SOL plasma, because of the fuel recycling and of the existence here of sufficiently low temperatures which could make the recombination of charged particles actually possible [8].

In detail, primary importance must be given to the presence of *ionization* processes, in which neutrals, after the impact with fast plasma electrons, gain enough energy to ionize and form a further couple of free electron/ion. For this, a source term for plasma particles will exist, given by the ionization rate density S_i, in $\mathrm{m}^{-3}\mathrm{s}^{-1}$, of neutrals, the last ones with density n_n, which is

$$S_i = n n_n \langle \sigma v \rangle_i \tag{2.6}$$

with $\langle \sigma v \rangle_i$ ionization rate coefficient.

Similarly, the presence of *recombination* processes must be also considered, which are basically the opposite of ionization, in which an electron is sufficiently slow for being captured by an ion to form a neutral atom. For this, a sink term for plasma particle will exist, given by the recombination rate density S_r, in $\mathrm{m}^{-3}\mathrm{s}^{-1}$, of plasma particles, which is

$$S_r = n^2 \langle \sigma v \rangle_r \tag{2.7}$$

with $\langle \sigma v \rangle_r$ recombination rate coefficient.

In the Fig. 2.4 rate coefficients for ionization and recombination in function of the plasma temperature are shown, for a hydrogenic plasma, as resulting from weighting the corresponding cross sections over a maxwellian velocity distribution for plasma particles.

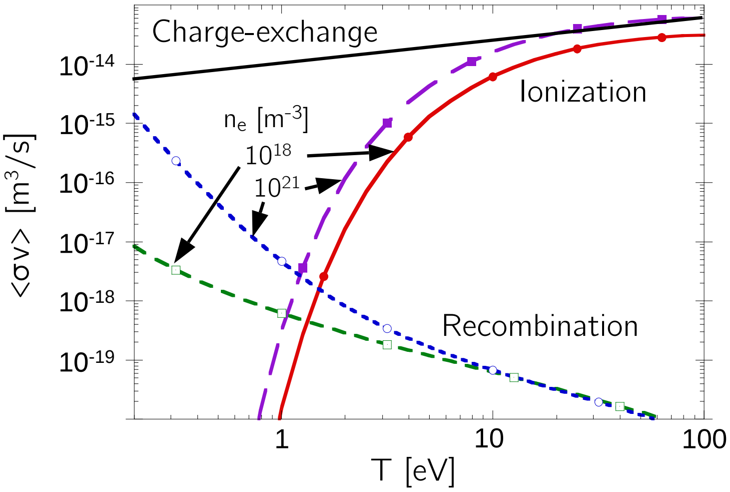

Figure 2.4: Rate coefficients for ionization, recombination and charge-exchange collisions for a hydrogenic plasma. Taken from [18].

As we can see, the ionization rate coefficient clearly increases with temperature, and it strongly drops for temperatures below about the hydrogen ionization energy (which is 13,6 eV). Moreover, at higher densities multi-step ionization processes become relevant, in which atoms ionize from excited states: this leads to an increase of the coefficient with density as well.

On the other hand, the recombination rate coefficient decreases with increasing temperature, since at larger temperatures electron-ion interactions decrease in frequency, and thus also their probability to recombine. In particular, for temperatures below about 2 eV it becomes larger than the ionization rate coefficient, so that large populations of neutrals must be expected where such low temperatures are reached. In each case, this also increases with density.

Ionization always represents a particle source and an energy sink for the plasma, because of the energy cost for each process and of the eventual residual energy emitted as radiation if the resulting ion is left in an excited state. Recombination, instead, always represents a particle sink for the plasma, but it does not generally represent an energy source. In fact, at low density the simple two-body recombination is dominant, and all of the recombination energy is emitted by radiation by the resulting excited neutral atom, being then lost from the plasma; instead, only at higher densities the so-called three-body recombination events become relevant, in which part of the recombination energy goes to a second electron involved in the process, resulting then in some energy source for the plasma.

Another non negligible feature is given by ion-neutral collisions. These are due the fact that, mainly in the divertor region, the plasma flows into a "sea" of cold neutrals; this gives rise to the so-called *charge-exchange collision* processes, in which the net charge is transferred from the ion to the neutral during the interaction, occurring with a rate density S_{CX}, in $\mathrm{m}^{-3}\mathrm{s}^{-1}$, given by

$$S_{CX} = n n_n \langle \sigma v \rangle_{CX} \tag{2.8}$$

with $\langle \sigma v \rangle_{CX}$ charge-exchange rate coefficient. Because of the friction effect due to the collision with the slower neutrals, this provides a relevant momentum loss term for the plasma, especially at low temperatures. In fact, for these collisions to be effective, a sufficiently large number of them should occur before neutrals start ionizing. As we see in Fig. 2.4, where also the charge-exchange rate coefficient for a hydrogenic plasma is shown, the ratio of charge-exchange collision rate and ionization rate rapidly increases below about 10 eV; so, only below this temperature ion-neutral collisions play a significant role in providing momentum losses. Moreover, since ions are effectively slowed down, this process also represents an energy sink for the plasma.

Finally, also other kinds of volumetric power losses have to be mentioned, in form of radiation emission processes, which are *bremsstrahlung emission* and *line radiation* of impurity ions, intrinsically produced after material erosion, and fuel neutrals; both these mechanisms are more relevant at higher plasma densities. Since, in future devices, a highly dissipative regime is desired, it will be tried to increase these losses, in order to relax the heat loads onto the divertor targets, by even deliberately seeding impurity atoms into the SOL plasma, contributing then as impurity radiation. Currently, the feasibility of argon, nitrogen, neon and krypton as possible seeding species for this purpose is being investigated [36][37].

2.1.4 Power and particle balance

Understanding the problem of particle and power exhaust from magnetic fusion devices, which is of crucial importance for this work, involves a deep comprehension of the global *power* and *particle balances* in the SOL. These, in fact, control the features of the exhaust processes as well as, ultimately, the impact on main wall and divertor materials.
The review of the basic surface and volumetric processes occurring in SOL plasma allows now to give a general overview on such global balances, a schematic picture of which is shown in the Fig. 2.5.

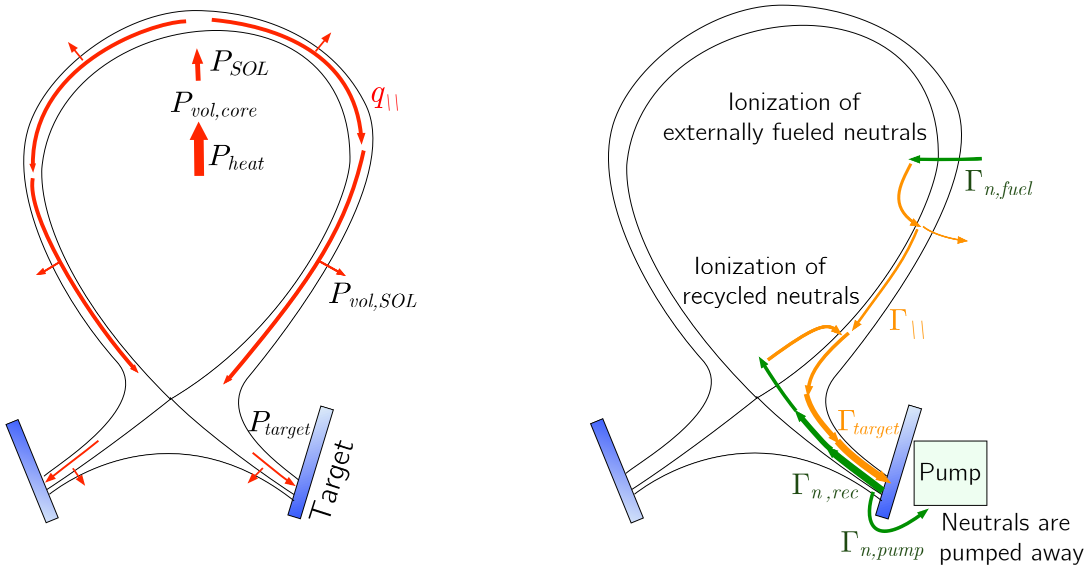

(a) Power balance **(b)** Particle balance

Figure 2.5: Schematic picture of the global power and particle balances in the SOL [28].

In the confinement region the plasma is heated with a total heating power P_{heat} which, in the current experiments, is provided by auxiliary heating systems (ohmic heating, radiofrequency heating and neutral beam injection). A fraction $P_{vol,core}$ of this power is dissipated inside the core plasma itself by radiative processes; then, the remaining part $P_{SOL} = P_{heat} - P_{vol,core}$ is radially transported across the separatrix, with a rate which depends on the employed confinement mode, and ultimately constitutes the SOL input power.
From here on, this power will flow predominantly parallel to the magnetic field lines, because of the sink action provided by the material targets at the divertor, with a heat flux density $q_{\parallel}$. However, in the meanwhile, in the SOL further volumetric losses $P_{vol,SOL}$ take place, so that the total power which results to be deposited onto the targets is $P_{target} = P_{SOL} - P_{vol,SOL}$.
The volumetric losses in the core and SOL plasmas mainly consist in the already mentioned bremsstrahlung emission and line radiation of impurity ions (both intrinsically produced and eventually deliberately seeded) and fuel neutrals, and in the plasma-neutral interactions.

Regarding, then, the particle balance, we have that, after crossing the separatrix, plasma particles flow to the targets, resulting in a particle flux density Γ_{target} onto these. For usual plasma temperatures of few eV near the targets, most of the incoming ions actually recombine to neutrals at the target surfaces, while for even lower temperatures these could already recombine in the SOL region before the targets.
The neutrals resulting from such processes can then leave the target again towards the plasma, leading to a flux $\Gamma_{n,rec}$ of recycled neutrals. At saturation, the recombination rate at the targets equates the neutral flux towards the plasma, and a large fraction of the neutrals coming from the targets is then re-ionized in the core plasma, where the temperatures are again sufficiently large; this leads to a new net plasma particles source in the SOL by fuel recycling. In order to control the particle content in the plasma, a part $\Gamma_{n,pump}$ of $\Gamma_{n,rec}$ can be actually pumped away near the targets, for limiting the rate of plasma particles which ultimately strike the targets.
Furthermore, the core plasma can also be fueled by an external neutral particle source $\Gamma_{n,fuel}$, named *gas puff* source, in order to keep a sufficient number of fuel species in the confinement region.

2.2 Scrape-off layer modelling

Predicting the particle and heat loads onto the divertor targets at any operating conditions involves a complete understanding of the plasma profiles and flux patterns in the scrape-off layer. These result from the competition between the *parallel transport*, along the field lines up to the divertor targets, and the cross-field *perpendicular transport* from the separatrix to the main chamber wall, as well as from the different loss processes taking place before the targets. Therefore, the underlying physics of particle and power exhaust from the SOL plasma needs to be discussed in some detail, in order to develop simple physical models of SOL transport and obtain simple general dependencies of the main SOL plasma parameters on the operating conditions; in this way, these could be finally used for a basic interpretation of experimental measurements and numerical results. In the following, [7] will be taken as main reference.

2.2.1 Parallel transport and conservation equations

As already mentioned, once that particles have crossed the separatrix entering the SOL region, the sink action given by the presence of material targets makes the parallel transport along magnetic field lines much stronger than cross-field diffusion. In a first approximation, it is reasonable to consider this transport component as purely collisional, so that it is possible to

describe it by means of fluid conservation relations, and consider the cross-field radial transport as a source/sink term.
In particular, this can be considered true when the self-collisional *mean free paths* λ of electrons and ions are small when compared with some characteristic parallel length of the SOL. These quantities are numerically related to the plasma conditions as [7]

$$\lambda_{ee} \approx \lambda_{ii} \approx 10^{16} \frac{T^2}{n} \tag{2.9}$$

with $n = [\mathrm{m}^{-3}]$, $T = [\mathrm{eV}]$. Assuming that a particle, when entering in the SOL, travels on average a distance given by the connection length $L_\parallel$, a fluid description turns out then to be reasonable when the ratio

$$\nu_{SOL} \equiv \frac{L_\parallel}{\lambda} \tag{2.10}$$

is greater than 1, which is usually the case for current devices. Moreover, as we will see later, the relative magnitude of this quantity also determines the actual SOL operating regime.

A very simple model for the parallel transport in the SOL can be developed in a one-dimensional geometry, along a curvilinear coordinate x parallel to the field direction, considering a steady-state situation. In this sense, focus is given to the balance of plasma quantities along one particular flux tube, as sketched in the Fig. 2.6.

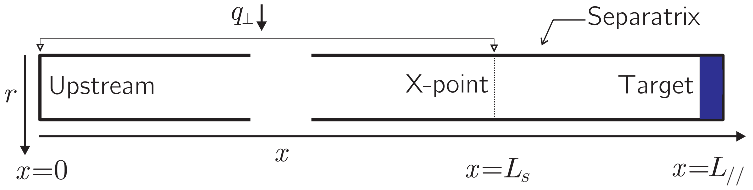

Figure 2.6: One-dimensional "slab" geometry for a given flux tube in the SOL. Taken from [18].

Although numerical codes usually make use of more complete two-dimensional models, as the one developed in the Appendix C.1 in the Braginskii formulation, a simple one-dimensional model for the plasma flow in the SOL towards the targets is still useful for a basic comprehension.
This flow can be characterized, in each point, by a density $n(x)$ and by electron/ion temperatures $T_e(x)$, $T_i(x)$. The static pressure for electrons and ions is $p_e(x) = n(x)T_e(x)$, $p_i(x) = n(x)T_i(x)$. Finally, given $v(x)$ the bulk velocity of the plasma flow, the particle flux density in parallel direction will be $\Gamma_\parallel(x) = n(x)v(x)$, in $\mathrm{m}^{-2}\mathrm{s}^{-1}$.
Starting from a general kinetic equation for the system, taking its lowest-order moments leads, with straightforward calculations [7], to the:

- *Continuity equation*

$$\frac{d}{dx}(nv) = S_p \tag{2.11}$$

  stating that the local variation of the particle flux is due to an eventual local particle source density S_p, in $\mathrm{m}^{-3}\mathrm{s}^{-1}$, resulting from cross-field diffusion $S_\perp$ and ionization of neutrals S_i (eq. (2.6)) minus recombinations S_r (eq. (2.7)).

- *Momentum conservation equation*

$$\frac{d}{dx}(p_e + p_i + m_i n v^2) = -m_i(v - v_n)S_{CX} + m_i v_n S_p \tag{2.12}$$

  stating that the local variation of pressure (static $p_e + p_i$ plus dynamic $m_i n v^2$) is due to losses caused by the interaction between ions and neutrals (i.e. charge-exchange collisions, eq. (2.8)), and by a viscous drag force given by the local creation of particles with source density S_p.

- *Energy conservation equation*

  $$\frac{d}{dx}\left[q_{\parallel,cond} + \frac{5}{2}\Gamma_{\parallel}(T_e + T_i) + \frac{1}{2}m_i v^2\right] = Q_{joule} + Q_{rad} \tag{2.13}$$

  stating that the local variation of the heat flux (by electron/ion conduction, electron/ion convection and kinetic energy flow) is due to the joule heating Q_{joule}, resulting from the electron-ion friction, and to the sink Q_{rad} resulting from various kinds of volumetric power losses (i.e. interaction with neutrals and radiation losses), both in W/m^3.

For closing the system of fluid equations, it is necessary to prescribe a constitutive relation for the parallel conduction heat flux density $q_{\parallel}$, in W/m^2. The most common prescription consists in assuming a linear proportionality with respect to the parallel temperature gradient. In the limit of high collisionality, it can be shown (cfr. Appendix C.1.3) that, for a one-dimensional geometry, in a direction parallel to the magnetic field, for electrons and ions we have, respectively,

$$\begin{aligned} q_{\parallel,cond,e} &= -\kappa_{0,e} T_e^{5/2} \frac{dT_e}{dx} \\ q_{\parallel,cond,i} &= -\kappa_{0,i} T_i^{5/2} \frac{dT_i}{dx} \end{aligned} \tag{2.14}$$

Here, the explicit temperature dependencies of the electron and ion parallel thermal conductivities (first eqs. of (C.22), (C.23)) is manifested, in which the quantities $\kappa_{0,e}$, $\kappa_{0,i}$, usually called *Spitzer-Härm conductivities*, are constant and given by

$$\begin{aligned} \kappa_{0,e} &\approx \frac{30692}{Z_i \ln\Lambda} \\ \kappa_{0,i} &\approx \frac{1249}{Z_i^4 m_i^{1/2} \ln\Lambda} \end{aligned} \tag{2.15}$$

with m_i = [amu]. The resulting values of these for a hydrogenic plasma are about 2000 for electrons and 60 for ions, in units of W/eV$^{7/2}$m; it can be then deduced that, at similar temperatures, the contribute of parallel electron conduction has a much larger magnitude with respect to ion conduction.

Finally, in the framework of parallel transport modelling, some physical phenomena occurring at the plasma-material interface at the divertor targets, acting as boundary surfaces for the parallel plasma flow, have to be mentioned, i.e. the so-called sheath formation.
It occurs that, when a material surface is in direct contact with the plasma, the flowing electrons reach it much more rapidly than the ions if their temperature is comparable, because of their much lower mass. The target surface therefore will tend to be negatively charged so that, as such induced negative potential at the target increases, other electrons begin to be reflected back; this reduces the electron flux from the plasma onto the surface and increases the ion flux [30]. The resulting potential will then spontaneously adjust up to an equilibrium situation in which the flux of ions directed to the surface and the flux of electrons reflected from it become equal in magnitude. What results in this way is the so-called *ambipolar flux*, characterized by no net current is flowing towards the surface. The resulting potential difference with respect to the plasma potential is called *floating potential.*
In this way, just near the target a plasma layer with more positive charges than negative ones will be created, being the positive charges attracted now by the negative potential at the target; thus, quasineutrality does not hold anymore here. In this region the electric potential will then drop from the plasma potential Φ_p to a lower target potential Φ_t within a distance which, for an unmagnetized plasma, is of the order of the Debye length λ_D (eq. (A.3)). Such region is

usually called *Debye sheath*. If, instead, a magnetic field with a component tangential to the target exists, a further region with slightly decreased potential will exist, usually called *magnetic pre-sheath*, formed in front of the Debye sheath, which has a thickness of the order of the ion gyroradius ρ_i (eq. (A.5)). This situation is schematically depicted in the Fig. 2.7.

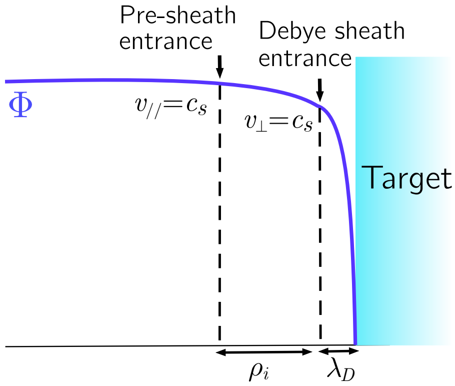

Figure 2.7: Illustration of the sheath and pre-sheath formation in front of a material target [28].

It can be shown that, at the entrance of the magnetic pre-sheath, the so-called *Bohm-Chodura criterion* for the parallel flow velocity of the plasma holds [38]:

$$v_\parallel \geq c_s \tag{2.16}$$

where

$$c_s \approx \sqrt{\frac{T_e + T_i}{m_i}} \tag{2.17}$$

is the *sound speed* at the sheath entrance. In addition, it can be also shown that, for avoiding singularities in the parallel velocity profile, the equality in (2.16) must hold; this act as an effective boundary condition for the parallel plasma flow.

From this, a boundary condition for the parallel heat flux at the sheath entrance $q_{\parallel,se}$ can be also deduced, which must be expressed as [7]

$$q_{\parallel,se} = \gamma T \Gamma_{\parallel,se} \tag{2.18}$$

having supposed an equal temperature for electrons and ions at the sheath entrance, where $\Gamma_{\parallel,se} = nv_{\parallel,se} = nc_s$, and γ is a sheath heat transmission factor. Although no complete theory exists for a rigorous determination of this factor, kinetic considerations allow to assume $\gamma \approx 7 - 8{,}5$ for a hydrogenic plasma [39].

2.2.2 The *two-point model*

Starting from the simple one-dimensional conservation relations derived in the previous section, it is finally possible to derive a simple analytic model for parallel plasma transport in the SOL, under some additional assumptions. The simplest model describes a situation with dominant electron conduction along the SOL, and is known as the *two-point model* [7], in which the presence of any volumetric process is, in a first approximation, neglected. The aim is to relate the properties at the *target* (denoted with t) to the properties at an *upstream* (denoted with u) position, the last one being defined as the stagnation point for the parallel particle flux (which, in a good approximation, usually coincides with the outer midplane position).

The same one-dimensional slab geometry as in the Fig. 2.6 is considered. Here, $x = 0$ is the stagnation point, while $x = L_\parallel$ is the position of the divertor target, with $L_\parallel$ SOL connection length given in eq. (2.1). The only heat source is represented by the heat flux entering the SOL across the separatrix between the stagnation point and the X-point ($x = L_s$).

The assumptions for the model are [7]:

- *Particle balance*: neglecting ionization processes, it is assumed that all the neutrals recycling from the targets are suddenly re-ionized in a thin layer just in front of the target. Therefore, it is assumed no net parallel plasma flow along the almost entire SOL, while in the ionization region the flow velocity increases from zero up to the sound speed at the sheath entrance. Moreover, neglecting recombination processes as well, target surfaces are assumed to be the only particle sinks.
- *Momentum balance*: neglecting ion-neutral collisions, it is assumed that neither friction nor viscous effects are present in the thin region of plasma flow, so that the total plasma pressure is constant along a field line.
- *Power balance*: it is assumed that no internal volumetric power sources or sinks are present within the SOL, being the sheath at the target the only sink and the core plasma the only source. Therefore, the total parallel heat flux density resulting from the input power into the SOL is constant along a field line.

So, at upstream we have a stagnant flow, meaning that $v_u = 0$, while at the target (which can be approximately taken as coincident with the sheath entrance, because of the thinness of the sheath with respect to the parallel SOL length) we have $v_t = c_s \approx \left(\frac{2T_t}{m_i}\right)^{1/2}$. Therefore, after the assumption of no parallel plasma flow, the pressure balance becomes $p_u = p_t + m_i n_t v_t^2$, that is

$$n_u T_u = 2 n_t T_t \tag{2.19}$$

Then, after the assumption of parallel heat transport driven purely by electron conduction and of uniform $q_\parallel$, for relating upstream and target temperature it is sufficient to integrate the first eq. of (2.14), obtaining

$$T_u^{7/2} = T_t^{7/2} + \frac{7}{2}\frac{q_\parallel}{\kappa_{0,e}} L_\parallel \tag{2.20}$$

Finally, having considered the sheath the only heat sink for plasma can be taken as a boundary condition by equating the heat carried through the sheath (eq. (2.18)) to the heat carried along the whole SOL, i.e. $q_\parallel = q_{\parallel,t} = q_{\parallel,se}$, obtaining

$$q_\parallel = \gamma n_t T_t c_s \tag{2.21}$$

The equations (2.19), (2.20), (2.21) together constitute the basic two-point model equations. From these we can deduce the dependence of the main SOL quantities in terms of the principal control parameters, namely the upstream density n_u and the parallel heat flux density $q_\parallel$ [7]:

$$\begin{aligned} T_u &\propto q_\parallel^{2/7} L_\parallel^{2/7} \\ T_t &\propto n_u^{-2} q_\parallel^{10/7} L_\parallel^{-4/7} \\ n_t &\propto n_u^{3} q_\parallel^{-8/7} L_\parallel^{6/7} \\ \Gamma_t &\propto n_u^{2} q_\parallel^{-3/7} L_\parallel^{4/7} \end{aligned} \tag{2.22}$$

As we see, T_u has no dependence on n_u, while is only slightly sensitive to $q_\parallel$; this is reasonable since a little change in temperature can accommodate a large change in heat flux density, being the parallel heat conductivity a strong function of the temperature. Then, with increasing n_u fortunately T_t decreases, and thus strong parallel temperature gradients arise in order to exhaust the SOL input power. Moreover, since density and particle flux onto the targets strongly increase with n_u, recycling at the targets also increases quickly with n_u increasing.

In order to further improve the validity of this model, we can now take into account some corrections which consider also the effects of the presence of volumetric processes [7]. Namely, we consider the presence of:

- *Volumetric power losses* due to radiation and atomic processes. This can be done by introducing a *power loss factor* f_{power}, defined as the fraction of the parallel heat flux which is dissipated in this way before striking onto the target, so that

$$q_{\|,t} = (1 - f_{power})q_{\|} \tag{2.23}$$

- *Momentum losses* due to frictional ion-neutral collisions, viscous forces and recombinations. This can be done by introducing a *momentum loss factor* f_{mom}, defined as the fraction of static pressure entering at upstream which effectively arrives to the target, so that

$$2p_t = f_{mom}p_u \tag{2.24}$$

Applying such corrections to the basic two-point model equations, the dependence of the target quantities on these corrective factors results to be [7]:

$$\begin{aligned} T_t &\propto \frac{(1 - f_{power})^2}{f_{mom}^2} \\ n_t &\propto \frac{f_{mom}^3}{(1 - f_{power})^2} \\ \Gamma_t &\propto \frac{f_{mom}^2}{1 - f_{power}} \end{aligned} \tag{2.25}$$

Evidently, the main consequence of volumetric power losses is to decrease the temperature at the target, while the main consequence of momentum losses is to decrease the particle flux striking the targets, which are both beneficial effects for the aim of reducing heat loads and erosion on target plates [7].

2.2.3 Perpendicular transport and radial profiles

In contrast to parallel transport, the cross-field perpendicular transport is experimentally shown to be highly anomalous [7]; therefore, no first-principle-based theory actually exists for predicting it. However, the presence of such transport component in the scrape-off layer is of critical relevance since the intensity of the heat flux impinging on the divertor targets, which is the most important parameter for the concern of power exhaust, will depend on how much the parallel heat flux density profile $q_{\|}$ is spread radially along the SOL; this is, indeed, a direct consequence of the presence of cross-field transport processes of both particles and heat.

Cross-field particle transport can be treated essentially as source/sink terms for the parallel particle flow to the targets, as seen in the previous section. In particular, under the assumption of pure diffusion (cfr. Appendix A.3), it can be described through empirical values of an anomalous *particle diffusivity* D_n, so that to assume the radial particle flux as

$$\Gamma_r = -D_n \frac{dn}{dr} \tag{2.26}$$

that is in each point proportional to the radial density gradient. As a first approximation, we can use the experimentally derived Bohm diffusivity (eq. (A.52)), which is of the order of $0{,}5 - 1$ m^2/s for usual SOL plasma parameters.

So, the resulting *radial density profile* $n(r)$ can be explained in terms of a simple radial balance equation which illustrates the competition between radial fluxes and parallel losses, that is

$$\frac{\partial n}{\partial t} = D_n \frac{\partial^2 n}{\partial r^2} - \frac{n}{\tau_\parallel} + S_i \tag{2.27}$$

Here $\tau_\parallel \approx L_\parallel / c_s$ is a characteristic loss time, following from the intensity of the parallel flow (having supposed the parallel velocity as the sound speed), and S_i is an eventual ionization source term. This simple balance motivates the ansatz of an exponentially decaying profile [7], that is in the form

$$n(r) = n_{sep} \exp\left(-\frac{r}{\lambda_n}\right) \tag{2.28}$$

where n_{sep} is the value of the density at the separatrix, where $r = 0$, and λ_n is a *density decay length* defined as $\lambda_n = -\left(\frac{1}{n}\frac{dn}{dr}\right)^{-1}$.

A similar approach can be followed for the cross-field heat transport, assuming empirical values of anomalous *thermal diffusivities* χ_e, χ_i, so that to assume the radial heat flux as

$$q_r = -n\left(\chi_e \frac{dT_e}{dr} + \chi_i \frac{dT_i}{dr}\right) + \frac{5}{2}\Gamma_r (T_e + T_i) \tag{2.29}$$

this is in each point proportional to the radial temperature gradients (*conduction* term) and to the radial particle flux, which also contributes to radially transport heat through the net radial particle motion (*convection* term). Both the electron and ion thermal diffusivities are experimentally shown to lie between $1 - 10$ m^2/s.

By applying the same ansatz done for the density, here also we can assume exponentially decaying *radial temperature profiles* $T_e(r)$, $T_i(r)$ [7], in the form

$$T_e(r) = T_{e,sep} \exp\left(-\frac{r}{\lambda_{T_e}}\right) \tag{2.30}$$

$$T_i(r) = T_{i,sep} \exp\left(-\frac{r}{\lambda_{T_i}}\right) \tag{2.31}$$

where $T_{e,sep}$, $T_{i,sep}$ are the values of temperature at the separatrix, and λ_{T_e}, λ_{T_i} are some *temperature decay lengths*, defined in analogous way as the density decay length.

2.2.4 Modelling the power exhaust

The radial spreading of the parallel heat flux profile $q_\parallel$ is one of the most important figures of merit for power exhaust calculations, from a given power P_{SOL} crossing the separatrix and entering the SOL plasma, for the aim of estimating the resulting divertor heat loads.

Experimental studies carried out in different devices [40][41] have shown heat fluxes impinging onto the targets which are consistent with a model where, in the SOL (precisely at the outer midplane), an exponentially radially decaying heat flux profile is also present [7], which is in the form

$$q_\parallel(r) = q_{\parallel,0} \exp\left(-\frac{r}{\lambda_{q_\parallel}}\right) \tag{2.32}$$

Here, $\lambda_{q_\parallel}$ is usually called *power scrape-off width*, and quantifies the thickness of the channel in which the parallel heat flux flows. Then, the value of $q_{\parallel,0}$ can be inferred by considering that the whole input power P_{SOL} is assumed to flow in parallel direction though a cross-sectional area $A_{q_\parallel} = 2\pi R \lambda_{q_\parallel} \left(\frac{B_\theta}{B}\right)_u$ radially extended in the poloidal plane; in particular, $\frac{B_\theta}{B}$ defines the inclination of the field lines, i.e. of the direction of the parallel heat flow, with respect to the poloidal direction, which actually reduces this effective area when referring to a projection of the parallel motion on a poloidal cross section. Therefore, it must be considered that

$$q_{\parallel,0} \approx \frac{P_{SOL}}{2\pi R \lambda_{q_\parallel}} \left(\frac{B_\theta}{B}\right)_u \tag{2.33}$$

Experimentally, it was tried to relate the measured values of the power scrape-off width to some physical and technological parameters. By fitting experimental multi-machine data, the following scaling laws were obtained, namely

$$\lambda^L_{q_\parallel} \approx 1{,}44\, B_\varphi^{-0{,}80}\, q_{95}^{1{,}14}\, P_{SOL}^{0{,}22}\, R_0^{-0{,}03} \tag{2.34}$$

for L-mode plasmas [40], and

$$\lambda^H_{q_\parallel} \approx 0{,}90\, B_\varphi^{-0{,}73}\, q_{95}^{1{,}16}\, P_{SOL}^{0{,}04}\, R_0^{-0{,}11} \tag{2.35}$$

for H-mode plasmas [41], in mm, where $B_\varphi = [\mathrm{T}]$, $P_{SOL} = [\mathrm{MW}]$, $R_0 = [\mathrm{m}]$ and q_{95} is the safety factor at the magnetic flux surface with normalized poloidal flux equal to 0,95. For current devices, the resulting values of such parameters are about few mm.

However, this measure of the radial spread of the parallel heat flux is valid only for the midplane region. When this flux arrives in proximity of the divertor targets, its radial profile is naturally broadened because of the magnetic flux expansion, parametrized by the factor f_x (eq. (2.3)): this, in fact, measures the "stretching" of the flux surfaces near the targets with respect to the midplane, due to the decrease of the poloidal field near the X-point, and thus also the radial broadening of the heat flux profile. This turns out to be a beneficial effect in mitigating the maximum heat load on the target surfaces.

The broadening of the channel of the parallel heat flow in proximity of the targets, with respect to the midplane, can be addressed by expressing with s the radial target coordinate and with s_0 the strike position of the separatrix line on the target. In this way, the radial profile of the parallel heat flux here can be described, for $\Delta s \equiv s - s_0 > 0$, by [42]

$$q_\parallel(\Delta s) = q_{\parallel,0} \exp\left(-\frac{\Delta s}{f_x \lambda_{q_\parallel}}\right) \tag{2.36}$$

where $\lambda_{q_\parallel}$ is still the power scrape-off width at the midplane.

Then, a second effect comes out from the fact that, in divertor region (more precisely, when the X-point is surpassed), the SOL plasma is not connected to the core plasma anymore. Therefore, in addition to the flux expansion, we have that perpendicular transport contributes to broaden the profile not only into the outer SOL anymore but also in the private flux region, symmetrically, as illustrated in the Fig. 2.8a; so, a further broadening of heat deposition onto divertor targets is obtained [43]. Here, the competition between the symmetric outward- and inward-directed perpendicular heat transport and the parallel flow could be described by a gaussian distribution with width parameter S, usually called *divertor power spreading* [42].

In this way, the definitive form of the parallel heat flux profile onto the targets can be obtained by convoluting such gaussian profile with the broadened exponential profile, leading to [42]

$$q_\parallel(\Delta s) = \frac{q_{\parallel,0}}{2} \exp\left(\left(\frac{S}{2\lambda_{q_\parallel}}\right)^2 - \frac{\Delta s}{f_x \lambda_{q_\parallel}}\right) \operatorname{erfc}\left(\frac{S}{2\lambda_{q_\parallel}} - \frac{\Delta s}{f_x S}\right) \tag{2.37}$$

In the Fig. 2.8b we can see the resulting heat flux profiles, for some realistic values of $\lambda_{q_\parallel}$, S, at the X-point and on the target, both mapped on the radial coordinate of the outer midplane.

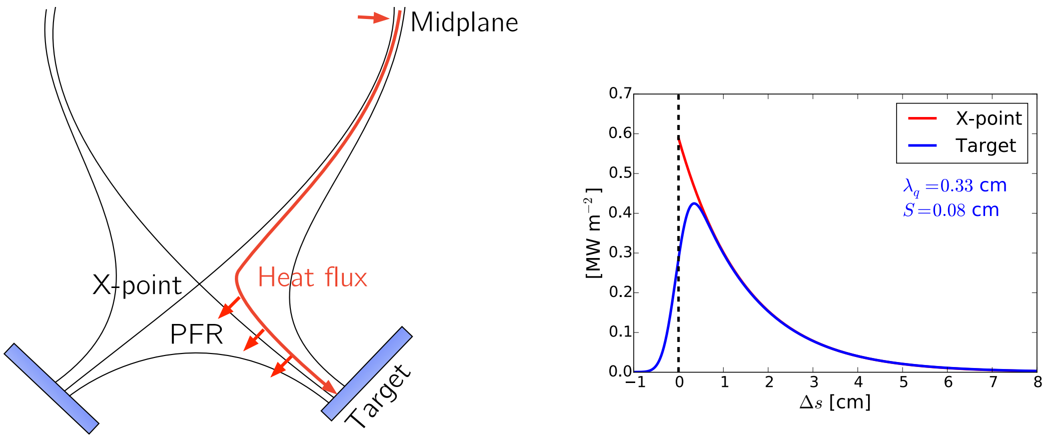

(a) Heat transport towards the private flux region near the divertor targets.

(b) Heat flux profiles at the X-point and on the targets, mapped onto the target radial coordinate.

Figure 2.8: Phenomenon of divertor power spreading [28].

Finally, it must be considered that the actual figure of merit, for what concerns the divertor heat load, is the heat flux perpendicularly striking it (when viewed in the poloidal plane). Its value is, in fact, naturally reduced with respect to the parallel heat flux because of the magnetic geometry. Moreover, a further beneficial effect in this sense can be obtained by slanting the material targets even with respect to the poloidal direction, by an angle β (cfr. fig. 2.2). Therefore, globally, for obtaining the heat flux perpendicularly striking the targets in the poloidal plane, the corresponding parallel heat flux $q_{||}$ must be decreased:

- by a factor $\left(\frac{B_\theta}{B}\right)_{\text{target}}$, for taking into account the inclination of field lines with respect to the poloidal plane.
- by a factor $\sin\beta$, for taking into account the inclination of the material targets with respect to the poloidal direction.

For current and future devices, where $\left(\frac{B_\theta}{B}\right)_{\text{target}} \approx 0{,}1$ and the target inclination is between about 1° and 3°, the heat load onto the targets can be decreased up to a factor 100 with respect to the parallel heat flux arriving here [6].

2.3 Operating regimes

According to the simple models which were just discussed, it is possible to identify different *operating regimes* for the divertor SOL [7]. These will depend mainly on the main particle source location (namely, where the neutrals recycling from the divertor targets are ionized again). The main SOL parameter driving the transition from one regime to another will be then, first of all, the density, and consequently the temperature in the divertor region, which in turn indicates which is the predominant atomic process here. The dependence of the operating regime on both these parameters can be then just expressed in term on the SOL collisionality ν_{SOL} (eq. (2.10)), which is larger for high densities and low temperatures.

2.3.1 Sheath-limited regime

A first situation is defined by a low density regime, so that the recycling neutrals can penetrate the plasma far away from the targets without suffering too many collisions (being their mean free path much longer than the X-point-to-target distance), being thus ionized in the core plasma. In this way, the particle source will be located at upstream, leading to a net and intense parallel particle flow along the entire SOL, which makes the parallel heat flux being carried predominantly by convection. This results in a small temperature drop along the SOL and thus also high temperatures in the divertor region. Such regime is called *sheath-limited regime* since the heat loss from the SOL is, in this way, limited only by the heat transmission properties through the sheaths at the targets, rather than by parallel conduction. Because of the low ion-neutral collisionality, momentum losses are also negligible.

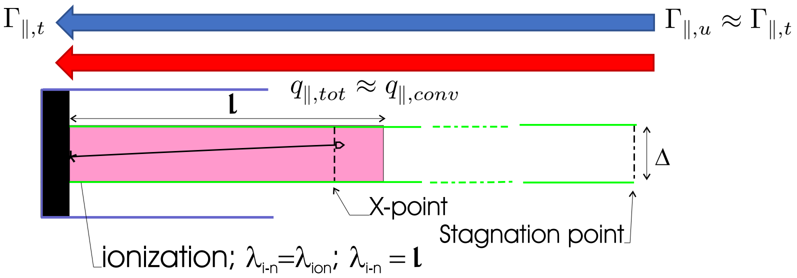

Figure 2.9: Physical picture of parallel transport in the sheath-limited regime. Adapted from [44].

Summarizing, in such regime the SOL is characterized by a net parallel particle flux, which is approximately constant from upstream to target, and a parallel heat flux driven by convection and limited only by the sheath conductivity. Clearly, this is not an interesting regime for future devices, being characterized by large temperatures at the targets, and thus risk of serious damage to the divertor materials such as melting or sputtering.

2.3.2 Conduction-limited regime

A more desirable operating regime must be then characterized by lower divertor temperatures. This can be obtained by rising the density regime, i.e. achieving a collisionality $\nu_{SOL} \gtrsim 10$ [7]; in fact, this would lead to an increased ionization rate in the divertor region, so that the recycling neutrals, suffering many interactions here with plasma particles, are suddenly re-ionized in a thin layer near the targets. In this way, the flow of recycled particles to the targets reaches very high values.

Since the recycled neutrals are re-ionized in proximity of the target, the dominant particle source is located here, resulting in a relatively weak parallel plasma flow along the almost entire SOL. Therefore, since only a low amount of heat can be parallel convected from upstream, the parallel heat flux is carried predominantly by conduction. This results in a large temperature drop along the SOL, and thus quite low temperatures in the divertor region, as desired. Since it is precisely such temperature drop which limits the magnitude of the heat flux which can be transported, such regime is called *conduction-limited regime*: this is the situation in which the two-point model, strictly speaking, is valid. In this case momentum losses start to be relevant near the targets, there temperatures have been lowered enough to make ion-neutral collisions relevant.

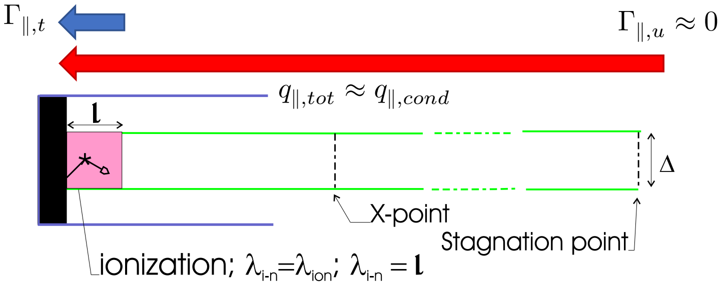

Figure 2.10: Physical picture of parallel transport in the conduction-limited regime. Adapted from [44].

Summarizing, in such regime the SOL is characterized by approximately no parallel particle flux along it, apart from a thin region near the target, and a parallel heat flux driven by conduction and limited only by the temperature drop.

2.3.3 Divertor detachment

Pushing the density regime even further, i.e. achieving a collisionality $\nu_{SOL} \gtrsim 85$ [7], radiative losses are so enhanced that divertor temperatures fall to still lower values. Therefore, also the heat flux striking the targets gets to be even more strongly reduced.
This general increase of the SOL density regime is, initially, followed by an increase of the target density. However, when target temperatures reach very low values, less than about 5 eV, it occurs that the target density starts to "roll over", i.e. starts decreasing again, followed by a strong decrease of the particle flux onto the targets [45]. According to corrected two-point model (eqs. (2.25)), for target density and particle flux to decrease together, significant momentum losses should occur; in fact, it is precisely in this temperature range that ion-neutral collisions are seen to become more effective than ionizations near the targets (cfr. fig. 2.4), so that the recycled neutrals get to induce very strong friction losses to the plasma before being ionized.
This new situation of strongly reduced density and particle flux onto the targets, seen as an evolution of the conduction-limited regime following from a significant pressure drop along the SOL, is usually called *detachment* [33][46]. This turns out to be the most desirable one for future devices since it minimizes both particle and heat loads onto the material targets [6].
In principle, this situation just requires significant pressure drops, rather than significant power losses; nevertheless, since the physical processes which can lead to momentum losses for the plasma (i.e. CX collisions and recombinations) require precisely low temperatures for becoming effective over other processes [47][48], a strong power dissipation along the SOL becomes a fundamental requirement for achieving the detachment. This is well shown in the Fig. 2.11, where the experimental trend of the momentum loss factor with target temperature was obtained from an actual device. This was done by measuring density and temperature on flux tubes at different distances from the separatrix (mapped on the midplane), and calculating the resulting pressure drop as a function of the temperature at the target. As we can see, the pressure along a flux tube keeps basically constant as long as the corresponding target temperature (i.e. measured at the end of the same flux tube) stays above about 5 eV; instead, it abruptly drops for lower target temperatures, which is a sign of the strong increase of momentum losses occurring at low temperatures, which ultimately define the detachment.

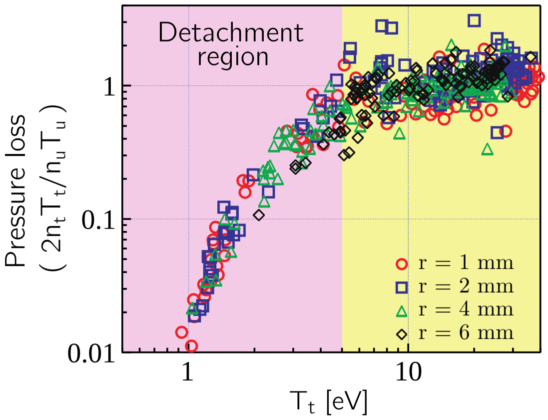

Figure 2.11: Experimental pressure loss in function of the target temperature. Taken from [49].

A first stage of this process is the so-called *partial detachment*, in which, the temperature in proximity of the targets is less than about 5 eV but larger than about 1 eV. So, here a region with dominant charge-exchange collisions emerges, and the neutrals effectively start removing some momentum from the plasma. Because of the relatively low divertor temperatures required for this, the heat flux striking the targets already exhibits a relevant decrease in this stage; however, in this case the particle flux onto the targets has not started falling yet, since temperatures are still not low enough to make the recombination processes relevant.

Then, for even lower target temperatures, less than about 1 eV, the drop in the heat flux onto the targets is even more relevant, presenting now a basically flat pattern. Moreover, a region with dominant recombination arises in proximity of the targets, so that also density and particle flux drop abruptly, and also the latter assumes a flattened profile. This is the *complete detachment*. The consequent fall of plasma density makes the divertor region transparent to neutrals again; therefore, these can diffuse out of it again until they reach the hotter zone at upstream, where they are finally re-ionized. This situation is characterized by a strong pressure drop in the divertor region, with loss factors up to the order of 10^{-2}.

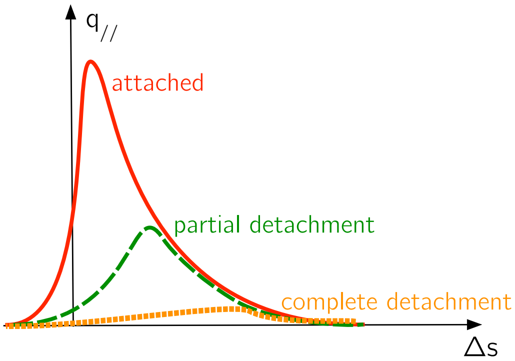

Figure 2.12: Qualitative heat flux profiles onto the target for different detachment regimes [28].

In the Fig. 2.13 a schematic picture of the main atomic processes involved in inducing pressure losses along a flux tube, and consequently the detachment, is shown, together with the resulting density and temperature profiles. First, when the temperature is still high, the high density regime contributes to a strong power dissipation via radiation emission and ionization of the recycling neutrals diffusing until here. Then, when the temperature is sufficiently low, charge-exchange collisions start dominating over ionization, so that neutrals start removing momentum from the plasma, slowing down the plasma flow; this induces a localized increase of the plasma density. Finally, at extremely low temperatures, we have the recombination region, in which most of the plasma particles recombine, leading to a further removal of momentum from it and, ultimately, to the decrease of density and particle flux.

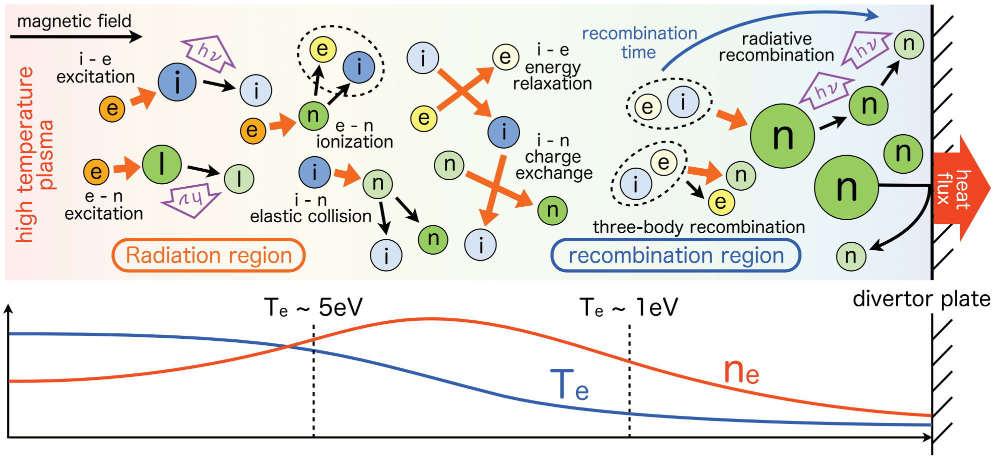

Figure 2.13: Schematic illustration of the main processes involved in the detachment. Taken from [50].

2.4 Perpendicular transport and density shoulder formation

We turn now to the main aspect of the scrape-off layer physics which will be investigated in this thesis, namely the perpendicular transport, starting with introducing some basic phenomena related to it.

Experimental measurements, firstly performed in the early 2000s on the Alcator C-Mod device [51], have shown that, in order to keep describing perpendicular transport in the SOL through a diffusive assumption (cfr. Section 2.2.3), the assumed anomalous particle diffusivity D_n should strongly increase radially through the SOL thickness. Moreover, this phenomenon was also shown to be more relevant as the general SOL density regime was higher.

For explaining this, it should be considered that the high-density plasmas in which this phenomenon is observed are characterized by the presence of large-amplitude *turbulent processes* in the SOL region (namely, density fluctuations of the order of the density itself), with an intermittent character [52][53]. When such turbulent regime is present, the presence of filamentary coherent structures radially propagating in the SOL plasma, with a density much larger than the background density, was experimentally revealed [54]. These structures, highly localized in the poloidal plane and extended along the magnetic field lines, were then believed to be responsible for the strong intermittency of the observed SOL plasma turbulence. The intermittency in the formation, and consequent propagation, of these structures was taken as a possible motivation for assuming an *intermittently enhanced perpendicular transport regime* in the SOL.

Moreover, the nature of these structures seriously questioned the validity of a purely diffusive approximation for the perpendicular SOL transport. Rather, since the appearance of these does not depend neither on the local density nor on the local density gradient, but instead is determined by the dynamics around the separatrix, it suggested that the radial propagation of these acts as a process of *non-local transport*; in this framework, the model for the radial particle balance as expressed in the equation (2.27) would be, substantially, wrong.

2.4.1 Mechanisms for blob formation and propagation

Currently, the most widely accepted picture for modelling formation and propagation of these coherent filamentary structures, responsible for the intermittency of SOL plasma turbulence, is the one firstly proposed in [14]. According to this picture, these structures appear as localized high-density *blobs* in the poloidal plane, as well as *filaments* aligned to the magnetic field lines in a full 3D representation (Fig. 2.14a). The theory formulated here assumes that, because of turbulence-driven interchange instability processes taking place in the vicinity of the separatrix, filaments with large density detach from the core plasma at some particular frequency. Such instability processes are expected to mostly occur where the curvature of field lines is "unfavourable", i.e. only in a poloidal region at the outer side of the torus. Therefore, according to this theory, blob formation can be also expected to take place only in this region, i.e. around the outer SOL midplane; in this sense, we can say that the phenomenon of blob formation has an inherently "*ballooning*" nature. More details about turbulence phenomena leading to blob formation can be found in the Appendix B.1.

According to this picture, when a blob is formed, plasma polarization is induced internally to it by effective gravity drifts, which also take place just at the outer side of the torus because of the "bad curvature" of field lines here. Because of this, on the plasma particles constituting the blob a net radially directed force $\boldsymbol{F}$ will act, as resulting from the ∇B and curvature effects, which is of the order

$$F \approx 2\, n_b m_i \frac{c_s^2}{R_b} \tag{2.38}$$

with n_b blob density, m_i ion mass, c_s sound speed and R_b curvature radius of the considered flux surface. Consequently, electrons and ions start moving in opposite directions due to the resulting $\boldsymbol{F} \times \boldsymbol{B}$ particle drift; this causes a net charge separation inside the poloidal cross section of the blob. This polarization results then in an internal vertical electric field $\boldsymbol{E}$; this ultimately induces a radial $\boldsymbol{E} \times \boldsymbol{B}$ drift motion of the structure in the direction of the original force $\boldsymbol{F}$, that is in the radially outward direction. The blob structure will then move towards the main chamber wall, acting as a net convective motion for the plasma, with some *radial propagation velocity* $\boldsymbol{v}_b$. If Φ is the electric potential field which is formed internally to the blob because of the charge-polarizing force, such that $\boldsymbol{E} = -\nabla\Phi$, then according to the particle drift theory (cfr. Appendix A.1.2), this velocity can be assumed to be

$$\boldsymbol{v}_b = \frac{\boldsymbol{B} \times \nabla\Phi}{B^2} \tag{2.39}$$

This situation is schematically illustrated in the Fig. 2.14b.

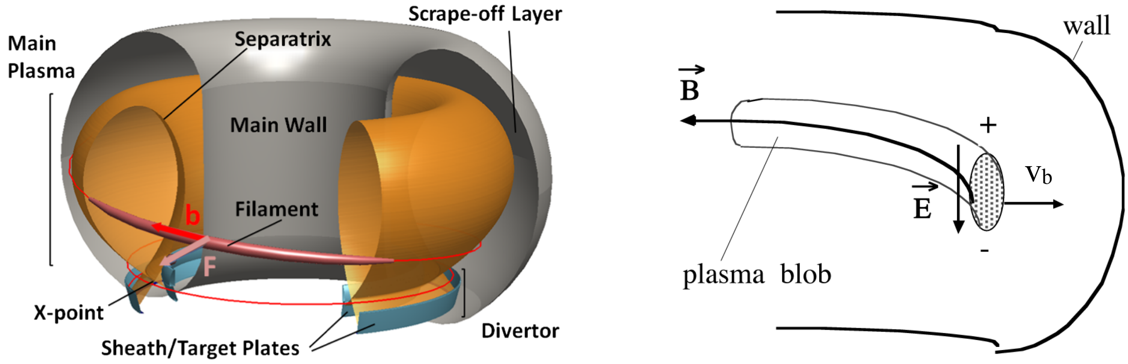

(a) 3D illustration of magnetic-field-aligned filaments. Taken from [12].

(b) Physical processes leading to radial blob propagation on the poloidal plane. Taken from [14].

Figure 2.14: Qualitative picture of blob-filaments in the SOL plasma.

This can be regarded as the reason why the radial propagation of these structures actually constitutes an efficient perpendicular transport mechanism in the SOL, with a non-local and strongly intermittent character.

More details about radial blob propagation, namely a simplified mathematical model leading to general scaling relations for blob properties in function of the plasma conditions, can be found in the Appendix B.2.

2.4.2 Density shoulders and *main chamber recycling regime*

Radial blob propagation can then be expected to have a strong impact on radial particle fluxes at the outer side of toroidal devices. Therefore, a proof of an enhanced perpendicular transport driven by such mechanism could be found by analyzing the radial profiles at the outer SOL midplane.

In particular, it was experimentally shown that, in high density regimes (which is the same situation in which radial blob propagation seems to be most enhanced), after some distance from the separatrix radial density profiles at the outer SOL midplane become considerably flattened, invalidating the ansatz of exponential decaying profiles beyond this point [11][55]. This region of flattened density profile was called *density shoulder*; the radial location of the breakpoint between the region of nearly exponentially decaying density, which was called the *near SOL*, and the region of flatter profile, which was called the *far SOL*, was put to define the starting point of the shoulder. This is readily visible in the Fig. 2.15, where some measurements of typical radial density profiles at the outer SOL midplane in the JET tokamak are shown. As we can see, at generally low SOL density regimes ($n_{e,sep}$ lower than 10^{19} m^{-3}) the profiles decay nearly exponentially, which is here visible as straight lines, since the plot is in semilogarithmic scale. Instead, at higher densities ($n_{e,sep}$ equal or greater than 10^{19} m^{-3}) the presence of density shoulders is evident, being these radially extended further as the density is increased.

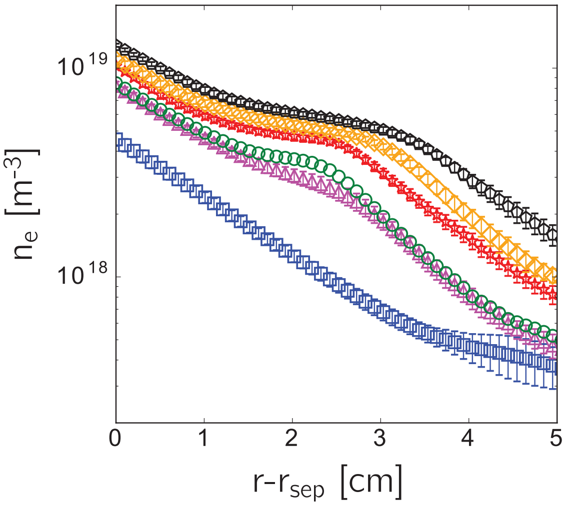

Figure 2.15: Radial density profiles at the outer SOL midplane showing different degrees of shoulder formation. Taken from [55].

A mechanism which strongly enhanced the radial transport of particles precisely at the outer side of the torus was then assumed to be necessary for a density shoulder to form. A net convective motion of plasma particles, driven by radial blob propagation, arose then as a possible explanation of this phenomenon. Such a regime, clearly, could not be consistent with a purely diffusive assumption for the perpendicular transport

Then, it was also discovered that, when density shoulders are present, a large fraction of plasma particles entering the SOL from the core plasma does not flow into the divertor (as believed in the classical picture of parallel transport), but is instead transported radially to the main chamber wall. As a result, in addition to the recycling processes taking place at the divertor targets, another independent recycling loop was assumed to exist at the main chamber walls; such "new" regime was then called *main chamber recycling regime* [56].

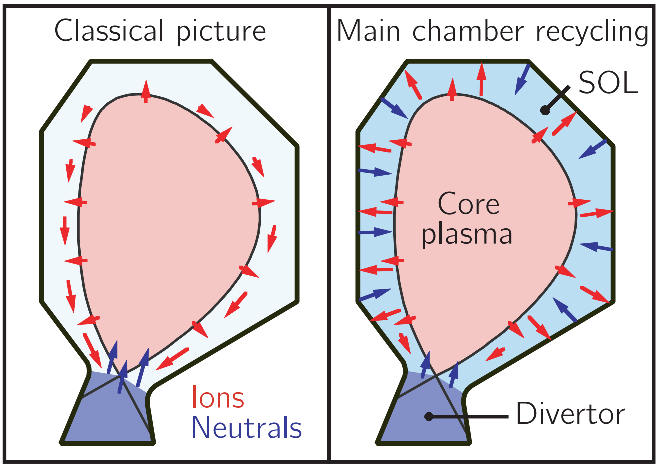

Figure 2.16: Physical picture of the main chamber recycling regime. Taken from [51].

In this situation, a particle balance showed that the plasma flow in the SOL was not dominated anymore by the parallel flow to the divertors, and that the radial transport to the main chamber wall played, indeed, a not negligible role. In particular, measurements showed that radially propagating blobs could transport roughly 50% of the particles present within the SOL in such situation [51][54]. Moreover, as they also carry heat with them, the fraction of the total SOL input power which is radially transported up to the wall, with respect to a classical situation, has been seen to increase up to 20% [16][17]. These large radial particle fluxes require, indeed, very large perpendicular transport coefficients for being described, even much larger than Bohm diffusivity.

2.4.3 Impact on scrape-off layer modelling

The just described phenomena deeply affect the fraction of particles and heat which are transported to the divertors. Therefore, the picture of the exhaust processes in the scrape-off layer needed to be revisited. In particular, less power will reach the divertor region, contributing to lower temperatures in front of the targets. This lets one think that the achievement of a detached regime could be significantly promoted in this new picture.
In the Fig. 2.17 the "classical" picture for the exhaust processes in the scrape-off layer and the new picture, in the framework of not negligible radial transport at upstream, are qualitatively compared.

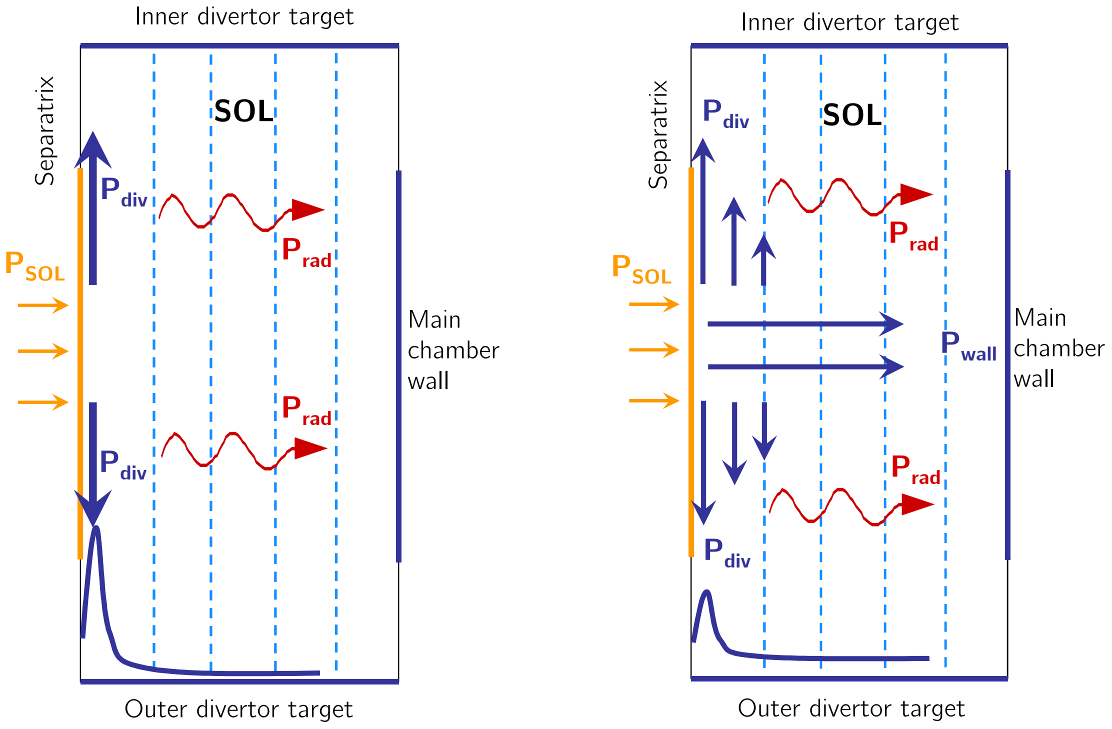

(a) "Classical" picture, in which all the input power is transported to the divertor or is radiated along the path.

(b) "New" picture, in the framework of enhanced perpendicular transport at the outer midplane, in which the radial heat transport to the wall is not negligible anymore.

Figure 2.17: "Classical" and "new" pictures of exhaust processes from the SOL plasma. Taken from [57].

How could such a new situation, characterized by enhanced radial particle and heat transport at the midplane and the existence of a density shoulder, be modelled?
In a first approximation, one could try to assume the existence of a strong convective particle

flux component in radial direction, with a total radial particle flux to be written as

$$\Gamma_r = -D_n \frac{dn}{dr} + n v_r \tag{2.40}$$

by assuming a purely diffusive background transport component, and a v_r profile to be derived from an experimental density profile. In this case, to capture the existence of an enhanced particle flux (and thus, eventually, a density shoulder), v_r should be substantially increased from a nearly zero value to some value at the radial position where the shoulder begins.
Alternatively, one could also make use of an "effective" particle diffusivity $D_{n,\mathrm{eff}}$, which takes into account also a convective motion, with a total radial particle flux to be written again as

$$\Gamma_r = -D_{n,\mathrm{eff}} \frac{dn}{dr} \tag{2.41}$$

but with an increasing value of $D_{n,\mathrm{eff}}$ as the shoulder begin.
In each case, for a correct modelling of this phenomenon its ballooning nature should also be taken into account, for reproducing the effects of blob formation and propagation only at the outer side of the torus (as it is currently assumed). Therefore, such an "artificial" increase of an effective diffusivity or a convective velocity should present some poloidal dependence which maximizes it near the outer SOL midplane, minimizing it instead near the inner SOL midplane. Such a procedure was first analytically validated in [56], for both a radially increasing $D_{n,\mathrm{eff}}$ and a constant D_n plus a radially increasing v_r. As a result, flatter radial density profiles were, indeed, obtained in the far SOL. In this case, the physical mechanisms which ultimately provided the formation of the shoulder were seen to be the enhanced radial fluxes and the enhanced recycling due to higher particle fluxes to the main chamber wall.

These results provided as a first theoretical explanation for the link between enhanced perpendicular transport and density shoulder formation, and the existence of a main chamber recycling regime.
However, the first actual experimental evidences of a link between radial blob propagation and such phenomena were achieved only later, with some recent works, which will be discussed in the Section 3.3.

Chapter 3

Experimental basis

In this chapter, the available experimental data supporting the work carried out in this thesis will be presented. In the Section 3.1 some basic features of the ASDEX Upgrade tokamak, in which the experiments considered in this work were performed, will be introduced. After that, in the Section 3.2 the diagnostics systems installed on ASDEX Upgrade which are most relevant for plasma edge studies, and with which the considered measurements were taken, will be presented: the working principle of these will be briefly discussed, and their arrangement on the machine will be presented. Finally, in the Section 3.3 the experiments considered in this work, focused on investigating the enhancement of perpendicular scrape-off layer transport driven by radial blob propagation, will be briefly explained: the main results from the performed discharges will be then reported, as well as the related measurements which were taken as basis for performing the numerical modelling work presented in this thesis.

3.1 The ASDEX Upgrade tokamak

ASDEX Upgrade (AUG) is a currently operating midsize tokamak experiment, located at the Max-Planck-Institut für Plasmaphysik in Garching bei München (Germany), whose operation started in 1990. It is the follow-up experiment of the former tokamak *ASDEX (Axial Symmetric Divertor EXperiment)*, which was in operation from 1980 till 1990. As suggested by its name, such device features a divertor configuration which, as well as the whole device geometry, was optimized to meet the requirements of a future fusion reactor. Overall, it is the largest toroidal plasma device in Germany, and one of the leading fusion experiments worldwide [58][24].

The main goal of ASDEX Upgrade is precisely to study the plasma boundary and the plasma-material interaction matters under conditions similar to those which are expected in a future reactor, in particular the heat loads onto the plasma-facing components, the control of impurities and the pumping of helium [24]. For this reason, it is considered a "stepladder" device for the study of the future ITER and DEMO operations; in fact, it presents the major features which will characterize these devices, such as an elongated plasma shape and a bottom divertor configuration producing a single-null plasma. The resulting magnetic geometry is then very close to the one which will be likely found in these, so that ASDEX Upgrade turns out to be essentially a geometrically scaled-down version of these.
The essential plasma properties have been also adapted to conditions that are expected in future devices: the density regime can be brought to values of the order of 10^{20} m^{-3} for the core plasma and of 10^{19} m^{-3} for the SOL plasma; then, the installed heating power, up to about 30 MW, ensures that the heat fluxes flowing in the plasma boundary and striking the plasma-facing components are equivalent to those expected in next-step devices.

In the following table, some typical *technical parameters* of ASDEX Upgrade are listed [59], while in the Fig. 3.1 we can see a photo of device taken from the inside.

Technical parameters of ASDEX Upgrade	
Total height of the experiment	9 m
Total radius of the experiment	5 m
Weight of the experiment	620 t
Number of toroidal field coils	16
Number of poloidal field coils	12
Maximum toroidal field	3,9 T
Maximum plasma current	1,4 MA
Pulse duration	$<$ 10 s
Internal vessel volume	32 m^3

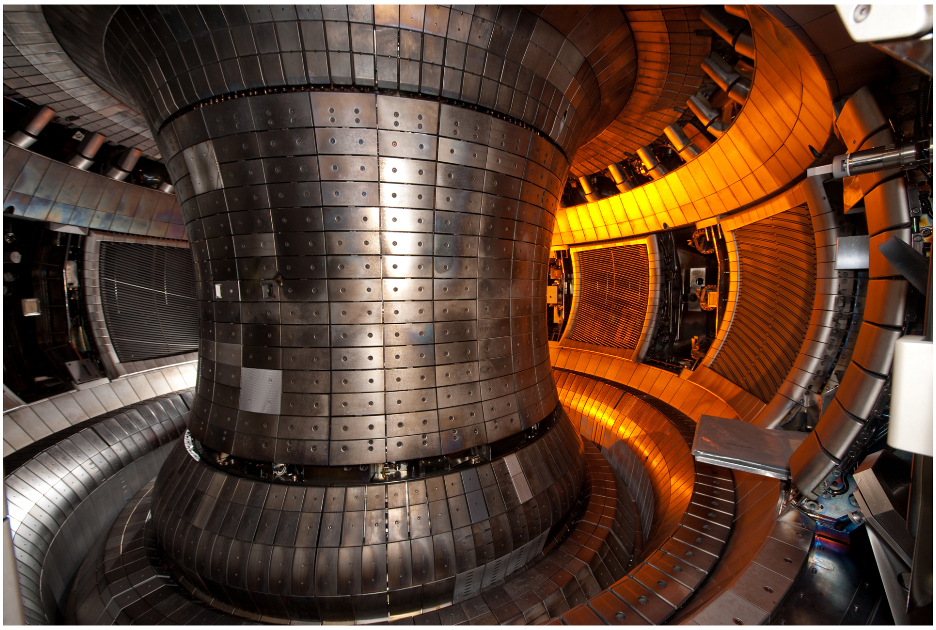

Figure 3.1: Photo of ASDEX Upgrade shot from the inside of the vessel. Taken from [59].

The plasma is kept inside an austenitic steel single-walled *vacuum vessel*, which is a rigid self-supporting structure composed of several wedge-shaped segments with poloidal cross section, in which the fuel gas is injected [60][61]. It is provided with toroidally distributed ports, through which different diagnostics systems, plasma heating components and pumping systems are inserted. Inside the vessel the various *plasma-facing components* are located, which are:

- The *heat shield*, located at the inner side, which is the surface covering the inner column.
- Two *limiters*, located at the outer side, which reduce the interaction between the plasma and the vessel wall.
- The *divertor targets*, located at the bottom of the vessel.

The bulk materials of these components is graphite; however, these are completely tungsten-coated, making ASDEX Upgrade a full tungsten experiment [62].

The overall coil system consists in several sections supported by independent structures, with the weight of the vessel being taken up by the toroidal magnet structure.

The toroidal field is generated by means of 16 D-shaped *toroidal field coils* made of an alloy of copper and silver [60]. The poloidal field, instead, is generated and controlled by means of a system of *poloidal field coils*, which create multipole components for shaping the plasma, defining the radial and vertical plasma positions and the nulls for diverting it. In particular, there are: five ohmic heating coils (OH), which drive the plasma current; six vertical field coils (V), which induce a vertical field used to keep the plasma in an elliptical shape; six correction coils (CO), which allow to control continuously the plasma position; two divertor coils, which create the diverted magnetic configuration [60]. All of these are located outside the vessel. The conducting coil systems typically limit the discharge duration to less than 10 s.

In the Fig. 3.2 a poloidal cross section of the device is shown, depicting the vessel and all the various plasma-facing components and coils, as well as a typical *magnetic configuration*, in which the set of nested flux surfaces is represented with red lines.

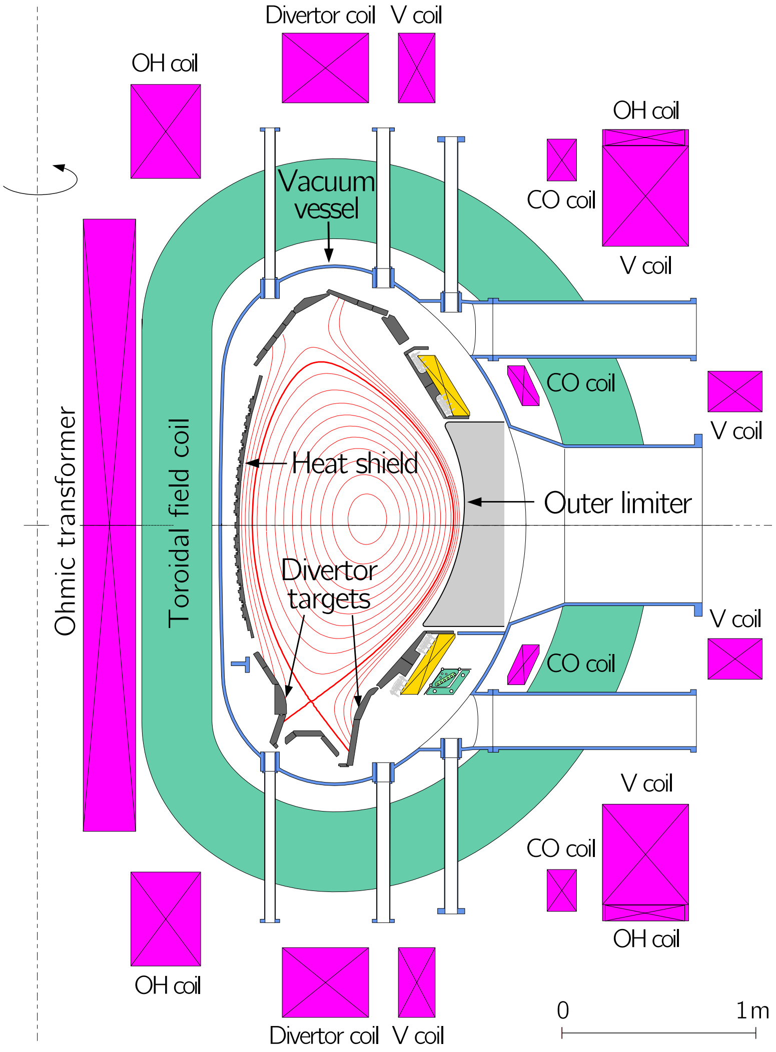

Figure 3.2: Poloidal cross section of ASDEX Upgrade. Taken from [59].

In the following table, finally, typical *plasma parameters* of ASDEX Upgrade are shown [59].

Plasma parameters of ASDEX Upgrade	
Major plasma radius R_0	1,65 m
Minor horizontal plasma radius a	0,5 m
Minor vertical plasma radius b	0,8 m
Plasma volume	14 m^3
Plasma types	*hydrogen, deuterium, helium*

The particular *divertor configuration* (geometry and materials) was changed several times during the years [63]. The current configuration, present since 2014, is characterized by a closed geometry, vertical targets (with the outer one made in massive full tungsten) and a roof baffle [64]. It features an improved particle control, allowed by the presence of 14 turbomolecular pumps, located on the bottom ports, with a pumping speed of 14 m^3/s, and a cryopump, located behind the outer target, with a pumping speed of 100 m^3/s.
In the Fig. 3.3 we can see a close-up of the divertor region in the current configuration.

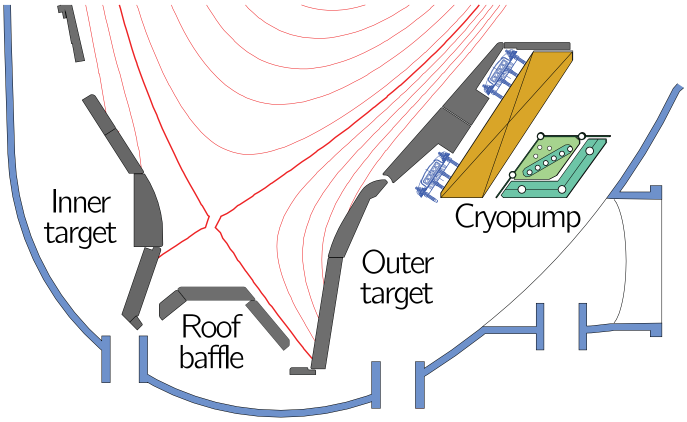

Figure 3.3: Divertor region in ASDEX Upgrade. Taken from [59].

As already mentioned, the plasma in ASDEX Upgrade can be heated up to a maximum of about 30 MW, which are provided by the following mechanisms [60]:

- *Ohmic heating*, which occurs because of the externally induced plasma current flowing in a medium with some electric resistivity; given the usual values of density and temperature, in ASDEX Upgrade a maximum ohmic heating of about 1 MW can be obtained.
- *Electromagnetic-waves heating*: it is obtained by injecting electromagnetic waves into the plasma at appropriate frequencies (multiples of the electron/ion gyrofrequencies) through a system of antennas; these are absorbed, heating then the plasma particles which thermalize with the colder ones via collisions. The resonance frequencies needed for this lie in the microwave range for electrons and in the radiofrequency range for ions for typical field intensities. In ASDEX Upgrade, the maximum power provided by the *Electron cyclotron resonance heating (ECRH)* system and the *Ion cyclotron resonance heating (ICRH)*, which use frequencies of 140 GHz and $30 - 50$ MHz respectively, is up to 8 MW each one.
- *Neutral beam injection (NBI)*: it is done by injecting a highly energetic beam of neutral atoms in the plasma; as these are not deflected by the magnetic field, they are able to penetrate into it, where they are ionized and then thermalized via collisions. In ASDEX Upgrade, the maximum heating power provided by such system is about 20 MW (from one source of 60 keV atoms and one of 100 keV atoms respectively, of 10 MW each one).

3.2 Diagnostics systems

A large part of the scientific program of ASDEX Upgrade is the development and the installation of *diagnostics systems*, each one optimized for the particular experimental feature under investigation. Currently, approximately 70 different raw data diagnostics measure different core and edge plasma parameters, while further physical information is stored in about 200 high-level diagnostics after post-processing of the raw data [24].
In this section, the most important diagnostics systems for plasma edge studies, which were used to measure the experimental data on which this thesis relies on, will be introduced.

3.2.1 Lithium-beam emission spectroscopy

A first major system for the analysis of the edge plasma is the *lithium-beam emission spectroscopy (LiBES)*. This is suitable for the measurement of density profiles and fluctuations at the outer midplane with excellent spatial (≈ 5 mm) and temporal (< 1 ms) resolution, and minimum introduction of disturbances in the plasma [65].
It consists in the injection of neutral lithium atoms into the plasma, with energies of the order of tens of keV, to induce collisional processes with the hot electrons; these, in turn, lead to characteristic *line radiation emission*, delivering the desired information detectable by spectroscopic techniques [66]. In fact, all the atoms are injected in their ground state, which is Li(2s); however, due to the collisions, excited atomic states will start to be populated, or, alternatively, the lithium atoms will be ionized. The most strongly populated state will be the Li(2p) one, that is the first excited state, which emits a characteristic photon via radiative de-excitation with wavelength of 670,8 nm: the characteristic line intensity is then measured along the lithium beam within the plasma, and from the spatial distribution of the emission of this radiation it is possible to deduce the electron density profile n_e.

The attenuation and composition of the injected neutral beam along its way into the plasma can be described by a system of coupled differential equations for the *occupation number* $N_j(z)$ of the atomic states of the lithium atoms (with $j = 1$ denoting the Li(2s) state, $j = 2$ denoting the Li(2p) state, and so on); these are in the form

$$\frac{dN_j(z)}{dz} = \sum_k [n_e(z) a_{jk}(T(z)) + b_{jk}] N_k(z) \tag{3.1}$$

where z is length variable along the beam axis (with $z = 0$ at the entrance of the beam into the plasma), and the sum is done over all the processes inducing a change in the occupation number of the lithium atoms [67].
The coefficients a_{jk}, which are functions of the local plasma temperature, describe the collisional processes of the lithium atoms with plasma particles; these are derived from the cross sections for the various interactions leading to variations of the occupation number of the lithium atoms from j to k and vice versa, namely *excitation* to a higher number, and *de-excitation* to a lower number. The coefficients b_{jk}, instead, describe the *spontaneous emission* processes. The knowledge of the absolute cross sections is required for all the different processes, which are taken from opportune atomic databases.

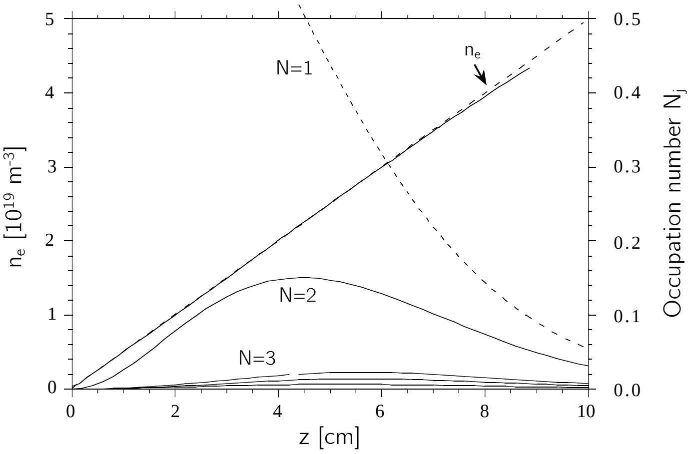

Figure 3.4: Solutions for the occupation numbers of Li atoms injected into the plasma. Taken from [67].

For example, in the Fig. 3.4 the evaluated solution of the eqs. (3.1) for the occupation number N_j of the first three lithium states along the beam axis z is shown. The assumptions were

a density profile $n_e(z)$ as represented, and the realistic boundary condition $N_j(z=0)=\delta_{1j}$ (meaning that all the atoms are in their ground state before entering the plasma).
The inverse procedure, that is the reconstruction of the electron density profile, is possible by measuring the intensity $I_{2\mathrm{p}\rightarrow 2\mathrm{s}}$ of the Li(2p→2s) emission line at 670,8 nm along the beam path. For this aim opportune algorithms have been developed. The most recent one is based on a probabilistic approach, by solving the eqs. (3.1) for a number of different test density profiles; the profile for which the solution and the intensity measurements agree best will be then the most likely one [68].

In ASDEX Upgrade, the *lithium beam injector system* is capable of producing a beam which is horizontally injected at the outer side of the torus, about 0,326 m above its equatorial midplane, with atoms in the energy range of $35-60$ keV. Such relatively high energy is required for guaranteeing that the beam can penetrate far enough into the plasma edge region before it is completely ionized. However, since the total power injected into the plasma with the beam is not higher than 180 W, it is not perturbative for the global plasma power balance [69].
As primary source for the lithium atoms a material of *eucryptite* is used. The emitter is resistively heated at a temperature of about 1300 °C, required for a sufficient Li^+ emission. Once the ions are extracted, they are accelerated by a potential difference of about 35 kV and then focused, after that they pass through a neutralizer tube to finally form the neutral beam. This, consisting in about 10^8 lithium atoms per cm of beam, is finally injected into the vessel along the horizontal direction, which is represented in red in the Fig. 3.5 [69].
Finally, the *optical observation system* for the measurement of the emitted photons is toroidally shifted with respect to the beam. The lenses have a diameter of about 10 cm, resulting in a high photon yield, and the collected signal is amplified through a photomultiplier. The lines of sight collecting the emitted radiation, which are represented in blue in the Fig. 3.5, are arranged in a 28 channels row [69].

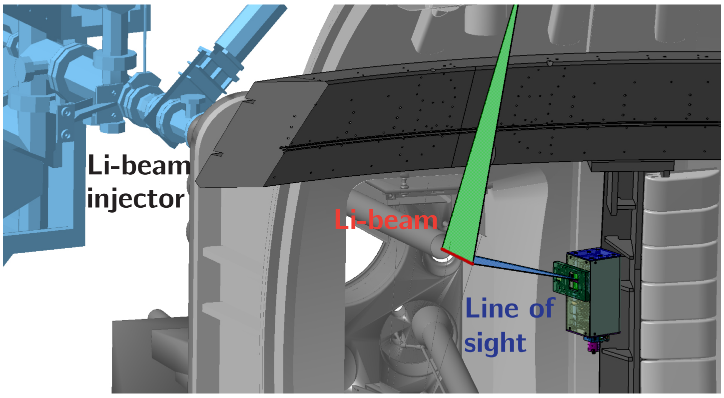

Figure 3.5: Line of sight for the optical observation system for the LiBES in ASDEX Upgrade. Taken from [69].

3.2.2 Edge Thomson scattering

Another important system for edge plasma studies is the *Thomson scattering system (TS)*. This consists in the analysis of the spectrum of a laser radiation which is shot inside the vessel, and is suitable for the measurement of radial profiles of both electron density and temperature with high spatial resolution [70].
The physical principle on which it is based is the spectral broadening of a monochromatic radiation injected in the plasma after the interaction of this with plasma particles. Due to the great difference in mass between electrons and ions, scattering of electromagnetic waves in the plasma is dominated by scattering from electrons. So, if a monochromatic radiation is

injected, the scattering of such radiation from the hot electrons leads to a spectral broadening due to *Doppler effect.* The broadening characteristics will then depend on the particular velocity distribution of the ensemble of electrons with which the radiation interacts [66]. In each case, since the dependence of the scattering effects on the plasma properties is very weak, very intense pulsed lasers are needed for this aim.
So, by measuring the amplitude of the broadening, it is possible to estimate the electron temperature, since the broadening width increases with increasing velocity of the electrons. For the practical calculations, theoretical scattering spectra are calculated for assumed maxwellian velocity distributions of the electrons; in this way, the temperature is determined by fitting these against the measured spectra. Moreover, since the intensity of the scattered radiation is proportional to the total number of electrons contained in the scattering volume, measuring this intensity allows to estimate the electron density as well. The radial plasma profiles are then determined by a least-square fit to the achieved scattering signals [71].
A qualitative example of spectrum broadening due to Thomson scattering in given in Fig. 3.6.

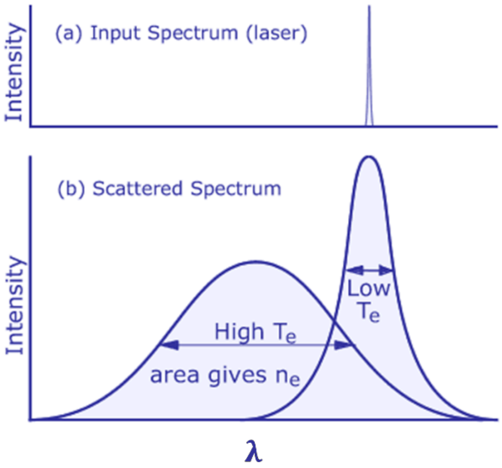

Figure 3.6: Broadening of the radiation spectrum due to Thomson scattering with the electrons.

Currently, typical values of spatial resolutions are in the range of 1 to few cm along the laser chord, for typical plasma densities. In order to obtain the desired radial plasma profiles, the laser beam passes tangentially the flux surfaces. The advantage of this is that the plasma parameters will vary slowly along the laser chord: in this way the spatial resolution turns into a much better resolution (of the order of mm) when the data collected along it, spanning all the flux surfaces of interest, are converted into radial profiles.

In ASDEX Upgrade, a configuration in which lasers are shot vertically into the plasma from the bottom of the torus is employed. In particular, a 10 channels system has been recently installed, to measure only the plasma edge profiles. The scattering volume has a length of 25 mm, and it is imaged directly through air to the observation system, to maximize the amount of the observed scattered light [72].
For this system, six *laser beams* are employed, consisting in Nd:YAG (neodymium-doped yttrium aluminium garnet) lasers with 1064 nm wavelength, passing vertically though the plasma; these are characterized by pulse energies about 1 J and pulse durations about 10 ns, at 20 Hz repetition rate [72]. The lasers are radially distanced by 2,7 mm. The final spatial resolution for the measurement of the outer midplane plasma edge profiles is determined by mapping the scattering volumes with a magnetic equilibrium to this spatial position.
Finally, the six beams are viewed by 11 "beams" of the observation system, with a vertical distance of 6 cm between the channels, looking radially inward through a radial port. In this

way, every 50 ms (that is at each laser pulse), a grid of 66 measuring points in the plasma edge region is scanned [72].
In the Fig. 3.7 we can see a poloidal cross section of the laser geometry, as well as the setup for the observation of the scattered radiation.

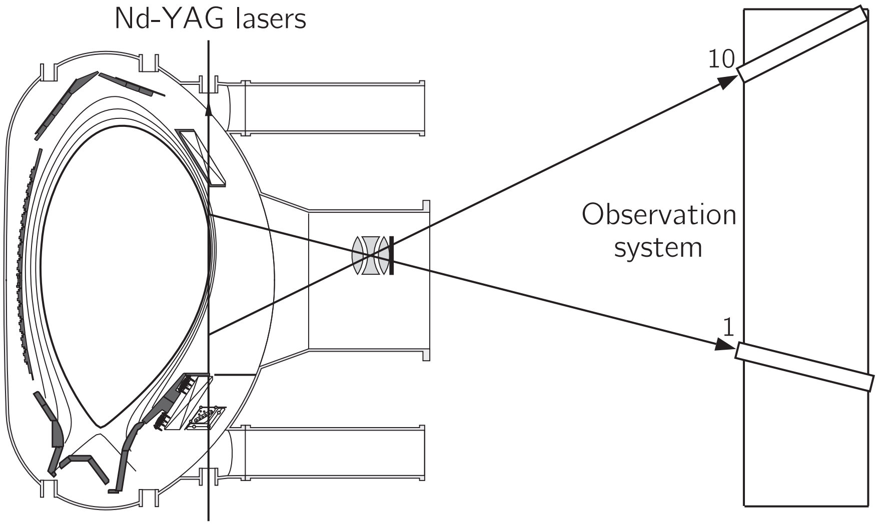

Figure 3.7: Scattering geometry for the edge TS system in ASDEX Upgrade. Adapted from [72].

3.2.3 Divertor Langmuir probes

A final major diagnostics relevant for this work, and one of the most widely used for plasma physics studies, is given by the *Langmuir probes*. These consist in one or multiple electrodes protruding into the plasma, collecting a current. They measure the current-voltage (I-V) characteristic of the sheath, the region with net positive charge density which forms spontaneously when any solid materials is brought in direct contact with the plasma (cfr. Section 2.2.1). In this way, it is possible to derive several plasma quantities by fitting a theoretically derived I-V curve to the measured one [66].

When a probe is put into the plasma, after the sheath is formed, we will have a ion flux density $\Gamma_i = n_i c_s$ onto is, according to the Bohm-Chodura criterion (eq. (2.16)), and thus a (saturation) current density

$$J_{i,sat} = e n_i c_s \tag{3.2}$$

So, if the floating potential V_{fl} (i.e. the potential difference at equilibrium between the plasma and the probe surface as zero net current) is known, then the total *probe current*, which is biased negatively with respect to the plasma, can be calculated as the difference between the ion and electron currents, that is as

$$I_{probe} = -A_{probe} J_{i,sat} \left[1 - \exp\left(\frac{e(V_{probe} - V_{fl})}{T_e} \right) \right] \tag{3.3}$$

where A_{probe} is the area of the probe. The equation (3.3) is derived considering that most electrons are reflected in front of the probe, so that only a small fraction, described by a Boltzmann factor, influences the total probe current [66]. In the Fig. 3.8 a typical *I-V characteristic curve* is shown, together with the equivalent electric circuit.
So, putting the probe at large negative voltages, all electrons will be effectively repelled, and the resulting *ion saturation current* will be given by

$$I_{i,sat} = A_{probe} J_{i,sat} \tag{3.4}$$

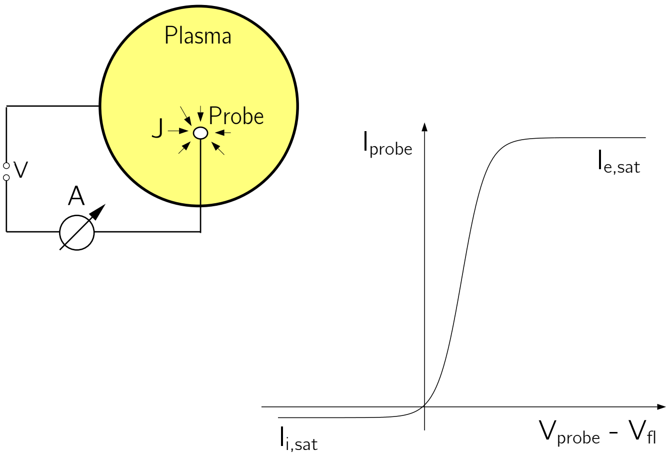

Figure 3.8: Equivalent circuit of a simple Langmuir probe, and its I-V curve. Taken from [44].

Knowing then the value of $I_{i,sat}$ from the I-V characteristic curve of the probe, it will be possible to deduce the ion (and electron) density of the plasma in front of it, assuming to know the local sound speed, as

$$n_i = n_e = \frac{I_{i,sat}}{ec_s A_{probe}} \tag{3.5}$$

Instead, reducing the negative probe voltage allows more and more electrons to reach it, thus reducing and finally reversing the current flow. From the slope of the I-V characteristic curve it is then possible to calculate also the electron temperature, as [66]

$$T_e = e(V_{probe} - V_{fl}) \left[\ln \left(1 + \frac{I_{probe}}{I_{i,sat}} \right) \right]^{-1} \tag{3.6}$$

Strictly speaking, such calculations require also the knowledge of the ion temperature, in order to evaluate the local sound speed; however, if we are interested in measurements in the divertor region, $T_i \approx T_e$ could be safely assumed.

In addition, the fluxes striking onto the probe could be calculated as well, since the ion saturation current is a direct measurement of the charged particle flux onto an area comparable with the probe surface. Therefore, since $\Gamma_\perp = n_i c_s$, it will be

$$\Gamma_\perp = \frac{I_{i,sat}}{eA_{probe}} \tag{3.7}$$

Finally, the heat flux onto the probe surface can be similarly calculated after the knowledge of the total sheath heat transmission coefficient γ, writing the heat which is brought to the surface by one incident electron-ion pair as $\gamma T_e + E_{rec}$. In fact, also the heat deposition E_{rec} on the surface derived from the energy released by the recombination of the ions on it must be taken into account, where $E_{rec} = 13{,}6 + 2{,}5$ eV for a hydrogenic plasma. Therefore, the total heat flux will be $q_\perp = \Gamma_\perp(\gamma T_e + E_{rec})$, i.e.

$$q_\perp = \frac{I_{i,sat}}{eA_{probe}}(\gamma T_e + E_{rec}) \tag{3.8}$$

In ASDEX Upgrade, several systems of Langmuir probes are currently installed. Among these, the most important one for particle and power exhaust studies is located on the divertor targets, and is used to determine the plasma parameters precisely in front of these. These are *flush-mounted probes*, meaning that they are employed in the material surfaces of the targets, exposed to the plasma at a grazing incidence: in this way, the impinging fluxes could be sustained also in steady state avoiding any risks of erosion or melting [73]. The data analysis is then performed taking into account the effects of the grazing incidence of magnetic field lines onto the probe surface [74]. Such probes cover the whole poloidal amplitude of the divertor region, and are installed at three different toroidal locations. In the Fig. 3.9 we can see a close-up of the probes as mounted on the divertor targets, together with a more detailed schematic design.

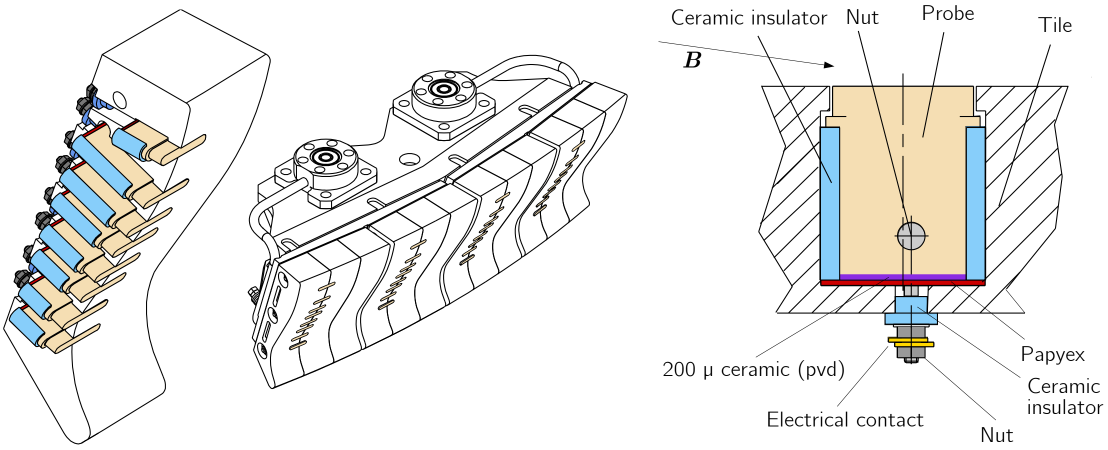

(a) Close-up of the probes.

(b) Schematic design of the probes.

Figure 3.9: Flush-mounted probes on the divertor targets in ASDEX Upgrade. Taken from [59].

3.3 Experimental evidence of enhanced perpendicular transport

Until recently, the phenomena of radial convective motion of blob-filaments in the scrape-off layer (cfr. Section 2.4.1) and density shoulder formation and related main chamber recycling regime (cfr. Section 2.4.2) were linked only on a theoretical basis. Then, recent experiments performed in ASDEX Upgrade [11][12][13][16] definitely linked the shoulder formation to an increase in blob size and associated perpendicular particle transport at the outer SOL midplane at high densities: in fact, the achievement of both these features was shown to take place over a common density threshold. The aim of this section is to briefly summarize these recent studies, which ultimately constitute the main experimental basis for this thesis.

3.3.1 The role of divertor collisionality

The experiments were carried out by analyzing the results of *L-mode discharges* with common magnetic parameters (namely, a toroidal field of 2,5 T and a plasma current of 0,8 MA). The discharges were performed with different heating powers (0, 300 and 600 kW by ECRH, plus the natural ohmic heating in all cases). All the discharges consisted in *density ramps* with a deuterium plasma (with, in some cases, the addition of nitrogen seeding). In this way, it was managed to span from a low density regime to a high density regime: in the first case the radial density profile at the outer SOL midplane was still nearly exponentially decaying and the "classical" picture of SOL transport was still valid; in the second case, instead, a shoulder was clearly present and an enhanced perpendicular transport regime was evidently achieved.

The mentioned studies were performed by taking the density decay length λ_n at the outer SOL midplane as a figure of merit for quantifying the broadening the density profile due to an eventual shoulder formation. For doing this, λ_n was evaluated by exponentially fitting the radial density profile, as derived from the LiBES data, in the first 25 mm outside the separatrix.

The earliest of these studies [11] proposed that a transition mainly occurs over a threshold in the line-averaged edge plasma density $\overline{n}_{edge}$. Anyway, it was seen later [13] that λ_n actually increased at different edge density values, depending on the heating power (see Fig. 3.10a). So, it was not possible to identify a simple density threshold for delimiting a transition between the two transport regimes.

Therefore, attention was focused on the properties of radial blob propagation in function of the plasma conditions: namely, it was investigated whether it was a change in the blob transport regimes which determined an increase of perpendicular transport and, thus, the formation of the density shoulder. This was motivated by the fact that, as it is theoretically known (cfr. Appendix B.2), the radial convective motion of blobs is expected to undergo an abrupt transition, depending on the plasma conditions (in particular, on the electric resistivity along the magnetic field lines), over the threshold $\Lambda = 1$. In blob theory, the parameter

$$\Lambda = \frac{\Omega_i}{\Omega_e} \frac{\nu_{ei}}{c_s} L_{\parallel} \tag{3.9}$$

is known as *collisionality parameter*; here, $L_{\parallel}$ is a parallel connection length, ν_{ei} is the electron-ion collision frequency, c_s is the plasma sound speed and $\Omega_{e,i}$ are electron/ion gyrofrequencies. Since Λ scales as $n_e T_e^{-2}$, a threshold in collisionality effectively represents also a threshold in density, whose value however increases with temperature (and thus with the heating power).

For investigating this, the behavior of the perpendicular transport regime, in terms of λ_n, was followed in terms of both a midplane collisionality Λ_{mid} and a divertor collisionality Λ_{div}. The first one was calculated using, in the eq. (3.9), the density and temperature measurements at the outer midplane from LiBES and TS and taking $L_{\parallel}$ as midplane-to-target connection length; the second one, instead, using the density and temperature measurements at the outer divertor target from Langmuir probes and taking $L_{\parallel}$ as X-point-to-target connection length.

It was found that the collisionality threshold $\Lambda = 1$, being achieved at different $\overline{n}_{edge}$ values depending on the heating power, was effectively involved in a global transition of the perpendicular transport regime. In particular, it was seen that the main driving parameter is the divertor collisionality rather than the midplane collisionality [13]. This can be clearly seen in the Fig. 3.10b, showing the experimentally fitted values of λ_n from the various discharges in function of the corresponding estimate for Λ_{div}.

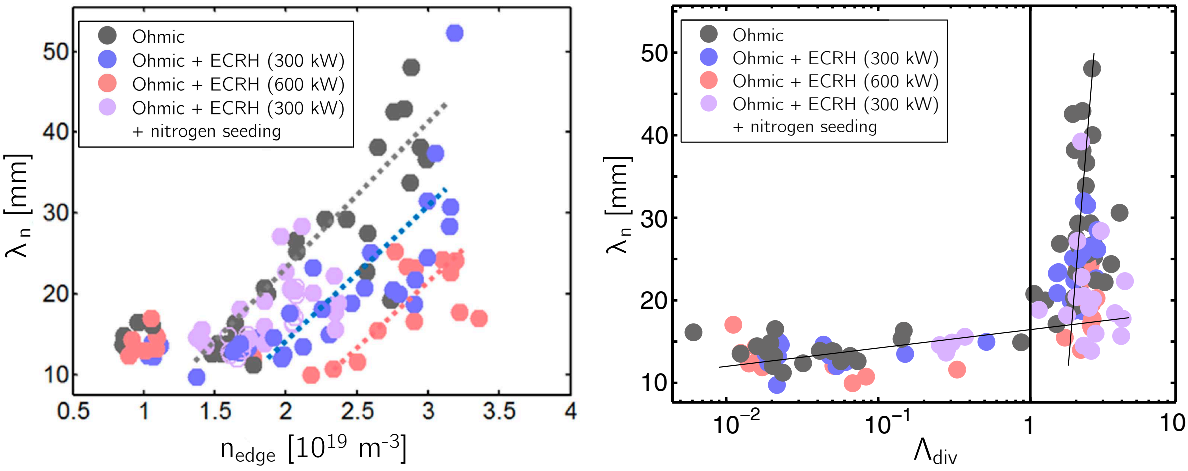

(a) Trend of λ_n with $\overline{n}_{edge}$.

(b) Trend of λ_n with Λ_{div}.

Figure 3.10: Trend of the experimentally fitted density decay length at the outer SOL midplane in function of line-averaged edge density and divertor collisionality, for different heating powers. Taken from [13].

All the points, in fact, converge into a single curve, regardless of the heating power. In particular, λ_n remains almost constant until the threshold $\Lambda_{div} = 1$ is surpassed; after that it rapidly increases, indicating then the formation of the density shoulder, and thus a substantial increase in the perpendicular transport.

From this it was definitely confirmed that an abrupt transition actually exists for the perpendicular SOL transport, such that, after its threshold is surpassed, the radial density profiles at the outer SOL midplane begin to flatten. This transition was seen to be strictly related with the evolution of collisionality, characterizing the radial convective motion of blobs: therefore, a correlation between the two phenomena, theoretically discussed in the Section 2.4, seemed to effectively take place in the reality as well.

3.3.2 Characterization of blob properties

For characterizing in a complete way the the correlation between the two phenomena, the evolution of *blob properties* with the increase of the density regime was also studied. This was done in another study [75], in which L-mode discharges performed with a magnetic configuration equivalent to the one considered in [12][13] were investigated.

Here, the experimental blob properties were obtained after conditional analysis; namely, it was chosen to consider only the detected positive density perturbations with amplitude greater than 2,5 times the standard deviation for density measurements, by means of the data obtained with the LiBES diagnostics. Following the increase of the density regime, characterized in this study by the so-called Greenwald fraction [76], the main blob properties were measured on a given flux surface. The results are reported in the Fig. 3.11, where we can observe:

- (a): the *auto-correlation time* τ_{AC} of the blobs, defined as the half width at half maximum of the detected fluctuation signal against the measurement time; this can be interpreted the duration of blob passage through the measurement point.
- (b): the *detection frequency* ν_b of the blobs, quantifying the number of blobs being detected per unit time in a given radial location.
- (c): the *density fluctuation* δn due to the blobs, that is the difference between the localized high density of blobs and the background density.
- (d): the *radial propagation velocity* v_b, obtained using the relative delays of the detection times in radially separated locations.

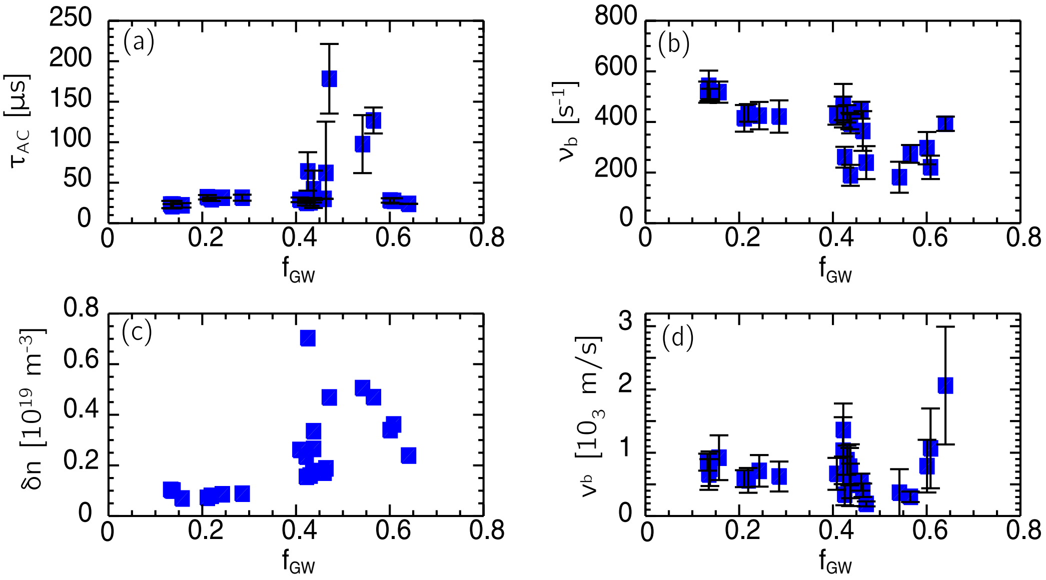

Figure 3.11: Evolution of blob properties with increasing density. Taken from [75].

As we can see, at high density a change in blob properties could be observed, manifested in some increase in the auto-correlation time, amplitude of density fluctuations and propagation velocity.

Starting from these results, and given the evidence of the transition in the perpendicular transport regime at high collisionality, in [12][13] the blob properties were then also characterized in terms of the different divertor collisionality regimes.
For this aim, the *average blob size* δ_b was obtained multiplying the measured radial velocities v_b of blobs by the measured passage duration, quantified by τ_{AC}. The values for δ_b measured in this way, in function of the evolution of the divertor collisionality, are shown in the Fig. 3.12. Two different regimes clearly appear also here, at the two sides of the $\Lambda_{div} = 1$ threshold: these are featured by an approximately constant blob size of about $5 - 10$ mm for low collisionality, and by a rapidly increasing size, up to $50 - 100$ mm, for high collisionality. Again, these data show no dependence on the heating power.

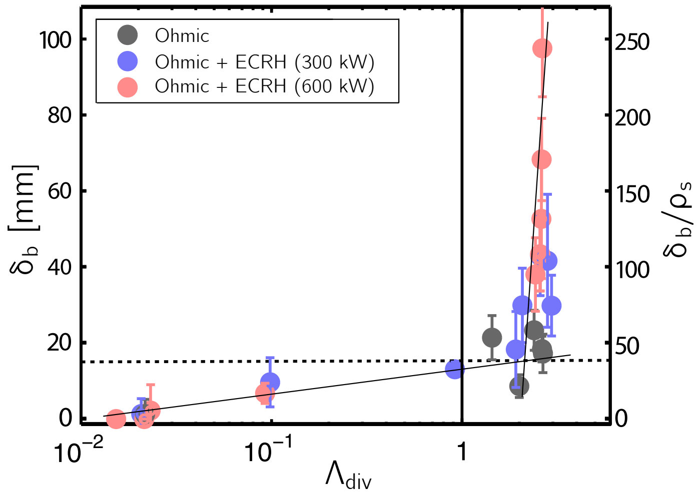

Figure 3.12: Measured blob size in function of the divertor collisionality. Taken from [13].

From these results it was confirmed that increasing the SOL collisionality (i.e. the SOL density regime) effectively changes the blob properties, that is size and radial propagation velocity. In this way it was concluded that this is precisely the main reason for the enhancement of perpendicular transport at high density. This appeared evident from the astonishing similarity between the evolution of density decay length and blob size with Λ_{div}, figures 3.10b and 3.12.
What does occur is that, at low collisionality, with a relatively low radial propagation velocity and a small size, blobs carry few particles inside them while radially convecting. At high collisionality, instead, with a higher velocity and a size, blobs constitute such an efficient channel for the radial particle transport to strongly impact on the global SOL transport regime.

3.3.3 Motivation and goals of the thesis

The just presented experimental results acted as a validation of a model for the impact of radial blob propagation in the scrape-off layer on its global transport regime; to this model it was given the name of *filamentary transport* [12][13]. The role of the divertor collisionality as the only control parameter for the transition of both blob properties (size and radial propagation velocity) and perpendicular transport regime (density shoulder formation) has been demonstrated.
Moreover, this model was experimentally validated also in other currently operating devices in addition to ASDEX Upgrade, as the same results obtained in the former were also successfully reproduced in the JET tokamak [77]. This suggests that a similar behavior could be expected in future devices which will likely share the same geometry of ASDEX Upgrade and JET. These

will be operated at high density, which will ensure with no doubt a high collisionality regime during their operation: therefore, a situation with enhanced perpendicular transport could have to be considered as routinely for these.

This could potentially lead to both beneficial and detrimental effects; in particular:

- By increasing the radial particle flux into the far SOL, main wall sputtering could be seriously increased due to the large impinging ion fluxes.
- By carrying heat in radial direction, the radial heat flow in the SOL can be strongly enhanced, resulting in an increase of the power losses along the SOL and a broadening of the power scrape-off width; this could contribute both to decrease the peak heat loads onto the targets and, eventually, to promote a detached regime.

In order to explore in the most complete way possible all the eventual risks and/or benefits deriving from such kind of operation, a deeper investigation than how achievable in the experiments came out as mandatory; namely, it was necessary to perform this by numerically reproducing an enhanced perpendicular transport regime. In particular, the aim was to investigate the eventual impact of the enhancement of perpendicular transport on the global momentum and power balances in the SOL region, focusing on the consequences on the exhaust processes in the divertor region.

The main idea of this thesis work, then, was to carry out different numerical simulations done with varying transport assumptions. In this way, the ultimate goal was to get simulated plasma conditions compatible with the experimental data, characterizing a situation of enhanced perpendicular transport, and to perform then a deep investigation of the simulations results.

The next chapters are dedicated to present and discuss the performed simulations. With such a simulation work it was tried to reproduce two situations in which an enhanced perpendicular transport regime is absent and present, respectively, as recognizable from the absence/presence of a density shoulder at the outer SOL midplane. The main challenge consisted in trying to derive an adequate radial profile for an effective particle diffusivity $D_{n,\mathrm{eff}}$, acting as a coefficient which averages the effects of the intermittent blob-driven convective transport on a sufficiently long time scale, in order to match the experimental density profiles.

Once this task was completed, an investigation of the simulations results was performed, focused on characterizing the impact of the enhanced perpendicular transport on two aspects:

- *Enhancement of radial particle* and *heat transport* at the outer SOL midplane, *fluxes onto the main chamber wall*, and impact on the *density shoulder formation mechanisms.*
- *Particle and power exhaust at the divertors*, with regard to the impact on the conditions at the targets and eventual achievement of a *detached regime*, focusing on the role of atomic processes in the divertor region.

Chapter 4

Numerical tools

In this chapter, the numerical tools used for performing the simulations will be briefly described. First of all, in the Section 4.1 a general overview of the SOLPS-ITER code package, which has been used for the modelling of the considered ASDEX Upgrade discharge, will be provided. In the Section 4.2 more details will be given about the two major modules of SOLPS-ITER, namely the B2.5 program for plasma particles modelling and the EIRENE program for neutrals modelling. Finally, in the Section 4.3 some details will be given about the general workflow of a SOLPS-ITER run.

4.1 The SOLPS-ITER code package

As pointed out in the last chapter, for a deeper comprehension of the processes involved in the enhancement of perpendicular SOL transport, detailed information about global balances, density, temperature, particle/heat fluxes and distribution of neutrals and atomic processes is needed. Most of these information can be extracted only with the help of numerical codes, simulating the plasma behavior as resulting by the competition of parallel transport and perpendicular transport, and by the interaction of this with neutrals and material surfaces. For this aim, it was necessary the use of advanced *computational plasma edge models*, developed precisely for the aim of understanding the complicated and inter-related processes characteristics of the edge plasma [18].

In principle, the most detailed model for plasma description is undoubtedly a kinetic one; nevertheless, such a treatment would be too much heavy, in terms of computation requirements, even for a pure hydrogenic plasma. Therefore, more simplified *fluid models* are usually adopted, in which plasma particles are treated by means of fluid equations. This is reasonably appropriate since, as discussed in the Appendix C.2.1, typical edge plasmas for fusion applications are sufficiently collisional that a fluid approximation can effectively be used. In this way, only to the neutral populations a kinetic treatment is left, which is instead necessary because of their larger mean free path; for this aim, *Monte Carlo methods* are currently adopted, being these able to support the complex atomic processes which are involved.
A good description for the plasma particles in the edge region has to include both the effects of parallel and perpendicular transport; therefore, at least a two-dimensional treatment for these is required, according to the axial symmetry present in toroidal devices. This translates in the need for two-dimensional fluid models, consisting in analytic conservation relations, describing the evolution of the plasma quantities in a poloidal plane of the torus. However, the anomalous transport is still unpredictable from first-principle-based theories, and thus a complete model for this is missing; therefore, this transport component is currently still isolated computationally, so

that an empirical description for perpendicular transport, derived from experimental evidences, is to be implemented in such models.

The just described ones are precisely the operating principles of *SOLPS-ITER* [20][78], the newest version of the *SOLPS (Scrape-Off Layer Plasma Simulator)* code package, one the most sophisticated tools for plasma edge modelling, and the one which was used for this work. This consists in a coupling of two distinct physical modules, namely *B2.5*, a 2D multi-fluid plasma transport code, and the most recent version of *EIRENE*, a 3D kinetic Monte Carlo neutral transport code [19].
It has been widely used for both interpretative and predictive purposes in the major currently operating tokamaks, such as ASDEX Upgrade [79][80][81][82], JET [83], Alcator C-Mod [84] and DIII-D [85]; moreover, it is currently the most employed tool to assess the performances of future devices [86], as well as to perform studies on the plasma-facing components [87].
SOLPS-ITER could actually work both in *standalone mode* (B2.5 only running), or in a full *coupled mode* (B2.5 + EIRENE running) [20]. In the first case, since it is made use of the fluid module only, the fluid equations are solved for both charged plasma particles and neutral particles. In the second case, instead, plasma particles are described using the fluid module, while the transport of neutral species and their interaction with the formers and the material surfaces is described by the Monte Carlo module; in detail, in this case the coupling acts with the surface and volumetric sources/sinks for the plasma in B2.5 due to the interactions with neutrals being computed by EIRENE. The main advantage of the standalone mode is its much faster achievement of the results and the avoidance of the typical Monte Carlo noise in the the results; however, simulations done in coupled mode are quite more accurate, especially for cases in which the neutral density is relatively high.
The coupling procedure, actuated at each time step of B2.5, presents the following scheme [18]:

1. When a plasma background has been prepared by B2.5, it is sent to EIRENE.
2. A number of neutral particles histories is simulated by EIRENE in the plasma background.
3. The neutral-plasma interactions modelled by EIRENE are transferred again to B2.5 in form of sources and sinks for particles, momentum and energy.
4. B2.5 re-computes the plasma solution by solving the conservation equations for electrons and ions, after which a new plasma background is prepared, which will be used in the successive iteration.

In addition, the package also contains other tools, namely *DivGeo* and *Carre*, which are used to generate the computational grid for B2.5.

The code solves the equations describing the behavior of a fluid plasma in the edge region, consisting in a thin annulus of the outer core plasma and the entire scrape-off layer, fully including private flux region and divertor region. For doing this, it takes as input [18]:

- A *computational grid*, derived from the discretization of the plasma volume following the magnetic equilibrium configuration for a particular experimental scenario, in which the fluid and kinetic equations are solved through finite-difference calculations [22].
- A set of *boundary conditions* about physical inputs, e.g. density regime and input power, and properties of the plasma-facing materials, e.g. geometry of the material surfaces and models for the plasma-material interaction [22].
- A choice of empirically evaluated anomalous *transport coefficients*, such as particle diffusivity and electron/ion thermal diffusivities, as for fitting experimental data [88].

The main goal of SOLPS-ITER is to fully capture a steady-state situation, obtained at the end of a time-dependent convergence process in which the plasma evolution is followed by solving the equations included in it, consistently with the just described inputs. Once this has been reached, it is possible to extract all the information of interest for the modelled scenario [18].
Since some aspects of the physics are most easily understood if the physics itself of the code is simplified, often the runs are performed with several simplifications. For example, usually a pure hydrogenic plasma is considered, neglecting drift motions of plasma particles and the presence of electric currents, and implementing the simplest choice for the anomalous transport coefficients. In this way, much of the basic qualitative understanding of scrape-off layer physics is still captured, requiring extremely less computational power [18]. In this work the effects of plasma contamination with impurity species and drifts and currents have been indeed neglected, but much effort was instead dedicated to the search for the best assumption for the transport coefficients, since this was precisely one of the main objectives to achieve.

4.2 Programs in SOLPS-ITER

4.2.1 B2.5

As already mentioned, *B2.5* is the fluid module of SOLPS-ITER, completely written in FORTRAN 90, which computes the evolution of the charged plasma particles. Its first version, consisting in the earliest version of the B2 program, was originally developed by B. Braams in 1986 [21]; this version was then improved in the geometry [89] and enlarged by adding several terms in the fluid equations which were firstly neglected, such as drifts and currents [22]. However, these earliest versions still contained major simplifications. In the following years, other physical processes originally neglected have been added, and the coupling with EIRENE was successfully achieved [90].

In particular, it solves the fluid transport equations (precisely a modified version of the Braginskii equations, cfr. Appendix C.1) for the electrons and a arbitrary number of ion species, the last ones sharing a same temperature, basing on a finite volume discretization method [22].
At each numerical iteration, corresponding to a single time step, volumetric and surface source terms are computed, and the conservation equations (particles, momentum and energy, in addition to potential if currents are also considered) are solved. This is repeated for a number of "internal iterations" to relax the equation solutions before proceeding to the next time step, or "external iteration" [22].
The equations are solved for the necessary number of time steps until the convergence is reached, which is monitored by analyzing the norm of the residuals of each conservation equation. Steady state is achieved if, independently of the time step chosen, no major variation of the main plasma parameters is observed. Currently, B2.5 can be run with time steps of $10^{-3} - 10^{-4}$ s when no steep time gradients are expected to occur during the convergence procedure (e.g. when drifts and currents are neglected); otherwise, time steps down to $10^{-5} - 10^{-6}$ s could be required, slowing down considerably the convergence process. Depending on the plasma conditions to simulate, a new case may require about 10^4 to 10^5 iterations before an acceptably converged steady state is obtained.

The equations are solved on a *curvilinear grid*, covering the entire plasma edge region, which strictly aligns with the magnetic field lines; for this reason, this grid must be prepared by importing the magnetic equilibrium configuration of the particular scenario to be modelled. The numerical calculations are performed on a topologically rectangular mesh: the transformation between the physical geometry and the computational mesh is provided in each cell through a set of metric coefficients [22]. The resulting curvilinear orthogonal system is characterized by a x direction representing the orthogonalized *poloidal coordinate* θ (with positive direction from the inner to the outer divertor target) and a y direction representing the orthogonalized *radial coordinate* r (with positive direction from the core outwards).

In the magnetic geometry of interest, namely the *lower single-null (LSN)* geometry, the grid is subdivided in four distinct regions: *core plasma* (region 1), *scrape-off layer* (region 2), *inner divertor region* (region 3) and *outer divertor region* (region 4). In the Fig. 4.1 we can see the actual subdivision of these regions in the physical domain, as well as how it appears when transiting to the computational domain. The classification of the various boundaries can then follow a NSWE subdivision, with west/east boundaries occurring along the x direction and the north/south boundaries occurring along the y direction. For this reason, the innermost grid boundary is usually called south boundary, while the grid boundary which looks out at the main chamber wall is usually called north boundary. Then, the west and east boundaries correspond to the inner and outer divertor targets, respectively.

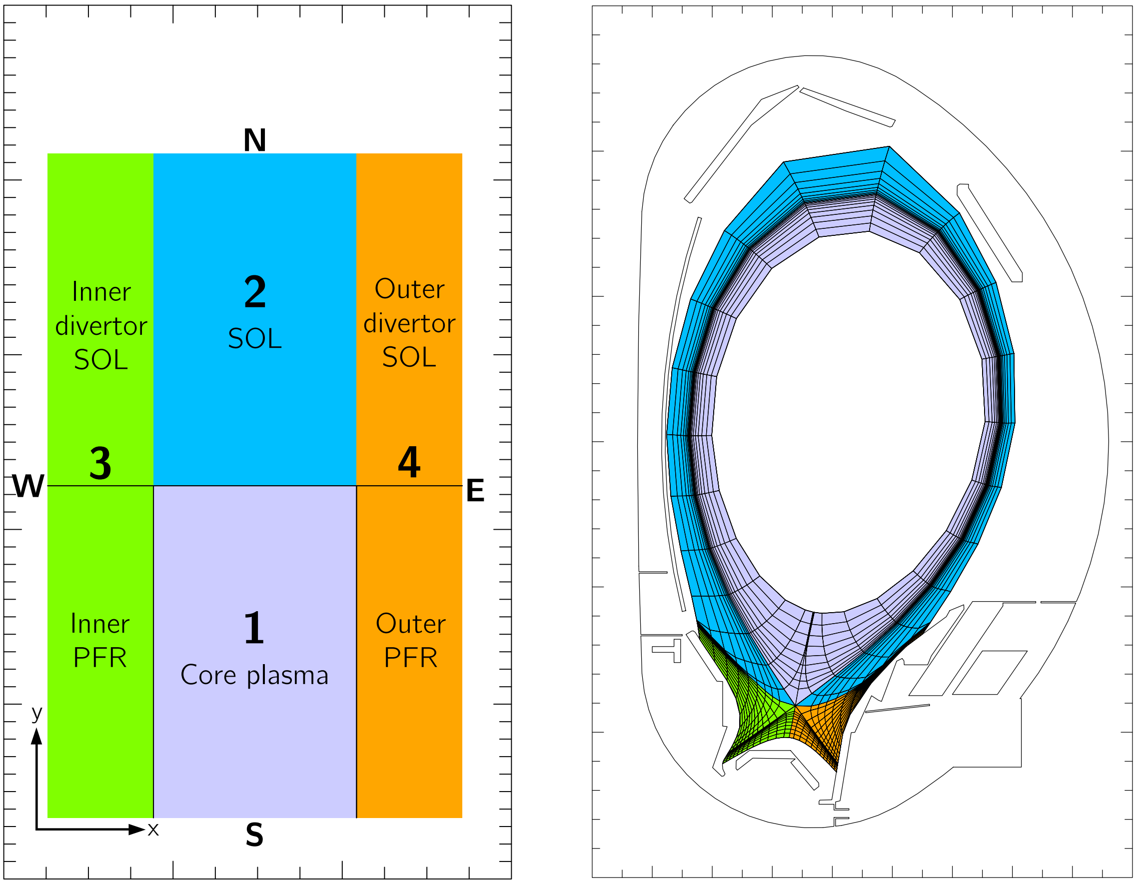

(a) Computational domain.

(b) Physical domain.

Figure 4.1: Regions definitions in B2.5 as in a single-null geometry in ASDEX Upgrade.

The grid resolution is generally adjusted so that it results higher in directions where strong gradients in plasma parameters are expected to exist, but it is left relatively coarse in directions of small or negligible gradients. Higher resolutions are then required in the divertor region along the poloidal direction and around the separatrix in radial direction.

During a run, *boundary conditions* must be specified for each conservation equation. These are usually specified in terms of fluxes or derivatives of the fluxes at the external grid boundaries, in order to act as sources or sinks for the equations at the outermost grid cells [22]. Furthermore, it is also possible to specify these in form of feedback schemes, i.e. adapting the magnitude of external physical outputs so that the desired values of some plasma quantities are achieved; for example, one can specify to control the external gas puff in this way so that a desired value of density at the outer midplane separatrix is obtained.

More details about the physics of B2.5, together with a deeper insight on the conservation equations which are solved, the specification of boundary conditions and some additional numerical aspects can be found in the Appendix C.2.

4.2.2 EIRENE

Then, *EIRENE* [91] is the module dedicated to the modelling of neutral species, also written in FORTRAN 90. Its first version was developed by D. Reiter in 1984 [92], but several updates have been introduced since then [23]. For example, the most recent version EIRENE-2010, which is the one included in SOLPS-ITER, includes the enlargement of the considered atomic and molecular processes, the possibility to simulate radiation losses and neutral-neutral and photon-neutral collisions, and the possibility to run it in parallel mode (that is following more histories for each step).

In particular, it solves the linear kinetic transport equations for the neutrals as *test particles* in 3D volumes by means of Monte Carlo methods; namely, it computes the statistical expectation values for the processes between such test particles and the plasma, following the history of a number of these when launched in the plasma [23].
The operating principle of EIRENE is as follows. A number of test particles is launched in a background medium from some particle source, with a given distribution in directions and velocities; in case of a coupled SOLPS-ITER run, such background medium is just the plasma as computed at each time step by B2.5. The lengths of the trajectories travelled by these are randomly generated, although proportional to the neutrals mean free path. Each test particle is followed, along its trajectory through the medium, until it is either absorbed at a material surface or ionized becoming a particle of the plasma background. All the events which can occur on the trajectories of test particles have probabilities depending on the cross sections of the related atomic process. At the end, a number of histories of test particles will have been created, from which averaged values for the related physical quantities in each point are derived.
Rate coefficients for the atomic processes which test particles can undergo when interacting with the particles of the plasma background are provided by external atomic physics databases such as AMJUEL [93] and HYDHEL [94].
Computations of EIRENE are done on tetrahedral volumes in a full 3D geometry, which reduces to a triangular grid in the poloidal plane. This extends over the entire grid of B2.5 and even further, up to the material boundaries of the main chamber wall. So, the grid boundaries coinciding with the material surfaces can be characterized by some absorption and reflection probabilities to take into account the interactions of the neutrals with the solid surfaces.

More details about the physics of EIRENE, together with a deeper insight on the methods which are used and the kinetic equations which are solved, can be found in the Appendix C.3.

4.3 SOLPS-ITER workflow

The general behavior of a SOLPS-ITER run is controlled through a number of input files, which are read by the various programs. The *workflow* for a B2.5-EIRENE coupled run can be briefly summarized as [78]:

1. Compile the *pre-processor input files* specifying the desired characteristics for the run:
   `b2ag.dat`, for setting up the *geometry* of the problem, e.g. specifying size of the grid and mesh file to be read;
   `b2ah.dat`, for setting up the *default physical parameters*, e.g. specifying number of species to be considered and basic parameters;
   `b2ar.dat`, for setting up the *atomic processes settings*, e.g. specifying atomic physics database to be used and considered range of densities and temperatures;
   `b2ai.dat`, for setting up the *initial plasma state*, e.g. specifying the initial values of densities and temperatures.
2. Run the *pre-processor programs*, which read the pre-processor input files and produce the geometry file `b2fgmtry`, the default physics file `b2fpardf`, the atomic processes file `b2frates` and the initial plasma state `b2fstati`, which will be read by the main program.
3. Insert/edit the desired *main input parameters* in the main input files:
   `b2mn.dat`, determining the operating regime of the B2.5 (e.g. duration of time steps, number of steps to be performed, activated switches);
   `input.dat`, determining the main parameters of EIRENE;
   and optionally in the files:
   `b2.boundary.parameters`, specifying the boundary conditions on each boundary segment for each equation;
   `b2.transport.parameters`, specifying a uniform value for the various anomalous transport coefficients;
   `b2.neutrals.parameters`, specifying data and parameters regarding the treatment of neutrals;
   `b2.numerics.parameters`, specifying the settings for the numerical computation of the equations;
   `b2.source.profile`, specifying arbitrary radially dependent profiles for the source term in each equation;
   `b2.transport.inputfile`, specifying arbitrary radially dependent profiles for the various anomalous transport coefficients.
4. Run the *main program* `b2mn.exe` in order to start the run. At the end of the run, a number of *output files* will be obtained, among which the final plasma state `b2fstate`, containing all the physical quantities for each cell as resulting after the last performed step.
5. If, at the end of the run, convergence has not been reached yet, the just produced final plasma state `b2fstate` is overwritten on the initial plasma state `b2fstati`, so that a new run can be initiated starting from the just achieved plasma conditions. This procedure is repeated, iteratively, until convergence is reached.

Chapter 5

Simulation activity

The aim of this chapter is to present the work which was performed to achieve reliable simulations for an actual ASDEX Upgrade discharge, presenting an enhanced perpendicular transport regime. The Section 5.1 will contain a brief description of the discharge which was modelled, explaining why it was chosen for this aim. Then, in the Section 5.2 all the steps followed for obtaining the final simulations will be described, which consisted in trying to reproduce several experimental features of the considered discharge. This will be followed, in the Section 5.3, by a brief description of the final results and brief considerations about the assumptions done for simulating the enhanced perpendicular transport.

5.1 Discharge parameters

The simulations work was carried out using the magnetic properties and the plasma parameters taken from the discharge #33341 of ASDEX Upgrade. This is one the discharges analyzed in [16][17] and from which the experimental results of perpendicular transport enhancement and blob properties presented in the Section 3.3 were taken. It is a *pure deuterium L-mode discharge* consisting in a *density ramp*; this means that the fuelling through gas puff was gradually increased in order to achieve an increasing density regime: in this way, a range of more than two orders of magnitude in the divertor collisionality Λ_{div} was covered, and both the situations $\Lambda_{div} \ll 1$, $\Lambda_{div} \gg 1$ were achieved, at different times. The divertor configuration present at the time of the discharge was the Div-III, the most recent one, characterized by a closed geometry and vertical tungsten-coated targets (with the outer made in massive full tungsten).
In the following table, the most important physical parameters for this discharge are listed.

Physical parameters of the discharge #33341	
Plasma type	Deuterium
Toroidal field B_φ	-2,518 T
Plasma current I_p	0,800 MA
Safety factor q_{95}	4,901
Plasma elongation κ	1,693
Heating power	Ohmic heating + $\approx$ 310 MW by ECRH

In this experiment, the relation between increase of divertor collisionality, enhancement of perpendicular transport driven by radial blob propagation and formation of a density shoulder at the outer SOL midplane was already shown. The goal of the simulation work was to use the advanced potentialities of SOLPS-ITER in order to try to reproduce the most relevant features which were achieved experimentally; these features were a strong enhancement of both particle and heat radial transport at the outer midplane, and a transition in the particle and power exhaust regime up to a partial detachment [16].

In detail, it was tried to reproduce two situations, occurred during the ramp, in which an enhanced perpendicular transport regime is absent and present respectively, as was expected to occur before and after the transition point $\Lambda_{div} \approx 1$. Two reference times were chosen, at low and high density respectively, whose measurements were taken as starting point for the simulations. In particular, for the *low density case* (case A) it was chosen to consider the time t = 1,77 s; then, for the *high density case* (case B) it was chosen to consider the time t = 3,56 s. Such choice was motivated by the fact that these are precisely the times at which the measurements presented in the works [16][17] were taken; in these works, in fact, it was observed how the radial density profile at the outer SOL midplane still exhibits an exponential decay in the first case, while in the second case a density shoulder is clearly visible. These measurements were then considered for performing a comparison of the simulation results with the experimental ones.

In the Fig. 5.1 the time traces of the main parameters for the discharge, namely toroidal field, plasma current, ohmic heating power, ECRH heating power, line-averaged edge density and fuelling rate by gas puff are reported; the two considered times are highlighted by vertical lines. As we can see, the two cases are characterized, respectively, by a total heating power of about $(310 + 310)$ MW = 620 MW and $(510 + 310)$ MW = 820 MW, a line-averaged edge density of $1{,}08 \cdot 10^{19}$ m^{-3} and $2{,}57 \cdot 10^{19}$ m^{-3}, and a gas puff fuelling of $0{,}46 \cdot 10^{21}$ s^{-1} and $10{,}73 \cdot 10^{21}$ s^{-1}

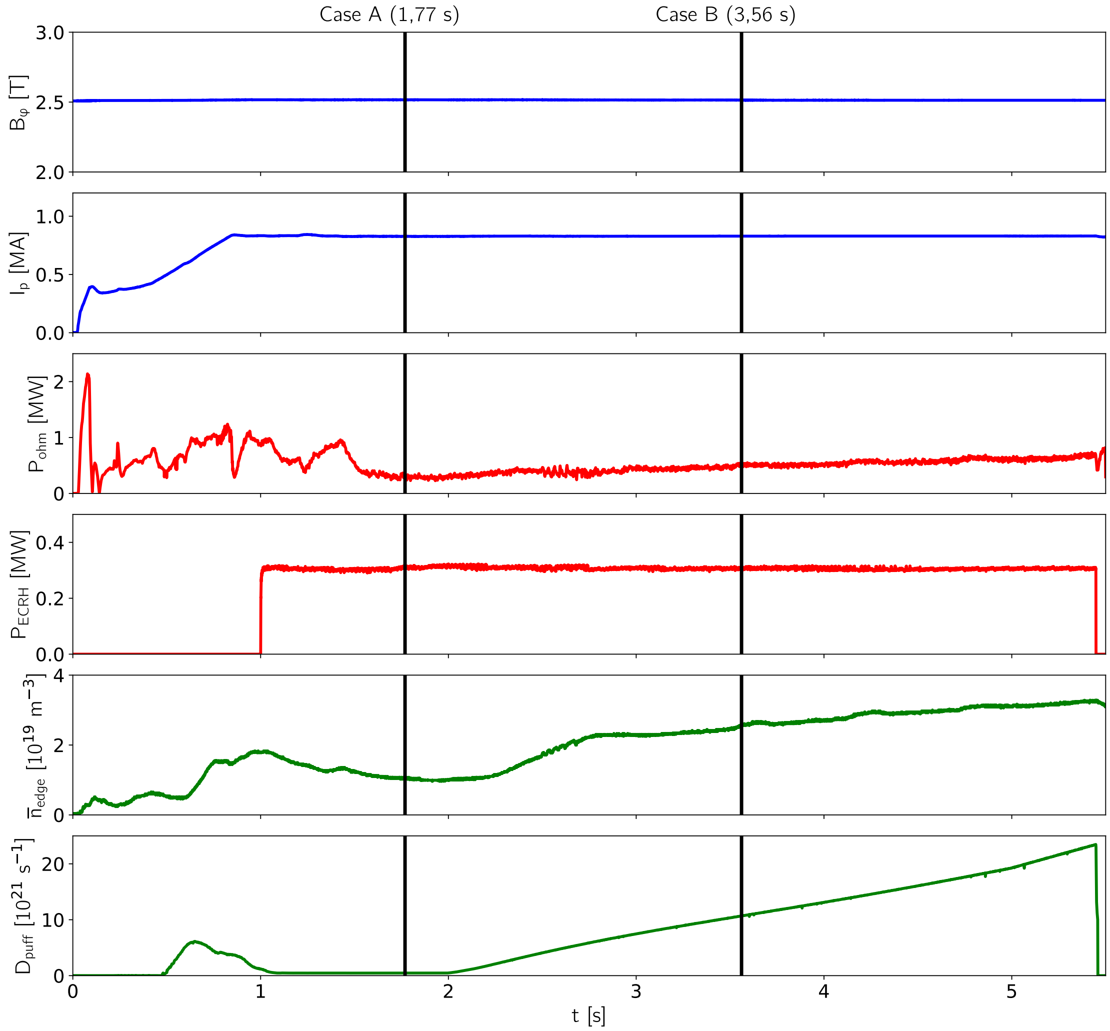

Figure 5.1: Time traces of the main parameters for the discharge #33341.

Then, in the Fig. 5.2 we can observe the *magnetic equilibrium configuration* of the discharge (which is almost unchanged between the two considered times); the position of the diagnostics systems involved in the considered measurements is highlighted with different colors.

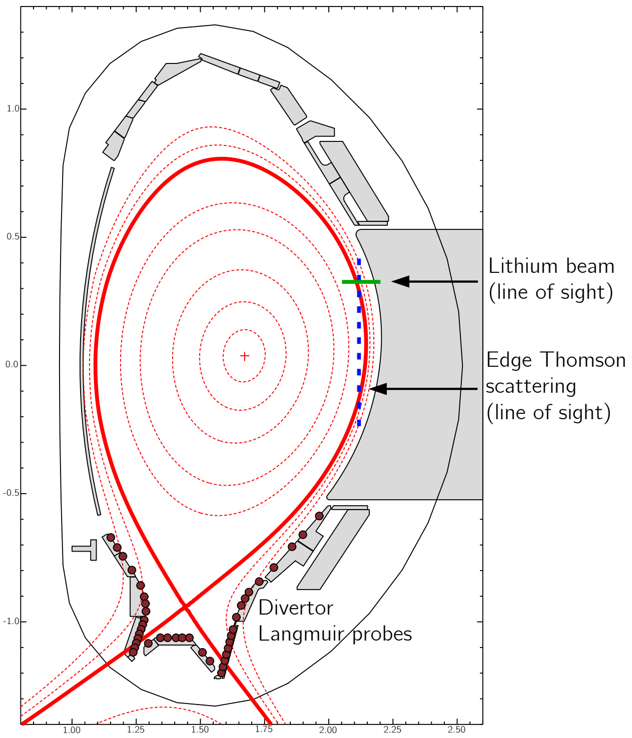

Figure 5.2: Magnetic equilibrium for the discharge #33341.

5.2 Simulations setup

The main goal of the simulation work consisted in setting up the input parameters for the runs in order to obtain physically reasonable results, which were in agreement with the measurements taken from the considered discharge. Reliable measurements are currently taken mostly at the outer side of the torus; therefore, the main concern was to try to reproduce the radial plasma profiles (in particular electron density and temperature) at the outer SOL midplane, in terms of physical inputs and choice of the anomalous transport coefficients. For doing this, reliance was given in particular to the measurements taken from the LiBES and edge TS diagnostics systems, taken precisely at the times defining the two considered cases.

In this section, the steps performed to obtain the final simulations will be presented, and the assumptions made during each step will be critically discussed. The methodology of the simulations setup was based on previous works about this topic [95][96] as well as on general references in literature about SOLPS modelling of ASDEX Upgrade [80][81].

The neutrals were expected to play a fundamental role in the framework of what was going to be investigated; therefore, in order to model the volumetric/atomic processes involving as accurately as possible, all the simulations were performed as coupled B2.5-EIRENE runs.

5.2.1 Computational grid

The SOLPS-ITER *computational grid* which was used for the simulations is shown in the Fig. 5.3a; it has a resolution of 48×18, i.e. it consists in 48 cells in poloidal direction and 18 cells in radial direction. Originally, the grid was developed for another scenario [82], whose magnetic equilibrium was, however, quite similar (i.e. the alignment between the flux surfaces for the discharge #33341 and the cells of the used grid was good enough). So, for achieving a realistic setup for the simulations it was sufficient to rescale the magnetic parameters for the grid to the actual values of the discharge #33341; namely, setting a (negative) toroidal field of 2,5 T and a plasma current of 0,8 MA.

In the Fig. 5.3b, instead, the full triangular grid of EIRENE which was used, extending in the entire vessel region, is shown. As can be seen, while the B2.5 equations for the plasma particles are solved only the former grid, which does not intersect any material boundary except for the divertor targets, the neutrals are instead followed everywhere in the vessel.

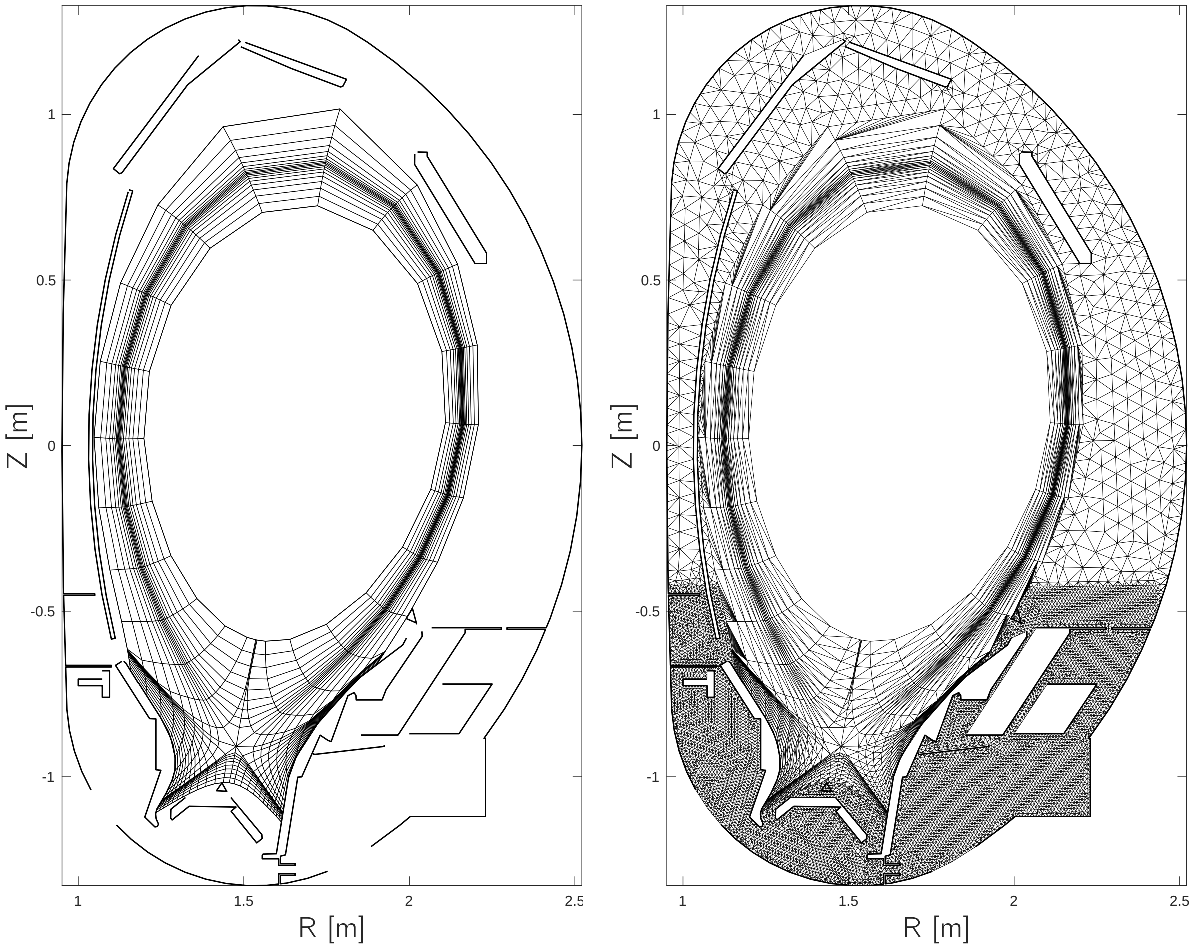

(a) Magnetic-field-aligned grid of B2.5.

(b) Triangular grid of EIRENE.

Figure 5.3

For the computational domain of B2.5, the following (default) subdivision was considered:

- Poloidal cells from 1 to 12 for the inner divertor region.
- Poloidal cells from 13 to 36 for the upstream region.
- Poloidal cells from 37 to 48 for the outer divertor region.

and

- Radial cells from 1 to 9 for the core plasma and the private flux region.
- Radial cells from 10 to 18 for the SOL region.

Finally, the outer midplane position was set on the cells with poloidal index $x = 27$. In fact, this approximately correspond to the location at which most of the plasma edge diagnostics (among which the LiBES system) measure the radial plasma profiles. In this way, a precise comparison between the simulated midplane plasma profiles and the experimental profiles could be done.

The original experiment consisted in a pure deuterium discharge, without any seeding species; therefore, the atomic species considered in the simulations were the atomic deuterium D and its ion D^+, the latter constituting the main ion species of the plasma. However, the molecular deuterium D_2 was actually used as puffing gas (as it is in the reality); therefore, also this molecular species and its ion D_2^+ were considered in the simulations.
The *atomic* and *molecular processes* activated in EIRENE were specified in the input file `input.dat`, and are listed in the following table. Through these processes all the species interact with each other (and with the electrons). All of these were modelled using the rate coefficients as present in the databases AMJUEL and HYDHEL.

Atomic/molecular processes activated in EIRENE	
Ionization processes	
$D + e \rightarrow D^+ + 2e$	Electron-impact ionization of D
$D_2 + e \rightarrow D_2^+ + 2e$	Non-dissociative electron-impact ionization of D_2
$D_2 + e \rightarrow D + D^+ + 2e$	Dissociative electron-impact ionization of D_2
$D_2^+ + e \rightarrow D^+ + D^+ + 2e$	Dissociative electron-impact ionization of D_2^+
Recombination processes	
$D^+ + e \rightarrow D$	Radiative electron-impact recombination of D^+
$D_2^+ + e \rightarrow D + D$	Dissociative electron-impact recombination of D_2^+
Molecular dissociation processes	
$D_2 + e \rightarrow D + D + e$	Electron-impact dissociation of D_2
$D_2^+ + e \rightarrow D^+ + D + e$	Electron-impact dissociation of D_2^+
Ion-neutral collisions	
$D + D^+ \rightarrow D^+ + D$	Charge-exchange collision between D, D^+
$D_2 + D^+ \rightarrow D_2^+ + D$	Charge-exchange collision between D_2, D^+
$D_2 + D^+ \rightarrow D_2 + D^+$	Elastic scattering between D_2, D^+

In the simulations, the gas puff source for the deuterium molecules (defined as the input of these in the computational domain) was located in front of the geometric outer midplane, that is at $R = 2{,}24$ m, $z = 0$ m. As such puffing system is enabled, active pumping was also required to remove the exceeding particles; this, in the simulations, took place at the actual pumping surfaces near the divertor targets.

5.2.2 Physical input parameters

The main physical inputs to be chosen as *input parameters* of the simulations are the density regime, the input power and the assumptions for the anomalous transport coefficients. In the following a brief overview on these three aspects is given.

First of all, the *density regime* for the various cases was imposed through a feedback scheme to be declared in the file `b2mn.dat`. Namely, arbitrarily chosen values for the separatrix electron density $n_{e,sep}$ at the outer midplane had to be defined: these were achieved through a feedback mechanism regulating the gas puff source inside the vessel. Although this assured to get the precise values of $n_{e,sep}$ as one could arbitrarily impose, it led to some convergence issues. In fact, this feedback system acts continuously, activating and deactivating the gas puff source to preserve the value of $n_{e,sep}$ as imposed (and consequently regulating continuously also the pumping intensity); therefore, the residuals for the balance equations never get really close to zero. Thus, as a criterion for convergence, it was checked whether the time oscillations of some

important plasma quantities lied within an acceptable difference from the expected value, and whether the concordance between initial and final steps of a run was good enough.
It has to be mentioned, however, that a strong uncertainty in estimating the position of the separatrix, during a discharge, exists, being this of the order of several mm. In detail, in the vicinity of the separatrix, the experimental radial plasma profiles present generally large gradients; therefore, this turns into a strong uncertainty also in determining which should be the best experimental estimate for $n_{e,sep}$. Furthermore, this is even more accentuated by the absolute uncertainties in the measurements, producing vertical error bars for each data point at a given radial location.
To handle with this issue it was chosen to consider the position of the separatrix as unknown a priori, and thus to take the experimental radial plasma profiles at the outer midplane in function of the major radius R as the only experimental basis. Such measurements are reported in the Fig. 5.4 for the electron density and in the Fig. 5.5 for the electron temperature, for both cases A, B. As we can see, a density shoulder is clearly evident in the case B.
In particular, the data for the electron density were extracted from the signal IDA: this provides the radial profiles computed after an integrated data analysis carried out fitting the measurements of more independent diagnostics systems (among which the most relevant is the LiBES) through a probabilistic approach [97][98]. It was chosen to use these data, rather than the simple LiBES data, because of their generally more reliability and their less uncertainty. Moreover, in this way it was possible to use the radial coordinate system in which the IDA data are plotted as a reference for performing an adequate radial shift of the TS data for the electron temperature, as it will be explained in the following.

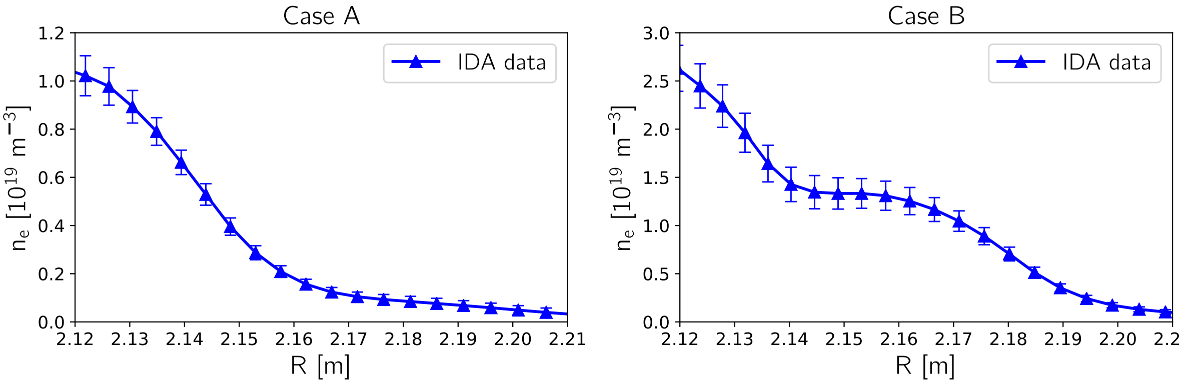

Figure 5.4: Experimental electron density data at the outer midplane after integrated data analysis.

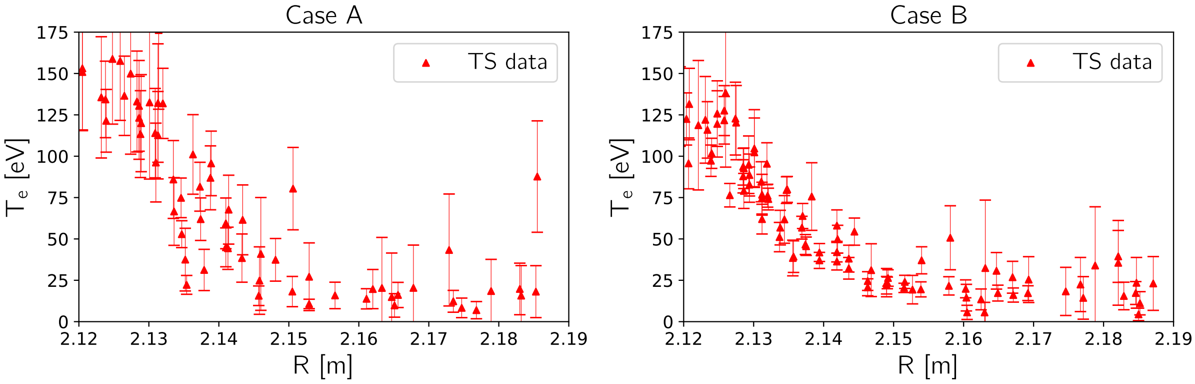

Figure 5.5: Experimental electron temperature data at the outer midplane from the edge TS system.

In the following subsections it will be explained how, starting from these experimental measurements, it was possible to estimate a value for $n_{e,sep}$ to give as input for the simulations.

Then, regarding the *input power*, this was declared in the input file `b2.boundary.parameters` by imposing, on the core plasma boundary, given values of electron/ion heat fluxes through it, whose sum corresponds to the power entering the edge plasma region. It was assumed that such input power is carried half by electrons and half by ions; different ratios, indeed, do not have a significant impact, because of the relatively strong energy equalization between the two species inside the edge plasma.

The total heating power for the cases A and B is, respectively, 620 kW and 820 kW. For obtaining the power crossing the separatrix it was necessary to estimate the fraction of radiated power in the core plasma. Actually, such values of heating power are relatively low; therefore, the correspondingly low radiated power was difficult to estimate, because of the weak reliability of the bolometry measurements at low power. The best estimates available for the fraction of radiated power in the core plasma, according to [16], are 0,15 for the case A and 0,25 for the case B. Taking this as good, the total input power in the computational domain for the two cases was assumed as $(0{,}85 \cdot 620)$ MW $\approx$ 520 kW and $(0{,}75 \cdot 820)$ MW $\approx$ 610 kW respectively. For taking into account this further uncertainty, the eventual effects of large deviations from these estimates, about 20%, were also considered.

The last assumptions to do regarded the *anomalous transport coefficients* with which SOLPS-ITER computes the perpendicular transport. It was chosen to define some radial profiles for the particle diffusivity D_n and the electron/ion thermal diffusivities χ_e, χ_i (cfr. Appendix C.2.4); this was possible by compiling the input file `b2.transport.inputfile`.

As it will explained in the following, it was tried to perform a fine tuning of these profiles in order to obtain the best match between the simulated radial plasma profiles and the experimental profiles at the outer midplane. At the beginning, however, some arbitrary profiles for these coefficients had to be assumed; the choice for such a first assumption was done according to the setup of similar SOLPS simulations of L-mode discharges in ASDEX Upgrade [81]. The resulting transport profiles at the outer midplane which were then assumed at the beginning are shown in the Fig. 5.6.

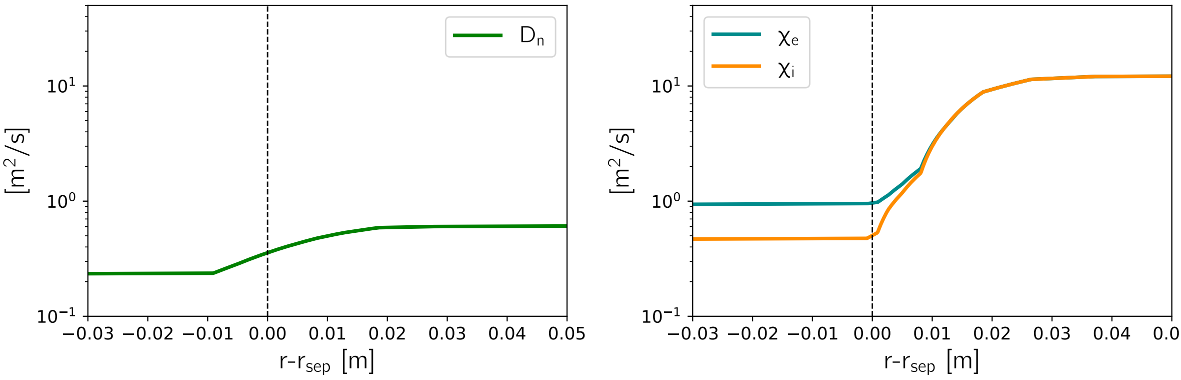

(a) Particle diffusivity.

(b) Thermal diffusivities.

Figure 5.6: First assumptions for the radial profiles of the anomalous transport coefficients in the simulations.

As we will see, these profiles for the thermal diffusivities turned out to be quite good in matching the radial temperature profiles with the experimental data for both cases A and B; in fact, as generally accepted in literature, radial blob propagation can be expected to not affect the temperature-gradient-driven thermal transport. Instead, relevant effort was needed for optimizing the radial profile of the particle diffusivity; this was true especially in the case B, characterized by the presence of a density shoulder, in which a strong enhancement of the particle transport in the region of the shoulder was expected.

For the anomalous transport coefficients the ballooning option was also activated in the simulations; this means that, at each location, the imposed value is rescaled by a poloidally varying scale factor. This was done for taking into account the effects of the bad curvature of the magnetic field lines at the outer side of the torus; in fact, as it was already pointed out, the enhancement of perpendicular transport could be assumed to be more relevant at the outer side than at the inner side. In absence of more reliable experimental basis for making assumptions about this, it was imposed an arbitrary poloidal dependence for the coefficients so that these were more or less the double at the outer midplane with respect to the inner midplane (fig. 5.7).

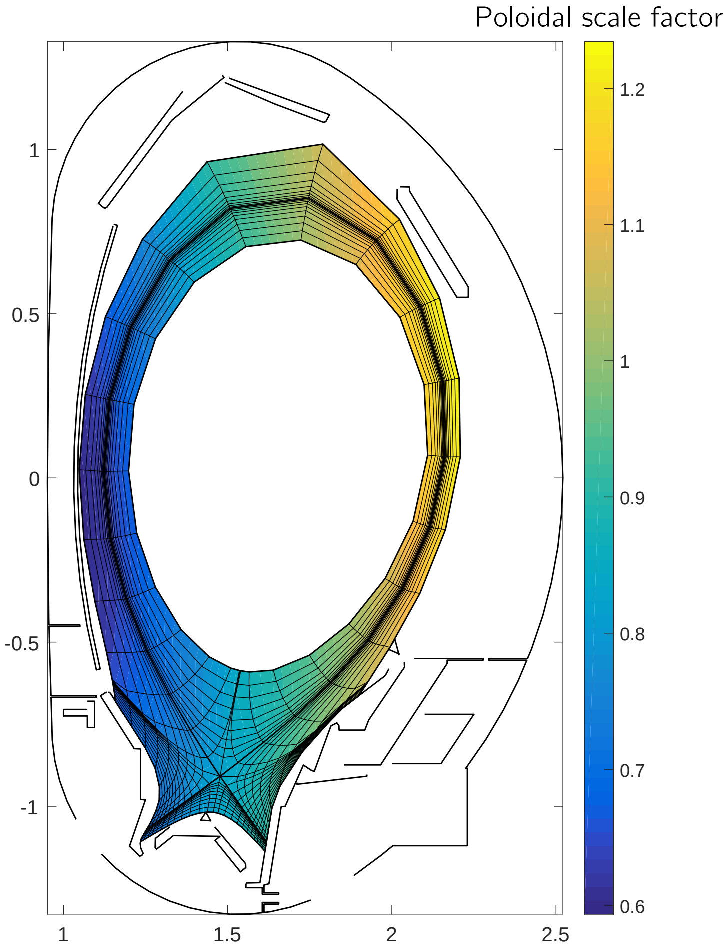

Figure 5.7: Poloidally varying scale factor imposed to the anomalous transport coefficients in the simulations.

Finally, some simplifications which were done in the simulations have to be mentioned.
First of all, in the simulations a pure deuterium plasma is considered, neglecting the presence of sputtered impurities; considering the eventual effect of these, in fact, was not among the main goals of this work. Therefore, at all the materials surfaces, the sputtering was disabled.
Then, all the drift terms in the B2.5 equations were also disabled, and no electric currents were considered; the need for such simplification came out due to exceedingly large time which would have been needed for convergence with drifts and currents activated. Because of this, and after the somehow arbitrary assumption done for the poloidal variation of the transport coefficients, the prospected results could be considered reliable only for the outer side. So, attention will be paid in the following only to the outer midplane and the outer divertor target.
Neglecting drifts, currents and impurities allowed to perform the runs with relatively large time steps for the B2.5 calculations, i.e. 10^{-4} s. This led to computation times required before reaching convergence in the results of the order of several weeks.

5.2.3 Radial shift of the diagnostics data

The first task to accomplish for having a reliable set of experimental data for the setup of the simulations was to manage to refer these to a common coordinate system. In fact, the radial coordinate in function of which the crude data can be extracted from the databases, i.e. as these were plotted in the Figs. 5.4, 5.5, cannot be considered as absolutely true. This is because each diagnostics could be affected by a systematic error, due to their independent calibration or phenomena of vibration of the device during the operation, in plotting the data into a coordinate system (R, z). As a result, the profiles as measured by different diagnostics could be shifted one with respect to the others. Therefore, a systematic work had to be performed to find the appropriate *radial shift* for each diagnostics, in order to have a consistent picture of the experimental radial plasma profiles at the outer midplane.

In order to properly refer all the profiles to a common coordinate system it was necessary to impose some profile as a reference. For doing this, it was chosen to refer to the radial coordinate system of the IDA profiles as reference, and to try to compute an adequate shift for the TS profiles. This choice was motivated by the fact that, in addition to the electron density profile, the integrated data analysis is capable to compute also an electron temperature profile at the outer midplane, using the same probabilistic approach [98]. So, since the density and temperature profiles computed by IDA lie on a same radial coordinate by definition, being extracted from the same analysis, it was necessary to "displace" the TS data for the temperature until they agreed with the IDA data.

For computing the displacement needed for both cases, in the assumed vicinity of the separatrix an exponential fit for the TS data was performed, of the type

$$T_e(R_{TS}) = A \exp\left(-\frac{R_{TS}}{B}\right) \tag{5.1}$$

where R_{TS} is the "original" (i.e. not shifted yet) radial coordinate of the TS data. This was motivated as, in this region, the electron temperature profile can be assumed to present a nearly exponential decay (cfr. Section 2.2.3). The fit, performed with a least-squares method in which the various data points were weighted according to their vertical uncertainty, provided the free parameters A, B for the two cases, the last one being a measure of exponential decay length for the profiles.

The next step was to perform a similar fit for the IDA data for the temperature, of the type

$$T_e(R_{IDA}) = A \exp\left(-\frac{R_{IDA} - \Delta}{B}\right) \tag{5.2}$$

where R_{IDA} is the radial coordinate on the IDA data, which was desired to be used as reference. For performing this fit, the same fitting parameters A, B for the TS fit were imposed, leaving Δ as the only free parameter. In this way, the obtained curve were exactly the same as for the TS fits, but displaced by a distance Δ: this could be then regarded as the relative displacements between the datasets from IDA and TS.

Since the relation $R_{TS} = R_{IDA} - \Delta$ holds, the TS data could be expressed from this moment in function of the IDA radial coordinate, performing a radial shift of these as $T_e(R_{IDA}) = T_e(R_{TS} + \Delta)$. As a result it was obtained that, in both cases, the TS data had to be shifted radially inward, namely of about 3,2 mm for the case A and about 5,7 mm for the case B. This is readily visible in the Fig. 5.8, where the steps performed for this procedure are visible for both cases.

At this point, the shifted TS data for the electron temperature became finally directly comparable with the IDA data for the electron density, lying now on a common radial coordinate.

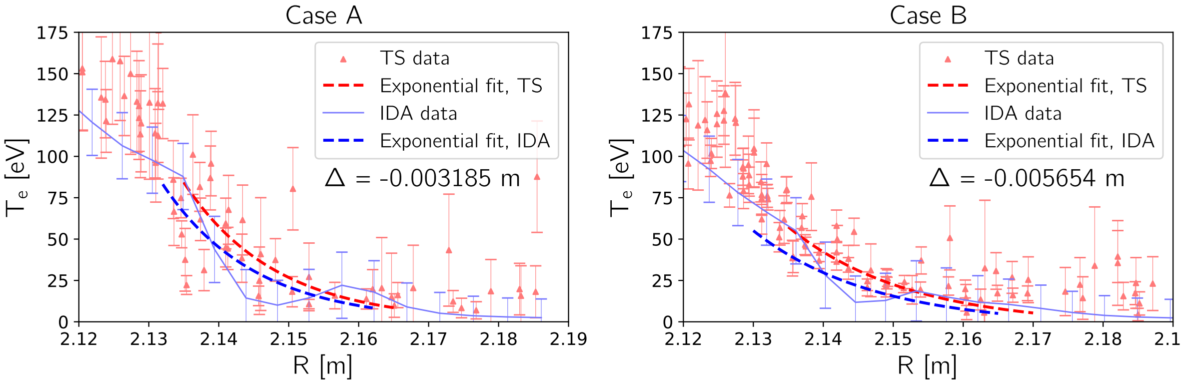

Figure 5.8: Radial shift for the TS electron temperature data needed for matching the IDA data.

5.2.4 Estimate of the separatrix position

After reaching an agreement between the experimental density and temperature profiles at the outer midplane, these were finally taken as starting point for the simulations.
As already mentioned, for properly simulating each of the two density regimes, a value for the electron density at the separatrix $n_{e,sep}$, at the outer midplane, had to be imposed. Since the available data were plotted in function of the major radius R, it was then necessary the knowledge of an exact *separatrix position* R_{sep} in order to know the corresponding density $n_{e,sep}$ from the IDA profiles. In principle, an estimate for R_{sep} could also be extracted as an experimental data, as resulting from the calculation of the magnetic equilibrium (namely, the one which was plotted in the Fig. 5.2); nevertheless, such an estimate was known to contain a systematic error of several mm.
Conventionally, in simulating L-mode discharges one is used to define the position of the separatrix at the R coordinate where the fitted experimental data for the electron temperature give a value $T_{e,sep} = 50$ eV [81]. However, this assumption could be not always fulfilled. Moreover, experimental considerations led to think that a lower temperature at the separatrix could be expected in the high density case, with respect to the low density case [16].

So, in order to find the best assumption for the position of the separatrix, it was tried to couple the experimental knowledge of the density and temperature profiles at the outer midplane with the actual results of the simulations in a self-consistent way. The expected goal was that the experimental value of the separatrix electron temperature $T_{e,sep}$ corresponding to the chosen separatrix position resulted to be the same temperature reproduced with the simulations.
The main steps for doing this could be summarized as:

1. Assuming a position for the separatrix as derived from different assumed values for the temperature $T_{e,sep}$, according to the shifted TS fit (Fig. 5.9). In particular, since the fit for T_e on the radial IDA coordinate is $T_e(R_{IDA}) = A \exp\left(-\frac{R_{IDA}-\Delta}{B}\right)$, then the radial IDA coordinate of the separatrix resulting from an assumed $T_{e,sep}$ could be written
$$R_{sep} = -B \ln\left(\frac{T_{e,sep}}{A}\right) + \Delta \tag{5.3}$$
2. Finding the value of the separatrix density $n_{e,sep}$ as resulting from the IDA data corresponding to each assumption for R_{sep} (Fig. 5.10).
3. Carrying out several simulations, each one having as input parameter different fixed values of $n_{e,sep}$ at the outer midplane, and checking at the end of these the corresponding simulated values of $T_{e,sep}$.

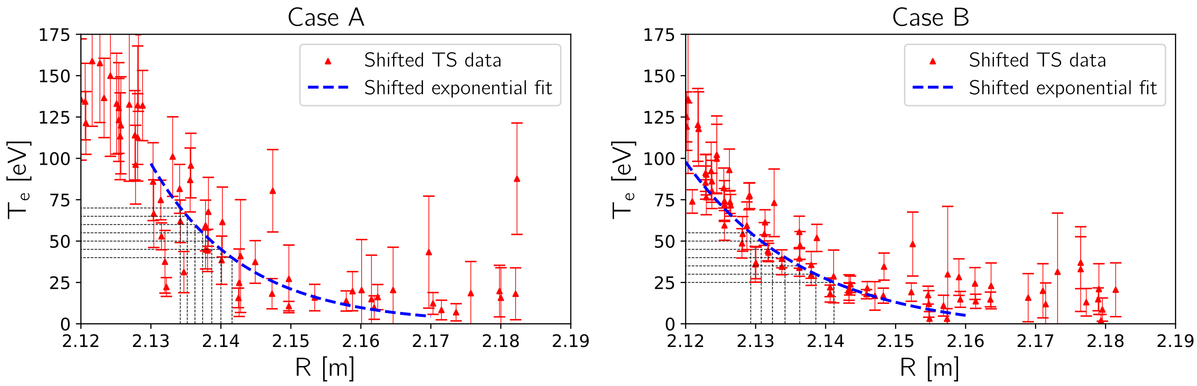

Figure 5.9: Assuming a position for the separatrix.

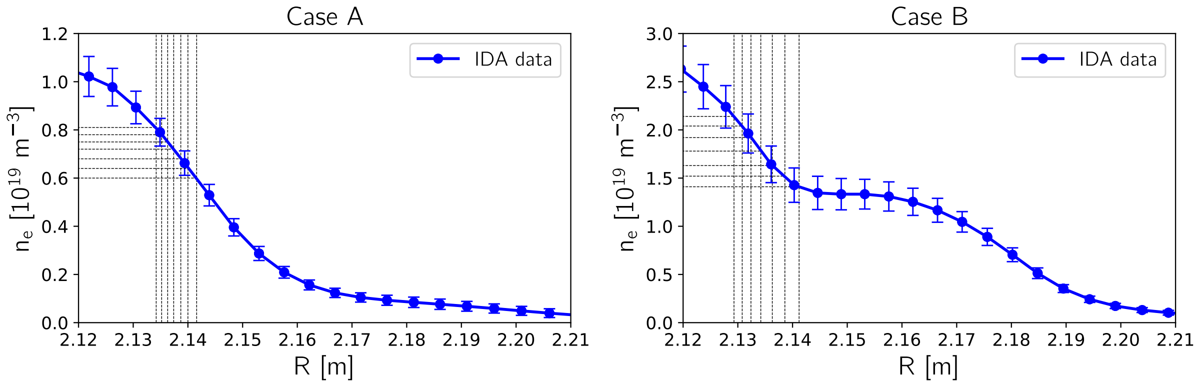

Figure 5.10: Assuming the density at the separatrix.

The values considered for the various quantities in both cases are listed in the following tables. The resulting values of $n_{e,sep}$ would have been the main input for performing each simulation; the corresponding simulated values of $T_{e,sep}$, then, would have been the key for determining which of these was the most realistic one. The results of this procedure will be presented in the Fig. 5.11.

Case A

Assumed $T_{e,sep}$ [eV]	$\longrightarrow$	Assumed R_{sep} [m]	$\longrightarrow$	Resulting $n_{e,sep}$ [10^{19} m^{-3}]
45		2,140		0,64 (±0,05)
50		2,139		0,68 (±0,05)
55		2,137		0,72 (±0,05)
60		2,136		0,75 (±0,06)
65		2,135		0,78 (±0,06)
70		2,134		0,81 (±0,06)

Case B

Assumed $T_{e,sep}$ [eV]	$\longrightarrow$	Assumed R_{sep} [m]	$\longrightarrow$	Resulting $n_{e,sep}$ [10^{19} m^{-3}]
25		2,142		1,41 (±0,18)
30		2,139		1,52 (±0,18)
35		2,136		1,63 (±0,19)
40		2,134		1,78 (±0,20)
45		2,132		1,92 (±0,20)
50		2,131		2,04 (±0,21)

5.2.5 Optimization of the diffusivity profile

The procedure described in the last section required carrying out realistic simulations, in order to select the best assumption for the temperature at the separatrix. Therefore, it was necessary that these were already performed with a realistic assumption for the transport coefficients.
As explained in the Section 2.4, the kind of phenomenon of interest for the case B, where a density shoulder is present, i.e. the radial blob propagation, is not a diffusive phenomenon, since a strong radial particle flux is expected to exist also in the region with flattened density profile; thus, it is physically not driven by a density gradient. Moreover, even a convective assumption, in which one assumes some anomalous radial velocity (as in eq. (2.40)) is not much accurate; in fact, as it was explained, radial blob propagation is basically a non-local phenomenon, and thus the induced radial particle flux does not even depend on the local density, being instead determined by the dynamics around the separatrix. So, a full self-consistent modelling of blob dynamics and perpendicular transport could not be included in a code like SOLPS-ITER, in which the anomalous transport can be only empirically imposed.

Nevertheless, it was possible to implement a description in which an "effective" particle diffusivity is used, taking into account any processes related to radial particle transport. Performing a fine tuning of the radial profile of this, it could be then possible to match the experimental radial density profiles (at least on the midplane, where reliable experimental data about it exist).
This is precisely what was done for the performed simulations. Relying on previous works [95][96], it was expected that the arbitrarily chosen profiles for the thermal diffusivities (Fig. 5.6b) could represent an already realistic assumption. Moreover, it was expected that the enhancement of blob transport regime would not affect at all these coefficients, since their impact of thermal transport is expected to be only via thermal convection [16]. Instead, the profiles for the particle diffusivity required to be manually adjusted, especially for the case B, in which the shoulder is present. From the previous works it was deduced that, in the high density case, a localized peak for such an effective particle diffusivity was required, in the radial region corresponding to the flat portion of the shoulder; the radial extension of this would represent the region where the blob-propagation-driven radial particle transport is most effective (i.e. neither so close to the separatrix that such radial transport is still small, in amplitude, with respect to the strong parallel transport, nor too much far from it, where the blobs would already have been destroyed by the parallel flow).

In order to automatically deal with all the free aspects related to imposing a radial profile for the particle diffusivity (such as magnitude and extension of the high transport peak), an iterative algorithm was carried out, following [99]. The aim of such a procedure was to get a radial profile of D_n which produces a theoretically perfect match between the simulated radial density profile at the outer midplane with the experimental one (from the IDA data) for all the cases. This is based on the fact that, if $n_{e,sep}$ is kept as a fixed input parameter, then in the SOL region the density profile $n_e(r - r_{sep})$ can be fully described by its radial gradient $\frac{\partial n_e(r-r_{sep})}{\partial r}$ in each point, with $n_e(r - r_{sep} = 0) = n_{e,sep}$ acting as a boundary condition.
In the simulations a purely density-gradient-driven particle diffusivity was assumed, and no drift motions were considered; therefore, the particle flux density in radial direction is simply computed as (cfr. Appendix C.2.4)

$$\Gamma_r = -D_n \frac{\partial n_e}{\partial r} \tag{5.4}$$

The iterative procedure started by running the simulations, for both cases and for each assumption on temperature/density at the separatrix, with the first assumed D_n profile as in the Fig. 5.6a. Since this profile was only a trial, in each case the simulated density gradient $\left(\frac{\partial n_e}{\partial r}\right)_{\text{SOLPS}}$ was

not equal to the experimental density gradient $\left(\frac{\partial n_e}{\partial r}\right)_{\text{exp}}$ (cfr. Fig. 5.10) in any point; this was especially true for the high density case.
The next step then consisted to calculate, for each radial location of the domain, a new value for the particle diffusivity as

$$D_{n,\text{ next}} = -\frac{\Gamma_{r,\text{ SOLPS}}}{\left(\frac{\partial n_e}{\partial r}\right)_{\text{exp}}} \tag{5.5}$$

where $\Gamma_{r,\text{ SOLPS}}$ is the radial particle flux calculated at the previous step. This new profile for the particle diffusivity was used as input for new runs, after which a next-step density gradient $\left(\frac{\partial n_e}{\partial r}\right)_{\text{SOLPS, next}}$ and a next-step radial particle flux $\Gamma_{r,\text{ SOLPS, next}}$ were obtained.
This procedure required very few steps until convergence was reached. At convergence, the final profile for the particle diffusivity gave $\left(\frac{\partial n_e}{\partial r}\right)_{\text{SOLPS, final}} \approx \left(\frac{\partial n_e}{\partial r}\right)_{\text{exp}}$ at each radial location. For all the cases, this final profile could then be considered the most realistic one for describing the perpendicular transport at the outer SOL midplane.

5.3 Final simulations

A consistent set of simulations was finally performed, according to the characteristics discussed in the last section. For each assumption for the separatrix position/temperature, the iterative algorithm aimed for optimizing the radial profile of the particle diffusivity at the outer midplane was carried out. Once the simulated density profiles converged with the experimental ones, the criterion for selecting the best assumption for the cases A, B, was to choose that providing the best match between the assumed and the simulated values of $T_{e,sep}$. Moreover, all the simulations were carried out with the "base" assumption for the SOL input power (i.e. 520 kW and 610 kW respectively) and for lower and upper values, corresponding to errors of ±20%; this was done for taking into account the strong uncertainty in the bolometry measurements of the power radiated inside the separatrix.
The results which led to this final choice can be seen in the Fig. 5.11.

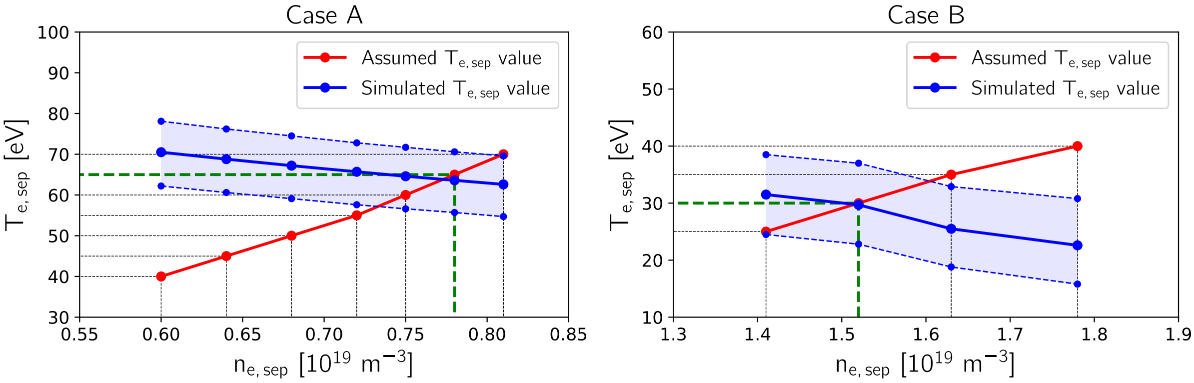

Figure 5.11: Selecting the best assumption for the separatrix temperature.

An unequivocal choice for the best assumption was then possible. In fact, with an increasing assumed value for $T_{e,sep}$, the corresponding assumed value for $n_{e,sep}$ increases (since this means assuming a more radially inward position for the separatrix). Vice versa, modelling an increasing density regime by imposing increasing values of $n_{e,sep}$ as input for the simulations provided a decrease in the simulated values of $T_{e,sep}$. So, an "optimum point" could be selected.

As we can see from the figures, for the case A the best assumption for $T_{e,sep}$ was 65 eV, corresponding to a position for the separatrix of $R_{sep} \approx 2{,}135$ m; for the case B, instead, the

assumption of a $T_{e,sep}$ of 30 eV seemed the best choice, corresponding to $R_{sep} \approx 2{,}139$ m. The corresponding density regimes, then, could be defined by a separatrix density given by $0{,}78\,(\pm 0{,}06) \cdot 10^{19}$ m^{-3} for the case A, and by $1{,}52\,(\pm 0{,}18) \cdot 10^{19}$ m^{-3} for the case B.
However, considering the uncertainty in the input power, a confidence band including the realistic cases was obtained. Especially for the case A, also the two "neighboring" cases were included in such confidence band, making the corresponding assumptions also realistic. Since the corresponding assumptions for $n_{e,sep}$ could not be excluded a priori, new uncertainties had to be considered for this. Nevertheless, for both cases these uncertainties are already "included" in the vertical uncertainty band in the IDA data. Therefore, hereafter the only remaining uncertainty in the results will be considered as the possible specification of lower/higher density regimes, in agreement with the vertical error bars of the IDA data.
So, hereafter the only remaining uncertainty to consider in the results is the possible specification of lower/higher density regimes, according to the vertical error bars in the IDA data. These lower/upper density limits will be used, in the next chapter, to define a confidence band in which the final results lie.

5.3.1 Radial plasma profiles at the outer midplane

In order to perform a first check of the validity of the simulations, the *radial plasma profiles* at the outer midplane were compared with the experimental data, i.e. the IDA data for the electron density and the edge TS data for the electron temperature.

In Fig. 5.12 the simulated *density profiles* for both cases (blue solid lines) are shown, together with the radial profile of the particle diffusivity obtained after the convergence of the iterative algorithm discussed in the last section (green dashed lines).

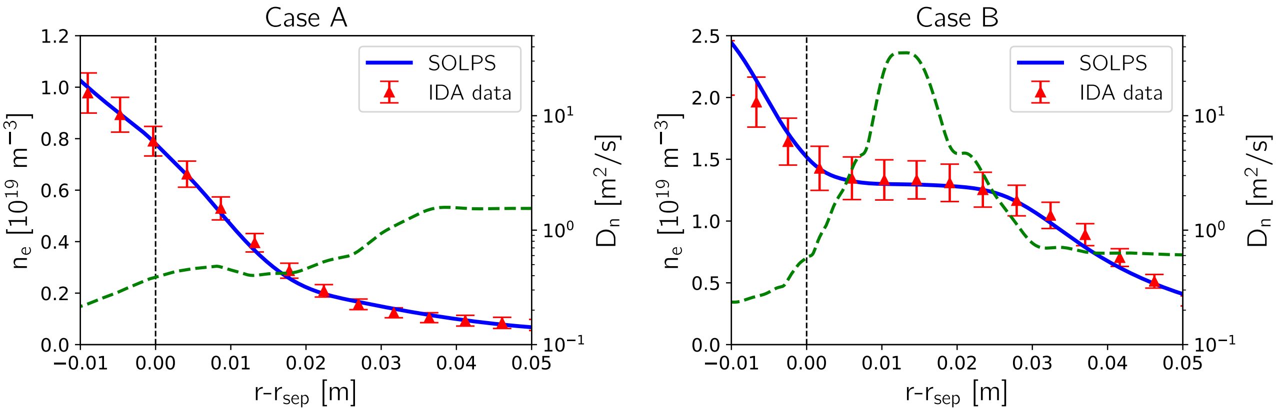

Figure 5.12: Simulated radial density profiles at the outer midplane and comparison with the experimental data.

As we can see, in both cases the iterative procedure led to a perfect fit between experimental and numerical results. In the low density case, the nearly exponential decay was reproduced through a particle diffusivity of the order of $0{,}5 - 1$ m^2/s, which slightly increases far from the separatrix. In the high density case, instead, a significant increase of the transport was needed to simulate the presence of the density shoulder, in the radial region between about 0,5 and 2,5 cm after the separatrix. In this region, the particle diffusivity had in fact to be strongly increased, up to an average value of about $15 - 20$ m^2/s, reaching a peak value of almost 40 m^2/s.
In order to give a measure of the broadening of the density profile when the shoulder is present, an exponential fit of the data was performed for a radial region corresponding roughly to the inner half of the SOL, similarly to how it was performed in [12][13]. It was then calculated a

decay length of about $\lambda_{n_e} \approx 1{,}8$ cm for the case A and about $\lambda_{n_e} \approx 7{,}2$ cm in the case B. The increase in such a length, which is of the order of 4, agrees nicely with the qualitative picture which was provided in the Fig. 3.10b, relating the abrupt increase in such a length with the transition to high collisionality.

Then, in the Fig. 5.13 the simulated *electron temperature profiles* (blue solid lines) are shown, as well as the expected variations on these when considering the uncertainty in the input power (thin blue dashed lines).

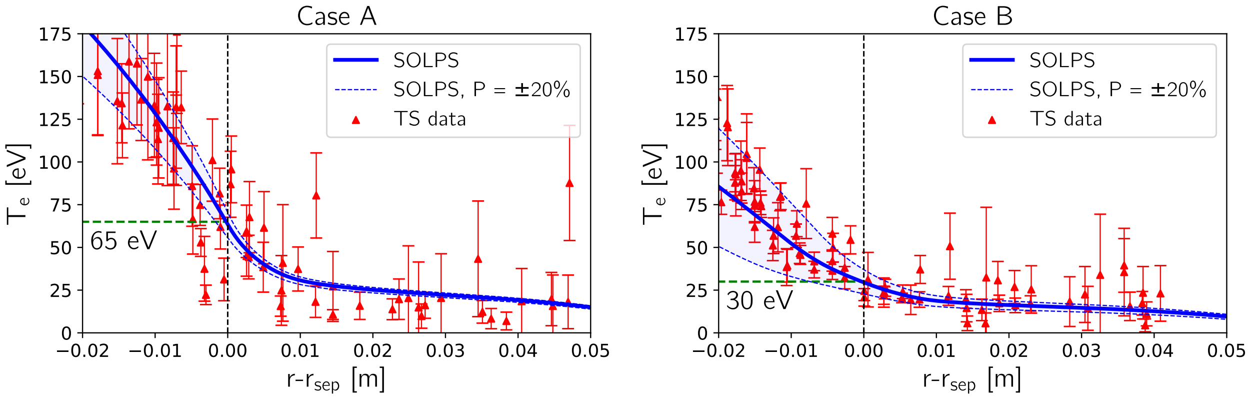

Figure 5.13: Simulated radial electron temperature profiles at the outer midplane and comparison with the experimental data.

Although the scatter of the TS data (red triangles), especially far from the separatrix, the simulated profiles exhibit a quite good agreement with the experimental data, without a need for a fine tuning of the thermal diffusivity profiles. In both cases a decrease of the temperature was obtained, which is quite steep before the separatrix and smoother in the SOL. An exponential fit of the simulated profiles was performed in the first 10 mm after the separatrix, similarly as it was done in in [16] for the same experimental profiles. As results, it was obtained a decay length of $\lambda_{T_e} \approx 12$ mm for the low density case and of $\lambda_{T_e} \approx 20$ mm for the high density case, in remarkably good agreement with what calculated from fitting the experimental data.
The decrease in the temperature at the separatrix at high density is much considerable; however, such difference is reduced going towards the far SOL.

Finally, in the Fig. 5.14 also the simulated *ion temperature profiles* are shown for both cases and considering again the uncertainty in the input power, although few reliable experimental data were available for comparison from this particular discharge.

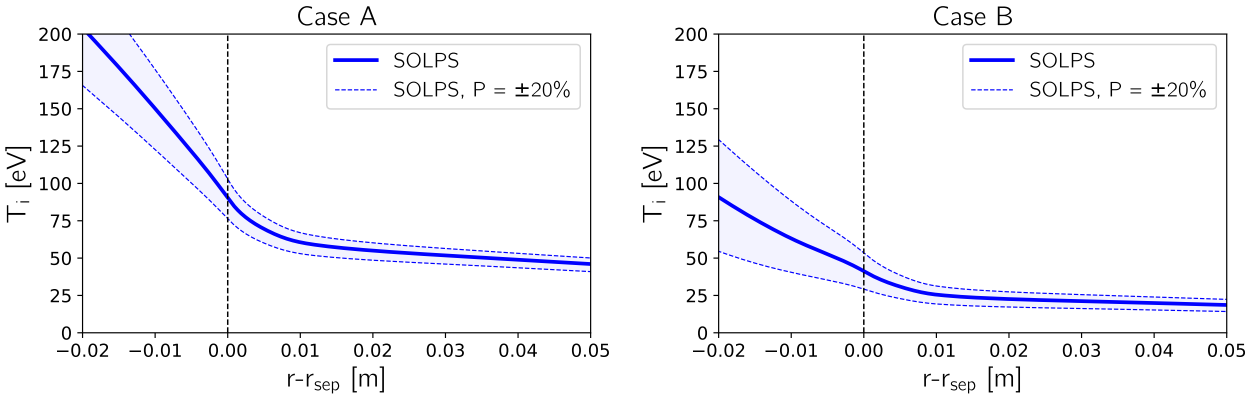

Figure 5.14: Simulated radial ion temperature profiles at the outer midplane.

In both cases the ion temperature remains higher than the electron temperature, coherently with what was measured from other L-mode discharges in ASDEX Upgrade [100]. However, here a strong decrease of the simulated ion temperature profile at high density in the entire SOL region can be observed. This becomes especially interesting considering that, in the high density case, the input power is even a little bit larger with respect to low density. It was then investigated which could be the reason for such a strong decrease of the ion temperature; a discussion on this will be given in the Section 6.1.

Summarizing, both cases exhibit a quite realistic agreement between numerical results and the available experimental data at the outer midplane; this was expected since the simulations were precisely set up according to these data. In particular, the density shoulder in the high density case was reproduced by imposing a strong localized increase of the particle diffusivity. Once the reliability of the final simulations was established, the next step was to perform a detailed analysis of such results. This will be one of the main matters of the next chapter.

5.3.2 Evaluation of the collisionality regime

For a further preliminary analysis of the results, the collisionality regimes achieved in both cases have been numerically evaluated. The aim was to check whether the the experimental assumption of the two cases being respectively in low and high collisionality regimes was consistent with the numerical results.

For doing this, the same approach considered in [96] was used; namely, the parameter

$$\Lambda = \frac{\Omega_i}{\Omega_e}\frac{\nu_{ei}}{c_s}L_{\parallel} \tag{5.6}$$

was evaluated in each cell of the computational domain of the SOL region. The dependence on the simulated plasma parameters in the eq. (5.6) came out as the electron-ion collision frequency ν_{ei} scales as $n_e T_e^{-3/2}$ and the plasma sound speed c_s scales as $T_e^{1/2}$.
In principle, the choice of the parallel length to use in (5.6) was not obvious; so, it was chosen to evaluate how this parameter evolves along the filed lines, varying together with the plasma conditions, on each flux surface. This was done calculating Λ in function of the poloidal location starting from the outer divertor target, that is integrating its local expression along each field line (i.e. along the poloidal cell coordinate x at each radial location y of the computational domain) as

$$\Lambda(x) = \frac{\Omega_i}{\Omega_e}\int_{x_{\text{target}}}^{x}\frac{\nu_{ei}(s_{\parallel})}{c_s(s_{\parallel})}\,ds_{\parallel} \tag{5.7}$$

where $s_{\parallel}$ is the parallel curvilinear coordinate (whose integral from outer to inner targets defines the SOL connection length). The integral (5.7) was calculated summing additively the local contribution of each poloidal cell, starting from the outer target, weighted on the parallel stepping of each cell. For the calculation, it was considered $\frac{\Omega_i}{\Omega_e} = \frac{m_e}{m_i} = 2{,}7 \cdot 10^{-4}$, using the the electron and deuteron masses, a collision frequency $\nu_{ei} = 5{,}7 \cdot 10^{-11}\, n_e T_e^{-3/2}$ and a sound speed $c_s = 8{,}9 \cdot 10^3\, T_e^{1/2}$, with $n_e = [\mathrm{m}^{-3}]$ and $T_e = [\mathrm{eV}]$ [101].
The results for both cases, in terms of 2D distributions of the collisionality parameter in the SOL region, are given in the Fig. 5.15. The two cases are, indeed, characterized by two strongly different collisionality regimes, precisely as it was experimentally assumed.

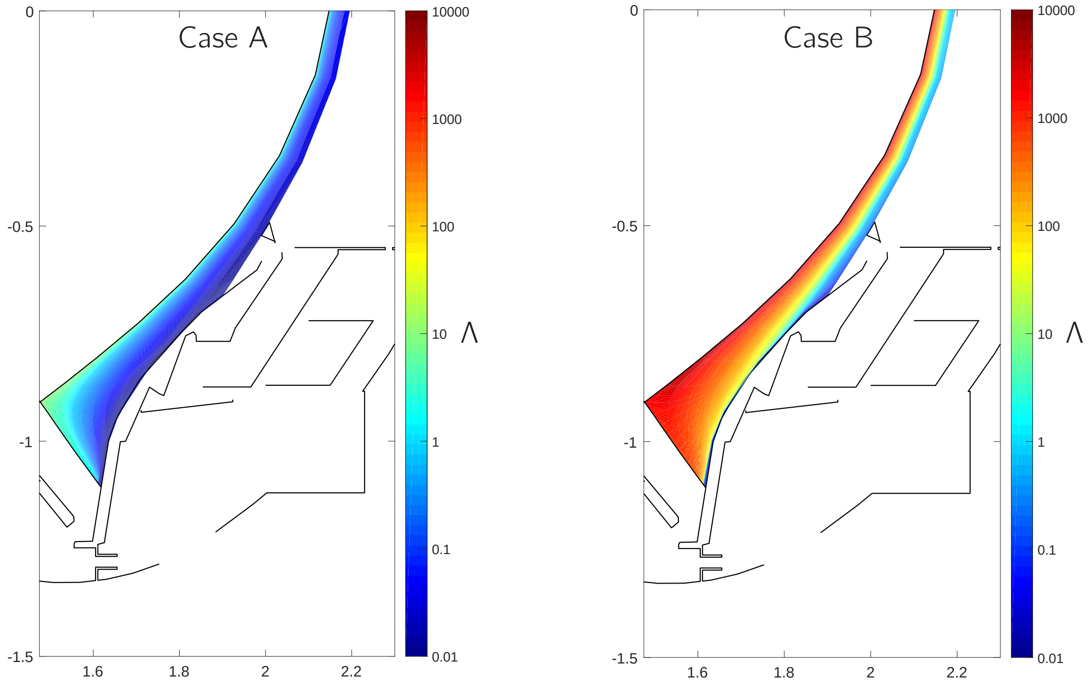

Figure 5.15: 2D distributions of the collisionality parameter in the outer SOL, calculated from the outer divertor target.

Starting from zero at the target, for both cases Λ rapidly increases while rising to upstream, reaching quickly a roughly constant trend. Such a saturation point is reached, along each field line, much close to the target in both cases. The reason of this is that, while integrating from the target to a given poloidal location, most of the contribute to the integral (5.7) is given by the first cells, near the target, where the temperature is very low (being Λ proportional to the inverse square temperature); once the near-target low temperature region is surpassed, the temperature is high enough that the upstream cells bring no relevant contribute to the integral.
This is readily visible in the Fig. 5.16a, where the poloidal evolution of the collisionality is plotted in function of the parallel distance from the target for both cases; this refers to a flux surface corresponding to a radial distance from the separatrix of about 2,5 cm when mapped at the outer midplane. This validates the experimental observation of the conditions in the divertor region controlling the evolution of this parameter, rather than the midplane conditions.
In the Fig. 5.16b, instead, the simulated radial profile of the divertor collisionality (i.e. evaluated at the X-point height) is shown, exhibiting clearly the two different collisionality regimes.

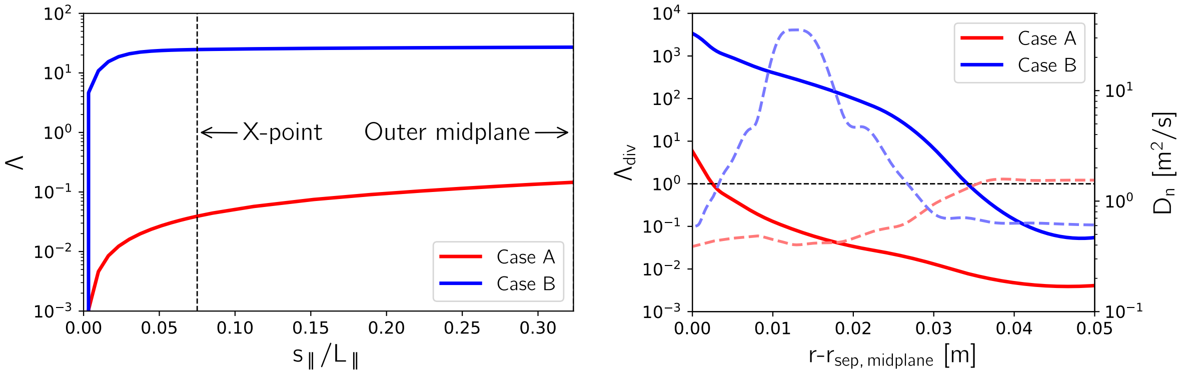

(a) Line-integrated collisionality along a given field line from the outer target to the outer midplane.

(b) Radial profile of the divertor collisionality, mapped on the radial coordinate of the outer midplane.

Figure 5.16: Simulated collisionality profiles.

It can be observed that, at a given poloidal location at upstream, Λ rapidly decreases after the separatrix while moving radially to the far SOL. While at low density it safely stays below one, at high density the high collisionality assumption is valid only until some radial location, after which Λ falls again below one.

This could potentially explain the presence of the peak in the perpendicular transport which is expected to exist, in the high density case, which was characterized by required values of the particle diffusivity of tens m^2/s. In fact, being a high collisionality regime present only in the first radial part of the SOL, only in this region blobs can be expected to undergo a regime transition implying a net enhancement of perpendicular transport (namely, a larger size and a larger radial propagation velocity), as discussed in the Section 3.3. When they reach the radial region in which the collisionality falls again below the unity, they can be expected to fall back to a low transport regime.

In the high density case, the flux surface where this breakpoint exists is characterized by a distance from the separatrix, if mapped at the outer midplane, of about $3 - 3{,}5$ cm; with a quite good agreement, this is just where the required transport peak falls down again to levels comparable with the low density case. This can be readily seen in the Fig. 5.16b as well, where the profile of particle diffusivity (at the outer midplane) which was required in both cases is represented as dashed lines.

This can be regarded as a numerical validation of the filamentary transport model discussed in the Section 3.3. The numerical results, in fact, seem to support a picture in which the regime transition which blobs undergo at high collisionality plays a fundamental role in determining the existence of an enhanced perpendicular transport regime in the scrape-off layer.

5.3.3 Physical meaningfulness of the enhanced transport assumption

This section is aimed to give a deeper consideration about the assumptions which, in this work, were done for modelling the perpendicular transport driven by radial blob propagation.

The imposition of large values of the particle diffusivity D_n at the outer midplane, of the order of tens m^2/s, seemed to be the best choice for correctly reproducing the experimental radial plasma profiles at high collisionality. Nevertheless, one could argue about the real need for such extremely large values, which are much larger than most of the cases which could be found in literature. For a comparison, the Bohm diffusivity (cfr. Appendix A.3.4), which is usually considered as a first approximation for modelling the anomalous transport in the scrape-off layer, for the considered plasma conditions would be of the order of $0,5 - 1$ m^2/s.

It was then questioned whether such a phenomenon could require effectively such large values of the particle diffusivity, if the related transport is regarded in a purely diffusive approximation (as it was done for this work).

For giving an answer to this, the results obtained by the simulation work were implemented in a novel theoretical transport model [102]. This model reduces a complete non-local description of the convective radial transport of microscopic structures with some typical radial velocity (such as radial blob propagation) to a diffusive limit, including the time intermittency by means of some auto-correlation time. In the following, a description of this model is given.

The usual diffusive ansatz for the radial particle balance in the scrape-off layer, characterized by a particle diffusivity D_n, can be expressed by the equation

$$\frac{\partial n}{\partial t} = D_n \frac{\partial^2 n}{\partial r^2} + S \tag{5.8}$$

with S being a general source term, e.g. given by the losses due to the parallel flow and by the ionization sources.

As already pointed out many times, the mechanism of blob propagation is non-diffusive: their radial transport is, indeed, due to a convective motion whose intensity does not depend on the local density gradient. A more correct expression for the radial particle flux driven by radial blob propagation, rather than the diffusive expression $\Gamma_r = -D_n \frac{\partial n}{\partial r}$, should be given, in a first approximation, by

$$\Gamma_r = n v_\perp \tag{5.9}$$

with $v_\perp$ being a *characteristic radial velocity* of the convective motion.
Anyway, $v_\perp$ cannot be simply equated to the radial blob velocity since, in a given radial location, blobs appear only intermittently in time. Therefore, such a characteristic velocity could be obtained by weighting the radial blob velocity v_b to the so-called *blob packing fraction* f_b: this quantifies the fraction of the total time during which a blob is being detected at a given radial location, being thus defined as

$$f_b \equiv \nu_b \tau_{AC} \tag{5.10}$$

with ν_b detection frequency and τ_{AC} auto-correlation time (cfr. Section 3.3.2). In this way, we could say that a convective model for describing the radial blob propagation could be, in a first approximation, described by a characteristic radial velocity

$$v_\perp \approx f_b v_b \tag{5.11}$$

However, although such a description properly takes into account the time intermittency of such convective transport by using a reduced characteristic radial velocity, it would be not correct yet. In fact, it still does not take into account the main characteristic of such kind of transport, i.e. the intrinsic *non-locality.* This means that a correct model should implement all the features characterizing the turbulence; namely, all the single blobs should be treated not as independent convecting structures, but through a *correlated random walk model.* This is what the model developed in [102] tries to do.

In particular, the characteristic radial velocity $v_\perp$ of the convective motion appears as a random variable, being different from zero only in randomly distributed times (when a blob is passing through a given location); therefore, it should be treated as a correlated random variable. Informally, this means that, in a given radial location, the value of such velocity is a function of the delay between two successive events, i.e. the time interval between the passing of two blobs. This expresses the concept of non-locality. The consequence of this is that, if one computes the time average of the product between the fluctuation in radial velocity $\delta v_\perp$ in two times t, t', the result is not zero but a function of the delay between these two times, as

$$\langle \delta v_\perp(t) \delta v_\perp(t') \rangle \equiv C(t - t') \tag{5.12}$$

The function $C(t-t')$ should then present a maximum for $t - t' = 0$ and tend to zero for $t - t' \to \infty$; this expresses the maximum correlation between the random fluctuations when they are close in time. In signal theory the function $C(t - t')$, describing the correlation between two identical, delayed signals, is known as *auto-correlation function.*

For developing such a model, the usual balance equation (5.8) is revisited considering a radial transport with characteristic convective velocity $v_\perp$, so that $\Gamma_r = -D_n \frac{\partial n}{\partial r} = n v_\perp$ which, substituted in (5.8), yields

$$\frac{\partial n}{\partial t} = -v_\perp \frac{\partial n}{\partial r} \tag{5.13}$$

In a given point, density and velocity can be decomposed in background and fluctuating quantities, as $n(t) = n_0 + \delta n(t)$, $v_\perp = \delta v_\perp(t)$. The fluctuating quantities can be considered as step functions, assuming values n_b (blob density) and v_b (blob velocity) when a blob is passing through a given location, and zero otherwise. When substituted (5.13), such assumptions imply

$$\frac{\partial}{\partial t}(n_0 + \delta n) = -\delta v_\perp \frac{\partial}{\partial r}(n_0 + \delta n) \tag{5.14}$$

Taking the time average of the eq. (5.14) on a sufficiently long time yields an equation for the background,

$$\frac{\partial n_0}{\partial t} = -\left\langle \delta v_\perp \frac{\partial \delta n}{\partial r} \right\rangle \tag{5.15}$$

and an equation for the the fluctuation,

$$\frac{\partial \delta n}{\partial t} = -\delta v_\perp \frac{\partial n_0}{\partial r} \tag{5.16}$$

Integrating the eq. (5.16) yields

$$\delta n(t) = \int_0^t \delta v_\perp(t') \frac{\partial n_0}{\partial r}\, dt' \tag{5.17}$$

which, inserted in (5.15), finally gives

$$\frac{\partial n_0}{\partial t} = \int_0^t \langle \delta v_\perp(t) \delta v_\perp(t') \rangle \frac{\partial^2 n_0}{\partial r^2}\, dt' \equiv \int_0^t C(t - t') \frac{\partial^2 n_0}{\partial r^2}\, dt' \tag{5.18}$$

It is common to consider the ansatz of an auto-correlation function of the type

$$C(t - t') \equiv C_0 \exp\left(\frac{-|t - t'|}{\tau_{AC}} \right) \tag{5.19}$$

This states that the correlation between two successive events decrease exponentially with the time delay between these, with a time scale given by the auto-correlation time τ_{AC} of the blobs. According to the eq. (5.12), the coefficient C_0 can be taken as the average square velocity fluctuation, i.e. $C_0 \equiv \langle \delta v_\perp^2 \rangle$.
Substituting the auto-correlation function in this form in (5.18) gives, after straightforward calculations, a final balance equation for the background density as

$$\frac{\partial n_0}{\partial t} + \tau_{AC} \frac{\partial^2 n_0}{\partial t^2} = C_0 \tau_{AC} \frac{\partial^2 n_0}{\partial r^2} \tag{5.20}$$

The balance equation (5.20) describes, in terms of background density evolution, the non-local transport driven by the convective motion of microscopic structures such as blobs, characterized by a typical time scale τ_{AC}, and a typical velocity appearing only on such time scale. In fact, on short time scales (comparable with τ_{AC}), it exhibits a wave-like behavior for the density, motivated by the intermittent passage of high density structures. Instead, on longer time scales, the second term at the left-hand side becomes negligible, and it reduces to a "common" diffusion balance equation for the density; in this case, a diffusion coefficient defined as $D \equiv C_0 \tau_{AC}$ would then describe such kind of transport, averaged on sufficiently long time scales, in a diffusive limit.

This could provide a reasonable interpretative tool for the results of SOLPS-ITER simulations, in which the defined particle diffusivity had precisely the aim to describe a steady-state perpendicular particle transport (i.e. on time scales sufficiently long with respect to the typical auto-correlation times).
For doing this, we could express the average square velocity fluctuation due to blobs, i.e. the

coefficient C_0, weighting the time-localized peaks in velocity, having a value v_b, in terms of the experimentally measured blob packing fraction f_b, i.e. as

$$C_0 \approx (f_b v_b)^2 \tag{5.21}$$

The experimental measurements of blob properties, in the same scenario as the one considered in the simulations (i.e. the discharge #33341), can be found in [16]. The results which are useful in this framework are reported in the Fig. 5.17, where the red/blue triangles correspond to the low/high density cases, respectively.

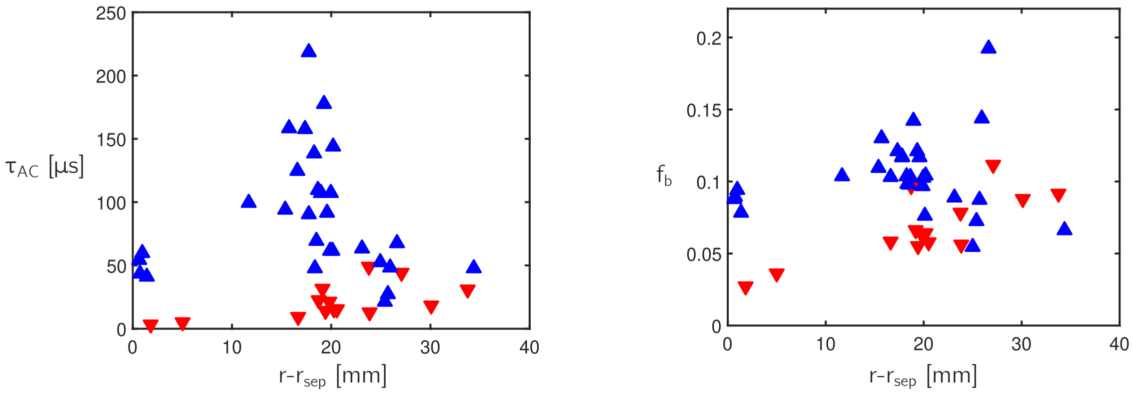

(a) Auto-correlation time.

(b) Blob packing fraction.

Figure 5.17: Blob properties as measured in the discharge #33341 at the outer SOL midplane, in function of the radial distance from the separatrix. Red/blue triangles correspond to the low density (t = 1,77 s) and high density (t = 3,56 s) cases. Adapted from [16].

For the low density case it is possible to estimate an auto-correlation time of about 50 μs and an average packing factor of about 0,05. Instead, for the high density case, we can take an auto-correlation time of about 150 μs and an average packing factor of about 0,1.

Now, it is possible to implement the simulations results in such a model, for checking whether it gives reasonable estimates on the radial convective motion of blobs, at least in terms of order of magnitude. For doing this, we take the average values of the particle diffusivity which were required for correct results at the midplane, namely of the order of 0,5 m^2/s and 20 m^2/s, respectively. Considering this as a time-averaged effective particle diffusivity according to the model introduced in this section, i.e. as $D = C_0 \tau_{AC}$, combining numerical and experimental results we could estimate a coefficient $C_0 = D/\tau_{AC}$ as about 10^4 m^2/s^2 and 10^5 m^2/s^2, respectively. These orders of magnitude, compared to the estimates for the blob packing fraction, would finally imply an estimate of radial blob velocity $v_b \approx (C_0 f_b^2)^{1/2}$ as $2 \cdot 10^3$ m/s for the low density case and $4 \cdot 10^3$ m/s for the high density case.
These order-of-magnitude estimates seem to be in more or less reasonable agreement with the measured radial velocity of blobs at low and high density regimes (cfr. Fig. 3.11). In this sense, the simulations results seem to support an interpretation of the perpendicular transport, which is dominated by intermittent fast radial propagation of blobs, through a time-averaged steady-state effective particle diffusivity of the order of tens m^2/s at high density, as assumed.

Chapter 6

Discussion of the results

In this chapter, the results of the performed simulations will be analyzed and discussed, focusing on the most important aspects for this work. First of all, in the Section 6.1 the general increase of perpendicular transport following the transition to high collisionality will be discussed, in terms of enhancement of radial fluxes at the outer midplane. The increase of both particle and heat fluxes in radial direction will be firstly characterized; then, it will be discussed how this physically impacts the mechanisms of density shoulder formation and the observed temperature profiles in the scrape-off layer. After that, the focus will be moved to how the enhancement of perpendicular transport impacts on particle and power exhaust at the divertors. In particular, in the Section 6.2 focus will be placed on what it does occur at high collisionality in a qualitative way; namely, the plasma and neutrals conditions in the divertor region, the profiles of particles and heat loads on the targets and the degree of an eventually achieved detachment will be discussed. The reasons for the occurrence of these features in the divertor region will be finally studied more in detail later, in the Section 6.3. Here, a deep analysis of the global momentum and power balances in the scrape-off layer from upstream to target will be carried out; this will be done by decomposing fluxes and sources in all their components, in order to capture which mechanisms are responsible for the observed momentum and power losses in the divertor region in each of the studied regimes.

6.1 Radial transport at the outer midplane

A crucial aspect characterizing the enhancement of perpendicular transport in the scrape-off layer is the impact on both radial *particle fluxes* and radial *heat fluxes* at the outer midplane. An increase of radial particle fluxes in an enhanced transport regime, physically due to the radial blob advection, is expected; an eventual increase of the radial heat fluxes, which could be driven by an increase of heat convection, is not obvious instead. A characterization of the radial transport of both particles and heat related to blob propagation is indeed an essential aspect for the design of the main chamber wall of future devices: in case of achievement of such a regime, in fact, these could have to sustain increased sputtering levels on their plasma-facing components. Therefore, a deep numerical investigation of this was necessary.
Radial transport at the outer midplane associated to radial blob propagation was experimentally characterized in [16][17]: in these works the same ASDEX Upgrade discharge considered in this thesis was studied, through several different diagnostics, at low and high density. The aim of the performed simulation work was to try to reproduce numerically the same results which were already obtained experimentally. In this section, these results will be used to interpret the underlying physics and to characterize numerically the mechanisms leading to the formation of the density shoulder.

In the performed simulation work, the effects of a mere increase of the density regime and the effects which purely follow from the enhancement of perpendicular transport were separated numerically. The aim was to be able to discriminate between the relative weights of the two matters on studied aspects, and see which one is most relevant. For this reason, besides considering the actual low and high density cases (cases A and B in the last section), a hypothetical "intermediate" case was considered as well; this corresponds to a high density regime (i.e. same $n_{e,sep}$ as in the case B) but low transport (i.e. same radial profile of D_n as in the case A). In the following, such color code will be used:

- **Red** for the actual low density case.
- **Purple** for the fictitious high density case characterized by low perpendicular transport.
- **Blue** for the actual high density case characterized by enhanced perpendicular transport.

The uncertainties in the measurements which were considered for constructing these cases (following from the uncertainty in the value of the density at the separatrix) were also taken into account. This was done imposing a density at the separatrix of $0{,}78\,(\pm 0{,}06)\cdot 10^{19}$ m^{-3} for the low density case and of $1{,}52\,(\pm 0{,}18)\cdot 10^{19}$ m^{-3} for the high density cases (cfr. table in the Section 5.2.4). This led to results lying in confidence bands: in the next sections, the "central value" of density will be represented as thick solid lines, while the "boundaries" of the band as thin dotted lines.

6.1.1 Radial particle fluxes

As a first result, the radial particle transport was characterized considering the simulated profiles of *radial particle flux densities*. As already pointed out, regardless of the actual nature of the radial motion of particles (diffusive or, as it is in the case of blobs, convective), in SOLPS-ITER particle fluxes in radial direction are calculated in a purely diffusive approximation, namely as (cfr. Appendix C.2.4)

$$\Gamma_r = -D_n \frac{\partial n_e}{\partial r} \tag{6.1}$$

In the Fig. 6.1, the resulting profiles for all the cases are shown.

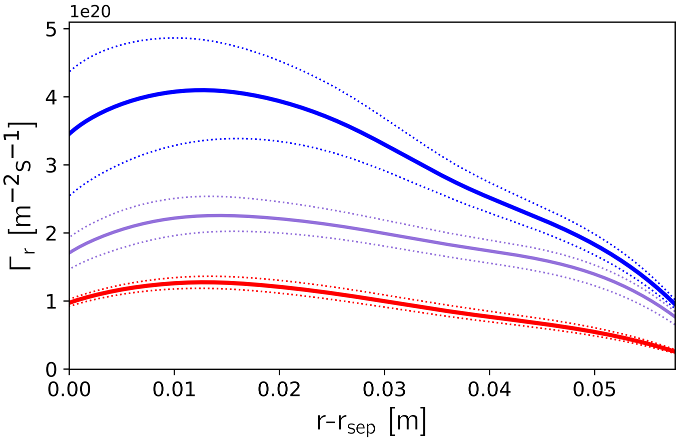

Figure 6.1: Radial particle fluxes at the outer SOL midplane.

These results can be exploited to provide a qualitative characterization of radial particle transport. A general increase of the radial particle flux at high density appears quite evident, although a large uncertainty in this profile, with an increase in the whole radial SOL extension of a factor of about $3-5$.

As expected, in the near SOL (i.e. where D_n was effectively enhanced) an increase in Γ_r driven by the enhancement of the particle diffusivity was found. It is indeed evident from the great increase of the blue line with respect to the purple line, despite the fact that both the cases are characterized by a same value of $n_{e,sep}$. At the outer boundary of the domain, i.e. approaching the wall, however, the blue and purple lines tend to converge. It may be concluded from this that increasing the transport in the near SOL may not necessarily result in an enhanced radial particle flux to the main wall, at least in the simulations. This was not obvious, and could question the real need for an enhanced flux of particles onto the main wall for contributing to the formation of the shoulder (which so far had been taken as granted): in fact, it seems that more or less the same number of particles impact the wall in the "intermediate" fictitious case, where no shoulder is present, and in the high density/transport case, where a shoulder is present. This motivated a deeper investigation of the eventual impact of main chamber recycling on the formation of the density shoulder in the simulated high density/transport case; this will be discussed later, in the Section 6.1.3.

In general, in the high density cases the number of particles arriving at the outer boundary of the domain is increased by a factor of about 4 with respect to the low density case. In the Fig. 6.2 the increase of the total particle flux striking the wall (i.e. integrated on the entire north boundary of the domain, spanning the whole poloidal extension of the SOL) is shown. The factors of increase between the various cases are more or less the same as at the outer midplane (i.e. rightmost values in the Fig. 6.1).

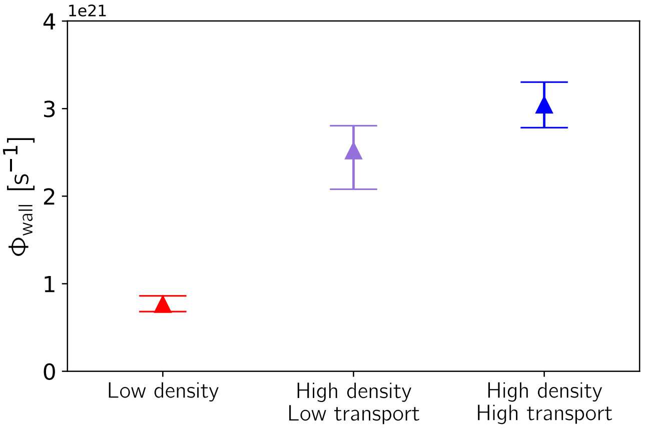

Figure 6.2: Integrated flux of particles impacting the main chamber wall in the entire SOL.

Another general consequence of this is that the sputtering rates at the main chamber wall, and the consequent erosion, could be seriously increased as a pure result of the increase of density regime, regardless the eventual increase of the transport. However, such matter is out of scope for this work.

In [16], the radial particle transport associated to blob propagation for the same discharge was experimentally investigated. First of all, the density fluctuations due to blob passing were measured; the results for both low and high density cases are shown in the Fig. 6.3a, in terms of ratio over background density n_e. Then, the radial particle flux was also experimentally estimated as the number of particles travelling radially in an average blob, factored by the blob packing fraction, i.e. as

$$\Gamma_{r,b} = n_{e,b} v_b f_b \tag{6.2}$$

under the assumption of radial blob convection dominating the perpendicular particle transport over the pure diffusion. Using the already considered values of radial blob velocity, the measured density fluctuations as in the Fig. 6.3a and the measurements on the blob packing fraction as in the Fig. 5.17b, the resulting profiles for $\Gamma_{r,b}$ were calculated as shown in the Fig. 6.3b.

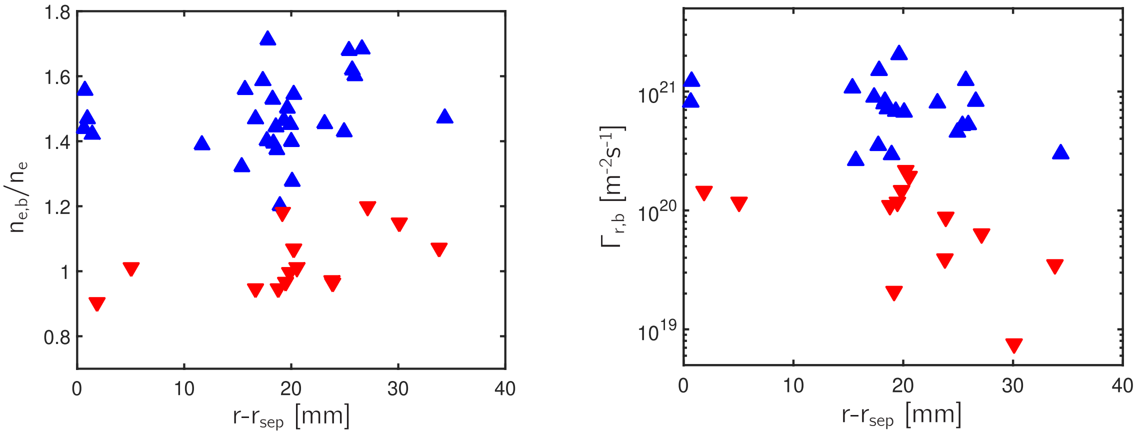

(a) Blob to background density ratio. **(b)** Radial particle flux related to blob propagation.

Figure 6.3: Properties of radial particle flux as measured in the discharge #33341 at the outer SOL midplane, in function of the radial distance from the separatrix. Red/blue triangles correspond to the low density and high density cases. Adapted from [16].

As can be noted, also from the experimental results an increase of the radial flux in the entire SOL region from low to high density emerged. However, in the experiment the increase was larger than how calculated numerically, i.e. of about one order of magnitude. A possible explanation for this could be the fact that, in the very far SOL, the imposed value of D_n is actually lower in the high density/transport case than in the low transport cases (cfr. Fig. 5.12). This merely came out from the optimization algorithm aimed to match the radial density profiles at the outer midplane, and no obvious physical reason for this actually exists. Therefore, although such an artificial imposition does not invalidate the qualitative trends in the simulated radial particle fluxes in the far SOL, it should be kept in mind that the simulated radial particle flux in the high density/transport case could be underestimated, especially in the far SOL.

6.1.2 Radial heat fluxes

Then, the radial heat transport was also characterized for all cases, considering the simulated profiles of *radial heat flux densities*. In SOLPS-ITER, these are calculated as (cfr. Appendix C.2.4)

$$q_r = \frac{5}{2}\Gamma_r(T_e + T_i) - n_e\left(\chi_e\frac{\partial T_e}{\partial r} + \chi_i\frac{\partial T_i}{\partial r}\right) \tag{6.3}$$

i.e. as a *convective component* plus a *conductive component*. The first component, associated to the radial particle motion, is proportional to the particle flux and the temperatures; the second one, associated to radial heat diffusion, is proportional to the thermal diffusivities and the temperature gradients. In the eq. (6.3), other terms such as kinetic energy flow and a term associated to the work of the viscous forces, which are also considered by SOLPS-ITER, were neglected; this is reasonable, being these usually much smaller than the other two components. Among the various cases, the particle diffusivity was the only transport coefficient which was changed; nevertheless, relevant differences in radial heat transport were also expected because of the direct impact that the enhancement of radial particle fluxes, associated to blob propagation, has in the convective component of the eq. (6.3).

In the classical picture of heat transport in the scrape-off layer is assumed that most of the power P_{SOL} crossing the separatrix is always rapidly lost by parallel heat transport, above all by electron conduction (cfr. Section 2.2.1): this would lead to rapidly decreasing profiles for q_r and very small fractions of P_{SOL} reaching the main chamber wall. This picture, however, does not take into account the effects associated to an enhanced perpendicular transport of particles at high density, which was being modelled. Therefore, in the modelled high density/transport case, the assumption of a small fraction of heat reaching the wall could be false; secondly, the impact of an enhanced transport on the temperature profiles in the SOL could also affect the way in which the heat is lost in parallel direction. This section is dedicated to the first of these matters, while the second one will be discussed later, in the Section 6.1.4.

First of all, the results about the radial heat flux densities at the outer midplane, calculated as in the eq. (6.3), were extracted for all the cases, with the resulting profiles shown in the Fig. 6.4.

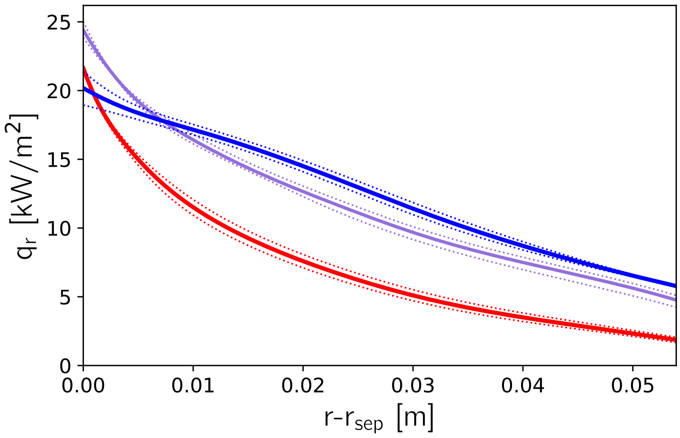

Figure 6.4: Radial heat fluxes at the outer SOL midplane.

At the separatrix we can note quite similar values for q_r for all the cases; this results from similar values of the total power crossing the separatrix, which reflects also on the situation at the outer midplane. The most striking difference is given by the slower decay of the profile for the high density/transport case (blue line), which is true especially the near SOL, i.e. precisely where the particle diffusivity was increased. This means that, effectively, more heat is being transported radially after the enhancement of particle transport, as it was supposed and in agreement with the experimental results [16][17].

This impacts directly on the heat which is still at the midplane after the whole radial extension of the SOL has been travelled, i.e. at the main chamber wall (supposed as the outer radial boundary of the domain). It can be already noted how the radial heat flux density here is increased by a factor of about 3, in the high density/transport case, with respect to the low density case.

Although the results presented in the Fig. 6.4 are locally referred at the outer midplane, the increase of the heat which is transported up to the main chamber wall is consistent with what is seen to occur in the entire SOL. This can be observed by considering the increase of the total heat flux arriving at the wall (i.e. integrated on the entire north boundary of the domain); this result, which is shown in the Fig. 6.5, allows indeed to note the same factors of increase as at the outer midplane (i.e. rightmost values in the Fig. 6.4).

In the Fig. 6.5, the total powers reaching the wall in all the cases are decomposed in their electron/ion components. Interestingly, it can be seen that the electron component drives, to a greater extent, the increase of power reaching the wall in the high density/transport case. The ion component, in fact, increases more weakly between the various cases, even presenting a small decrease between the high density cases with low and enhanced transport.

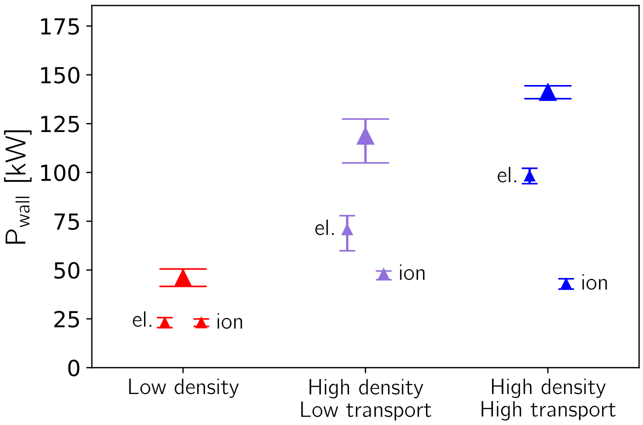

Figure 6.5: Integrated heat flux arriving at the main wall in the entire SOL.

Then, in order to discuss in more detail the extracted profiles of radial heat flux densities at the outer midplane, these were decomposed in all their components (conductive and convective), for both electrons and ions. The results shown, for all the cases, in the Fig. 6.6.

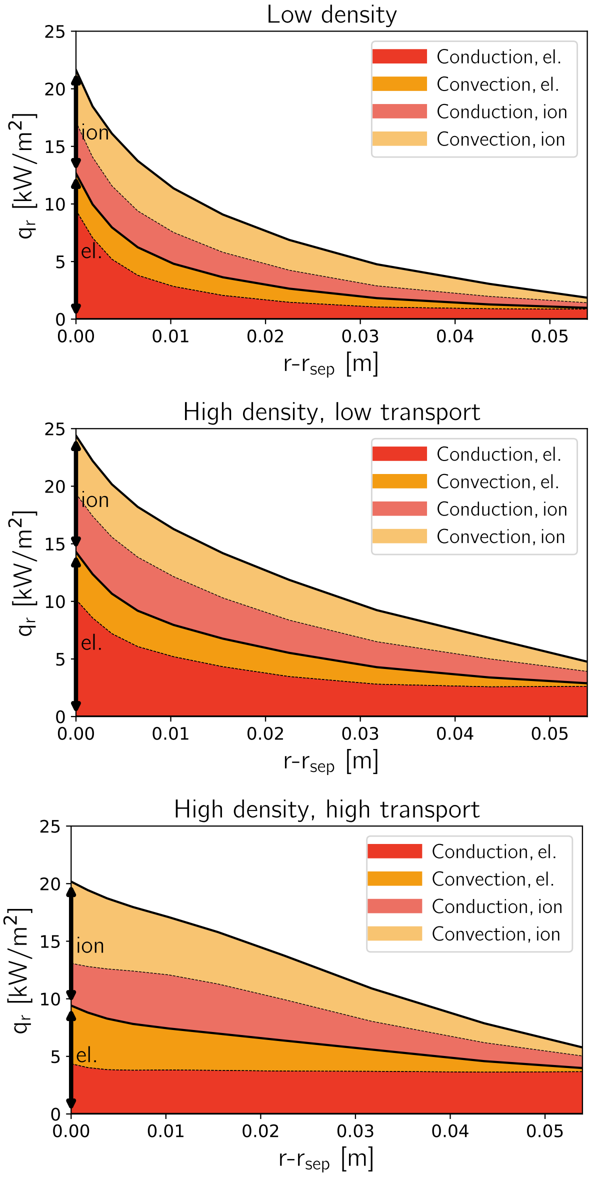

Figure 6.6: Components of the radial heat flux at the outer SOL midplane.

At low density all the components exhibit a quite fast decay; this decay gradually slows down while transiting to high density and then to high transport. This was expected for the convection component, because of the corresponding increase of the radial particle flux. In fact, the convection component for both electrons and ions is larger than the conduction component in the high density/transport case in the region closest to the separatrix; this is precisely where the particle diffusivity was increased in this case, and thus the radial particle flux was increased as well.
A not expected feature, instead, was the trend of the conduction components: at high density/transport the conduction components dominate in the far SOL, for both electrons and ions. It could be concluded that, while the increase of the particle diffusivity directly produces an increase of the convection components near the separatrix, it is the conduction components which, instead, drive the increase of power which ultimately reaches the main chamber wall.
A possible explanation is that the localized increase of the particle diffusivity in the high density/transport case, besides producing a region with flattened density, has increased the number of particles transported up to the very far SOL. Since the conduction component is also proportional to the density (eq. (6.3)), the net result of this is the conduction component dominating over the convection one while approaching the wall because of larger number of particles existing here now.

Then, the relative contributions of electrons and ions in the various cases was considered. This could be discussed by computing the ratio between the radial heat fluxes of the two species at each radial location; the results are shown in the Fig. 6.7.

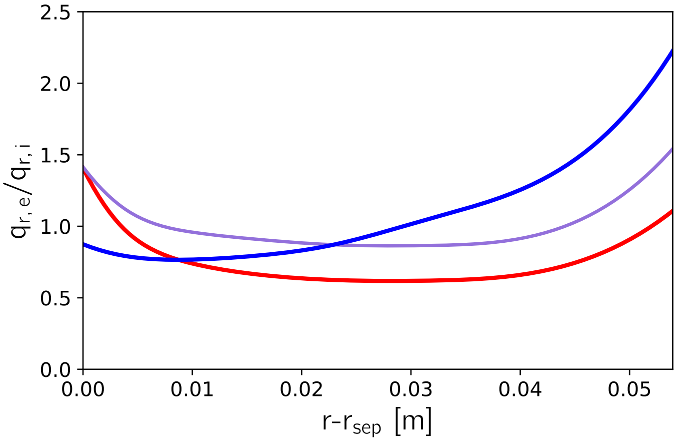

Figure 6.7: Ratio between electron and ion channels in the radial heat flux at the outer SOL midplane.

While the trend is not clear close to the separatrix, far from it an increase of ratio $q_{r,e}/q_{r,i}$, from low to high density and then to high transport, is evident. This means that, at high transport, the relative contribute of the ions in the radial heat transport undergoes a relevant decrease; this is consistent with the results about the integrated heat flux at the main chamber wall, which was in fact dominated by the electron component in the high density/transport case (cfr. Fig. 6.5). This is qualitatively in agreement with the experimental results presented in [16][17], although the absolute values of the ratio is a little bit different with respect to the measured ones. Therefore, the experimentally revealed decrease in relevance of the ion component at high transport has been successfully captured by the simulations.
This behavior could likely have to do with the simulated decrease of the ion temperature profiles in far SOL at high density/transport (cfr. Fig. 5.14); this will be discussed in more detail later, in the Section 6.1.4.

Finally, a global *power balance* for the outer SOL midplane was performed, on a domain extended over the radial cells at the outer midplane poloidal location (cfr. Fig. 6.8). In detail, the power Q_r radially transported up to each radial location was compared to the integrated parallel losses between $r - r_{sep} = 0$ and that given radial location. All the considered values were normalized to the input power P_{SOL} in the considered domain.
For doing this, P_{SOL} was considered as the power coming from the core plasma crossing the left boundary of the first cell of such domain after the separatrix. Then, at each radial location, the radial heat flux was calculated as

$$Q_r = q_r A_r \tag{6.4}$$

where q_r is the simulated radial heat flux density (eq. (C.62)) entering each cell from its left boundary, and A_r is the surface area of the cell corresponding to such boundary. Finally, the amount of power $Q_\parallel$ leaving this domain before a given radial location was calculated as

$$Q_\parallel = 2\pi \int_0^{r-r_{sep}} \left(\frac{B_\theta}{B} q_\parallel \right) R \, dR \tag{6.5}$$

This is the poloidal projection of the simulated parallel heat flux density $q_\parallel$ (i.e. the poloidal heat flux density $q_\theta = \frac{B_\theta}{B} q_\parallel$, eq. (C.61)) which crosses a cross-sectional area radially extended in the poloidal plane further from the separatrix. For the calculation of $Q_\parallel$, the flux $q_\parallel$ was taken as the net parallel heat loss from each cell, i.e. the net difference between the heat flux entering it from its top boundary and the heat flux leaving it from its bottom boundary. The integral (6.5) was then discretized considering each radial step as the radial extension of the considered cell.

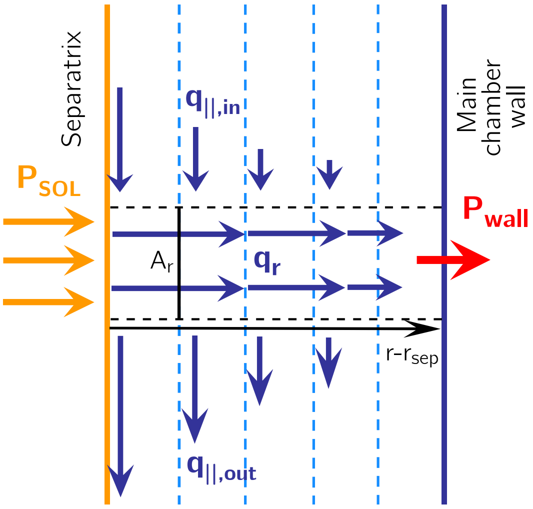

Figure 6.8: Geometry in which the calculations concerning the power balances at the outer SOL midplane were performed. Adapted from [57].

The results of this balance for all the cases, in which all the various components for both radial and parallel fluxes are distinguished, is shown in the Fig. 6.9. This graphically illustrates, for all the cases, the competition between radial heat transport and parallel heat losses at the outer SOL midplane.
At the separatrix Q_r/P_{SOL} is exactly equal to one, by definition. Then, going further the fraction of power which is still at the midplane Q_r/P_{SOL} decreases as the integrated parallel loss $Q_\parallel/P_{SOL}$ increases. However, hereafter the sum of normalized power still present at the midplane and total normalized parallel loss up to a given location is not equal to one, continuously decreasing instead: it is the consequence of the volumetric power losses occurred between the separatrix and that location, which are indeed reasonably more relevant in the high density cases. Finally, once arrived at the outer boundary of the domain, we can distinguish the total fraction of the

power which is still present at the midplane (P_{wall}/P_{SOL}) and the total fraction which has been lost in parallel direction. This last component has been decomposed in fraction of power which ultimately reaches the divertors (P_{div}/P_{SOL}) and fraction of power which is instead radiated during the parallel path before reaching it (P_{rad}/P_{SOL}).

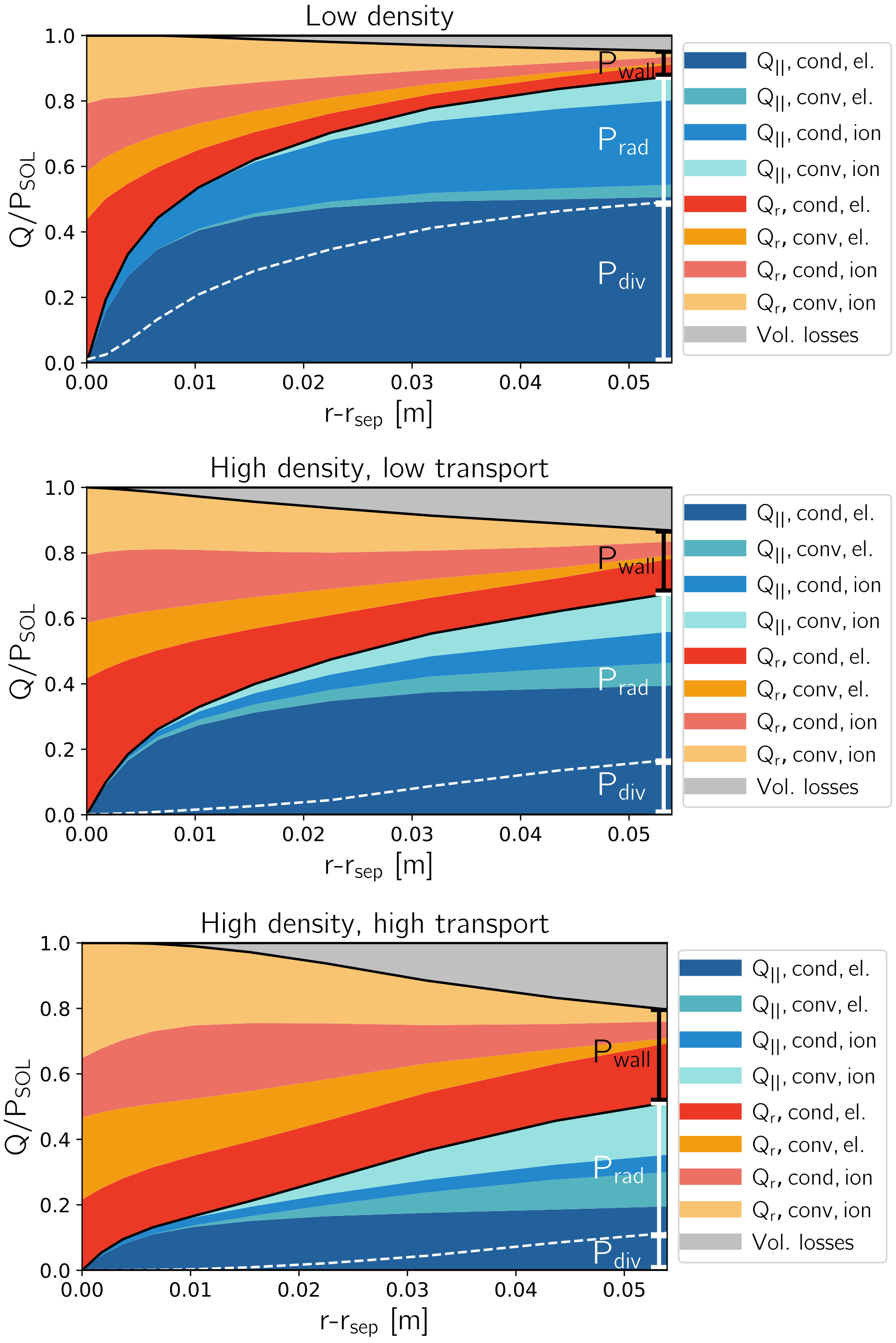

Figure 6.9: Power balance at the outer SOL midplane.

It is evident that, at high transport, more power tends to stay at the midplane also after several cm from the separatrix. In particular, the fraction of input power which reaches the outer boundary of the domain increases from less than 10% in the low density case to almost 30% in the high density/transport case. This is a remarkable result, since it confirms the presence of a non negligible fraction of power transported up to the main chamber wall also on the numerical side, after the experimental evidences presented in [16][17].

Other features which were already revealed in the Fig. 6.6 are confirmed by the Fig. 6.9. Namely, at high transport, in the near SOL this radial power spreading is mainly due to an increase of the radial heat convection components; instead, in the far SOL this is mainly due to an increase of the radial heat conduction components. Also, a relevant decrease of the relative ion contribute to the total radial heat transport in the high density/transport case can be noted here as well, coherently to what discussed so far.

Finally, the integrated volumetric losses increase with a nearly constant rate in all the cases while going far from the separatrix. This means that, in the high density/transport case, the slower radial decay of the radial heat flux implies a slower radial increase in the integrated parallel losses (and, consequently, also in the power collected at the targets). Consequently, the parallel heat flux pattern will be broadened as well. This is the first proof that enhanced perpendicular transport at the midplane has actually a strong impact on the power exhaust at the divertor targets; later, this aspect this will be discussed in more detail.

Summarizing, the simulations have confirmed that an enhancement of perpendicular transport at the midplane is effectively accompanied by an increase of radial heat transport as well. It was indeed confirmed that a large fraction of the power crossing the separatrix still remains at the midplane, also after several cm from it. This is attributable to both the enhancement of radial particle transport itself and to the increase of the SOL density regime, which promoted both radial heat convection and conduction mechanisms respectively.

The numerical results about this are even more exceeding than how experimentally measured in [16][17]. In these works, the radial heat flux density was evaluated as

$$q_{r,b} = \frac{5}{2}\Gamma_{r,b}(T_{e,b} + T_{i,b}) - n_e\left(\chi_e\frac{\partial T_e}{\partial r} + \chi_i\frac{\partial T_i}{\partial r}\right) \tag{6.6}$$

where $T_{e,b}$, $T_{i,b}$ are the blob temperatures, measured as $T_{e,b} \approx T_e$, $T_{i,b} \approx 2\,T_i$ for the low density case and as $T_{e,b} \approx 1{,}25\,T_e$, $T_{i,b} \approx T_i$ for the high density case. The convection component was assumed as resulting purely from radial blob transport, while the conduction component was calculated after the gradient of the background temperature. The results of these estimates, in terms of ratio between heat still present at the outer midplane and power crossing the separatrix are shown in the Fig. 6.10.

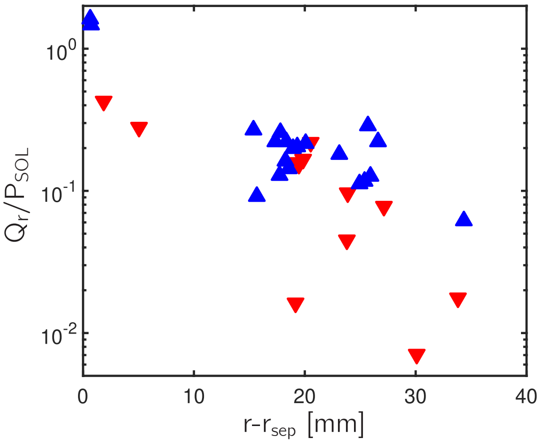

Figure 6.10: Radial heat flux as measured in the discharge #33341 at the outer SOL midplane, in function of the radial distance from the separatrix. Red/blue triangles correspond to the low density and high density cases. Adapted from [16].

In these experimental studies, the electron/ion thermal diffusivities were assumed equal to the Bohm diffusivity (eq. (A.52)), i.e. lying on a range of about $0,5 - 1$ m^2/s. In the simulations, instead, large values of these coefficients were required, especially far from the separatrix (up

to 10 m^2/s), for correctly reproducing the experimental temperature profiles, despite such high values may not be motivated physically. This could explain the slight overestimate of the radial heat transport which results from the simulations. Indeed, a large fraction of the heat still present at the midplane in the simulated high density/transport case was precisely driven by the conduction component for both electrons and ions, which is more weakly considered in the experimental estimates given in the Fig. 6.10.
Otherwise, the further features experimentally revealed are similar as the simulated ones; namely, a general increase of the Q_r/P_{SOL} ratio in the high density/transport case, especially far from the separatrix, reflecting a broadened profile for the parallel losses.

The most immediate consequence of these results is that radial heat transport related to radial blob propagation could have a non negligible impact on the heat fluxes striking the plasma-facing components at the wall. This could imply eventually dangerous effects, mainly in terms of enhanced main wall sputtering: this will have certainly to be taken into account in the design of future devices.
On the other hand, a possibly beneficial consequence of this, which for now has been only briefly introduced, is the broadening of the channel of the parallel heat flow towards to the divertors: this would imply, indeed, a spread of the heat loads on the targets and a relaxation of the exhaust onto these. This motivates a deeper discussion about it, which will be in fact the main goal of the Section 6.2.

6.1.3 Impact on density shoulder formation

The achieved results allow now to study in more detail the physical mechanisms which, in the simulations, led to the *density shoulder formation*. Namely, it was tried to investigate which is the mechanism which most contributed to provide the additional plasma particles required to flatten the density profile in the simulations. Then, it was also investigated how such phenomenon was exactly related to the enhancement of perpendicular transport.
Currently, two distinct feedback mechanisms are assumed to contribute, independently, to the formation of the shoulder [13]:

- A *transport feedback*, where the key role is played by an increase of the radial particle fluxes in the SOL driven by radial blob propagation. Here, as the global density regime increases, the consequent decrease of the temperatures in the divertor region causes a strong increase of the divertor collisionality; this leads to the regime transition of blob transport. The enhanced radial particle fluxes contribute to provide more particles in the far SOL region to form the shoulder, and the enhanced radial heat fluxes contribute to bring more heat to the wall. This makes decrease further the divertor temperatures, closing the loop.
- A *ionization feedback*, where the key role is played by an increase of the particle source by ionization in the SOL. Here, the rise of neutral population in the far SOL, initially driven by an increase of the gas puff fueling, leads to an increase of the ionizations; this provides additional plasma particles to form the shoulder. Because of the consequent density increase, the far SOL plasma becomes even more opaque to the neutrals; this promotes the electron-neutrals collisions and then increases the ionization density rate even more, closing the loop. Eventually, this loop is strengthened by the increase of main wall recycling, following from the larger particle fluxes striking the wall, which contributes even more to increase the neutral density in front of it.

This picture is summarized in the Fig. 6.11. In this section, the validity of these mechanisms in terms of agreement with the simulations results is discussed.

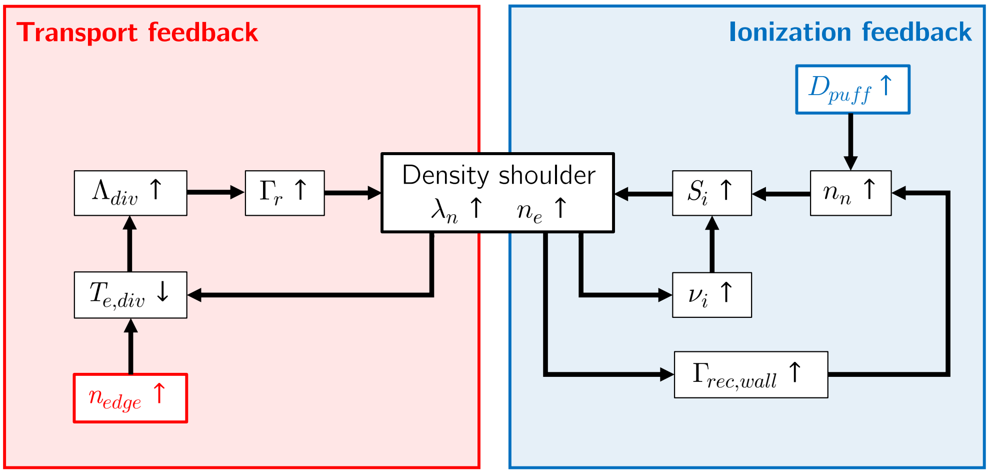

Figure 6.11: Feedback loops leading to the formation of the density shoulder as usually considered in literature [13].

These two mechanisms act both as a way for opposing the parallel particle loss in the region of the shoulder. Considering, in fact, the usual radial balance equation

$$\frac{\partial n_e}{\partial t} = D_n \frac{\partial^2 n_e}{\partial r^2} - \frac{n_e}{\tau_\parallel} + S_i \tag{6.7}$$

the first mechanism tends to oppose the parallel loss term $\frac{n_e}{\tau_\parallel}$ through an increase of the radial transport term $D_n \frac{\partial^2 n_e}{\partial r^2}$, while the second one tends to oppose it through an increase of the ionization source term S_i.

For discussing the first mechanism, it was checked how much the ratio of radial to parallel particle fluxes was changed, in the region of the shoulder, in the various cases, with the second one defined as (cfr. Appendix C.2.4)

$$\Gamma_\parallel = n_e v_\parallel \tag{6.8}$$

The results are shown in the Fig. 6.12.

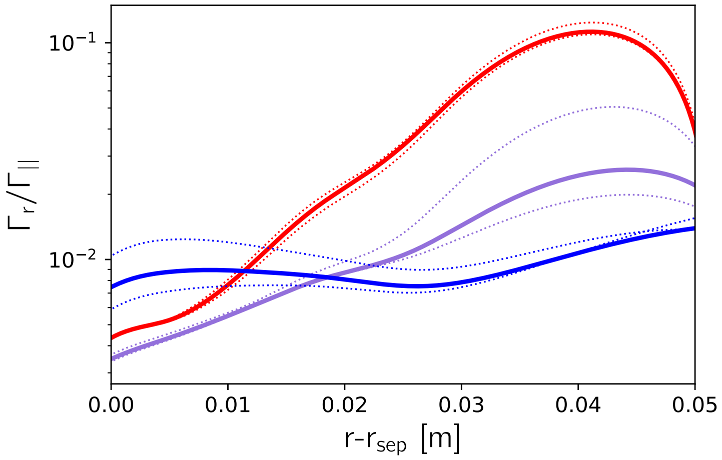

Figure 6.12: Ratio between radial and parallel particle fluxes at the outer SOL midplane.

Quite surprisingly, this ratio is generally smaller in the high density/transport case with respect to the low transport cases, in which no shoulder is present, even in the region where the shoulder is present. Differently from the previously presented ones, this result is in stark contrast with what experimentally revealed in [16].

It could be questioned if the simplifications done for the simulations (such as neglecting any drift motion) could have played a role in this. Nevertheless, regardless of the reliability of the performed simulations, the fact that a region with flattened density profile was successfully reproduced numerically is a valuable information. In fact, this lets one think that the source of particles which "feeds" the shoulder in the simulations, opposing the parallel losses, must have been driven by another process.

Evidently, the focus had to be moved on the second possible mechanism, related to a possible increase of a source of particles by ionization.
For this aim, the distribution of neutral atomic and molecular deuterium was extracted for the various cases, resulting as the solid lines shown in the Fig. 6.13, representing the overall *neutral density* n_n.

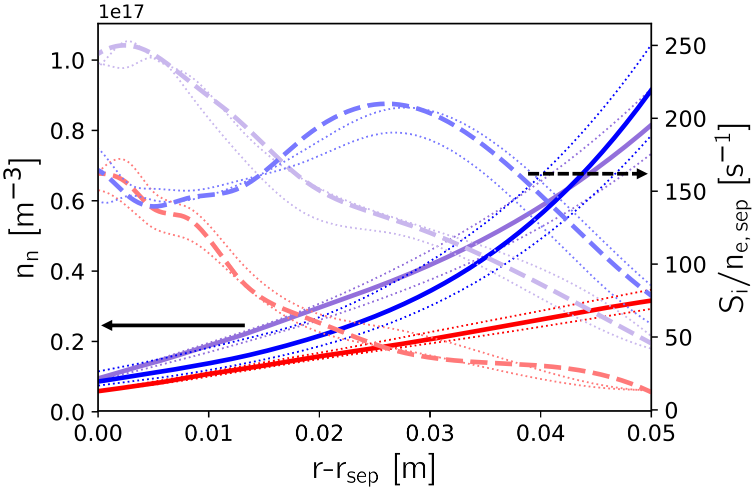

Figure 6.13: Distribution of the neutral population and the source of plasma particles by ionization at the outer SOL midplane, normalized to the density regime.

The neutral density is much larger near the wall in the high density cases than in the low density case, with a quite similar value at the outer boundary regardless of the presence of the shoulder. In all the cases a decay of the neutral population as approaching the separatrix is evident; however, this decay is much faster in the high density/transport case, where the shoulder is present, which could be just explained by the appearance of a strong ionization peak.
This is precisely what was revealed by plotting the *ionization sources* for each radial location: this is also reproduced in the Fig. 6.13 as dashed lines, normalized to the density at the separatrix, to account for the increase of the ionizations merely related to the increase of the density regime. In the cases without the shoulder this continuously increases up to the separatrix (simply following the increase of plasma density); instead, in the case where the shoulder is present, a sharp ionization peak appears, whose radial location corresponds exactly to the point where the shoulder starts degrading.
This strongly suggests that it is precisely an increase in the source term S_i which alone is able to provide the "additional" plasma particles which contribute to the formation of the shoulder, rather than a modification of the ratio of radial to parallel fluxes.

What remains to be discussed is the eventual role played by *main chamber recycling* on the shoulder formation. This question arises noting that, in the results presented so far, shoulder-related quantities at the outer boundary of the domain did not differ much between the two high density cases (the first one presenting low transport and no shoulder, and the second one presenting enhanced transport and a fully formed shoulder). The particle flux striking the wall

is indeed increased from the first to the second case, but not in such a dramatic way (Figs. 6.1, 6.2); the same is for the density of neutral population (Fig. 6.13). So, has main chamber recycling really increased in such a relevant way in the case where the shoulder is present?
An answer for this was given by decomposing, for all the cases, the ionization source of plasma particles in terms of the origin of the neutrals which were ionized. This is shown in the Fig. 6.14.

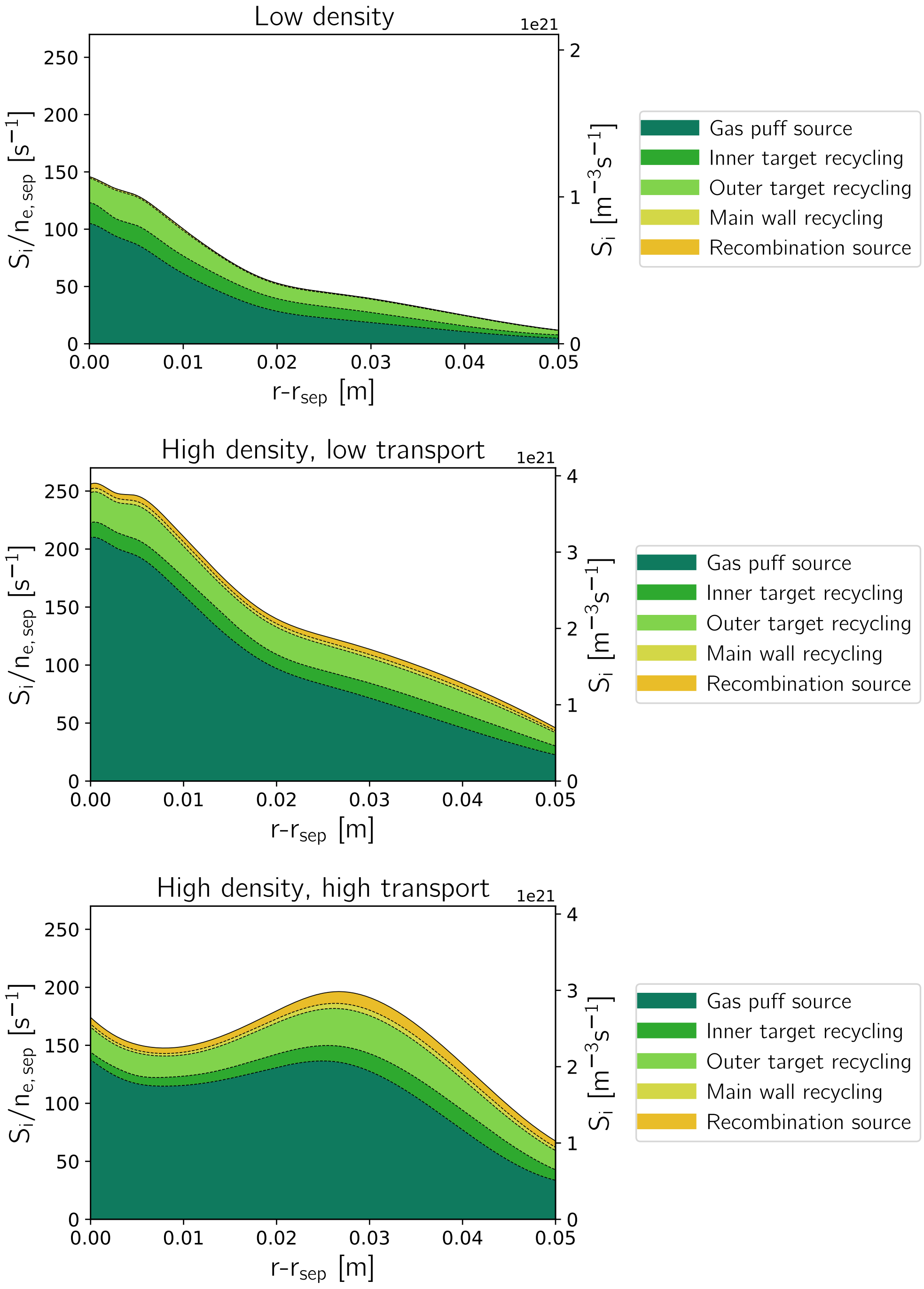

Figure 6.14: Components of the ionization particle source referred to the outer SOL midplane, in terms of the origin of the ionized neutrals.

Surprisingly, in terms of the usual picture of density shoulder formation, it can be seen that the ionization source in the case with formed shoulder originated only in a very small part from neutrals recycled at the wall. Most of the ionized neutrals were seen to come, indeed, from the gas puff source and from divertor recycling. A small increase of main chamber recycling is actually present at high density, following the increase of the particle fluxes striking the wall;

nevertheless, the consequent particle source remains absolutely negligible in the particle balance at the midplane. Therefore, the absence or presence of the shoulder seems to not be affected at all by the intensity of main chamber recycling. This result is consistent with a similar neutral density in both high density cases (cfr. Fig. 6.13). What does change between these two cases is only how fast the neutral population decays while approaching the separatrix.
For consistency, it has to be mentioned that this result is in contrast with old simulations works, such as [95]: in this work, in fact, the presence of main chamber recycling was seen to be fundamental for promoting a sufficient particle source for forming the shoulder, since deactivating the recycling at the wall surface implied not achieving a flattening of the density profiles, although the imposition of high transport coefficients. A possible underestimate of such contribute in SOLPS-ITER could be motivated by the fact that, in this case, the computational grid cannot be actually extended up to the physical walls. This means that recycling at the wall surface can be only reproduced by imposing some realistic recycling coefficients to a fictitious "wall" corresponding to the north boundary: in this way some physical features such as the dependence of the plasma-wall interaction on energy of the striking particles, wall materials, and angle of impact of these with this fictitious wall are then not considered in SOLPS-ITER. Furthermore, an underestimate of main chamber recycling in the simulated high density/transport case could be also motivated by the simulated particle flux at the wall being, in this case, probably lower than in reality, as discussed in the section 6.1.1.
Therefore, the just presented results cannot provide a definitive and reliable answer for the matter of main chamber recycling, leaving this as an open question.

Nevertheless, the simulations results provided an important important information: imposing an increase of the particle diffusivity was sufficient for producing an enhanced and localized ionization front, with or without an increase of main chamber recycling, and without an increase in the radial-to-parallel particle fluxes ratio. So, if in both the high density cases (with and without the shoulder) a comparable neutral population is present in front of the wall, what causes a relevant fraction of these being ionized much before approaching the separatrix only in the high transport case?
Possibly, it could be related with the fact that, only in the high transport case, a much larger fraction of the input power was transported far from the separatrix, up to the region of the shoulder, as discussed in the last section. This could explain the presence of the ionization peak only in the high transport case, which prevents most of the neutrals to reach the separatrix with respect to the case without the shoulder. In detail, as a larger amount of energy was transported up to the far SOL (where a larger population of neutrals is present), more energy could be used for supplying the energy cost needed for each ionization event; this would imply an increase of the ionization density rate far from the separatrix, which provides the additional plasma particles to form the shoulder.
From the view arising from these results, a slightly different explanation for the formation of the shoulder, with respect to the usual one, could be speculated. Namely, it seems to be not the increased radial particle flux itself to provide the additional plasma particles; rather, it is the accordingly increased radial heat flux which provides the energy needed for the ionizations, contributing to the ionization feedback loop.
According to this picture, the processes leading to the formation of the shoulder could be summarized as following:

1. As the global density regime increases, the temperatures at the divertors decrease, and the collisionality rises enough to let the blob transport regime undergo the transition; this implies increased radial fluxes in the entire scrape-off layer.
2. The increase of radial fluxes in the "central" SOL region tends, as immediate effect, to

transport more heat in the far SOL, although a localized increase of density does not exists yet. This amount of heat exists now in a region closer to the wall, where a stronger neutral population is present: this strongly enhances the ionization of these neutrals, promoting the formation of a ionization peak.

3. The enhanced ionization particle source leads to a net localized increase of the plasma density, resulting in a flattening of the density profile. At this point the shoulder is formed, and the ionization feedback is activated as well: this means that the increase of plasma opacity contributes further to promote even more the ionization particle source.

Summarizing, the results of the performed simulations seem to promote a new picture in which the net source of particles feeding the shoulder comes purely from the ionizations rather than from a modified radial-over-parallel particle balance. The existing ionization peak, then, seems to be caused mainly by the increased radial heat transport due to the enhancement of blob-driven radial fluxes, rather than by an increase of neutrals due to main chamber recycling.
The transport feedback and the ionization feedback described in [13] still seem to be both required for the shoulder formation. However, the first one now seems to act only in activating the second one, rather than in directly form the shoulder. This explains why, in the simulations, an increase of the particle diffusivity in the shoulder region was, alone, enough to successfully reproduce it, being its formation initially driven by the increase of radial heat transport.
This picture, which results slightly modified with respect to the one proposed in [13], is presented in the Fig. 6.15.

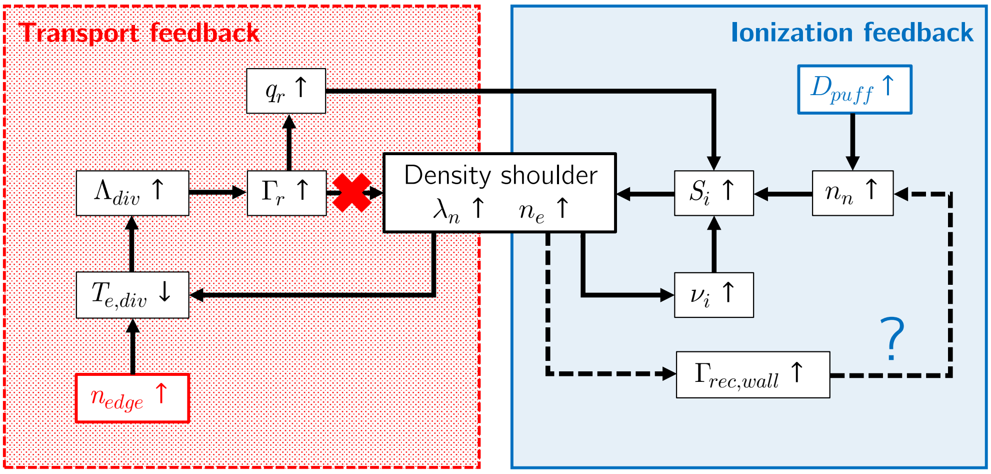

Figure 6.15: Feedback loops leading to the formation of the density shoulder in the revisited picture which arose from the performed simulations.

6.1.4 Impact on temperature profiles and parallel heat losses

The final matter of this section is the investigation of the eventual impact that the enhanced radial transport at the outer SOL midplane, revealed in both experiments and the simulations, has on the *radial temperature profiles* at the midplane.
One of the most striking features initially revealed by the simulations, following from the self-consistent procedure aimed to select the best assumption for the position of the separatrix, was a required decrease of the electron temperature at the separatrix from the low to the high density case, in spite of a similar value of the SOL input power. In [16], a value $T_{e,sep} = 50$ eV for the first case and a value $T_{e,sep} = 30$ eV for the second case were estimated. In the simulations, this difference was even more accentuated, as it was required to select a value $T_{e,sep} = 65$ eV for the first case and a value $T_{e,sep} = 30$ eV for the second case. The motivation of this strong decrease of the electron temperature at the separatrix was an open question.

Another feature revealed in both the experiment and the simulations was a less amount of energy radially carried by the ions with respect to the electrons. This was evident by noting both the integral value of heat flux striking the wall in the high density/transport case (cfr. Fig. 6.5) and the relative contribution of the electron and ion channel to the radial heat fluxes (cfr. Fig. 6.7); the last figure allowed to note that, at high density, electrons and ions carried radially comparable values of energy near the separatrix, but, approaching the wall, the ion contribute became gradually less relevant. With the performed simulations it was then tried to answer the question of why do ions carry less energy radially in the high density/transport case.

First of all, in the Fig. 6.16 the simulated temperature profiles, for both electrons and ions, are recalled for all the cases.

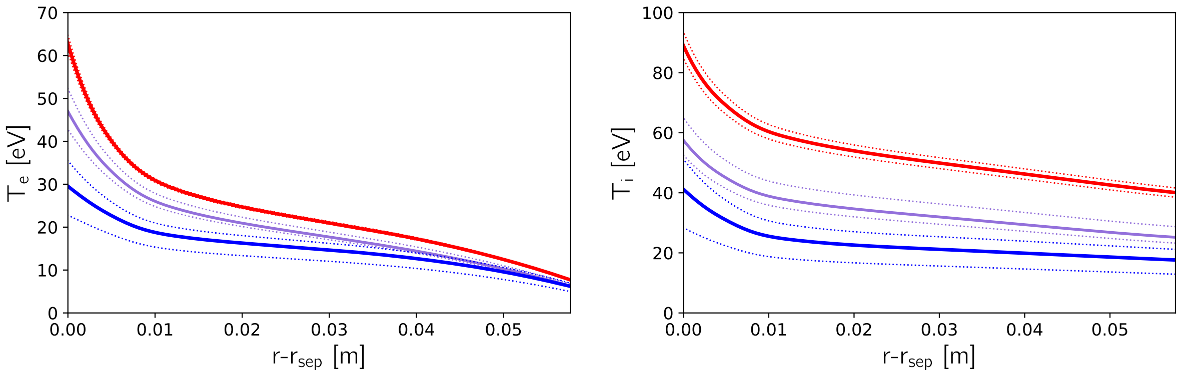

(a) Electron temperature.

(b) Ion temperature.

Figure 6.16: Radial temperature profiles at the outer SOL midplane.

The features which can be immediately noted from these figures are:

- The electron temperature is strongly decreased at the separatrix with the increase of density/transport. This decrease becomes gradually less relevant while going far from it: approaching the wall all the profiles tend, in fact, to converge to a common value.
- The ion temperature is also strongly decreased at the separatrix with the increase of density/transport, with factor of decrease equivalent to the one for the electrons. However, differently from the electron case, this decrease remains true in the entire SOL extension.

All the features recovered in the simulations were also present in the experiment [16]. In this experimental work it was assumed the usual picture of the electrons losing most of their energy by parallel heat conduction within the first few mm radially outside the separatrix; so, an enhancement of radial blob propagation after the separatrix was assumed to have only a limited impact of the electron temperature profiles, being these basically already strongly cooled as soon as the separatrix was surpassed.
For the ions, instead, it was speculated that the strong decrease of their temperature in the far SOL as well was not due to a cooling down of the hot ions coming from the separatrix; rather, it was assumed to be due to the fact that these hot ions would join a population of cold ions being originated here after the interactions with neutrals (either by ionization or by charge-exchange collisions). In principle, this is consistent with the presence of the localized ionization peak in the far SOL, also recovered by the simulations (cfr. Fig. 6.13), which leads indeed to the emergence of a cold ion population in this region.

All the features characterizing the electron and ion temperature profiles could be investigated in even more detail according to the simulation results.

First of all, regarding the decrease of both electron and ion temperatures at the separatrix, a possible explanation could be the enhancement of radial heat transport itself: namely, the impact of this on the parallel heat loss patterns. For investigating this, the *parallel heat fluxes* at the outer SOL midplane were plotted for all the cases, considering the usual distinction in convective and conductive components, i.e. as (cfr. Section 2.2.1)

$$q_{\|} = \frac{5}{2}\Gamma_{\|}(T_e + T_i) - \frac{2}{7}\left(\kappa_{0,e}\frac{\partial T_e^{7/2}}{\partial s_{\|}} + \kappa_{0,i}\frac{\partial T_i^{7/2}}{\partial s_{\|}}\right) \tag{6.9}$$

where $s_{\|}$ denotes the parallel coordinate, and $\kappa_{0,e}$, $\kappa_{0,i}$ are the classical parallel heat conductivities (eq. (2.15)). The results for all the cases, showing the distinction between the various components, are given in the Fig. 6.17.

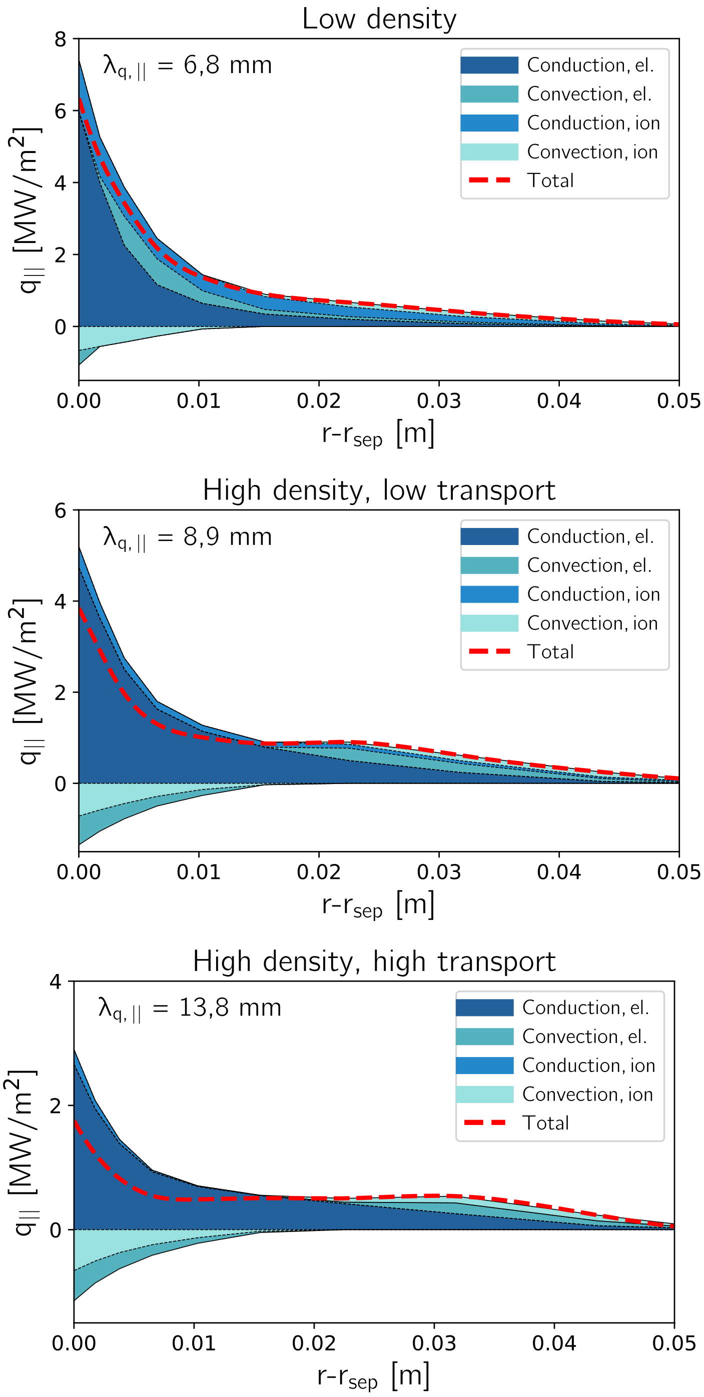

Figure 6.17: Components of the parallel heat flux at the outer SOL midplane.

A positive value indicates the heat flowing towards the outer target. So, while the conduction components are everywhere positive, the convection components are negative near the separatrix, indicating a reversed flow here; this decreases the net value of the total heat flux density (red dashed lines) in this region.
First of all, a relevant broadening of the parallel heat flux profile in the high density/transport case was found, following from the enhancement of radial heat transport, as was anticipated in the Section 6.1.2. This is quantified by an increase of the power scrape-off width $\lambda_{q,\parallel}$ (fitted on the entire radial domain) by a factor of about 2 (from 7 to 14 mm), in rough agreement with the experimental results [16].
Another feature is a decrease of the total value of $q_{\parallel}$ at the separatrix in the high density/transport case. This could be motivated also by the strong increase of the radial heat fluxes in the near SOL, driven here especially by radial heat convection: in fact, the result of such increase is less heat being lost by parallel heat conduction. The impact of this on the temperature at the separatrix could be analyzed by means of the simple two-point model (cfr. Section 2.2.2). According to this, the upstream temperature on some flux surface follows a dependence on the parallel heat flux as $T_u \propto q_{\parallel}^{2/7}$; this arises from the fact that, for similar values of the target temperature, a smaller temperature drop is needed for accommodating a smaller parallel heat flux (supposed transported only via conduction). From the actual low density case to the actual high density case, the total parallel heat flux at the separatrix has decreased approximately by a factor 1/3: this, according to the two-point model, should lead to a decrease of the upstream temperatures approximately by a factor 0,7. So, this feature effectively explains the decrease of both the electron and ion temperatures at the separatrix, as following from the decrease of $q_{\parallel}$.
Obviously the two-point model is a very crude model, which in principle does not even include the effects of parallel convection. So, it is not surprising that such simple estimate of the decrease of the temperature at the separatrix is not quantitatively in agreement with what observed. Nevertheless, it remains a useful tool for explaining this, at least in a qualitative way.

Then, it was tried to explain the different evolution of the electron and ion temperature profiles in the far SOL from case to case. For this aim, the *volumetric heat losses* occurring in the scrape-off layer were analyzed in each case. According to the power balances shown in the Fig. 6.9, these losses can be expected to increase, in terms of fraction over the total SOL input power, at high density/transport. What was tried to investigate is whether the particular subdivision of these losses between electrons and ions was able to explain the observed temperature profiles.
In the Fig. 6.18 the volumetric heat losses computed by the fluid module (including viscous losses, losses due to inter-species friction, etc.) are shown, for both electrons and ions.

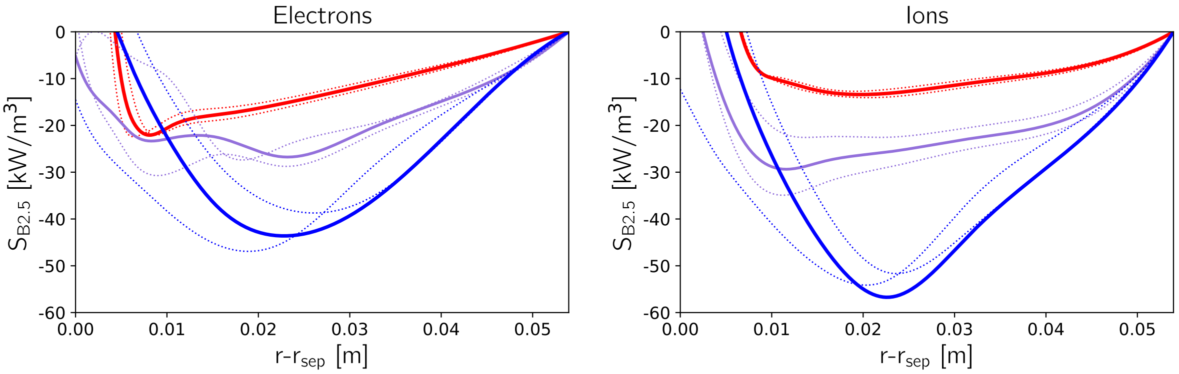

Figure 6.18: Volumetric heat losses at the outer SOL midplane for electrons and ions computed by the fluid module.

As expected, the fluid losses increased at high density. However, no useful information could be deduced from these profiles, since they are almost identical for electrons and ions; therefore, they are unable to justify a different evolution of the relative temperature profiles.
In the Fig. 6.19, instead, the volumetric heat losses caused by plasma-neutrals interactions are shown, also for both electrons and ions.

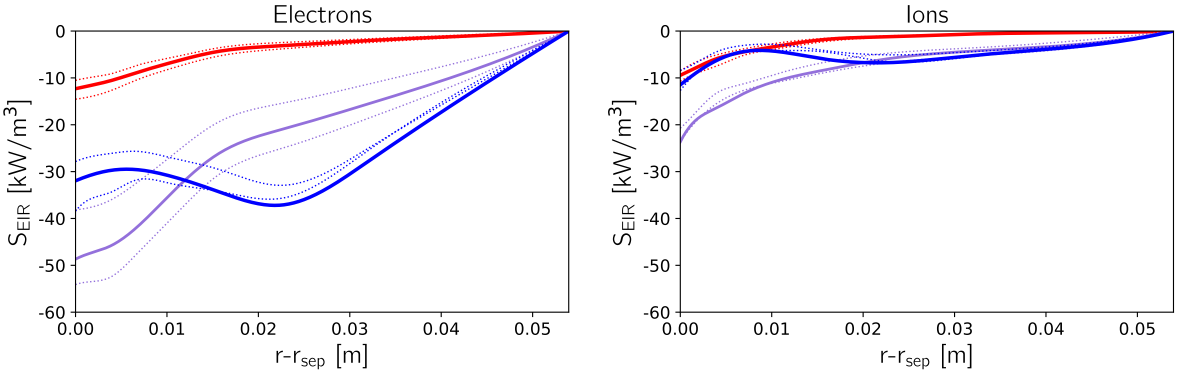

Figure 6.19: Volumetric heat losses at the outer SOL midplane for electrons and ions caused by plasma-neutrals interactions.

These losses increase at high density as well, as resulting from the corresponding increase of the neutral population; for the electrons these are basically due to the energy cost needed for the ionizations, while for the ions are due to charge-exchange collisions. In this case, an "asymmetry" between electrons and ions can be noted: namely, electrons are seen to lose much more energy because of the interactions with the neutrals. These much larger losses for the electrons could be motivated recalling the temperature dependence of the rate coefficients for plasma neutrals-interactions (cfr. Fig. 2.4): at the temperatures of interest, ionizations and CX collisions have nearly the same probability to occur; however, the energy which is lost by one electron for ionizing a neutral is larger than the energy which one ion loses while colliding with a neutral. Therefore, these results are reasonable. Moreover, this is a further confirmation of the hypothesis, discussed in the last section, of more energy needed to be transported in the far SOL to sustain the ionizations here and thus form the shoulder. This results evident as the position of the ionization peak corresponds to a peak in the volumetric heat losses by the electrons.
Nevertheless, this result does not explain yet the observed temperature profiles; according to this, in fact, it is the electron temperature which should be decreased also in the far SOL at high density/transport, and not the ion temperature.

A final phenomenon which could be invoked for explaining the observed temperature profiles was the *ion-electron thermalization*. Although this does not imply a net volumetric heat loss from the plasma, it could contribute to transfer energy from one species to the other via collisions, if their temperature is, initially, different.
The intensity of this phenomenon is proportional to the inverse of the collision time between electrons and ions, which increases with increasing temperature and decreasing density. In particular, the thermalization time, as expressed in the eq. (A.14), in its complete form reads

$$\tau_{th} = 2^{1/2} 3 \pi^{3/2} \varepsilon_0^2 \frac{m_i T_e^{3/2}}{n_e Z^2 e^4 m_e^{1/2} \ln \Lambda} \tag{6.10}$$

The resulting density rate of energy transfer between the ions (which are hotter in principle) to the electrons through this mechanism, according to the simulations results, is plotted in the Fig. 6.20.

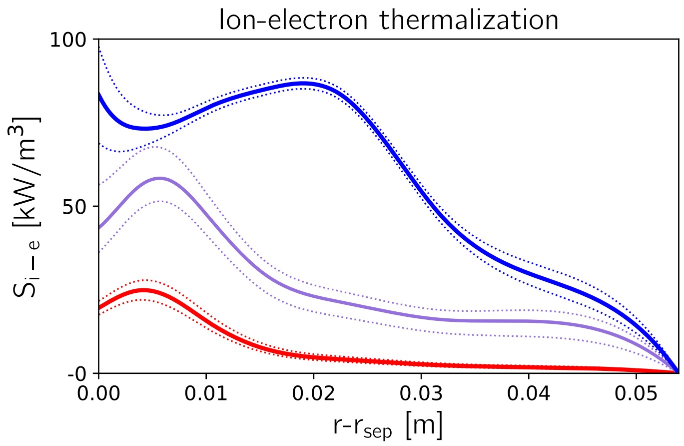

Figure 6.20: Volumetric energy exchange from ions to electrons due to thermalization at the outer SOL midplane.

Quite evidently, ions transfer a much larger amount of their energy to the electrons in the high density/transport case. This can be regarded as a result of more particles being still at the midplane much far from the separatrix, due to the existence of the shoulder. As such a large number of particles exists in a region where the absolute temperatures are lower, a strong decrease of the thermalization time results in this region.
It could be concluded that the ion-electron thermalization mechanisms is, indeed, dominant in cooling down the ion population, "giving back" to the electrons the energy which these had lost in promoting the ionizations. This could be then invoked for explaining the strong decrease which was observed for the ion temperature in the entire radial profile (including the far SOL) in the high density/transport case.

Summarizing, the discussion presented in this section allowed to explain the occurrence of the observed temperature profiles at the outer SOL midplane, in both the experiment and in the simulations. Moreover, this also explained the less relevant contribute of the ion channel in the radial heat transport in the high density/transport case, which was discussed in the Section 6.1.2; namely, this feature was seen to arise because of a strong cooling down of the ion population due to an ion-electron thermalization.
This is also confirmed plotting the ratios of ion over electron temperature in the entire SOL extension, for all the cases, which is shown in the Fig. 6.21.

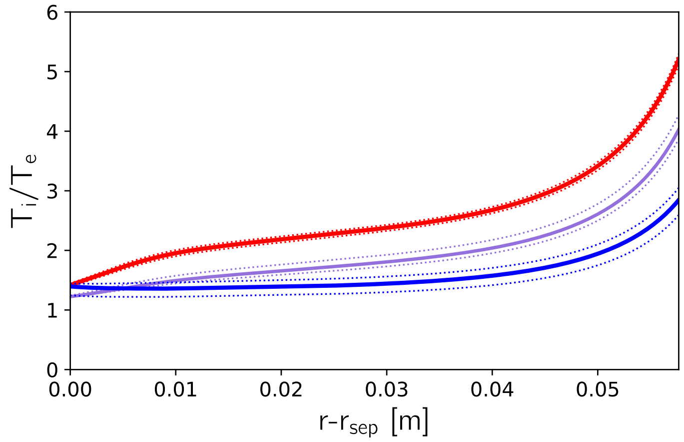

Figure 6.21: Electron over ion temperatures ratio at the outer SOL midplane.

At low density this ratio grows up to large values in the far SOL, following a strong thermal de-coupling of electrons and ions because of the lower rate of collisions. At high density/transport, instead, this stays everywhere at quite low values.

It is interesting to analyze the impact of this on the relative components of the parallel heat losses (Fig. 6.17). In fact, the relation

$$\frac{q_{\parallel,e}}{q_{\parallel,i}} \approx \frac{\kappa_{0,e}}{\kappa_{0,i}} \left(\frac{T_e}{T_i}\right)^{7/2} \approx \left(2{,}7\,\frac{T_e}{T_i}\right)^{7/2} \tag{6.11}$$

must hold everywhere, after the assumption of purely classical parallel heat conduction. So, because of the very large difference in the classical electron and ion conductivities, only where $T_i/T_e > 2{,}7$ comparable values of the electron and ion parallel heat conduction component could be expected. Otherwise, the usual assumption of $q_{\parallel,i} \ll q_{\parallel,e}$ remains true.

This is exactly what can be seen by comparing the Fig. 6.21 the Fig. 6.17: only in the low density case in the far SOL it is found that $T_i/T_e > 2{,}7$; so, here the two components are effectively comparable in magnitude. In the high density cases, instead, everywhere $T_i/T_e < 2{,}7$ holds; in fact, in these cases we find $q_{\parallel,i} \ll q_{\parallel,e}$ everywhere.

6.2 Particle and power exhaust at the divertors

The second major matter of discussion concerns the impact of perpendicular transport enhancement in the divertor region, with the goal of characterizing the *particle* and *power exhaust* processes. Although radial blob propagation is physically most effective at the outer midplane (which was reproduced in the simulations imposing a poloidal dependence for the anomalous transport coefficients), a relevant impact on the conditions at the divertors is to be expected as well. A possible motivation is the cooling down of the divertor region which follows from a larger fraction of heat being transported to the wall at upstream. This was indeed revealed in the experiment [16]: while going raising the density regime, the operating regime was seen to transit from a high-recycling regime to a partially detached regime, at least for the outer target.

The aim of this section is to investigate whether the simulations successfully reproduced this behavior as well. A first proof of this was found in the last section, in which a broadening of the power scrape-off width at upstream was, in fact, revealed: this could involve a wider spread of the exhausting power on the outer target.

It should be mentioned that the reliability of the results concerning the divertor conditions, in the performed simulations, could be likely affected by some errors. These mainly result from:

- Having imposed a somehow arbitrary poloidal dependence for the anomalous transport coefficients: this did not ensure to capture the intensity of the radial transport in the most accurate way in poloidal locations other than the outer midplane.
- Having neglected drifts and currents: this could have seriously affected the simulated parallel flows, at least at high density. The main feature which could not be captured by neglecting drifts, in particular, was a non negligible amount of power transported in parallel direction carried by particles driven by such drift motions; this could likely lead to underestimate the divertor temperatures in the high density cases [18].

Nevertheless, the simulations results could still be used for correctly interpretating the considered phenomena, consistently with an at least qualitative agreement with the experimental results.

6.2.1 General characterization of the divertor solutions

In order to perform a general characterization of the simulations results in the divertor region, the *poloidal profiles* of the main plasma quantities (*electron density* and *electron temperature*), at the separatrix, were plotted from the outer midplane up to the outer target. In the Fig. 6.22 these profiles are plotted for all the cases.

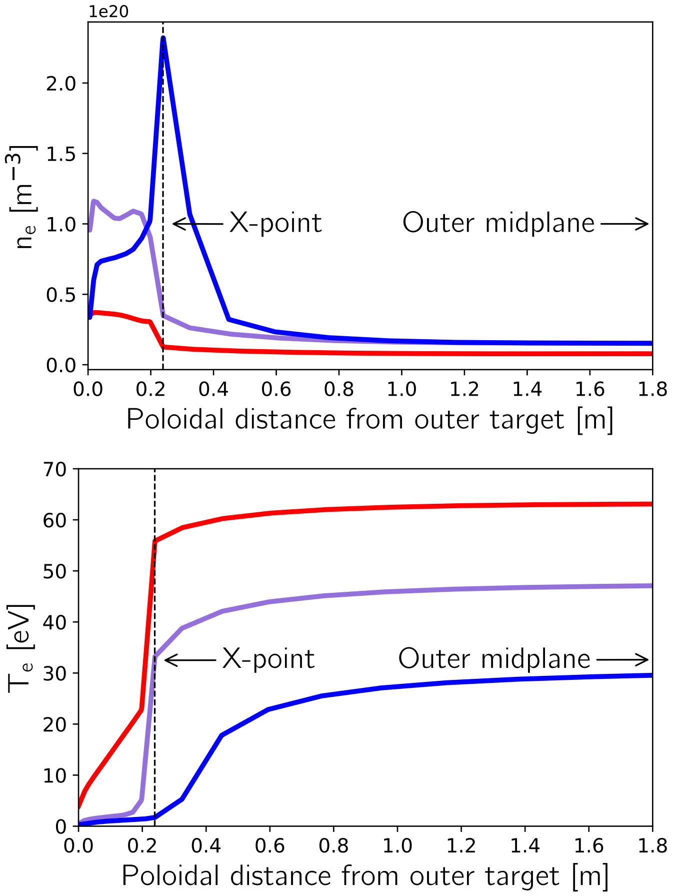

Figure 6.22: Poloidal plasma profiles at the separatrix at the outer side of the device.

Regarding the temperature profiles, as expected, these decay monotonically towards the target in all the cases. In the upstream region, where atomic processes are relatively uncommon (at least compared to what occurs at the divertors) the temperature drop is quite slow; this is sign of a parallel heat transport mainly governed by classical conduction. Then, approaching the divertor region, when the temperatures are small enough to allow the existence of a large population of neutrals, a sudden drop can be noted. In the low transport cases such drop takes place after the X-point, while for the high transport case this starts before approaching it; in particular, in this last case the temperature remains very low in the entire divertor region, which is in agreement with the strong cooling down of the divertors because of an enhanced radial heat transport at upstream, as was assumed so far.
Then, regarding the density profiles, these are uniform at upstream, since no relevant sources or sinks exist here. Then, when recycling neutrals start to emerge in proximity of the targets, the ionization of these leads to an increase of the density in all the cases. Such increase is, evidently, more relevant in the high density cases; however, while in the low transport case this remains true up to the target, in the high transport case the density exhibits a sharp peak at the X-point, before strongly decaying again. This feature, which could be motivated by a lower temperature reached in the divertor in this case, and thus by the massive arise of recombination processes, is a first proof of a simulated detachment in this case.

Another source of information for the divertors conditions is the resulting *flow pattern*, i.e. by the direction of the plasma flow, which influences many aspects of the divertor physics. This is shown in the Fig. 6.23 for all the cases, where blueish colors indicate a flow towards the inner target while reddish colors indicate a flow directed to the outer target.

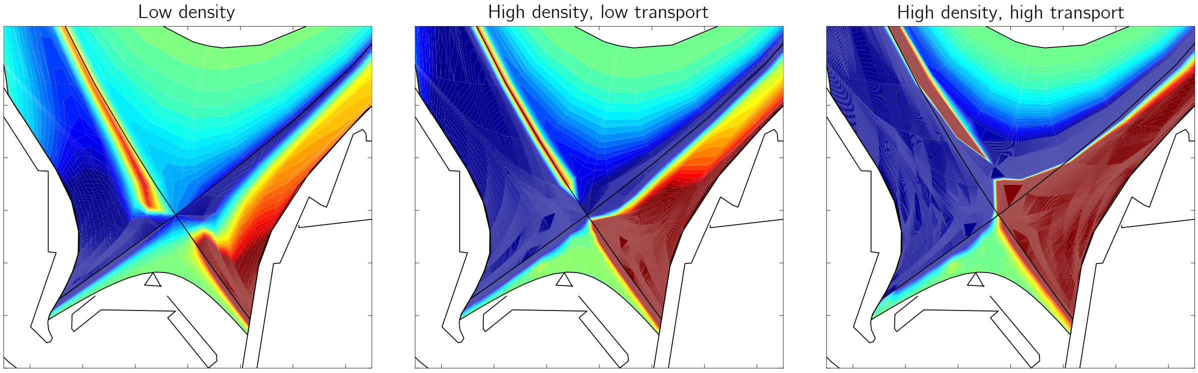

Figure 6.23: Flow pattern in the divertor region.

In the first two cases flow reversal can be noted in some flux tubes near the separatrix, meaning that the particle flux on these field lines is actually leaving the divertor region. In the high transport case, instead, this occurs only more at upstream, so that no flow reversal is observed in the divertor region; this indicates that, in this case, the stagnation point is moved upwards.

6.2.2 Conditions at the outer target

Then, attention was paid on the conditions at the *outer target*, in terms of plasma properties and parallel fluxes striking the target surfaces. These results were compared to the experimental Langmuir probe data for the discharge #33341, in order to provide a degree of reliability of the results in the divertor region. Finally, they were used to understand whether a *detached regime* was effectively reproduced in the simulated high density/transport case.

In the following, the profiles referred to the target will be reported as mapped on the radial coordinate of the outer SOL midplane, but the relative position on the actual target coordinate will be shown as well.

In the Fig. 6.24a, the *electron density* profiles at the outer target are plotted for all the cases. Going from low to high density regimes an increase of the peak density can be observed. Its radial position does not correspond anymore to the position of the separatrix but is radially shifted: this is an effect of the radial particle diffusion acting also towards the private flux region from the X-point onwards. In the high transport case the density peak is even more radially shifted (as an effect of the enhanced perpendicular transport); however, it has also relevantly decreased in magnitude with respect to the low transport cases. This is interesting, considering that the purple and the blue lines share a common overall density regime. This acts as a further proof of an effectively achieved detachment in the high transport case, at least in the near SOL region.

This supposition is even more strengthened analyzing the *electron temperature* profiles, plotted in the Fig. 6.24b. Although a strong cooling down in front of the target can be appreciated already after the mere increase of the density regime, this is quite more accentuated in the high transport case: for most of the target extension, in fact, the temperature remains below 1 eV in this case. This is a sign that a strong presence of recombination processes is to be expected in front of the targets in this case, at least in the near SOL; this would motivate the flattening of the density profile in the near SOL region and would support further the hypothesis of detachment being achieved in this region at high transport.

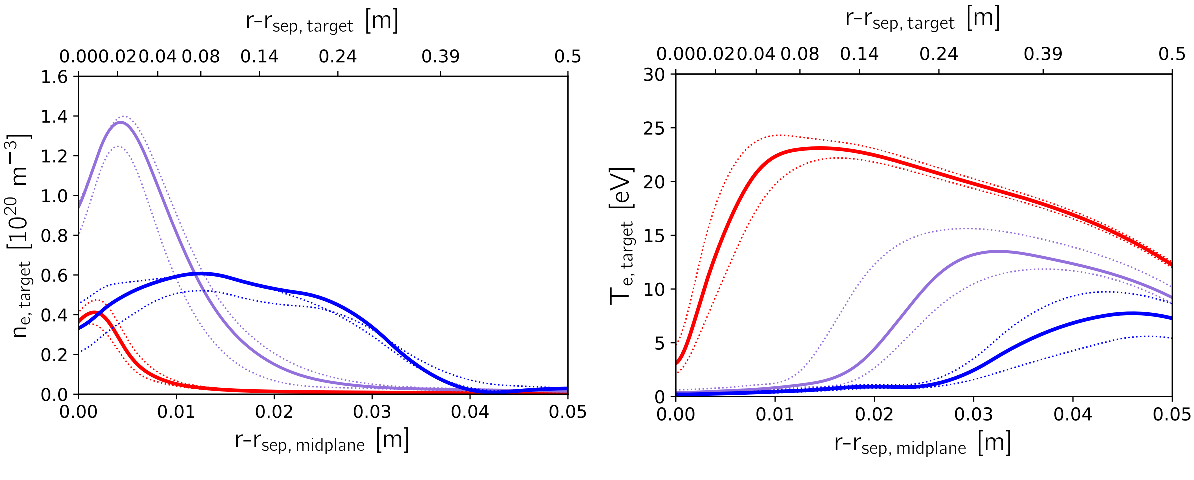

(a) Electron density.

(b) Electron temperature.

Figure 6.24: Plasma properties in front of the outer divertor target.

For validating these results, these were compared to the experimental data taken by the flush-mounted Langmuir probes installed on the outer target. This provided direct measurements of the electron temperature and the ion saturation current, with the latter used for estimating the electron density (cfr. Section 3.2.3). The resulting experimental profiles are plotted in the Fig. 6.25 in function of the poloidal flux coordinate.

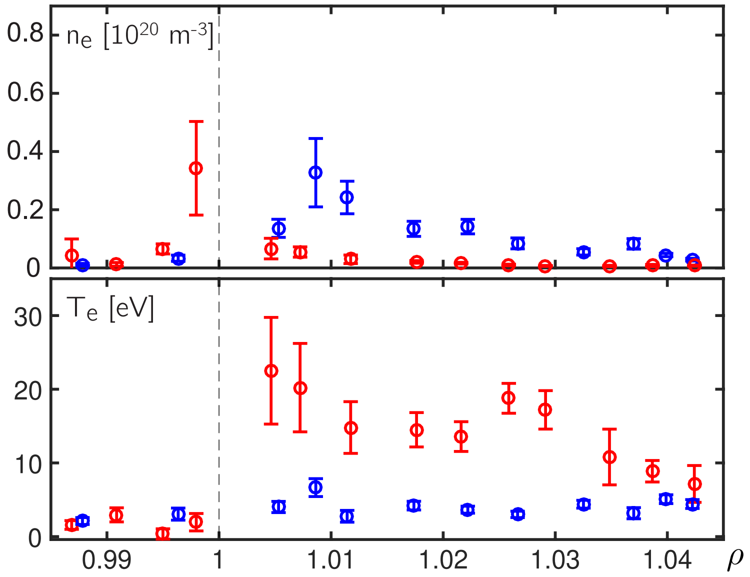

Figure 6.25: Experimental plasma properties in front of the outer divertor target, measured by the Langmuir probes. Red/blue dots correspond to the low density and high density cases. Adapted from [16].

The agreement between numerical and experimental results is quite good at in the low density case. In the high density/transport case, instead, the simulations slightly underestimate the temperature; consequently, this results in a slight overestimation of the density. This feature was expected, as this could be motivated by having neglected drifts in the simulations, as already mentioned. Nevertheless, this does not invalidate the obtained numerical results, as a general qualitative agreement has been obtained.

For investigating further the eventual achievement of detachment in the simulations at high density/transport, the parallel fluxes striking the targets were also computed.
In the Fig. 6.26a, the resulting *parallel particle flux density* is plotted for all the cases.

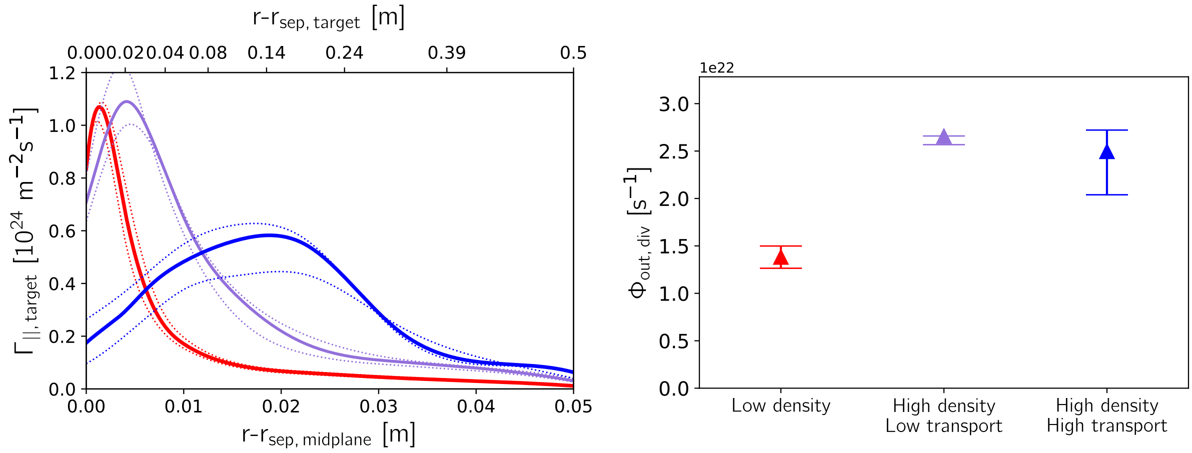

(a) Parallel particle flux density.

(b) Integrated particle flux.

Figure 6.26: Particle exhaust at the outer divertor target.

From this, a clear answer can be finally given. Namely, a partial detachment has been indeed achieved also in the simulations at high transport. This can be inferred by noting the sensible flattening of the particle flux pattern, the strong decrease of its peak value and its radial shift outwards. Since this flattening is not present in high density case without enhanced transport, it can be supposed that the enhancement of perpendicular transport has played a fundamental role in this, maybe in sufficiently cooling down the divertor and thus achieving such regime.
This was investigated in detail by looking at the onset of detachment for the two high density cases (without and with enhanced perpendicular transport), looking at the behavior of the outer limits of the confidence bands in the Fig. 6.26a. In this way, it was noted that:

- For high density and low transport (purple line) it can be observed that, raising the density regime, an increase of the particle flux onto the target takes place at each radial location; namely, the upper density value of the confidence band for $\Gamma_{\parallel,\mathrm{target}}$ lies above the lower density value.
- For high density and high transport (blue line) it can be observed that, raising the density regime, a decrease of the particle flux onto the target takes place in the near SOL; namely, the upper density value of the confidence band for $\Gamma_{\parallel,\mathrm{target}}$ lies below the lower density value. This trend is reversed again only in the far SOL, after about 2,5 cm from the separatrix strike line.

It was then observed that only increasing the density regime was not able to let the rollover peak be surpassed in any radial location. Only after the transport enhancement this was seen, instead, to occur in the near SOL; this could mean that, in this region, the pressure drop was enough to fully achieve a detached regime. This is also confirmed by looking at the integrated particle flux onto the outer target, plotted in the Fig. 6.26b: consistently with what already observed, a decrease of the total number of particles striking the target takes place after the transport enhancement, although not extremely relevant in magnitude.
This is a very interesting result, and confirms (at least qualitatively) the key role which the enhancement of perpendicular transport plays in achieving the detachment. A quantitative investigation on how enhancing perpendicular transport could have raised the pressure drop along the SOL will be given later, in the Section 6.3.

A similar investigation was also done for the *parallel heat flux density* at the target, which is plotted in the Fig. 6.27a for all the cases.

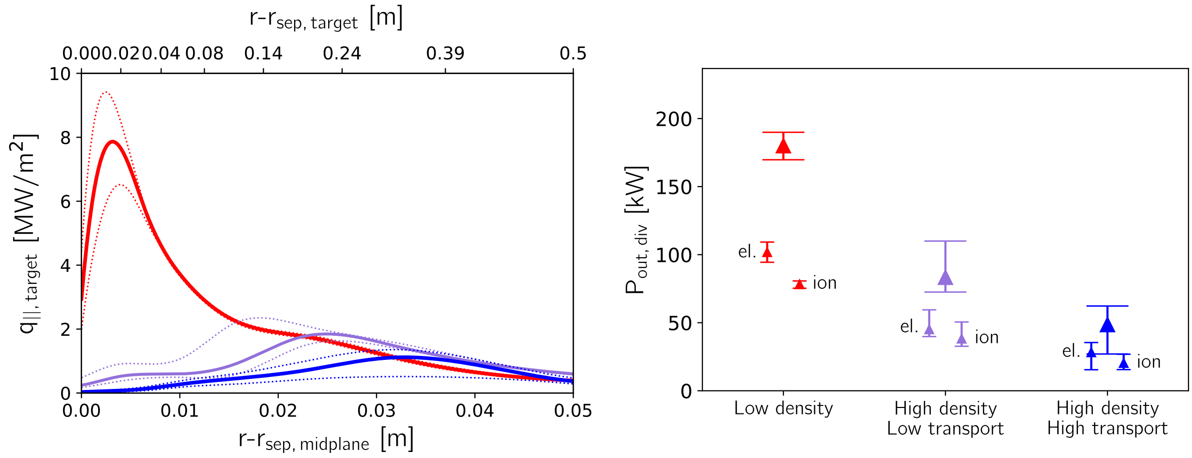

(a) Parallel heat flux density.

(b) Integrated heat flux.

Figure 6.27: Power exhaust at the outer divertor target.

Differently from the case of particles, the heat flux pattern onto the target is evidently flattened already after the mere increase of density, even without the enhanced transport. At high transport the flattening is even more consistent, and the peak heat load is even more decreased (up to about one sixth of the one for the low density case) and radially shifted.

The total power which arrives onto the outer target, instead, is plotted in the Fig. 6.27b. This undergoes a substantial decrease at high density and then even more at high transport. This power is more or less equally distributed between electrons and ions; this is more easily visible in the high density cases, where the temperatures in front of the target are sufficiently low that the two species are basically completely thermalized.

6.2.3 The role of the atomic processes

The conditions in the divertor region could be explained in terms of how the distributions of the *atomic processes* in the divertor region change from case to case. In fact the presence of atomic processes, which is a peculiar characteristics of this region, strongly impacts on the particle, momentum and power balances here. The physics of the divertor is indeed largely influenced by the presence of neutrals, whose creation, history and destruction are controlled by recombination processes, electron-impact ionizations and ion-neutrals interactions (cfr. Section 2.1.3).

For extracting some qualitative results about this, 2D contour plots referred to this region were produced. Since all the runs were performed with the kinetic module for the neutrals activated, the computed density rates (in $\text{m}^{-3}\text{s}^{-1}$) could be assumed realistic enough, as achieved through Monte Carlo calculations.

The key parameter which controls the relative importance of the various atomic processes is the temperature. Because of the monotonic drop of the temperature towards the target, which was reproduced by the simulations, we have that recombination and ionization, which play a dominant role in distinct temperature regimes, define two well-separated regions.

For temperatures between about $5-10$ eV, the ionization rate coefficient has a value comparable with the one for charge-exchange collisions (cfr. Fig. 2.4). Therefore, neutrals will be ionized after one or very few collisions with plasma particles; thus, these cannot survive in this region. So, all the neutrals recycling from the targets will be ionized as soon as such high-temperature

region is approached, so that this region is usually called "ionization front". Then, the position of such front will be moved upwards with decreasing divertor temperatures.
For lower temperatures, below about $5 - 10$ eV, neutrals can survive also somehow far from the targets. This will reflect in a massively increased neutral population in the divertor region, up to level almost comparable to the plasma density.
Finally, for very low temperatures, below about 2 eV, the recombination rate coefficient becomes even comparable with the ionization rate coefficient (cfr. Fig. 2.4), so that here the plasma density undergoes a sudden drop while the neutral population undergoes an even more drastic increase.

The *electron temperature* is plotted in the entire region, for all the cases, as in the Fig. 6.28.

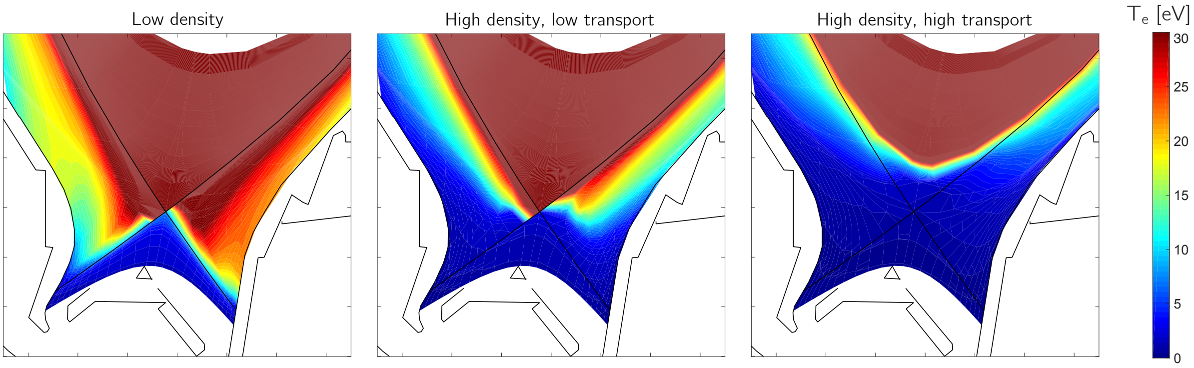

Figure 6.28: Electron temperature in the divertor region.

The entire divertor region is cooled down at high density. Then, at high transport, this is even more accentuated, so that also above the X-point a T_e uniformly below 10 eV could be noted. So, since the temperature in front of the targets is so different from case to case, it could be expected to find differences in the distributions of the atomic processes as well.

This is precisely what was seen after investigating in this direction.
In the Fig. 6.29 the distribution of the *volumetric recombination processes* is shown, for all the cases.

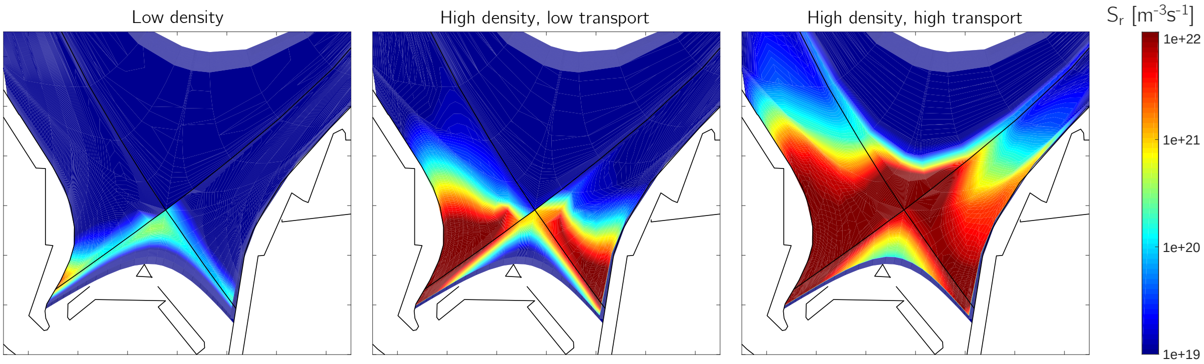

Figure 6.29: Distributions of volumetric recombination processes in the divertor region.

At low density the presence of volumetric recombinations is almost negligible, because of the too high temperatures. At high density, instead, this becomes more relevant, being however still concentrated near the targets and close to the separatrix. After the enhancement of transport, instead, recombination is even more relevant in the entire divertor region, because of the much low temperatures achieved in this case.

An opposite effect can be instead seen by plotting the distribution of the *volumetric ionization processes*, shown in the Fig. 6.30 for all the cases.

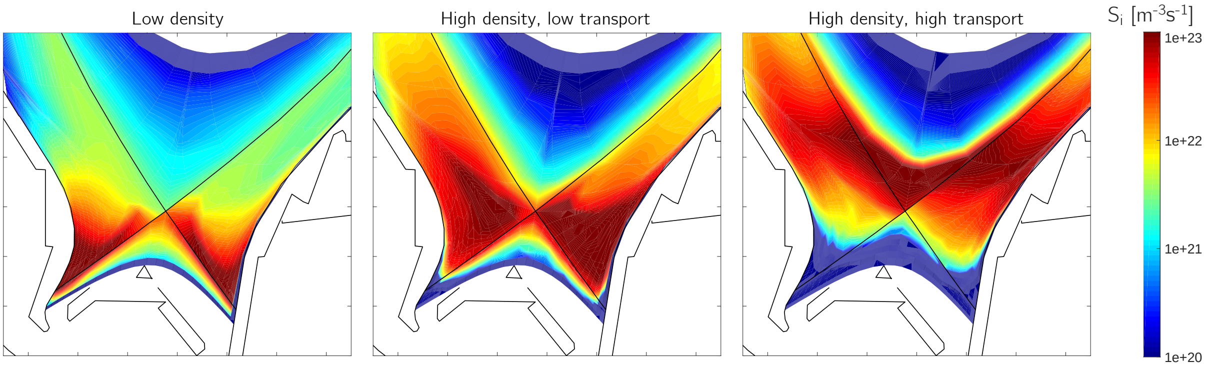

Figure 6.30: Distributions of volumetric ionization processes in the divertor region.

In the low density case a high-recycling regime is already present; therefore, a thin ionization zone exists in front of the targets, being this still too hot for the neutrals to survive here. As the density is increased the ionization zone is more extended, because of both an increase of divertor recycling and a decrease of the temperature. Finally, at high transport, the ionization front is evidently upwards shifted. This feature could be motivated by the fact that the temperature in region in the immediate vicinity of the targets is too low for the neutrals for being ionized. This implies that, in this case, most of the heat losses due to the ionizations take place above the X-point rather than below, with a non negligible presence of ionizations also in the core plasma.

What is seen from the last figures is an increase in relevance of the recombinations and the upwards shift of the ionization front in the high/transport case. Both these features suggest that a net raise of the *neutral population* in the entire divertor region (and also, at some extent, above the X-point) could be expected. The Fig. 6.31, showing the neutrals density in the divertor region for all the cases, confirms this hypothesis.

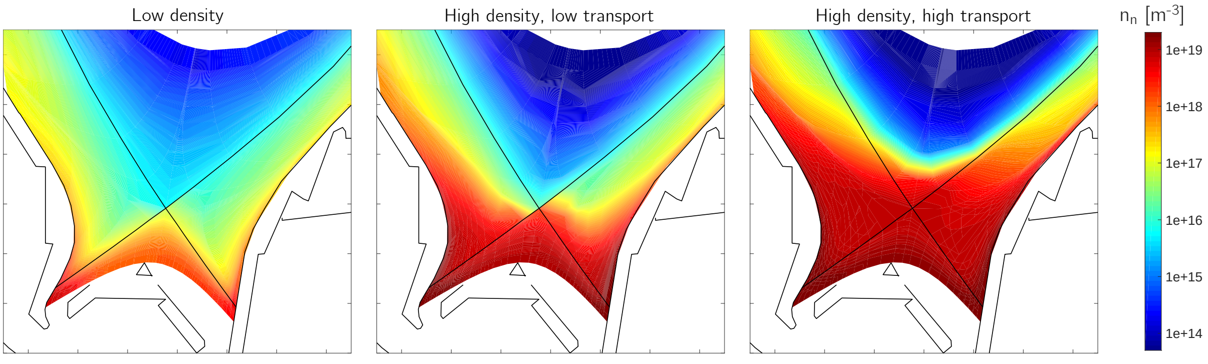

Figure 6.31: Neutral population in the divertor region.

Such strong raise of the neutral population could represent a motivation for the achievement of the detachment in the high transport case. In fact, as the neutral population increases, the density rate of momentum-removing processes (such as charge-exchange collisions and elastic scattering) increases as well. Then, also the recombination itself acts as a non negligible momentum-removing process for the plasma. These features are expected to lead to a strong pressure drop, which would contribute to the achievement of a detached regime (cfr. section 2.3.3).
Only qualitative information, however, could be extracted from the just presented figures. In the following section the conditions at the divertors will be analyzed in more detail, with the precise goal to confirm quantitatively such hypothesis.

6.3 Quantitative analysis of momentum and power dissipation at the divertors

The aim of the last section was to provide a merely qualitative picture of the exhaust processes at the divertors. A qualitative correlation with the presence of volumetric atomic processes was provided by investigating the 2D distributions of the rate densities for each process. From this two features were understood: first, the strong increase of the neutrals populations could motivate the achievement of a detached regime in the high density/transport case, through an increase of momentum-removing processes; second, the altered space distribution of the volumetric power losses (i.e. following the ionization processes) could have led to more power being dissipated above the X-point rather than inside the divertor region.
The aim of this section is to present some global *momentum* and *power balances* for the SOL plasma, performed for all the cases, to confirm these features in a more quantitative way. Performing such detailed balances was indeed needed to characterize as accurately as possible the various different mechanisms for momentum and power dissipation in the divertor region. With these, it was tried to check if plasma-neutrals interactions effectively play a major role in the high density/transport case for inducing the detachment, as it was qualitatively assumed; moreover, it was also tried to check if the loss channel given by the radial particle transport itself could have contributed in a relevant way to strengthen both momentum and power losses.

6.3.1 Pressure drop in the divertor

As a first task, a quantitative calculations of the *pressure drop* along each single flux tube from upstream to target was performed, relating this to the detachment properties in each case (considering, as usual, the outer divertor).
The total pressure was considered, as usual, as static plus dynamic pressure, i.e. as

$$p_{tot} \equiv n_e(T_e + T_i) + m_i n_e v_{\parallel}^2 \tag{6.12}$$

In order to quantify the total pressure drop between an upstream position and a target position, it was made use of a *momentum loss factor* f_{mom}. This is the fraction of the total pressure present at upstream which can still be found in the same flux tube at the target, i.e.

$$f_{mom} \equiv \frac{p_{tot,\,\text{target}}}{p_{tot,\,\text{upstream}}} \tag{6.13}$$

Such an expression for the momentum loss factor is more complete than the one provided by the simple two-point model (cfr. Section 2.2.2), which assumed the upstream position as a stagnation point for the plasma flow, and sonic flow and complete thermal coupling between electrons and ions at the target. In this way, $f_{mom} \approx 1$ means no pressure drop, while f_{mom} approaching zero means that some pressure losses have taken place.

In the literature, some relations have been already derived for estimating the magnitude of the pressure drops in the divertor under specific plasma conditions. It was found that the only key parameter which controls the value of f_{mom} on each single flux tube is the electron temperature at the target $T_{e,\,\text{target}}$ corresponding to the same flux tube. This was consistent with the experiments: in fact, plotting experimental estimates for f_{mom} in function of the measured $T_{e,\,\text{target}}$ for a heterogeneous experimental dataset produced a clear trend, with f_{mom} strongly decreasing with $T_{e,\,\text{target}}$ for temperatures lower than about 5 eV (cfr. Fig. 2.11).
For modelling such a behavior, in [103] a very simplified analytical relation was derived, in a one-dimensional geometry considering upstream as the entrance of the recycling region, under the assumption of isothermal flux tubes (i.e. having everywhere the same temperature as at

the target) and considering a uniform neutral population. The result is the so-called *Self-Ewald model*: the resulting momentum loss factor is estimated as

$$f_{mom,\ \text{Self-Ewald}} = 2\left(\frac{\alpha}{\alpha+1}\right)^{\frac{\alpha+1}{2}} \tag{6.14}$$

in which

$$\alpha \equiv \frac{1}{1+\frac{\langle\sigma v\rangle_{CX}}{\langle\sigma v\rangle_{i}}} \tag{6.15}$$

where $\langle\sigma v\rangle_{CX}$, $\langle\sigma v\rangle_{i}$ are the charge-exchange and ionization rate coefficients, to be extracted from adequate atomic databases in function of the target temperature. Such model is, however, very crude as neglects the presence of other momentum loss channels from a flux tube, such as viscosity, recombination processes and radial particle transport.
In [79] a numerical scaling relation was instead derived. This was based on an extensive set of numerical simulations (also performed for ASDEX Upgrade with previous versions of SOLPS) under different plasma conditions; again, a relation which is a function of the target temperature only was obtained, i.e. the *Kotov-Reiter scaling*

$$f_{mom,\ \text{Kotov-Reiter}} = 1-\exp\left(-\frac{T_{e,\,\text{target}}}{0{,}8}\right)^{2{,}1} \tag{6.16}$$

The curves resulting from both these relations are in qualitative agreement with what results from experimental studies made on different devices [49][8].

With the simulations results, an analysis of the temperature dependence of the momentum loss factor was carried out, considering the poloidal location of the X-point as the upstream position (as no relevant momentum losses were expected below this position). Such assumption was supported by plotting the poloidal profiles of the total pressure on a single flux tube for each case, as in the Fig. 6.32 (in which the evolution of the pressure at the separatrix is considered).

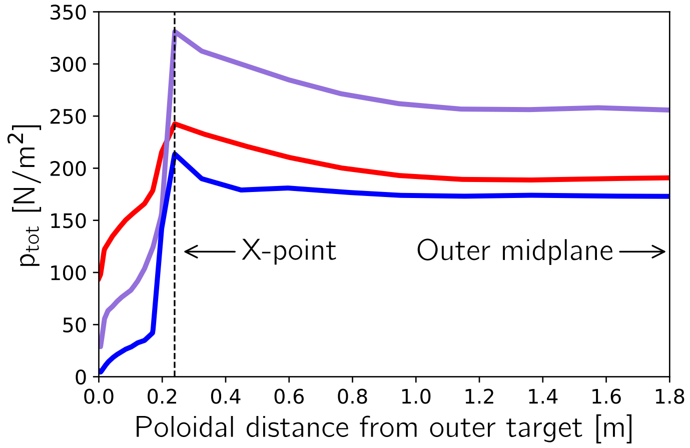

Figure 6.32: Poloidal pressure profiles at the separatrix.

This figure shows that, at upstream, the total pressure is different for all the cases, but maintains a more or less constant value. As p_{tot} is dominated by its static component at upstream, such different values could be motivated by the different values of upstream temperature. Going from the red curve to the purple one the increase of upstream density has driven the increase in pressure; then, going from the purple curve to the blue one, a decrease of pressure came out from a decrease of the upstream temperature, being the upstream density the same for these two cases (cfr. Fig. 6.22). Most important, this figure shows how, indeed, all the pressure losses are concentrated below the X-point, as assumed.

The momentum loss factor was then calculated as defined from the eq. (6.13) for each flux tube in each of the simulated cases. The results are plotted as markers in the Fig. 6.33, in which the curves deriving from the Self-Ewald model and the Kotov-Reiter scaling are shown as well. Different colors indicate the different simulated scenarios; instead, different markers indicate, for each case, different distances of the considered flux tubes from the separatrix (as usual, as mapped on the midplane radial coordinate).

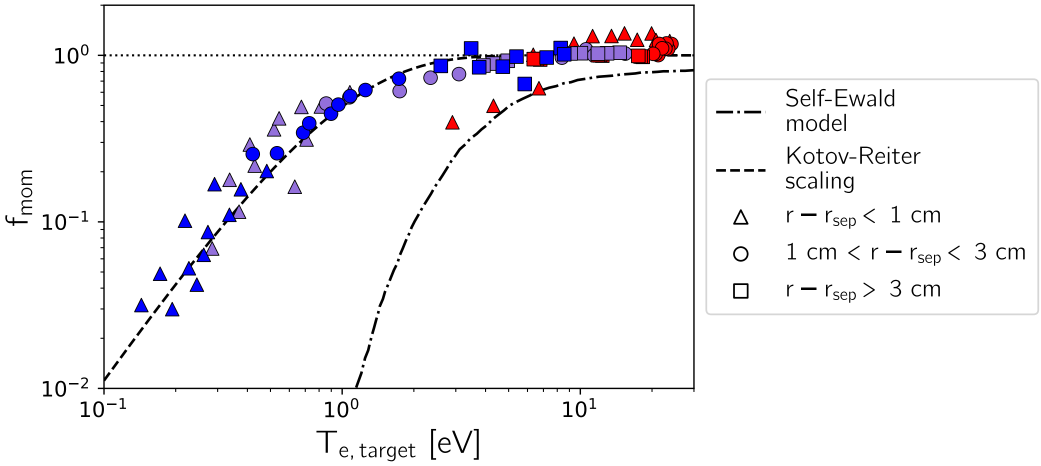

Figure 6.33: Momentum loss factor calculated for each flux tube for all the simulated cases, plotted in function of the corresponding electron temperature at the target.

The first feature arising from this figure is that, also according to the performed simulations, the pressure drop along single flux tubes follows a trend which is function of the target temperature $T_{e,\,\text{target}}$. No dependence on the particular scenario is seen to exist, meaning that the points referred to all the simulated cases seem to belong to a precise curve, with $T_{e,\,\text{target}}$ ordering parameter.

In each case, pressure drop starts to take place only for very low $T_{e,\,\text{target}}$, below about 5 eV, as experimentally seen. What does change from case to case is the presence, in the flux tubes close to the separatrix, of lower $T_{e,\,\text{target}}$, which induces larger pressure drop here. This is more evident at high density rather than at low density, and even more at high transport.

In fact, pressure drop is very strong in the high density/transport case close to the separatrix (i.e. blue triangles in the Fig. 6.33). This could be, indeed, motivated by these flux tubes being characterized by a lower $T_{e,\,\text{target}}$ (cfr. Fig. 6.24b), so that recombination could arise as main loss mechanism here, as well as CX collisions due to a larger neutral population. This explains well why, in the high density/transport case, detachment was seen to occur (i.e. the rollover peak was surpassed) only near the separatrix: only in this region, according to the Fig. 6.33, a very strong pressure drop could be indeed observed, with $f_{mom} < 0{,}1$.

These results seem then to suggest that the enhanced pressure losses at high density/transport mainly follow from the general decrease of the temperatures in the divertor and the consequent increase of momentum-removing processes such as CX collisions and recombinations, which are indeed accentuated at low temperatures.

The agreement of these results with the scaling law (6.16) is very good; this was expected since this also was derived from numerical simulations.

The Self-Ewald model (6.14), instead, seems to underestimate f_{mom}, which is more evident at lower temperatures. This could explained by the fact that, in reality, the temperature in divertor plasma is larger than the one found at the target, while the model assumes it as equal to $T_{e,\,\text{target}}$ along the corresponding flux tube: for this reason, this model strongly overestimates both the neutral population and the presence of recombination processes in the entire divertor region. This explains why the values of f_{mom} evaluable with this are so exaggerated.

Then, for obtaining a quantitative measure of the global pressure drop in the entire divertor region from upstream to target, an "integrated" momentum loss factor was calculated, for each case, as

$$f_{mom,\,\mathrm{int}} \equiv \frac{\int_{\mathrm{target}} p_{tot}\, dr}{\int_{\mathrm{upstream}} p_{tot}\, dr} \tag{6.17}$$

The result of such calculation yielded a value of:

- $f_{mom,\,\mathrm{int}} = 1{,}05$ for the low density case.
- $f_{mom,\,\mathrm{int}} = 0{,}56$ for the high density, low transport case.
- $f_{mom,\,\mathrm{int}} = 0{,}37$ for the high density, high transport case.

In the first case the global pressure drop in the divertor is absolutely negligible, being $f_{mom,\,\mathrm{int}}$ even larger than 1 (because of some momentum gain appreciable along some flux tubes). At high density, instead, this becomes quite relevant, mainly following the decrease of the divertor temperatures. Interestingly, $f_{mom,\,\mathrm{int}}$ is even more lowered at high transport with respect to the "intermediate" case, with these sharing a common density regime. This is, indeed, consistent with detachment being observed only at high transport.

This is a further proof that the enhancement of perpendicular transport strongly contributes to remove even more momentum from the plasma, in addition to what occurs because of the mere increase of the density regime. So, it likely plays a key role in the achievement of a detached regime, which was experimentally observed and numerically reproduced. As observed in this section, this occurs via a stronger cooling down of the divertor region.

6.3.2 Global SOL power balance

A similar analysis was carried out for quantitatively estimating the *power losses* as well. This was done extracting, from the simulation results, the energy flows crossing the main boundary surfaces of the computational domain.

The total power P_{SOL} crossing the separatrix was taken as reference for the input power in the scrape-off layer. Some of this power, P_{wall}, is radially transported up to the main chamber wall, by crossing the radial-directed surfaces poloidally extended at the north boundary of the domain. Another part of this, $P_{div,\,in} + P_{div,\,out}$, is transported towards the divertor region and enters it, crossing the poloidal-directed surfaces radially extended at the left and at the right of the X-point. The remaining part, i.e. $P_{vol,\,SOL} \equiv P_{SOL} - P_{wall} - P_{div,\,in} - P_{div,\,out}$, can be regarded as the volumetric power losses occurring in the SOL.

Other information which could be extracted are the powers $P_{target,\,div,\,in}$, $P_{target,\,div,\,out}$ which are poloidally transported up to the targets and cross the poloidal-directed surfaces extended at the west and east boundaries of the domain. So, $P_{vol,\,div,\,in} \equiv P_{div,\,in} - P_{target,\,in}$ and $P_{vol,\,div,\,out} \equiv P_{div,\,out} - P_{target,\,out}$ can be considered as the volumetric power losses occurring in the divertor region.

The just described situation is schematically depicted in the Fig. 6.34. The resulting global power balance extracted from the simulation results, with terms normalized to the total input power P_{SOL}, is then shown in form of pie charts in the Fig. 6.35.

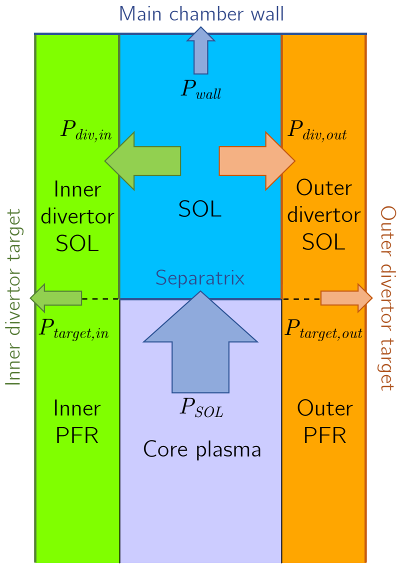

Figure 6.34: Power flows in the computational domain of SOLPS-ITER.

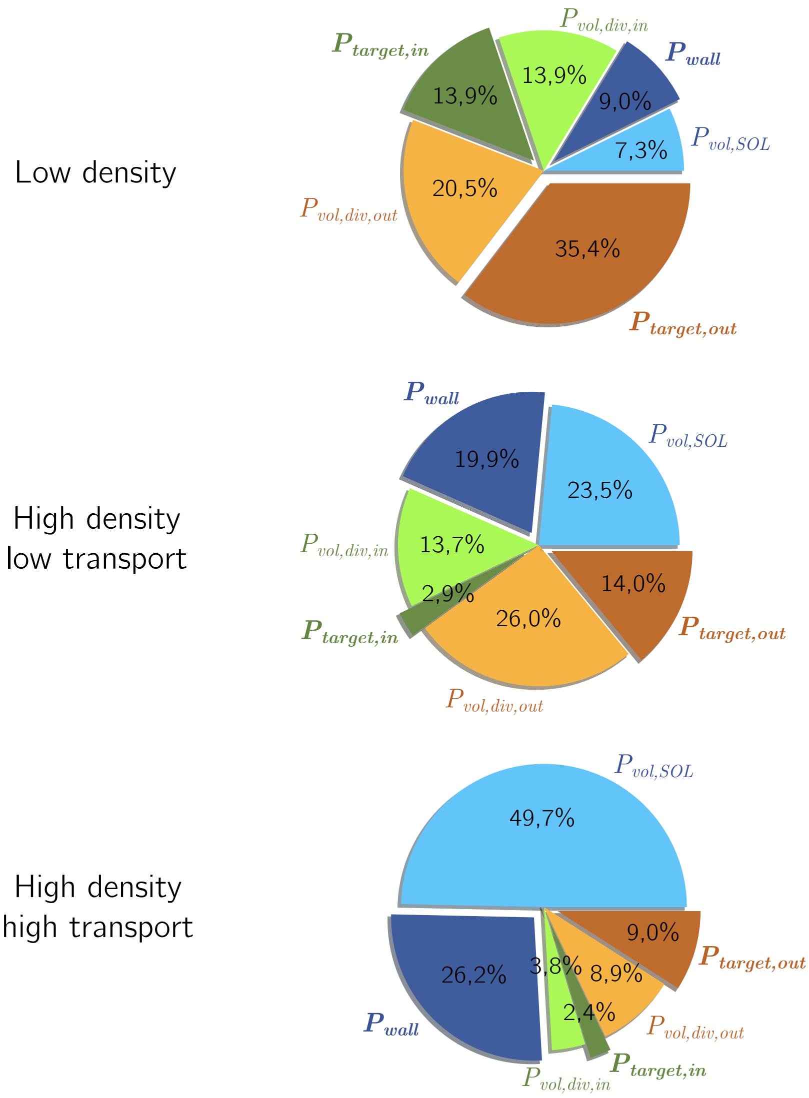

Figure 6.35: Global power balances for the SOL plasma.

At high density a quite smaller fraction of the input power reaches the divertor targets. This can be quantified through the *power loss factor* f_{power}. This is defined, according to the two-point model (cfr. Section 2.2.2), as the total fraction of the input power being dissipated in some way before reaching the targets. This, calculated for each case as

$$f_{power} \equiv 1 - \frac{P_{target,\,in} + P_{target,\,out}}{P_{SOL}} \tag{6.18}$$

gives as result:

- $f_{power} = 0{,}51$ for the low density case.
- $f_{power} = 0{,}83$ for the high density, low transport case.
- $f_{power} = 0{,}89$ for the high density, high transport case.

In the two high density cases, without and with enhanced transport, the calculated values of f_{power} are quite similar and larger than in the low density case. So, differently from the case of momentum losses, a more highly dissipative regime is achieved mainly with the mere increase of density regime, rather than with the enhancement of perpendicular transport itself.

The difference between the two high density cases can be found in the particular distribution of these volumetric losses: in the high transport case, in fact, such losses are concentrated mainly above the X-point rather than below it, which can be inferred be the strong increase of the $P_{vol,\,SOL}$ fraction. This is consistent the ionization front being moved more at upstream (cfr. Fig. 6.30). Namely, this feature would result from a relevant fraction of the neutrals recycled at the targets being ionized above the X-point; this could be motivated by the stronger cooling down of the divertor region occurring in the high transport case.

In particular, the difference in the fraction of the total input power which does not reach the targets anymore transiting from one high density case to the other (about 6%) corresponds exactly to the increase in the fraction which reaches the wall. Therefore, the total volumetric power losses in the two high density cases are basically the same: they are only "moved" more at upstream.

These results can be regarded as a further confirmation of the achievement of a highly dissipative regime in conditions similar to the simulated ones (being, however, not so affected by the enhancement of perpendicular transport). Nevertheless, the feature of the ionization front moved above the X-point at high transport (and the consequent radiation being concentrated in a region closer to the core plasma) could also lead to detrimental instability effects for the core plasma, which should be investigated in more detail.

6.3.3 Mechanisms for momentum and power dissipation

Finally, after having well established the simulated degrees of momentum and power dissipation in the various scenarios, it was investigated the relative importance of the various *dissipation mechanisms* in the divertor region.

Performing such an analysis with the results of a complex modelling tool such as SOLPS-ITER was not straightforward, due to the large number of physical components included in the transport equations, as well as the presence of the interaction with the neutrals. For doing this a two-point approach was considered, relating the plasma parameters at the target with those found at the X-point, through deriving two-point relations from the fluid equations solved by B2.5 (cfr. Section C.2.4).

For this aim, the treatment presented in [79] was considered. In this work integral relations for the momentum and power balances between two poloidal positions were derived; namely, the fluid equations solved by B2.5 were integrated between such two poloidal locations, assuming a

steady-state situation (i.e. assuming the numerical convergence being reached).
Here, the derivation of the equations is briefly summarized. Because of the mapping of the curvilinear poloidal and radial coordinates (θ, r) in an orthogonal system (x, y) performed by B2.5, the use of *metric coefficients* h_x, h_y, h_z is necessary for writing the balance equations. Here, it is sufficient to recall that the quantity $\sqrt{g} \equiv h_x h_y h_z$ represents the jacobian of the coordinate transformation between the two systems. More detail about the use of metric coefficient can be found in the Appendix C.2.2.

A *momentum balance* between the X-point and the target can be obtained starting from the steady-state form of the parallel momentum balance equation solved by B2.5 (eq. (C.52)). This can be written in a compact form as

$$\frac{1}{\sqrt{g}}\frac{\partial}{\partial x}\left(\frac{\sqrt{g}}{h_x}\pi_x\right) + \frac{1}{\sqrt{g}}\frac{\partial}{\partial y}\left(\frac{\sqrt{g}}{h_y}\pi_y\right) = -\frac{B_\theta}{B}\frac{1}{h_x}\frac{\partial p}{\partial x} + S_{mom,\, vol} \tag{6.19}$$

where

- π_x is the *poloidal momentum flux density* (eq. (C.59)).
- π_y is the *radial momentum flux density* (eq. (C.60)).
- $p \equiv n_e(T_e + T_i)$ is the *static pressure.*
- $S_{mom,\, vol}$ is the *volumetric momentum source density*, including the source evaluated by the fluid module (i.e. by thermal and friction forces), the source due to plasma-neutrals interactions (ion-neutral collisions and ionizations) and the source due to recombinations.

The quantity for which an integral balance equation is desired is

$$\frac{B_\theta}{B}A_x(p + m_i n_e v_\parallel^2) \tag{6.20}$$

which is the poloidal projection of the total pressure force acting in parallel direction along a given flux tube, in N. After some calculations, the eq. (6.19) can be written isolating the term describing the poloidal momentum balance, i.e. as

$$\frac{1}{\sqrt{g}}\frac{\partial}{\partial x}\left[\frac{\sqrt{g}}{h_x}\frac{B_\theta}{B}(p + m_i n_e v_\parallel^2)\right] = S_{mom,\, tot} \tag{6.21}$$

Here, $S_{mom,\, tot}$ represents the total volumetric momentum source density while travelling from the X-point to the target, including separately the various momentum loss mechanisms, and is writable as

$$\begin{aligned} S_{mom,\, tot} = {} & \frac{1}{\sqrt{g}}\frac{\partial}{\partial x}\left(\frac{\sqrt{g}}{h_x^2}\eta_{x,i}\frac{\partial v_\parallel}{\partial x}\right) + \frac{1}{\sqrt{g}}\frac{\partial}{\partial y}\left(\frac{\sqrt{g}}{h_y^2}\eta_{y,i}\frac{\partial v_\parallel}{\partial y}\right) \\ & - \frac{1}{\sqrt{g}}\frac{\partial}{\partial y}\left(\frac{\sqrt{g}}{h_x}m_i \Gamma_y v_\parallel\right) + p\frac{1}{\sqrt{g}}\frac{\partial}{\partial x}\left(\frac{\sqrt{g}}{h_x}\frac{B_\theta}{B}\right) + S_{mom,\, vol} \end{aligned} \tag{6.22}$$

In this way all the various momentum loss mechanisms appear as separate. Following the order in which these appear in the eq. (6.22), they can be listed as due to *poloidal viscosity*, *radial viscosity*, *radial momentum transport*, *flux expansion* and *volumetric processes.*
Integrating the eq. (6.21) finally yields the momentum balance equation from the X-point to the target as

$$\left[\frac{B_\theta}{B}A_x(p + m_i n_e v_\parallel^2)\right]_{\text{target}} - \left[\frac{B_\theta}{B}A_x(p + m_i n_e v_\parallel^2)\right]_{\text{X-point}} = \int_{\text{X-point}}^{\text{target}} S_{mom,\, tot}\, h_x A_x \, dx \tag{6.23}$$

The results of such momentum balance are shown in the figures at the next page for all the cases, considering as usual the outer divertor. At the left side, the eq. (6.23) is plotted for all the cases: the integrated momentum loss from the X-point to the target is equal to the difference of the quantity (6.20) between target and X-point. At the right side, the integrated momentum loss term is decomposed, showing the positive momentum sources and the negative momentum sinks for each flux tube, in order to show the relative importance of each loss mechanism.

For the low density case, as expected, there are almost no momentum losses between the X-point and the target, apart from near the separatrix (mainly due to particle transport in the private flux region). In other locations of the near SOL, the pressure at the target is even larger than at the X-point. This gain is mainly via poloidal viscosity, which could be motivated by the already revealed presence of flow reversal in this region (cfr. Fig. 6.23). Losses from plasma-neutrals interactions and recombination processes are quite low everywhere (apart, again, from near the separatrix), due to the large temperatures and the poor neutral population in this case (cfr. Figs. 6.28, 6.31).

At high density, instead, much stronger momentum losses are visible, with these being even more larger after transport enhancement. At low transport relevant momentum losses are still concentrated in the near SOL; at high transport, instead, they are relevant everywhere. Moreover, the pressure peak at the target in the last case is visibly radially shifted to the far SOL, making the momentum losses in the flux tubes near the separatrix more accentuated. For both high density cases, in each flux tube a strong momentum removal is due to the plasma-neutrals interactions plus recombinations; this was expected since in these cases the neutral density is large enough and the temperature is low enough to promote these mechanisms (cfr. Figs. 6.28, 6.31).

The radial momentum transport mechanism (i.e. including the momentum sources/sinks from each flux tube due to the momentum directly removed or gained via radial particle transport) is quite negligible for a net momentum balance in any flux tube, also in the high transport case. Nevertheless, in this last case, it implies a non negligible redistribution of momentum from the near SOL to the far SOL. It cannot be excluded then that this feature, which was quite negligible at low transport, could have played some role (even if not dominant) in achieving the detachment, which was indeed observed only in the near SOL after the transport enhancement.

Finally, the same kind of analysis was performed for achieving a *power balance*, starting from the steady-state form of the energy balance equations solved by B2.5 (eqs. (C.55), (C.56)). Summing these two yields

$$\frac{1}{\sqrt{g}}\frac{\partial}{\partial x}\left(\frac{\sqrt{g}}{h_x}q_x\right)+\frac{1}{\sqrt{g}}\frac{\partial}{\partial y}\left(\frac{\sqrt{g}}{h_y}q_y\right)=S_{en,\,vol} \tag{6.24}$$

where

- q_x is the *poloidal energy flux density* (eq. (C.61)).
- q_y is the *radial energy flux density* (eq. (C.62)).
- $S_{en,\,vol}$ is the *volumetric energy source density*, including the source evaluated by the fluid code (i.e. by viscous heating, inter-species friction, radiation losses etc.), the source due to plasma-neutrals interactions (ion-neutral collisions and ionizations) and the source due to recombinations.

In this case, the achievement of the desired integral balance equation is straightforward, as the quantity for which an such a balance equation is desired is

$$A_x q_x \tag{6.25}$$

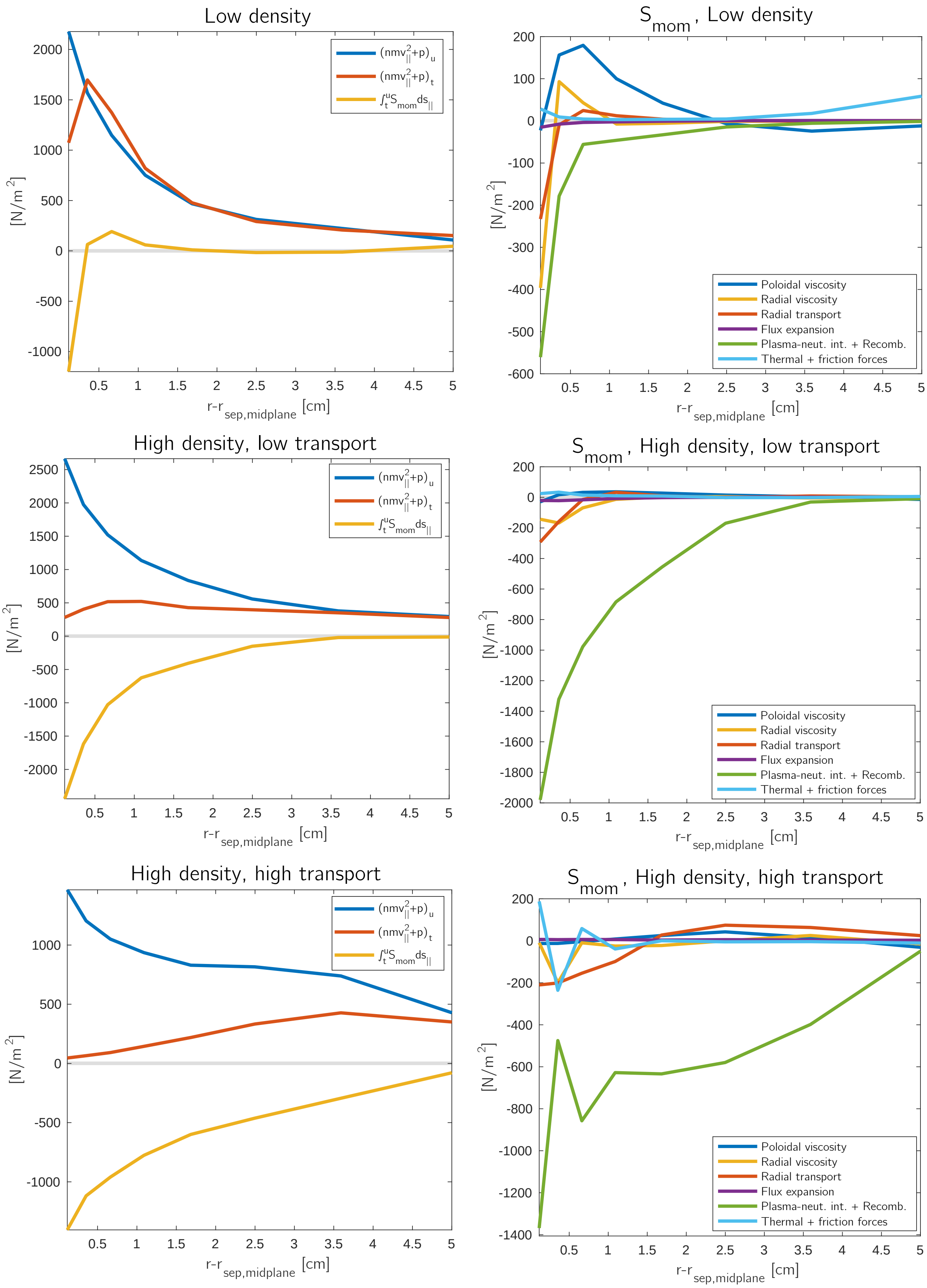

Figure 6.36: Momentum balances for each flux tube. Left plots show the radial profiles of the total pressure at the X-point and at the target, with difference between these being the poloidally integrated momentum source, with decomposition of this shown in the right plots. Each term of the eq. (6.23) is divided by the value of $\frac{B_\theta}{B} A_x$ taken at the target.

which is just the total energy flowing in poloidal direction along a given flux tube per unit time, in W. So, the term describing the poloidal energy balance is simply isolated as

$$\frac{1}{\sqrt{g}}\frac{\partial}{\partial x}\left(\frac{\sqrt{g}}{h_x}q_x\right) = S_{en,\,tot} \tag{6.26}$$

Similarly as for the momentum case, $S_{en,\,tot}$ represents the total volumetric energy source density while travelling from the X-point to the target, and is writable as

$$S_{en,\,tot} = -\frac{1}{\sqrt{g}}\frac{\partial}{\partial y}\left(\frac{\sqrt{g}}{h_y}q_y\right) + S_{en,\,vol} \tag{6.27}$$

i.e. as simply following from *radial energy transport* and *volumetric processes.*
Similarly as before, integrating the eq. (A.62) yields the energy balance equation from the X-point to the target as

$$[A_x q_x]_{\text{target}} - [A_x q_x]_{\text{X-point}} = \int_{\text{X-point}}^{\text{target}} S_{en,\,tot}\, h_x A_x \, dx \tag{6.28}$$

The results of such energy balance are shown in the figures at the next page for all the cases, still considering the outer divertor. Again, at the left side, the eq. (6.28) is plotted for all the cases: the integrated energy loss from the X-point to the target is equal to the difference of the quantity (6.25) between target and X-point. At the right side, the integrated energy loss term is decomposed, showing the positive energy sources and the negative energy sinks for each flux tube, in order to show the relative importance of each loss mechanism.
For the low density case a weakly dissipative regime can be recognized, consistently with the previously discussed results: the peak energy flux at the target is, in fact, still close to the separatrix, and has a quite large value. Only in the flux tubes near the separatrix relevant power dissipation takes place; this is mostly due to radial energy transport into the private flux region (caused by the presence of a strong radially inward directed temperature gradient at the target, cfr. Fig. 6.24b). Plasma-neutrals interactions and recombination processes give a weak contribute to the power dissipation, as expected.
At high density, instead, a highly dissipative regime is recognizable. Both high density cases are characterized by strong energy losses everywhere and by an incident energy flux onto the target drastically dropped. As expected, these losses are dominated by plasma-neutrals interactions and recombination processes, because of a large neutral population and a lower temperature in these cases (cfr. Figs. 6.28, 6.31). Instead, the effect of radial energy transport into the private flux region is not evident anymore, because of the divertor temperatures presenting more flattened radial profiles (cfr. Fig. 6.24b). Consistently with the previously shown global power balance (cfr. Section 6.3.2), the relative degree of power dissipation is similar between the cases without and with enhanced transport: in both these cases, in fact, the energy flux pattern at the target is strongly flattened and its peak value is visibly radially shifted from the separatrix. The main difference is that, at high transport, the energy flux density is quite small already at the X-point; this is consistent with the revealed features of more power being radially transported to the wall at the midplane and more power being radiated also above the X-point. This makes the absolute values of the energy flux density at the target quite smaller in the high transport case, despite the same relative degree of power dissipation in the divertor region.
Finally, the radial energy transport mechanism does not contribute much to a net power dissipation in any flux tube. However, similarly to what occurs for the momentum balance, in the high transport case a non negligible redistribution of energy to the near SOL to the far SOL can be seen. This contributes further to radially shift even more the peak value at the target.

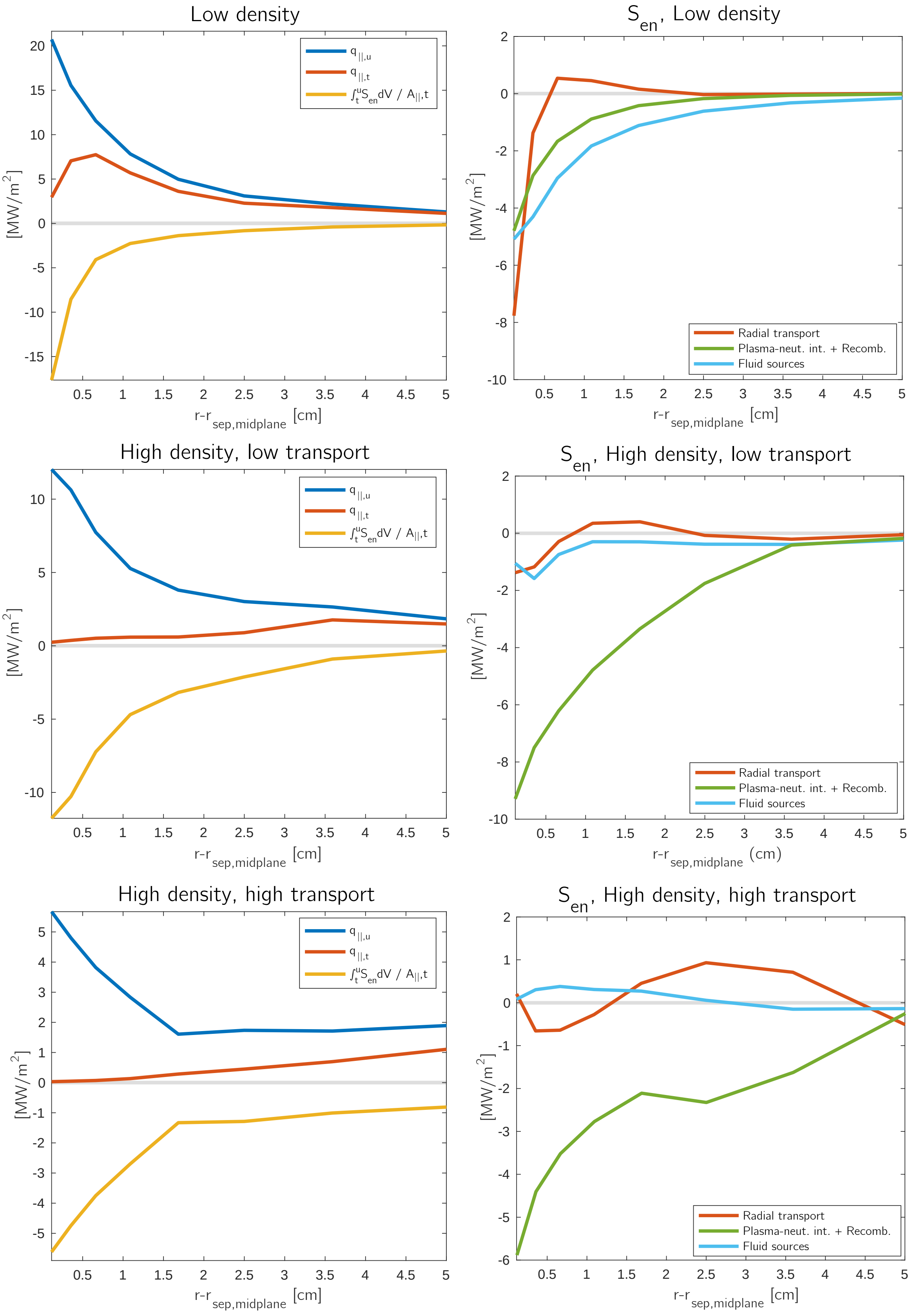

Figure 6.37: Power balances for each flux tube. Left plots show the radial profiles of the energy flux patterns at the X-point and at the target, with difference between these being the poloidally integrated energy source, with decomposition of this shown in the right plots. Each term of the eq. (6.28) is divided by the value of $\frac{B_\theta}{B}A_x$ taken at the target, so that the lines in the left plots effectively correspond to parallel energy flux densities (i.e. per unit of parallel area at the target).

Summarizing, from the performed quantitative analysis of momentum and power dissipation in the divertor it was confirmed that the enhancement of perpendicular transport at the midplane does play a role in achieving a highly dissipative regime:

- Regarding momentum dissipation, stronger momentum losses is observed mainly with enhanced transport. This can be motivated by a strong cooling down of the divertor region, because of a larger fraction of power radially transported to the wall at the midplane. The low temperature, in turn, promotes the existence of a large neutral population. In this way, momentum-removal processes (i.e. CX collisions and recombination processes) become sufficiently relevant to induce the detachment. In addition, a stronger radial momentum transport arises as a possible explanation for even more accentuated momentum losses in the near SOL. This features probably contributes in a decisive way to induce the detachment in this region.
- Regarding power dissipation, instead, the relative magnitude of power-removal processes in the divertor is not much affected by the enhanced transport. A large power dissipation, in fact, is already achieved after the mere increase of the density regime. Less power reaching the target at high transport is, indeed, simply induced by much more power removed from the plasma even before entering the divertor region. Again, the reason for this is a larger fraction of power radially transported to the wall at the midplane. Consequently, the ionization front the recycled neutrals is moved quite far from the targets.

Chapter 7

Conclusions and outlook

The extensive analysis performed in this work allowed characterizing thoroughly the impact of enhancing radial blob propagation in the scrape-off layer, occurring at high divertor collisionality (i.e. at high density), on the particle and power exhaust processes in the divertor. The simulations, performed with the SOLPS-ITER code package, provided quite realistic results, despite the imposition of some simplifications. This allowed to formulate reliable general conclusion on this topic.

A pure deuterium plasma was modelled, neglecting impurities, drifts and currents. All the simulations were performed as coupled runs, i.e. with the kinetic module for the neutrals, EIRENE, activated.
An experimental scenario, consisting of an L-mode discharge of the ASDEX Upgrade tokamak, exhibiting enhanced perpendicular transport at the outer SOL midplane, was reproduced numerically. The underlying physical process which drives such transport, i.e. radial blob propagation, is not diffusive. Nevertheless, an "effective" particle diffusivity, which averages an intermittently enhanced transport on a sufficiently long time scale, had to be imposed on the numerical side for modelling such a highly anomalous transport. Assuming a diffusive transport was indeed necessary as SOLPS-ITER computes the radial particle transport in a purely diffusive approximation.
Imposing extremely high values of such a coefficient in the near SOL was required for correctly reproducing the experimental measurements. In particular, average values of $15 - 20$ m^2/s, with a peak value of almost 40 m^2/s (more than one order of magnitude larger than the Bohm diffusivity) had to be used. Some theoretical considerations, however, corroborate the choice of an effective particle diffusivity for modelling this transport. These suggest that, for reducing the radial transport of convective structures like blobs to a diffusive limit, using precisely such values of an effective particle diffusivity, i.e. of the order of some tens of m^2/s, is indeed required.

According to the simulations results, the most direct consequence of the transport enhancement is a relevant increase of radial particle transport at the midplane. This, in turn, increases the radial heat transport as well: this is seen to be mainly driven by a convective component, as particles carry heat with them in their enhanced radial transport. This leads to a large fraction of the SOL input power still present at the midplane even several cm away from the separatrix, prevailing over the parallel losses. Ultimately, this implies a non negligible increase of the power being radially transported towards the main chamber wall: in particular, this is observed to be almost 30% of the entire SOL input power.
In addition to this, the formation of a density shoulder, observed in the experiment, was also successfully reproduced. This arises as a side effect of the enhanced perpendicular transport. The

simulations results seemed to confirm the assumption, currently proposed in the literature, for the mechanism responsible for the shoulder formation. Namely, it was seen that a particle source by ionization is required for providing a sufficient number of plasma particles to balance the parallel losses and produce a flattening of the radial density profile at the midplane. It was then concluded that the link between the enhancement of perpendicular transport and the shoulder formation is given by the increase of the radial heat transport: this, in fact, contributes to bring a sufficient amount of energy in the far SOL for sustaining an increased ionization rate.
Finally, the simulations seemed also to suggest that, despite the increase of particles reaching the main chamber wall, recycling at the wall surfaces may not be a dominant mechanism in providing the neutrals which are ionized to form the shoulder. This is in contrast with other experimental and numerical results. In fact, SOLPS-ITER is not much reliable in modelling the interaction of the plasma with the main chamber wall, since the computational grid cannot be extended up to the physical wall of the device. Therefore, this cannot be considered as a definitive conclusion.

A highly dissipative regime, occurring at high density, was also successfully achieved in the simulations. A drastic drop of the power reaching the divertor targets and the achievement of a partial detachment in the near-separatrix region of the outer target were observed, in agreement with the experimental results.
A quantitative analysis of momentum and power dissipation in the divertor was performed. Three different scenarios, i.e. an actual low density case, a fictitious high density, low transport case, and an actual high density, high transport case, were considered. The aim was to discriminate the consequences which purely arise from transport enhancement from the consequences which arise after the mere increase of the density regime. In this way, the role played by the enhanced perpendicular transport in achieving such a highly dissipative regime could be clarified.
For the momentum dissipation, a strong increase of the pressure drop in the divertor was observed at high density, mainly arising after the transport enhancement. This can be explained by the divertor region being sufficiently cooled down in this case, because of more power radially transported to the wall at the midplane. In this way, momentum-removal processes (i.e. CX collisions and volumetric recombination) become sufficiently relevant to induce the detachment. In addition to this, after the transport enhancement, a stronger radial momentum transport was observed as well. This is a possible explanation for an even more accentuated pressure drop in the near-separatrix region, because of a redistribution of momentum to the far SOL. This has likely contributed in a decisive way to induce the detachment on the near-separatrix portion of the outer target.
For the power dissipation, instead, the relative intensity of power-removal processes in the divertor was seen to be not much affected by the transport enhancement. A highly dissipative regime was, indeed, already achieved after the mere increase of the density regime. Less power reaching the target at high transport can be explained by more power dissipated even before entering the divertor region. The direct reason for this is, again, more power radially transported to the wall at the midplane. Moreover, the consequent cooling down of the near-target region was seen to contribute to move the ionization front of the recycled neutrals further away from the targets. This leads to even more power radiated above the X-point rather than below it.

Although the achieved results were in a satisfyingly good agreement with the experimental results, further simulation efforts should be devoted to improve these results.
Firstly, drifts and currents in the transport equations solved by SOLPS-ITER could be fully activated, despite this would imply a much more complicate setup for the simulations. In this way, the parallel flows could be modelled in a more reliably way, and so consequently also

the conditions in the divertor region, allowing to investigate further features such as eventual asymmetries between inner and outer divertor.

Furthermore, more accurate results regarding the interaction between the plasma and main chamber wall could be obtained in the near future, as soon as SOLPS-ITER will allow using a computational grid that extends up to the physical wall of the device. This could allow to achieve more realistic results about main chamber recycling as well.

Both experimental and numerical results concerning the research topic of perpendicular transport in the scrape-off layer are of critical importance for predicting the operation of future fusion devices. The recently developed filamentary transport model, in which the divertor collisionality acts as the only control parameter, was, indeed, experimentally shown to be valid on more currently operating devices, i.e. on both ASDEX Upgrade and JET. Future devices such as ITER and DEMO will be characterized by a magnetic configuration similar to these. Therefore, they could be expected to achieve an enhanced transport regime as well: in fact, the high-density operations planned for these for sure will bring them to work at high divertor collisionality.

The combination of the existing experimental results and the numerical results achieved in this work led to the individuation of a number of potential consequences, both beneficial and detrimental:

- By increasing the radial particle flux into the far SOL, and thus increasing both number of ions striking the wall and power reaching it, main wall sputtering could be seriously increased. The consequences for ITER could be dramatic as its wall is expected to be made of beryllium which, differently from tungsten, is a low-Z material. This strongly motivates further research effort about possible erosion effects on the main chamber wall at conditions similar to those which where studied in this thesis.
- By increasing the power losses along the SOL, due to more power radially transported to the wall at the midplane, a significant decrease of the peak heat loads onto the targets could be obtained. The general decrease of the divertor temperatures, indeed, could likely promote a detached regime. This result clearly arises from the performed simulations, and implies the probable achievement of an at least partial detachment in ITER at its expected plasma conditions, which is precisely the desired operational regime for it.

Both these features should be considered both in planning ITER operations and in performing the design of DEMO, with the goal of optimizing the lifetime of the plasma-facing materials (for both main chamber wall and divertor targets) in such devices.

Appendices

Appendix A

Useful concepts of plasma physics

In this appendix the concepts of plasma physics which are useful for a full comprehension of this thesis will be briefly summarized, together with the references to more general textbooks devoted to this topic. In particular, in the Section A.1 the most basic quantities defining a plasma will be defined, and some of the most peculiar and interesting phenomena occurring in a plasma will be explained. Then, in the Section A.2, the topic of magnetic confinement of a plasma will be addressed, focusing in particular to the confinement of toroidal plasmas which are of interest for current magnetic fusion research. After that, in the Section A.3 some useful concepts and results about macroscopic transport processes in magnetically confined plasmas, namely collisional processes and turbulence, will be presented. Finally, in Section A.4 the simple power balance for a fusion plasma, which was presented in the text, will be rigorously deduced, together with the formal definition of the various related quantities.

A.1 Basic plasma properties

Matter in state of *plasma* is defined as a ionized gas, which constitute the greatest part of matter in the universe [1][26]. Such state of matter exists a sufficiently high temperature so that some neutral atoms turn out to possess enough thermal energy to ionize, giving rise to a quite large concentration of positively charged *ions* and negatively charged *electrons* besides neutrals. A plasma state in *thermodynamic equilibrium* can be determined only by its composition, density of constituents and temperature. So, considering a *simple plasma*, constituted by neutral atoms, single-valence ions of the same type and electrons (therefore with all charged particles having charge $\pm e$), its equilibrium state can be fully defined by a *maxwellian distribution function* [26], giving both the average energy of particles and their velocity distribution. Anyway, often a plasma is only in partial equilibrium, meaning that distributions of velocities of ions and electrons are both maxwellian, but with different temperature scales. So, we have a separate equilibrium between these, and we need to define separately an ion temperature and an electron temperature.

A.1.1 Plasma quasi-neutrality

Since a plasma is constituted by charged particles, each of these will generate an electric potential distribution $\Phi(r)$ around them, evaluable by solving the Poisson equation [104]

$$\nabla^2\Phi = \frac{\rho}{\varepsilon_0} = \frac{e}{\varepsilon_0}(n_i - n_e) \tag{A.1}$$

where $e(n_e - n_i)$ is the net charge density existing around the particle, arising since this attracts opposite charges and repels equal charges. Considering an equilibrium situation, the equation

(A.1) can be integrated to obtain a rapidly decaying potential with trend

$$\Phi(r) \propto \frac{1}{r} e^{-r/\lambda_D} \tag{A.2}$$

where λ_D is called *Debye length*.
It occurs that, far from the particle, its potential is "shielded" as a consequences of particles with opposite charge which get to be present around it, so that any electric field generated by the particles is nearly suppressed over distances of the order of λ_D. In particular, for electrons and ions, this length is calculated to be [1]

$$\lambda_{D_{ei}} = \sqrt{\frac{\varepsilon_0 T_{ei}}{e^2 n_0}} \tag{A.3}$$

where n_0 is the "unperturbed" plasma density. For usual fusion plasmas having a temperature about $15 - 20$ keV, this length is of the order of $7 \cdot 10^{-5}$ m, meaning that internal electric fields are effectively shielded over distance comparable to reactor scales.

It can be concluded that the main characteristic of plasmas is their macroscopic neutrality due to the compensation of all the positive and negative charges, and the shielding of internal electric field over large distances. This, however, becomes not true anymore for length scales of the order of the Debye length, at which the effects of the presence of charged particles must be taken into account. Such condition in a plasma is usually referred to as *quasi-neutrality*.

A.1.2 Single particle motion

However, although a plasma is a macroscopically neutral medium, its charged particles are still subjected to the effect of an external electromagnetic field.

In particular, in presence of an externally induced magnetic field $\boldsymbol{B}$, the charged particles of species α constituting the plasma will be subject to the *Lorentz force* [104]

$$\boldsymbol{F} = q_\alpha \boldsymbol{v}_\alpha \times \boldsymbol{B} \tag{A.4}$$

where q_α is the charge of the particles (equal to $-e$ for the electrons and $+e$ for the ions, in case of a simple plasma).
The most basic single-particle behavior could be deduced by considering charged particles moving in an external magnetic field, supposed straight, uniform and constant. Solving the equations of motion as resulting from the Lorentz force (A.4), in the framework of the so-called *orbit theory* [1], that, because of the Lorentz force, charged particles in a magnetized plasma will move along the magnetic field lines, encircling them on a small circular orbit (Fig. A.1); the particles are then said to "gyrate" around the field lines, in a uniform circular motion whose radius is called *gyroradius*, given by

$$\rho_\alpha = \frac{m_\alpha v_{\perp\alpha}}{|q_\alpha| B} \tag{A.5}$$

where B is the magnitude of the external field, m_α, q_α are the mass and the charge of the particles of the species α and $v_\perp$ is their perpendicular velocity with respect to the field direction. For usual fusion plasmas, having a temperature about $15 - 20$ keV, in a magnetic field of about 5 T, this radius is about $8 \cdot 10^{-5}$ m for electrons and $5 \cdot 10^{-3}$ m for ions, meaning that the "deviation" of particle motion with respect the path of magnetic field lines keeps very small. The frequency of this motion, then, is called *gyrofrequency*, and is given by

$$\Omega_\alpha = \frac{|q_\alpha| B}{m_\alpha} \tag{A.6}$$

For this reason, if a plasma is subject to an externally induced magnetic field, all its particles will follow the magnetic field lines, making the general plasma behavior mainly influenced by the long-range effects induced by an external field, rather than by single-particle interactions, much differently from a neutral gas.

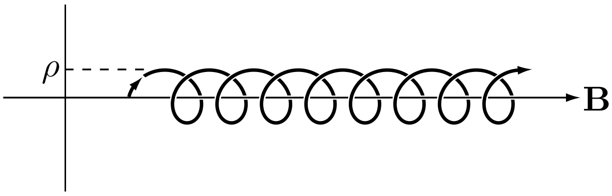

Figure A.1: Helical trajectory of a charged particle along a magnetic field line. Taken from [1].

In a more general description, including for example eventual gradients of the magnetic field, curvature of the field lines, or the presence of an external electric field, the characterization of the charged particle motion becomes far more complicate, and several *drift motions* (with respect to the simple translation of the center of the gyromotion parallel to the magnetic field lines) arise. For example if, in addition to a straight, uniform and constant magnetic field, charged particles are also subjected to a generally directed uniform and constant electric field $\boldsymbol{E}$, the Lorentz force assumes is most general form [104]

$$\boldsymbol{F} = q_\alpha(\boldsymbol{E} + \boldsymbol{v}_\alpha \times \boldsymbol{B}) \tag{A.7}$$

Now, solving the equations of motion [1] leads to an uniformly accelerated motion along the direction of the magnetic field, due to the component of $\boldsymbol{E}$ parallel to $\boldsymbol{B}$, while on a plane orthogonal to $\boldsymbol{B}$ we have, in addition to the gyromotion, a constant drift motion of the center of the gyration circle (usually named guiding center) in a direction perpendicular to both $\boldsymbol{E}$, $\boldsymbol{B}$, usually named $\boldsymbol{E} \times \boldsymbol{B}$ *drift*, with a velocity

$$\boldsymbol{v}_E = \frac{\boldsymbol{E} \times \boldsymbol{B}}{B^2} \tag{A.8}$$

However, in addition to this, several types of drift motions of the guiding center, which sum to the gyromotion along magnetic field lines, arise in more general situations, including curvature of magnetic field lines (*curvature drift*), non-uniform fields (∇B *drift*) and non-constant fields (*polarization drift*) [1].

A.1.3 Collisions in plasmas

Apart from long-range interactions occurring in a plasma, another fundamental feature is given by the *collisions* taking place between charged particles. In fact, despite macroscopically a plasma could be considered as quasi-neutral, being the total number of negative charges approximately equal to the total number positive charges, on a microscopic level (at distances of the order of the Debye length or less) charges are not shielded, so that each particle interacts with the other one through *coulomb interactions*. These cause deviations in the motion of single particles, and in addition momentum and energy can be exchanged between particles; such phenomena give rise overall to *transport processes* occurring on a macroscopic level (cfr. Section A.3).

The calculation of the rate with which collisions occur is very complicate, first of all because microscopic electric fields generated by the single particles must be considered for calculating the cross sections for coulomb interactions; secondly, because collisions depend also on the relative velocities of particles, so that the overall collision rate must be found by integrating the effects

of collisions at any relative velocity.
Assuming a Rutherford cross section for coulomb collisions [104], and performing the integration over the relative velocity assuming a maxwellian distribution of velocities for electrons and ions [26], it can be shown [2] that the *collision times* for electrons and ions, in s, stating the average time passing between two consecutive collisions, are respectively

$$\tau_e = 3(2\pi)^{3/2}\varepsilon_0^2 \frac{m_e^{1/2} T_e^{3/2}}{nZ^2 e^4 \ln\Lambda} \approx 3{,}44 \cdot 10^{11} \, \frac{T_e^{3/2}}{nZ^2 \ln\Lambda} \tag{A.9}$$

$$\tau_i = 12\pi^{3/2}\varepsilon_0^2 \frac{m_i^{1/2} T_i^{3/2}}{nZ^4 e^4 \ln\Lambda} \approx 2{,}09 \cdot 10^{13} \, \frac{m_i^{1/2} T_i^{3/2}}{nZ^4 \ln\Lambda} \tag{A.10}$$

in which the temperatures are expressed in eV, where Z is the charge of ions in the plasma, and $\ln\Lambda$ is the so-called *coulomb logarithm*, which for fusion-related plasmas lies between 15 and 20. We could note that both times scale as $T^{3/2}$, meaning that hotter is the plasma, and more rarely collisions between particles occur; this could be simply explained noting that larger temperatures correspond to larger thermal velocities of the particles: as they travel faster, then, less is the time in which one particle can stay close enough to another one to "feel" the electric force exerted by the microscopic field produced by the latter. Moreover, the ratio τ_e/τ_i of these times is of the order $(m_e/m_i)^{1/2}$, reflecting the larger thermal velocity of electrons compared to ions, at a same temperature, since $m_e \ll m_i$.

One important consequence of collisions between particles is the net momentum and energy exchange between the two species of particles.
Regarding the momentum exchange, it occurs that if the electron and ion populations have different macroscopic velocities u_e, u_i, with collisions faster particles will tend to slow down, losing momentum, with slower particles gaining momentum. Such process can be characterized by a *momentum exchange time* defined by

$$\frac{du_i}{dt} = \frac{u_e - u_i}{\tau_{ei}} \tag{A.11}$$

which can be shown [2] to be

$$\tau_{ei} = \sqrt{2}\,\tau_e \tag{A.12}$$

Regarding, then, the energy exchange, similarly, if electrons and ions are initially at different temperatures, faster particles give energy to the slower ones via collisions, approaching then an equilibration in the overall thermal energy of the two species, lowering thus the temperature difference.
Such process can be characterized by a *thermalization time* τ_{th} defined by

$$\frac{dT_i}{dt} = \frac{T_e - T_i}{\tau_{th}} \tag{A.13}$$

which can be shown [2] to be

$$\tau_{th} = \frac{m_i}{2m_e}\tau_e \tag{A.14}$$

In the same way, instead of collision times, we could also make use of *collision frequencies* ν, in s^{-1}, for characterizing such processes, simply defined as the inverse of the former.

A.2 Magnetic plasma confinement

The main goal of magnetic fusion devices is to produce magnetic geometries which are capable of stably confining a sufficiently high-density plasma at a sufficiently high temperature for a sufficiently long time to produce net thermonuclear power. In particular, the macroscopic equilibrium and stability properties of such geometries can be described by means of a simple single-fluid model for the plasma, namely the *MHD (magnetohydrodynamics)* model [105]. Such model describes how magnetic, inertial and pressure forces interact within the plasma, and which magnetic geometry is capable to provide a stable plasma confinement.

A.2.1 MHD equations

For deducing the MHD equations is necessary to set up a global, despite being simplified, description of the plasma, involving a self-consistent model for a macroscopic number of charges particles, each one moving according the equations of motion for charges in electromagnetic fields. Globally, this requires the coupling of a fluid model for the plasma and the Maxwell equations. First of all, the two-fluid equations can be derived by taking the lowest moments of the distribution function f_α for each population of particles, which obey a Boltzmann equation (cfr. Appendix C.1.1), after closing the system with an opportune closure, in order to take into account the dynamics of particles belonging to a fluid system (cfr. Appendix C.1.2). Then, the system of equations which is obtained in this way is then coupled with the general set of Maxwell equations, in order to include also the dynamics of charged particles into electromagnetic fields.

Now, in order to simplify and close this general model, the following assumptions are done [105]:

- Some asymptotic approximation are introduced to eliminate the very high-frequency, short-wavelength information, which are not necessary for describing the macroscopic behavior of the plasma. Such approximation involve the subsistence of the global quasi-neutrality over the length scale of the plasma, supposed much larger than its Debye length, and the neglect of any macroscopic charge separation for the considered time scales, due to fast response of electrons after any perturbation of the local neutrality.
- The two-fluid balance equations are rewritten as a set of single-fluid equations by the introduction of single-fluid variables, common for both electrons and ions. This involves then an isothermal assumption for the electron and ion populations.

So, single-fluid conservation relations can be deduced by introducing a single *mass density* $\rho = m_i n$ where $n = n_e = n_i$ (having supposed $m_e \approx 0$), a single *macroscopic velocity* $\boldsymbol{v}$, and a single *temperature* $T = T_e = T_i$ (after the isothermal assumption), considering then a *kinetic pressure* given by $p = nT$. Then, Maxwell equation can be reduced to a simplified low-frequency long-wavelength form after the the first assumption. Finally, a closure for the system can be done by providing a constitutive equation relating the current density $\boldsymbol{J}$ with the electric field $\boldsymbol{E}$, which is in the form of a generalized Ohm law with η plasma resistivity.
The resulting final set of *MHD equations* will be constituted by [105]:

- *Global conservation relations*:

$$\begin{aligned} &\frac{d\rho}{dt} + \rho\nabla\cdot\boldsymbol{v} = 0 \\ &\rho\frac{d\boldsymbol{v}}{dt} + \nabla p = \boldsymbol{J}\times\boldsymbol{B} \\ &\frac{d}{dt}(p\rho^{-5/3}) = 0 \end{aligned} \tag{A.15}$$

- *Generalized Ohm law*:

$$\boldsymbol{E} + \boldsymbol{v} \times \boldsymbol{B} = \eta \boldsymbol{J} \tag{A.16}$$

- *Reduced Maxwell equations*:

$$\begin{aligned} \nabla \cdot \boldsymbol{B} &= 0 \\ \nabla \times \boldsymbol{E} &= -\frac{\partial \boldsymbol{B}}{\partial t} \\ \nabla \times \boldsymbol{B} &= \mu_0 \boldsymbol{J} \end{aligned} \tag{A.17}$$

Usually, a further approximation is done by considering the plasma a perfectly conducting medium (which is usually nearly the case for a fusion plasma), dropping then the resistivity and considering the Ohm law in the form $\boldsymbol{E} + \boldsymbol{v} \times \boldsymbol{B} = \boldsymbol{0}$. What we get then are usually called the *ideal MHD equations*.

A.2.2 Plasma equilibrium

The goal of solving the ideal MHD equations is the discovery of magnetic geometries which are able to confine and isolate a hot plasma from the material wall of the device.
In particular, *plasma equilibrium* can be achieved by finding a combination of external and internally induced magnetic fields which provide an exact balance of magnetic forces and pressure pushes, keeping the plasma in static equilibrium inside the vacuum chamber of the device.
For a toroidal plasma configuration, as we have in tokamaks, the need is to provide:

- A *radial pressure balance*, for opposing the uniform radial expansion of the plasma due to its internal heat (Fig. A.2a).
- A *toroidal force balance*, for opposing the effects of the toroidicity of the plasma, which generates horizontal forces which push it in radial outward direction (Fig. A.2b).

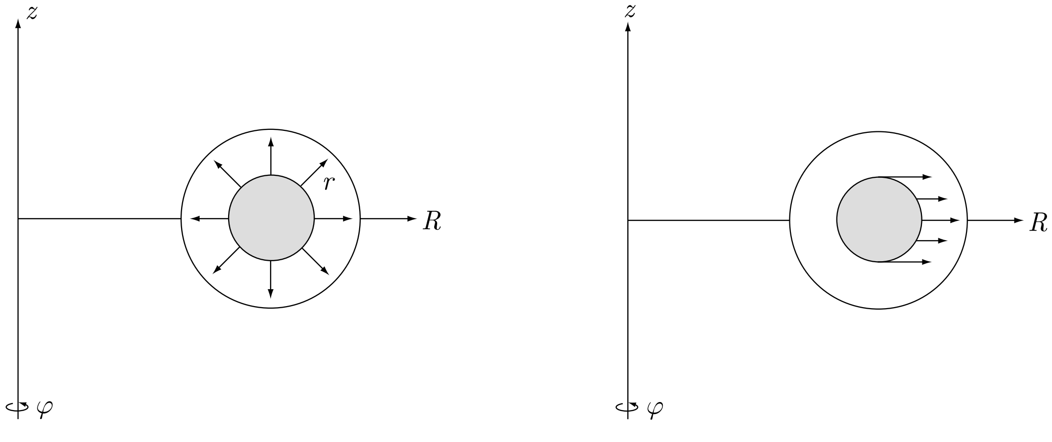

(a) Pressure expansion **(b)** Radial toroidal forces

Figure A.2: Internal forces which need to be balanced to provide plasma equilibrium. Taken from [1].

Thus, an adequate magnetic configuration should induce an internal radial pressure force, in order to keep the plasma compressed, and an inward directed toroidal force.

For the plasma to be in equilibrium, all the quantities in the MHD equations must be time-independent ($\frac{\partial}{\partial t} = 0$), and the plasma should be static ($\boldsymbol{v} = \boldsymbol{0}$). Thus, apart from the mass and energy balance equations (first one and third one of (A.15)), trivially satisfied in this case, the

Ohm law simply becomes $\boldsymbol{E} = \boldsymbol{0}$, implying that also the Faraday law (second one of (A.17)) is trivially satisfied. What remains constitute the *MHD equilibrium equations* [105]:

$$\begin{aligned} \boldsymbol{J} \times \boldsymbol{B} &= \nabla p \\ \nabla \times \boldsymbol{B} &= \mu_0 \boldsymbol{J} \\ \nabla \cdot \boldsymbol{B} &= 0 \end{aligned} \tag{A.18}$$

Thus, the external magnetic field applied to the plasma should generate a magnetic force density $\boldsymbol{F} = \boldsymbol{J} \times \boldsymbol{B}$ such that balanced the pressure-gradient-driven expansion force ∇p. Substituting the second and the third equations in (A.18) here allows to write this force as [105]

$$\boldsymbol{F} = \nabla : \left(\frac{\boldsymbol{B}\boldsymbol{B}}{\mu_0} \right) - \nabla \left(\frac{B^2}{2\mu_0} \right) \tag{A.19}$$

so that we are able to distinguish between the confining effects given by the *magnetic pressure* $\frac{B^2}{2\mu_0}$, due to the magnitude of the applied field, and the *magnetic tension* $\frac{\boldsymbol{B}\boldsymbol{B}}{\mu_0}$, due to the curvature of the lines of the applied field.

A.2.3 Equilibrium of toroidal plasmas

The equations (A.18) constitute a sufficient tool for dealing with the problem of calculating a magnetic geometry which confines the plasma in stable equilibrium in axisymmetric toroidal configuration, as we find in tokamaks.
A characteristic feature of toroidal confinement is the existence of *magnetic flux surfaces*, covered by magnetic field lines nesting around them, so that in a first approximation charged particles following the field lines stay on these toroidally closed surfaces, being then confined. In this sense, an index of the helicity of field lines around the magnetic surfaces is the so-called *safety factor* q, i.e. the numbers of toroidal transits completed during one poloidal rotation of a field line [2].

Equilibrium in an axisymmetric toroidal configuration can be deduced by solving the MHD equations in a proper coordinate system, where all the parameters and the magnetic field itself do not depend on the toroidal coordinate φ, in order to obtain an equilibrium configuration for the magnetic field which addresses for both radial pressure balance and toroidal force balance. The geometry in which the problem is addressed is schematized in the Fig. A.3.

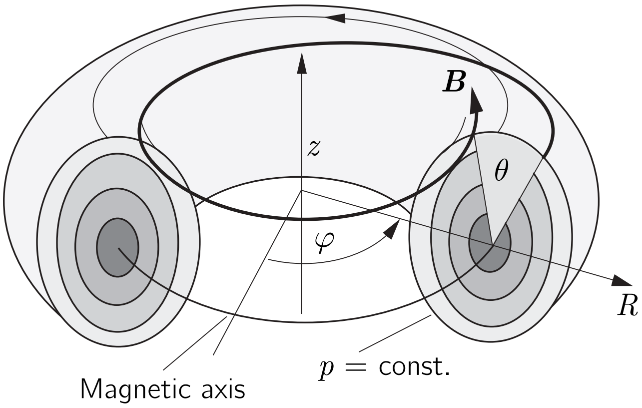

Figure A.3: Coordinates in toroidal geometry. Taken from [106].

Because of the toroidal symmetry, the resulting magnetic surfaces can be described by a flux function ψ of the type $\psi(R, z) = const.$, in a two-dimensional poloidal cross section. Since, from the first equation of (A.18) we have $\boldsymbol{B} \cdot \nabla p = 0$, magnetic surfaces defined in this way will be

also surfaces with constant pressure, so that $p = p(\psi)$.
An analytical relation for MHD equilibrium in such configuration can be derived by considering a flux function

$$\psi(R, z) = RA_\varphi \tag{A.20}$$

with A_φ toroidal component of the vector potential $\boldsymbol{A}$ of the magnetic field, such that $\boldsymbol{B} = \nabla \times \boldsymbol{A}$, and an auxiliary function

$$F(\psi) = RB_\varphi \tag{A.21}$$

In this way, the total magnetic field and the total plasma current (toroidal plus poloidal components) can be written as

$$\boldsymbol{B} = \frac{F}{R}\boldsymbol{e}_\varphi + \frac{1}{R}\nabla\psi \times \boldsymbol{e}_\varphi \tag{A.22}$$

$$\boldsymbol{J} = J_\varphi \boldsymbol{e}_\varphi + \frac{1}{\mu_0 R}\nabla F \times \boldsymbol{e}_\varphi \tag{A.23}$$

with $\boldsymbol{e}_\varphi$ unit vector in the toroidal direction. Substituting this expressions in the equilibrium equations (A.18) yields, after calculations, the partial differential equation for ψ

$$\Delta^*\psi = -\mu_0 R^2 \frac{dp}{d\psi} - F\frac{dF}{d\psi} \tag{A.24}$$

called *Grad-Shafranov equation* [107], where $\Delta^* \equiv R\frac{\partial}{\partial R}\left(\frac{1}{R}\frac{\partial}{\partial R}\right) + \frac{\partial^2}{\partial z^2}$. This has two free functions $p(\psi)$, $F(\psi)$, meaning that various equilibrium configurations can be found with different choices of such free functions, allowing to obtain different shapes for the poloidal cross section of the plasma.
In each case, solving the equation (A.24) yields a characteristic feature of any toroidal equilibrium profile: the nested magnetic surfaces are not concentric, being the magnetic axis displaced in direction of the major radius with respect to the geometric axis of the plasma. This feature, visible in the Fig. A.4, is called *Shafranov shift*, and the reason why current devices produce plasmas with elongated D-shaped poloidal cross sections is just to reduce such shift.

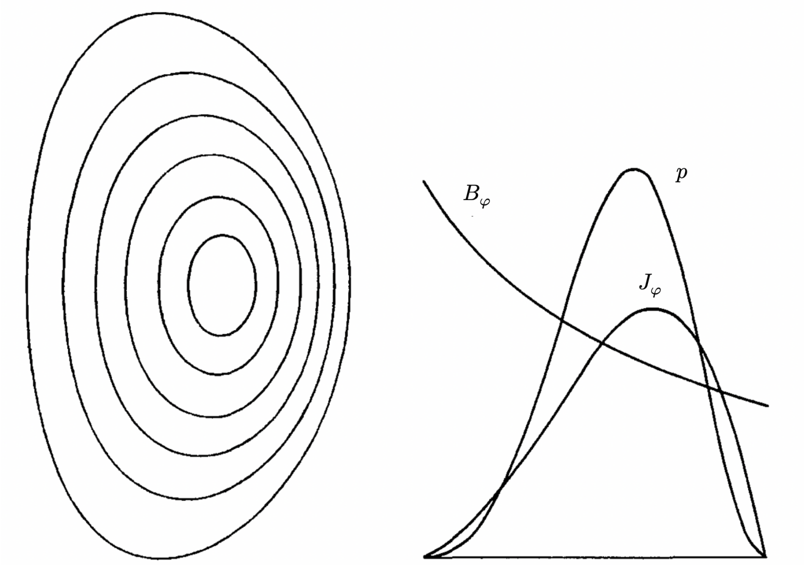

Figure A.4: Poloidal cross section of a typical equilibrium profile of magnetic surfaces in a vertically elongated plasma, and the corresponding profiles of toroidal field, plasma current and pressure. Taken from [2].

Now, the equation describing the field line trajectories on a toroidal surface is $\frac{Rd\varphi}{B_\varphi} = \frac{rd\theta}{B_\theta}$, since the lines of the toroidal field B_φ are circles in toroidal direction, having angle φ, with radius R, while he lines of the poloidal field B_θ are circles in poloidal direction, having angle θ, with radius r. As the line of the total field wraps once around a poloidal circle, that is making a poloidal angle $\Delta\theta = 2\pi$, then the toroidal angle Δ along which it travels is

$$\Delta\varphi = \int_0^{\Delta\varphi} d\varphi = \int_0^{2\pi} \left(\frac{rB_\varphi}{RB_\theta}\right)_S d\theta \tag{A.25}$$

where the integrand is evaluated on the flux surface S on which the considered field line lies. The average number of full poloidal rounds traversed during a single toroidal transit on such surface is the definition of the safety factor, namely $q = \frac{\Delta\varphi}{2\pi}$, which is then given by

$$q = \frac{1}{2\pi}\int_0^{2\pi} \left(\frac{rB_\varphi}{RB_\theta}\right)_S d\theta \tag{A.26}$$

Often, tokamak plasmas are characterized by a large aspect ratio, meaning that a particular toroidal flux surface has a major radius quite larger than the minor radius. If this occur, a *cylindrical approximation* is allowed, which considers all quantities as depending on the radial coordinate r alone. In this case, any flux surface can be considered as a cylinder of length $2\pi R_0$, as in the Fig. A.5.

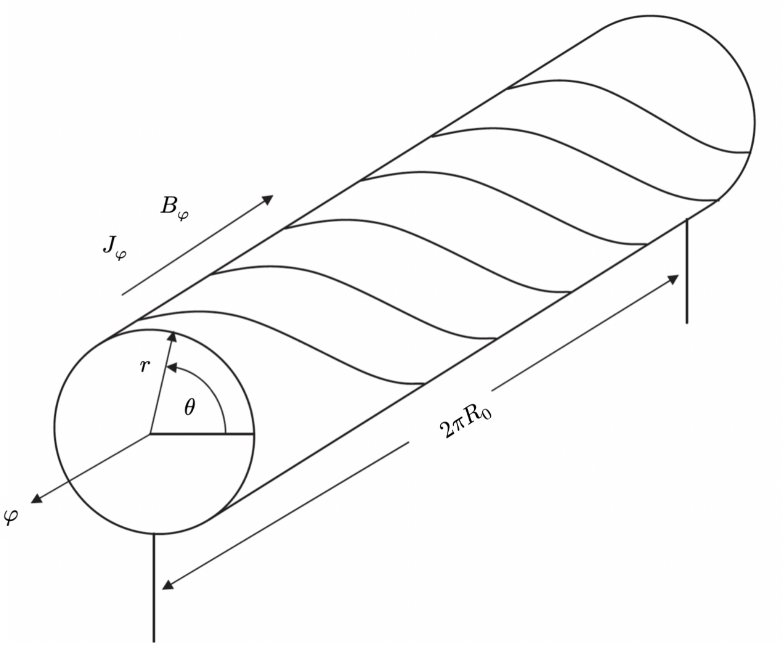

Figure A.5: Plasma cylinder. Taken from [105].

In this case, solving the equations (A.18) in cylindrical coordinates leads straightforwardly to the equilibrium condition [105]

$$\frac{d}{dr}\left(p + \frac{B_\varphi^2 + B_\theta^2}{2\mu_0}\right) + \frac{B_\theta^2}{\mu_0 r} = 0 \tag{A.27}$$

which provides the pressure profile $p(r)$ needed for satisfying the pressure balance, once the magnetic configuration has been imposed through the free functions $B_\varphi(r)$, $B_\theta(r)$. In particular, in this approximation, if the poloidal field is produced by means of an externally applied plasma current I_p flowing purely in toroidal direction, then the relation between these has the simple form

$$B_\theta = \frac{\mu_0 I_p}{2\pi r} \tag{A.28}$$

with r minor radius of the considered flux surface.
Finally, since in this approximate situation we have no dependencies on θ, the safety factor for a given flux surface of minor radius r is simply given by

$$q = \frac{rB_\varphi}{R_0 B_\theta} \tag{A.29}$$

A.3 Transport processes in magnetized plasmas

Transport processes in plasmas play a crucial role not only for this thesis but also, in general, in study of magnetic confinement in a fusion plasma. The presence of such processes, in fact, definitely makes the magnetic confinement of a fusion plasma not perfect, despite the presence of a magnetic equilibrium configuration, and makes a finite value of the energy confinement time τ_E arise, because of the induced escape of particles from the plasma, and consequently also energy. In particular, these arise both from *binary collisions* between particles, which get to be scattered in this way while gyrating around field lines, tending then to shift more radially outward, and from *turbulence phenomena*, including turbulent movement of magnetic field lines and density and potential fluctuations.
The framework of interest here is the transport theory of gases, which has been developed starting from the Boltzmann work in kinetic theory, as resulting purely form binary collisions between particles, being then expanded and finalized with the work by Chapman and Cowling [108]. Then, a first complete discussion of transport theory in a plasma, including also the effects of external fields on charged particles, has been proposed only with the work by Braginskii [109], initially applying only to plasmas in constant magnetic fields; this framework did then develop under the name of *classical transport* [110]. Additional effects given by curvature and inhomogeneity of magnetic field lines, clearly present in usual magnetic configurations for fusion applications, were later taken into account by works such as the one by Balescu [111]; in particular, the framework of transport processes in toroidal plasmas, peculiar of fusion devices, took the name of *neoclassical transport*. Finally, the experimentally deduced additional transport mechanisms which could not be explained by means of collisions between particles, requiring instead the consideration of collective turbulence phenomena, were accounted as *anomalous transport* [112].
This section will have, as a goal, the derivation under different assumptions of proper transport coefficients D_Φ describing the radial transport (with respect to magnetic field lines) of a scalar quantity $\Phi(\boldsymbol{x}, t)$ (which is the density n in case of particle transport, or the temperature T in case of heat transport), under the assumption of pure *diffusion*. The evolution of such scalar field, eventually convecting with velocity $\boldsymbol{v}$, can be modelled with a conservation law in the form

$$\frac{\partial \Phi}{\partial t} + \nabla \cdot (\Phi \boldsymbol{v}) = 0 \tag{A.30}$$

supposing no sources or sinks for Φ. Assuming a purely local transport, meaning that the scale of the process driving the transport mechanism is much shorter than the scale of variation of the transported quantity, then a *flux density* $\boldsymbol{\Gamma}_\Phi$ can be defined in terms of a local diffusion coefficient as

$$\boldsymbol{\Gamma}_\Phi \equiv \Phi \boldsymbol{v} = -D_\Phi \nabla \Phi \tag{A.31}$$

that is as simply proportional to the negative gradient of the considered quantity.
In this way, since the conservation law (A.30) can be written as

$$\frac{\partial \Phi}{\partial t} = \nabla \cdot (D_\Phi \nabla \Phi) \tag{A.32}$$

the knowledge of its velocity field is no more necessary, making the knowledge of the diffusion coefficient sufficient to completely characterize all the transport properties.

A.3.1 Random walk model

At a first level, adequate transport coefficients (of both particles and heat), quantifying the particles/heat transport as arising from the motion of an ensemble of particles, can be deduced as purely arising from binary collisions.
Considering, initially, a situation in which particles diffuse from their initial positions due to a series of collisions only, a description the consequent transport processes could be set up by means of the so-called *random walk model* [108], according to which each particle moves in an undisturbed straight line until it is subject to an abrupt random change in the direction of its motion when colliding with another particle. After a number N of collisions, each one characterized by displacement in space $\Delta\boldsymbol{x}_j$ with respect to the the position in the former step, the particle will have moved of the overall distance

$$\Delta\boldsymbol{x} = \sum_{j=1}^{N} \Delta\boldsymbol{x}_j \tag{A.33}$$

Performing an average over an ensemble of particles, it can be shown than $\langle\Delta\boldsymbol{x}\rangle = \mathbf{0}$, but $\langle(\Delta\boldsymbol{x})^2\rangle \neq 0$, meaning that a particle does not have a preferential direction in its random motion, but actually tends to move away from its initial location due to the collisions. In this way, an average square distance travelled from one particle between two successive collisions can be defined as

$$L^2 = \frac{\langle(\Delta\boldsymbol{x})^2\rangle}{N} \tag{A.34}$$

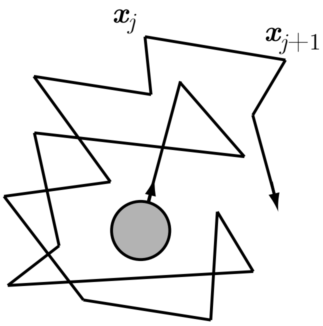

Figure A.6: Trajectory of a particle undergoing random collisions. Taken from [1].

So, if the average time between two successive collisions is τ, and thus the time required for N collisions is $\Delta t = N\tau$, then it is possible to rewrite $\langle(\Delta\boldsymbol{x})^2\rangle$ as

$$\langle(\Delta\boldsymbol{x})^2\rangle = D\Delta t \tag{A.35}$$

where the coefficient D_n, measured in m^2/s, called *diffusivity*, is defined as

$$D_n = \frac{L^2}{\tau} \tag{A.36}$$

and describes the net motion of an ensemble of particles as resulting from random collisions.

A.3.2 Classical transport

A somehow more detailed description of transport processes should consider the consequences of the plasma being subject to an external magnetic field with magnitude B, which definitely guides along the particles along its field lines influencing how they collide. In particular, we must consider the problem of gyrating particles subject to coulomb collisions in a random walk process; this produces a net diffusion of particles perpendicular to magnetic field lines, causing definitely a lack of confinement.

Again, we must deal then with coulomb collisions (cfr. Appendix A.1.3), after which two particles are assumed to be randomly scattered at an arbitrary angle, with consequent displacement as the difference in their center-of-mass position before and after the collision. In particular, it can be shown [1] that collisions between identical gyrating particles do not lead to net diffusion, since the center-of-mass remains unchanged, while only collisions between unlike gyrating particle lead to a net change of the center-of-mass, and thus to net diffusion, as it can be seen in the Fig. A.7.

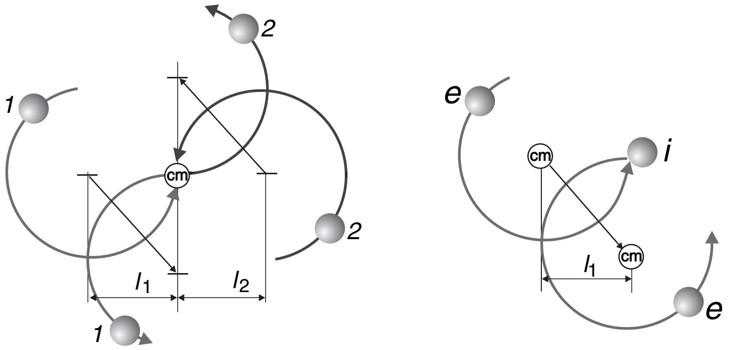

Figure A.7: Collisions between like (a) and unlike (b) gyrating particles in a magnetic field. Taken from [113].

Therefore, what it must be taken into account in this case are the electron-ion collisions, and thus the relevant time step for such collisions is τ_{ei} (eq. (A.12)).
Finally, since electrons and ions have different gyroradii, two different diffusivities seem to arise in a first approximation. Anyway, after the assumption of quasi-neutrality, the diffusion fluxes of the particle species have to be equal, and thus the component with the smallest diffusivity must determine the flux. This makes the electron diffusion dominate so that, using the electron gyroradius $\rho_e = \frac{m_e v_{\perp e}}{eB}$ where, supposing thermodynamic equilibrium, $v_{\perp e} = \left(\frac{2T}{m_e}\right)^{1/2}$ (which is the thermal velocity for electrons).
We can conclude that the *particle diffusivity* can be obtained as

$$D_n \sim \frac{\rho_e^2}{\tau_{ei}} \tag{A.37}$$

which then results to be [1]

$$D_n \approx 2\,\frac{m_e \nu_{ei} T}{e^2 B^2} \approx 2 \cdot 10^{-3}\,\frac{n}{B^2 T^{1/2}} \tag{A.38}$$

with $n = [10^{20}\ \mathrm{m}^{-3}]$, $T = [\mathrm{keV}]$. For usual fusion plasma parameters, we would have about $D_n \approx 3,5 \cdot 10^{-5}\ \mathrm{m}^2/\mathrm{s}$.
A similar approach can be followed for deducing the *thermal diffusivities* χ_e, χ_i, considering that, in this case, only collisions between identical particles lead to heat transport [1]. Therefore, here it must be considered that

$$\chi_e \sim \frac{\rho_e^2}{\tau_e} \tag{A.39}$$

$$\chi_i \sim \frac{\rho_i^2}{\tau_i} \tag{A.40}$$

Since $\chi_i \sim \left(\frac{m_i}{m_e}\right)^{1/2} \chi_e$, it can be understood that, differently from particle diffusion, in this case a dominant role is played by ion-ion collisions. In fact, it will result that [1]

$$\chi_e \approx 4{,}8 \cdot 10^{-3} \, \frac{n}{B^2 T^{1/2}} \tag{A.41}$$

$$\chi_i \approx 0{,}1 \, \frac{n}{B^2 T^{1/2}} \tag{A.42}$$

with, again, $n = [10^{20} \text{ m}^{-3}]$, $T = [\text{keV}]$. For usual fusion plasma parameters, the dominant ion thermal transport would be characterized by a thermal diffusivity of about $\chi_i \approx 1,8 \cdot 10^{-3} \text{ m}^2/\text{s}$.

However, such very simple picture of transport processes in magnetized plasmas, usually referred to with the name of *classical transport* [110], considers only a pure gyromotion of particles along magnetic field lines, neglecting any drift motion such as, in particular, curvature drift and ∇B drift, which are instead relevant in toroidal configuration of the magnetic fields as we find in tokamaks. Therefore, the picture of classical transport will be valid, strictly speaking, only in cylindrical plasma geometries. Instead, the evaluation of transport coefficients in a toroidal geometry will require a proper evaluation of realistic particle orbits.

A.3.3 Neoclassical transport

The theory which deals with collisional transport processes in toroidal magnetic configurations is usually referred to with the name of *neoclassical transport* [111]. In this case, curvature and inhomogeneity of magnetic field lines causes particle drifts and other mechanisms which give rise to perpendicular fluxes which are, often, quite more relevant than the "classical" fluxes.

For understanding what it does occur in this case is necessary to introduce the concept of *magnetic mirror*. In particular, defining the *magnetic moment* μ of a particle as

$$\mu = \frac{E_\perp}{B} \tag{A.43}$$

with $E_\perp$ its perpendicular kinetic energy, it is possible to prove that this is a conserved quantity [1]. Therefore, when a charged particles travels along a field line in an inhomogeneous field, when moving towards a stronger field also its perpendicular kinetic energy must increase, meaning that its parallel kinetic energy must inevitably decrease. Consequently, its parallel velocity will decrease while moving towards a region with stronger field up, eventually, to the annulment of this velocity and the consequent inversion of the motion. So, if the particle is moving in a so-called magnetic mirror, which is a symmetric configuration presenting a minimum of the magnetic field at its center and two maxima at its ends, then the particle will result to be mirror-reflected again and again before reaching the ends, at the so-called turning points, if its parallel velocity at the center, when the field is minimum, is sufficiently low.
Now, in a toroidal configuration, when particles are doing a poloidal round are actually moving in a magnetic mirror, because of the dependence $\sim \frac{1}{R}$ of the magnetic field, which makes it stronger at the inner side of the poloidal cross section and weaker at the outer side. Particles with high parallel velocity will get to complete a poloidal round, and are then called *passing particles*. In particular, during the poloidal round, the curvature drift leads to a displacement of the guiding center of these particles from their "original" flux surface, which is constant with magnitude [1]

$$\delta_p \approx \varepsilon \rho_\alpha \frac{B_\varphi}{B_\theta} \tag{A.44}$$

with ρ_α gyroradius of the considered particle (eq. (A.5) and $\varepsilon = \frac{r}{R_0}$ inverse aspect ratio of the torus. Therefore, the trajectory of passing particles on a poloidal plane will be a circle slightly

shifted from the original flux surface. These new orbits define the so-called *drift surfaces*. The direction of such displacement (inward or outward radially directed) will depend on the charge of the considered particle and the direction of its velocity with respect to the field direction.
Instead, particles which have sufficiently low parallel velocity will not complete a poloidal round, but will oscillate back and forth between the turning point in an effective magnetic mirror, being thus called *trapped particles*. Moreover, because of the toroidicity, net vertical drifts of plasma particles will arise, which tend to move the trajectories radially away form the flux surfaces, with a consequent displacement which is more intense where the field is weaker, that is halfway between the turning points, with maximum magnitude [1]

$$\delta_t \approx \varepsilon^{1/2} \rho_\alpha \frac{B_\varphi}{B_\theta} \tag{A.45}$$

and decreases up to zero just at the turning point. The peculiar shape of the resulting orbits of the trapped particles, when viewed on a poloidal cross section, brought them the name of *banana orbits* (fig. A.8).

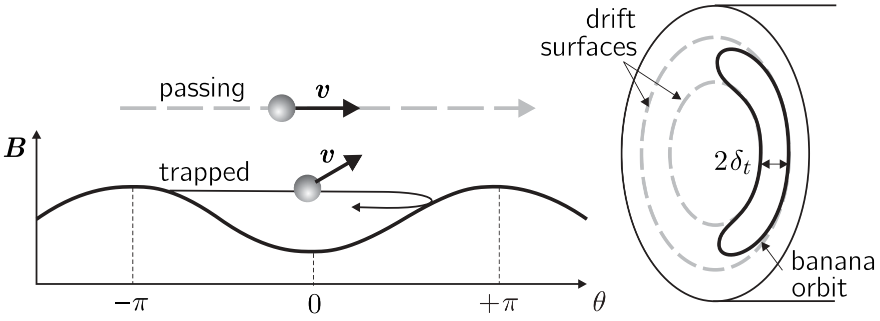

Figure A.8: Banana orbit resulting from the motion of a trapped particles. Taken from [113].

The fraction of trapped particles among all the plasma particles will clearly depend on the temperature of the system, since more energetic particles have higher probability to "escape" from the magnetic mirror and being then not trapped: assuming, as usual, a maxwellian distribution function, this fraction can be shown to be $f_t \approx \varepsilon$ [1].
Although only a minor fraction of all the particles result to be trapped at usual tokamak temperatures and magnetic field, the contribute of these to transport processes is dominant. This basically arises from the fact that trapped particles have a lower parallel velocity than the passing ones, being then subject for a longer time to a vertical drift, and thus experiencing a much more relevant drift distance with respect to their "original" flux surfaces. This ultimately increases the displacement for trapped particles following a collision; in fact since, in usual toroidal configurations, we have $\varepsilon \ll 1$, it will result that $\delta_t \gg \delta_p$.

In particular, by applying again a random walk model, it can be shown [1] that the average square step length is given now by

$$L^2 = 2q^2\varepsilon^{-1}\rho_e^2 \tag{A.46}$$

while the "effective" collision time is given by

$$\tau_{eff} = \varepsilon\tau_{ei} \tag{A.47}$$

Therefore, evaluating the effect of trapped particles only, the neoclassical particle diffusivity can be calculated as

$$D_{n,neo} \sim f_t \frac{L^2}{\tau_{eff}} \tag{A.48}$$

which then results to be [1]

$$D_{n,neo} \approx 2{,}2\, q^2 \varepsilon^{-3/2} D_n \tag{A.49}$$

where D_n is the classical particle diffusivity (eq. (A.38)). As it can be seen, for usual tokamak geometries, this can be larger than the classical diffusivity up to a factor 10^2, obtaining a neoclassical particle diffusivity of the order of 10^{-3} m^2/s.

Again, with a similar approach, the neoclassical thermal diffusivities can be shown to be [1]

$$\chi_{e,neo} \approx 0{,}89\, q^2 \varepsilon^{-3/2} \chi_e \tag{A.50}$$

$$\chi_{i,neo} \approx 0{,}68\, q^2 \varepsilon^{-3/2} \chi_i \tag{A.51}$$

where χ_e, χ_i are the classical thermal diffusivities (eqs. (A.41), (A.42)).

A.3.4 Anomalous transport

Although the neoclassical theory predicts transport coefficients much larger than the classical ones, neoclassical coefficients are still rather small for usual fusion plasma parameters, especially for the particle transport and the electron thermal transport cases, whose neoclassical coefficients fall from 10^{-3} to 10^{-2} m^2/s, as we just saw. Instead, experiments with toroidally confined plasmas exhibit far stronger particles and heat losses than how predicted even by the neoclassical theory, obtaining experimental diffusivities from 0,1 to 10 m^2/s. This "anomaly" in transport calculations cannot be explained by means of collisions between particles, for which reason such dominant component is usually called *anomalous transport* [112].
Definitely, this must be attributed to *turbulence phenomena* driven by microinstabilities. In particular, these non-linear processes eventually lead to the formation of coherent structures which, because of the long-range nature of electrostatic interactions in a plasma, tend to move collectively: it is the collective propagation of these structures which definitely results in a strongly enhanced particle and heat transport. However, since in a magnetized plasma there is a very high number of possible sources of microinstabilities, theory of plasma turbulence is an extremely complex field, and no complete theory predicting turbulent transport exists. Therefore, in order to predict anomalous transport, nowadays it is still necessary to rely on empirical *scaling laws* derived by experimentally measuring anomalous losses in current devices after multi-machine data interpolation. Such empirical laws are primarily based on the possibility to easily derive the energy confinement time (eq. (A.64)) from a given experiment by measuring the total energy stored within the plasma.

Theoretical models for anomalous transport require then to give up the purely diffusive approximation as it was is eq. (A.30), since now the presence of periodic micro-fluctuations in plasma quantities must be considered. In particular, such fluctuations give rise to small localized structures which are moved by *convection*: the collective radial propagation of such structures ultimately defines the anomalous transport. Moreover, since this collective radial motion is not related to neither absolute values of plasma quantities nor their relative gradients, this should be treated as an inherently non-local phenomenon.
There are several kinds of microinstabilities, in a magnetized plasma, each one characterized by a different interactions of the various fields in the plasma (density, temperature, electric potential and magnetic field) and describable by different length scales, which lead to the formation of such structures; this "multi-phenomena" feature also contributes to the extreme complexity of this topic.

Although a purely diffusive description of anomalous transport cannot be evidently justified, for what we just saw, there has been much effort for deriving empirical relations describing it by means of diffusion coefficient, in such a way that local flux densities could be still described with a diffusive assumption as in eq. (A.31). One of the best-known scaling laws is the one provided by Bohm in some early studies on magnetized plasmas [114], which reads

$$D_{Bohm} \approx \frac{1}{16}\frac{T}{B} \tag{A.52}$$

with $T = [\mathrm{eV}]$, $B = [\mathrm{T}]$. Such transport, usually called *Bohm diffusion*, gives rise to numerical values of diffusivities which are coherent with the experimentally measured ones, and the dependence on T, B^{-1} is also seen to be roughly satisfied; in particular, the dependence $\propto B^{-1}$ on the magnetic field seems to be, according to the experimental results, quite more realistic than the classical one, which was $\propto B^{-2}$. For this reason, the Bohm coefficient is usually used as a first approximation for describing anomalous transport in fusion plasmas.

A more detailed view of such turbulent phenomena, together with the main microinstabilities which generate them, will be given in Section B.1, with particular emphasis to the mechanisms responsible for anomalous transport driven by radial blob propagation, which was addressed in this thesis.

A.4 Power balance in a fusion plasma

In this section, the simple power balance for a fusion plasma, presented in the Section 1.1, will be rigorously deduced, after having properly defined the used quantities.

A.4.1 Fusion cross sections

The *cross sections* σ for fusion reactions were defined for quantifying the the probability of occurrence of fusion reactions in a plasma constituted by the two species of particles 1, 2, with density of the corresponding populations of nuclei (in m^{-3}) given by n_1, n_2. Clearly, these cross sections will depend on the speed v at which these nuclei travel in the plasma. Considering, for simplicity, the nuclei of the population 1 constituting a "target" at rest, with thickness dx and surface area A, and the nuclei of the population 2 constituting "projectiles" all travelling with a same speed v, then in one time interval $dt = dx/v$ there will be n_2Adx incident nuclei which will have crossed the target volume, among which only a fraction Fn_2adx will have reacted; according to the definition of cross section, then this fraction F can be written as $F = \frac{\sigma N}{A} = \frac{\sigma nAdx}{A} = \sigma ndx$, with $N_1 = n_1Adx$ total number of target nuclei in the considered volume. So, defining the *reaction rate* as the number of fusion reactions taking place each second per unit volume in the system between the two populations, will be

$$R = \frac{Fn_2Adx}{dVdt} = \frac{Fn_2Adx}{Adx\frac{dx}{v}} = \frac{\sigma n_1 n_2 dx}{dx/v} \Rightarrow R = n_1 n_2 \sigma v \tag{A.53}$$

In this way, the *fusion power density* S_F produced by fusion reactions, that is the generated power per unit volume of fuel, in $\mathrm{W/m^3}$, will be

$$S_F = E_F n_1 n_2 \sigma v \tag{A.54}$$

if E_F is the energy released in the plasma for each reaction.

Actually, it has to be taken into account that the various nuclei in a system will travel with different velocities, according to a certain distribution in the 3D velocity space. Therefore, the physical density has to be generalized by introducing, for the two populations, their *distribution functions* $f(\boldsymbol{x}, \boldsymbol{v}, t)$, defined in such a way that the total number of nuclei at, at time t, have position $\boldsymbol{x}$ and velocity $\boldsymbol{v}$ is $f(\boldsymbol{x}, \boldsymbol{v}, t)d^3\boldsymbol{x}d^3\boldsymbol{v}$. So, the physical density can be obtained integrating the values of the distribution function over all the possible velocities, as

$$n(\boldsymbol{x}, t) = \int f(\boldsymbol{x}, \boldsymbol{v}, t)\, d^3\boldsymbol{v} \tag{A.55}$$

In this way, for generalizing the definition of reaction rate for a case in which the velocities of the nuclei of the two populations in the system follow some distributions f_1, f_2, we must consider the whole distributions in the six-dimensional phase space rather than the simple densities, and consider the relative velocity between two nuclei of the different populations as $v = |\boldsymbol{v}_2 - \boldsymbol{v}_1|$, so that the cross section for single reactions will have a dependence $\sigma = \sigma(|\boldsymbol{v}_2 - \boldsymbol{v}_1|)$.
So, for obtaining the global reaction rate, we must integrate over all the possible velocities of the nuclei of the two populations, as

$$R = \iint \sigma(|\boldsymbol{v}_2 - \boldsymbol{v}_1|)|\boldsymbol{v}_2 - \boldsymbol{v}_1| f_1(\boldsymbol{v}_1) f_2(\boldsymbol{v}_2)\, d^3\boldsymbol{v}_1 d^3\boldsymbol{v}_2 \tag{A.56}$$

In particular, defining the quantity

$$\langle\sigma v\rangle = \frac{1}{n_1 n_2} \iint \sigma(|\boldsymbol{v}_2 - \boldsymbol{v}_1|)|\boldsymbol{v}_2 - \boldsymbol{v}_1| f_1(\boldsymbol{v}_1) f_2(\boldsymbol{v}_2)\, d^3\boldsymbol{v}_1 d^3\boldsymbol{v}_2 \tag{A.57}$$

having the meaning of a velocity-averaged *rate coefficient*, in m^3/s, the reaction rate can be finally generalized as

$$R = n_1 n_2 \langle\sigma v\rangle \tag{A.58}$$

and, consequently, the fusion power density will be written as

$$S_F = E_F n_1 n_2 \langle\sigma v\rangle \tag{A.59}$$

In order to evaluate practically the fusion power density from a reacting, some explicit expression for the cross sections and the distribution functions will be needed. Since cross sections for coulomb interactions are much larger than any fusion cross sections, the former will bring the whole plasma in a situation of thermodynamic equilibrium, so that the populations can be supposed to obey a *maxwellian distribution function*

$$f(\boldsymbol{v}) = n \left(\frac{m}{2\pi T}\right)^{3/2} e^{-\frac{mv^2}{2T}} \tag{A.60}$$

which is function only of the velocity $\boldsymbol{v}$, where T is the temperature of the system, in energy units.
So, supposing the function $\sigma(K)$, with $K = \frac{3}{2}T$ average center-of-mass kinetic energy of two interacting particles, as known (cfr. Fig. 1.1), the quantity $\langle\sigma v\rangle$ can be found after integrating over all the possible relative velocities between these, taking as basis maxwellian velocity distributions as (A.60). Analytic calculations [1] lead to the formula

$$\langle\sigma v\rangle = \frac{8\pi}{m_R^2} \left(\frac{m_R}{2\pi T}\right)^{3/2} \int_0^\infty \sigma(K) K e^{-K/T} dK \tag{A.61}$$

with m_R reduced mass of a system of two interacting particles. So, substituting in (A.61) the experimental trend of $\sigma(K)$, the rate coefficient $\langle\sigma v\rangle$ as a function of the temperature of the system (cfr. Fig. 1.2) is obtained.

A.4.2 Ignition condition

At this point, it is possible to deduce the values of density and temperature which would be necessary in a D-T plasma in order to have a favorable power balance, with more power produced than power required to keep the plasma hot.
A very simple *power balance* can be done, following [1], by assuming that:

- The fuel is a quasi-neutral 50-50 mixture of deuterium and tritium, with negligible concentration of alpha particles (product of the reactions), so that $2n_D = 2n_T = n_e \equiv n$.
- Each population of particles has the same temperature, that is $T_D = T_T = T_e \equiv T$.
- The plasma is in partial thermodynamic equilibrium, so that each population of particles has an internal energy density $u_j = \frac{3}{2}n_jT_j$, so that the total internal energy density is $u = \frac{3}{2}nT + \frac{3}{2}\frac{n}{2}T + \frac{3}{2}\frac{n}{2}T \Rightarrow u = 3nT$

In a steady-state situation, a local power balance could be written in the form $S = \nabla \cdot \boldsymbol{q}$, with S including all the sources and sinks of power density and $\nabla \cdot \boldsymbol{q}$ representing the flow of energy out of a plasma volume by heat transport. In particular, we have

$$S = S_F + S_H \tag{A.62}$$

with S_F fusion power density and S_H power density eventually externally provided to the plasma, neglecting any power density lost due to bremsstrahlung emission (which is a realistic assumption at high temperatures).
First of all, regarding S_F, it must be considered that the internal heating due to fusion reactions is given by the contribution of alpha particles only, since after their production they are released as fast particles and stay confined in the plasma, acting as a heat source through collisions with other particles while thermalizing, differently from neutrons which, instead, escape from the plasma and hit the walls of the device. Therefore, having supposed $n_D = n_T \equiv \frac{n}{2}$, we can write

$$S_F = \frac{1}{4}E_\alpha n^2 \langle \sigma v \rangle \tag{A.63}$$

where E_α=3,5 MeV.
Finally, the loss term due to heat transport away from the plasma can be modelled by averaging the local heat losses over the whole plasma volume as $\frac{1}{V}\int_V \nabla \cdot \boldsymbol{q}\, dV$ or, considering an integral of the energy flowing out of the system through the plasma surface, $\frac{1}{V}\int_A \boldsymbol{q} \cdot \boldsymbol{n}\, dS$. This term can be quantified by means of an experimentally determined *energy confinement time* τ_E, acting as a figure of merit for the thermal insulation of the plasma against heat transport phenomena; in this way, the total thermal content of the plasma (that is the total internal energy density $u = 3nT$) divided by the the loss term of power density by heat transport, that is

$$\tau_E = 3nT \left(\frac{1}{V} \int_A \boldsymbol{q} \cdot \boldsymbol{n}\, dS \right)^{-1} \tag{A.64}$$

Therefore, in seeking the so-called *ignition* condition, for which the power released in the plasma by alpha particle heating after fusion reactions is alone sufficient for balancing both heat transport and radiation losses, without a need for external heating, we must solve the balance equation (A.62) for $S_H = 0$, for which a situation of positive balance can be expressed by

$$\frac{1}{4}E_\alpha n^2 \langle \sigma v \rangle \geq \frac{3nT}{\tau_E} \tag{A.65}$$

This is best written in the form

$$n\tau_E \geq \frac{12}{E_\alpha}\frac{T}{\langle \sigma v \rangle} \tag{A.66}$$

which is the final form of the criterion for the ignition, represented in the Fig. 1.3 for the D-T reaction: for any value of temperature, the quantity $n\tau_E$ must be larger than a limit value in order to have a self-sustained burning plasma.

Appendix B

Further aspects of filamentary scrape-off layer transport

In this appendix some further physical aspects about perpendicular transport processes in the scrape-off layer driven by the radial convective motion of blob-filaments will be reviewed in more detail. In particular, in the Section B.1 a general insight of turbulence in magnetized plasmas will be given, with particular reference to the phenomena leading to an enhancement of perpendicular transport in the scrape-off layer plasma, namely interchange instability and consequent blob formation. Then, in the Section B.2 a simple mathematical model for describing the radial blob propagation in the scrape-off layer will be deduced, and some scaling laws identifying different transport regime for the blob convective motion will be presented, highlighting the dependence of the transport regime on SOL plasma conditions.

B.1 Turbulence phenomena in the edge plasma

As it was already mentioned in the Appendix A.3.4, experimental measurements for a particle and heat transport in radial direction in magnetized plasmas describe a picture which cannot be accounted by the collisional transport coefficients, even taking into account the effects of toroidicity. Rather, it has been established that *fluctuations* in plasma parameters, i.e. density, temperature and electric potential, are the actual responsible for the observed strong transport losses. These fluctuations are ultimately due to turbulence processes. Therefore, the need for a better understanding of the particular phenomena leading to an enhanced perpendicular transport in the SOL plasma, namely formation and radial propagation of blob-filaments, whose global effects were investigated in this thesis, requires a review of the general topic of turbulence.
In any fluid system, *turbulence* can be defined in principle as a state characterized by vortices which appear with basically random sizes, spanning from microscopic to macroscopic length scales, and frequency. In other terms, the presence of these inevitably causes periodic micro-fluctuations in all the quantities, which makes an exact numerical modelling of such state of extreme difficulty. The main consequence of vortex formation is an increased mixing of the fluid, which ultimately enhances all kinds of transport (of particles firstly, and consequently also of heat), being this vortex-driven motion much stronger than any density-gradient-driven diffusive motion in a fully developed turbulent state.

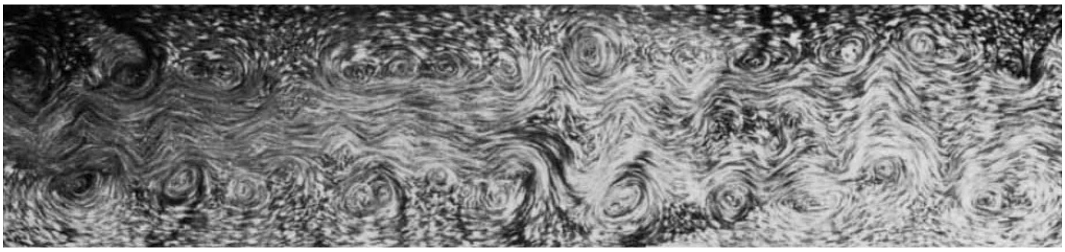

Figure B.1: Example of fully developed turbulent flow in a fluid system. Taken from [115].

B.1.1 Turbulence-driven fluctuations in magnetized plasmas

In a plasma, turbulence-driven fluctuations are the reason for the development of the anomalous transport. The way in which this occurs is the interaction between the various fluctuating fields (density, temperature, magnetic field and electric potential), which induce *collective modes*, characterized by many different length and time scales. All these collective modes, each one for its peculiar length/time scale, are responsible for the enhanced perpendicular transport in the plasma.

In fusion experiments it has been shown that the biggest part of the anomalous radial transport is caused by the the presence *electrostatic fluctuations*, where a localized fluctuating potential $\widetilde{\Phi}$ creates a fluctuating electric field $\widetilde{\boldsymbol{E}}$ which drives particles in a circular flow around the potential monopole due to the $\widetilde{\boldsymbol{E}} \times \boldsymbol{B}$ drift motion [113]. In particular, it can be seen that net radial transport occurs only when also density fluctuations exists, and if they are out of phase with respect to the potential fluctuations.
Let's consider the three different situations depicted in the Fig. B.2 (where higher density regions are represented in darker grey). If only a fluctuation $\widetilde{\Phi}$ in the potential field exists (left box), but the density, presenting a radial gradient, has no fluctuations, then the fluctuation $\widetilde{\Phi}$ creates a circular flow, which advects the same number of particles outward (at the bottom) and inward (at the top), therefore no net radial takes place. Instead, if also fluctuations in density $\widetilde{n}$ exist, and are out of phase with respect to $\widetilde{\Phi}$ (central box), then the circular flow will advect more particle outward than inward, since the circular motion is outward-directed where the density fluctuation is positive, therefore now we have net radial transport. Finally, if both perturbation still exist but are in phase (right box), then the circular flow will advect the same number of particles outward and inward again, and the net radial transport is again zero.

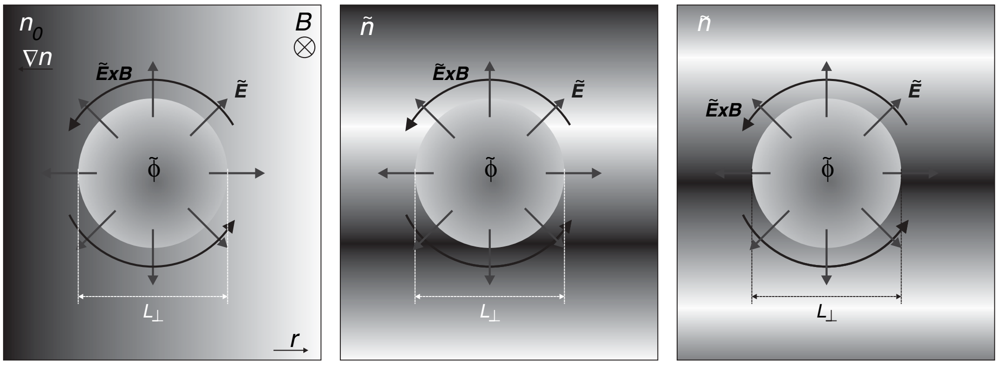

Figure B.2: Mechanism of radial transport due to electrostatic fluctuations. Taken from [113].

In toroidally confined plasmas, the microscopic mechanism leading to radial transport through the effect of electrostatic fluctuations out of phase with density fluctuations is the the so-called mechanism of *interchange instability*, whose model was originally developed in [116].
This mechanism takes place only in regions with "bad" magnetic curvature (namely on the low

field side of toroidal geometries, where the magnetic field gradient is radially inward directed), and is characterized by two-dimensional density fluctuations (in which the density keeps constant along field lines) (Fig. B.3). Because of the charge-dependent curvature drift, ions tend to mode upward while electrons tend to move downward. In this way, more positive charges will arrive at the border between low and high density where the density gradient is downward directed, than negative charges, creating a region with net positive charge; on the other hand, more negative charges will arrive at the border between low and high density where the density gradient is upward directed, than positive charges, creating a region with net negative charge. The result is the creation of electrostatic fluctuations which are out of phase by $\pi/2$ with respect to the density fluctuation, in such a way that the resulting vertical electric field will drive again the particles to the $\boldsymbol{E} \times \boldsymbol{B}$ advecting the background density, causing net radial transport.

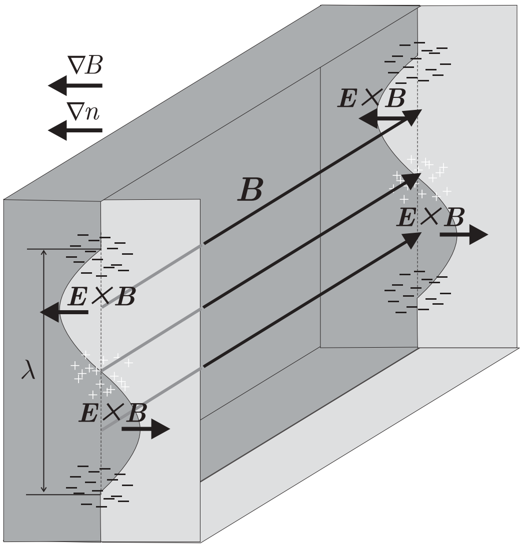

Figure B.3: Mechanism of the interchange instability. Taken from [113].

B.1.2 Blob formation and propagation

It can be readily understood how the mechanism of interchange instability can be seen as most probable responsible for the process of *blob formation* in the vicinity of separatrix (cfr. Section 2.4.1), whose radial propagation was seen to be the main cause for perpendicular transport in the scrape-off layer, and crucial aspect for this thesis.

In fact, when this mechanism takes place, low-density regions suffer an inward directed drift while high-density regions suffer an outward directed drift, so that, as a result, the original density fluctuation is amplified. This leads to a "lamination" of the plasma density, with high-density regions streaming outward and low-density regions streaming inward. As it was discusses in the previous section, interchange instability is caused, in principle, by the curvature drift of particles, so that this lamination effect gets to be most accentuated where the "worst" curvature of magnetic field lines, i.e. at the outer midplane of the torus; here, the lamination can be extremely relevant, as it can be appreciated in the Fig. B.4 (in which the effect is, however, clearly exaggerated). If the original density fluctuations perpendicular to the magnetic field arise in the vicinity of the separatrix, where the background density rapidly starts decreasing when moving outward, then this lamination effect tends to bring regions with high-density from the core plasma far away in the SOL, where the background density is much smaller. Therefore, the high-density ends finish up to being "ripped off" from the core plasma leading to the formation of isolated high-density structures, localized on a poloidal plane and elongated along the magnetic field lines, just as the original positive density fluctuations were; that is, the blob-filaments.

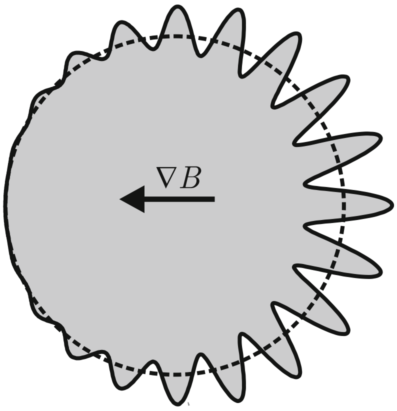

Figure B.4: Lamination of positive density perturbations at the separatrix due to the interchange instability. Taken from [113].

The mechanism of the interchange instability as the reason for the formation of these structure is very reasonable since it perfectly succeeds in explaining the experimentally observed ballooning nature of this phenomenon, with blob formation and propagation mainly concentrated in a poloidal region around the outer midplane. In fact, in the inner midplane, where the curvature of magnetic field lines is good, the effect of the radially directed drift is instead the opposite, finishing up to damp the original density fluctuation rather than amplifying it; and, indeed, no blobs are seen to form here.

Such picture has been confirmed by recent numerical and experimental works [53][54], in which blobs were seen to be effectively generated as part of a nonlinear saturation process of interchange instabilities in the edge plasma. In particular, the formation of blobs in the vicinity of the separatrix as result of the evolution of the radially extended *streamers* (i.e. the radially extended high-density structures resulting from the interchange instability) was observed to depend on whether *mean sheared flows* (i.e. flows in the binormal direction) are present [54]:

- If no mean sheared flows are present, streamers are unperturbed and do not break up.
- If we have weak sheared flows, as it is in actual L-mode discharges in fusion devices, then these tend to break up the streamers into localized blobs; however, they are not strong enough so suppress them, so that these can propagate radially in the SOL after charge polarization within them has occurred.
- If we have strong sheared flows, as it in actual H-mode discharges in fusion devices, then these are so strong that they suppress the turbulence locally by tearing apart the coherent structures, reducing then the blob generation rate.

This succeeds in explaining the experimental observation that the number of detected blobs per unit time in a given radial location is higher in L-mode discharges than in H-mode discharges, which is the reason why perpendicular SOL transport by radial blob propagation is currently much more investigated in L-mode [12][13][16][17], and why this thesis was devoted to this, too.

Next figures show measurements of the resulting 2D structure of blobs on a poloidal plane. Although many devices were analyzed in last years [54], the common feature of these measurements is, indeed, the presence of localized region of unusually high density in the scrape-off layer, typically some cm in size, which move radially outwards with a propagation velocity of the order of 10^3 m/s, that is with the same characteristics of the measurements considered in [12][13].

In particular, in the Fig. B.5 a series of images obtained with the technique of gas puff imaging in the NSTX device [54] are shown. The image frame rate is of 7,5 μs per frame, and the field of view is 25×25 cm near the outer SOL midplane (the yellow solid line represents the separatrix). A bright blob is seen to form near the separatrix, after which it moves radially outwards toward the limiter shadow (yellow dotted line) at a velocity of about 10^3 m/s.

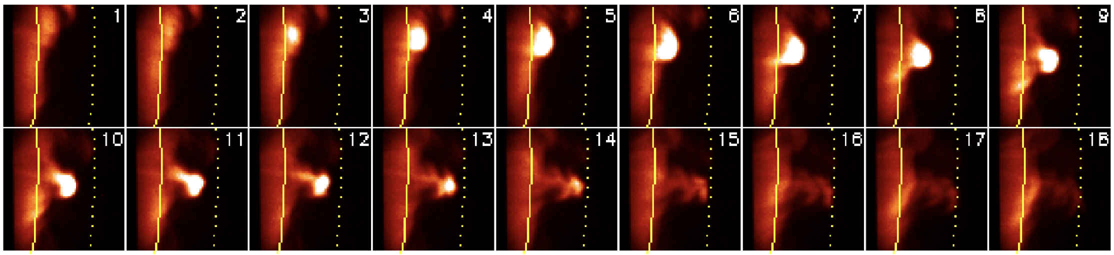

Figure B.5: Blob formation and propagation about the outer SOL midplane seen by gas puff imaging. Taken from [54].

Then, the physical mechanism of radial blob propagation, which was briefly explained in Section 2.4.1, was also confirmed by measuring their electric potential structure through Langmuir probes. In the Fig. B.6, the electric potential structure internal to a blob, measured in the VTF device [54], is shown, together with the density contours (solid lines) and velocity field (arrows). The dipole structure of the potential field, due to the internal charge polarization, is clearly visible, which creates the internal vertical electric field which, in turn, gives rise to the characteristic $\boldsymbol{E} \times \boldsymbol{B}$ velocity field, sign that the structure is radially propagating while whirling into vortices.

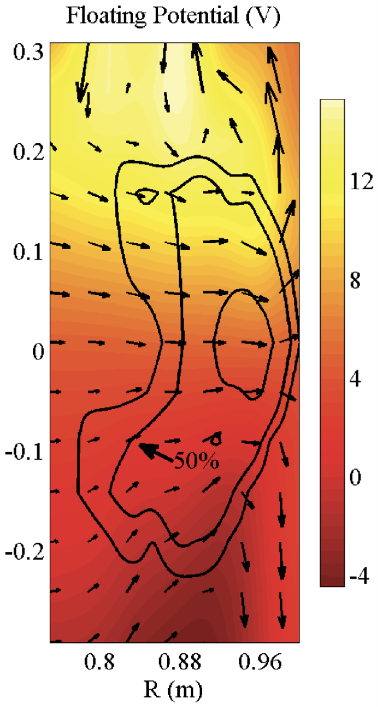

Figure B.6: Electric potential structure internal to a blob as seen by Langmuir probes. Taken from [54].

Such measurements, which resulted to be common in all toroidal plasma devices [54], have widely and unequivocally confirmed the theory of radial convective transport by blob propagation at the outer SOL midplane. This has resulted in observing the effective existence of localized radially propagating high-density structures as large, intermittent, positive fluctuations in the SOL density, and the actual presence of internal charge polarization in such structures, which confirms the mechanism for the observed convective transport.

This picture, finally, was also confirmed through numerical simulations, following the evolution of seeded blobs into a plasma background, imposing a magnitude of blob density significantly larger than the background plasma density. The results have shown that, during the propagation, blobs evolve very quickly from their original monopole shape into a mushroom-like structure, as in the Fig. B.7, in which hotter colors represent higher density regions.
This is coherent with the picture of the two vortices in the $\boldsymbol{E} \times \boldsymbol{B}$ velocity field, generated due to the internal electric field, characterizing the propagation of structures arising from interchange-instability-driven fluctuations [117].

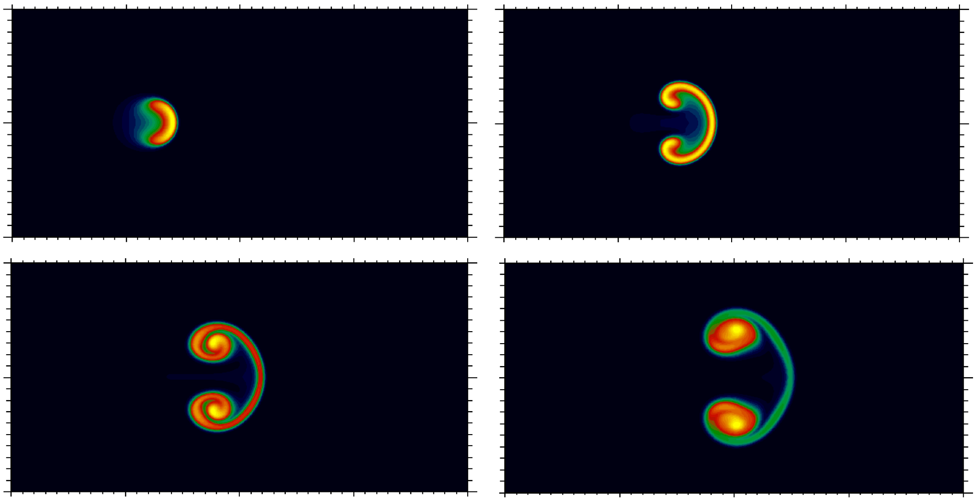

Figure B.7: Simulated radial motion of a high-density blob in a plasma background. Taken from [117].

B.1.3 Statistical observations of fluctuations in the scrape-off layer

Finally, we conclude this section with a brief review of some *statistical observations* of turbulence-driven fluctuations in the scrape-off layer. A statistical analysis is, indeed, necessary since what it is actually observed is an ensemble of many random appearing blobs, whose propagation causes, in a given radial location, randomly time-distributed positive density perturbations.
This can be carried out in terms of a *probability distribution function* $P_X(x)$, denoting the probability that a fluctuating measured quantity X lies between the values x, $x + dx$. In particular, the measured fluctuations in the SOL density are positive and large, about $\delta n/n \sim 1$; since density is a positively definite quantity, large positive density fluctuations, as the ones caused by a blob passing through the measurement point, will necessarily imply a deviation from a gaussian probability distribution function for the density [118].
The best way for characterizing the measured fluctuations, in this sense, is to plot a version of the resulting probability distribution function which the fluctuations are normalized to the mean, that is defining a *normalized probability distribution function* for a quantity X as

$$\overline{P}_X\left(\frac{x-\overline{x}}{\sigma_x}\right) = \sigma_x P_X(x) \tag{B.1}$$

where the *mean value* $\overline{x}$ of the measured data, and their *standard deviation* σ_x, are defined by

$$\overline{x} = \frac{1}{N}\sum_{j=1}^{N} x_j \tag{B.2}$$

$$\sigma_x = \sqrt{\frac{1}{N}\sum_{j=1}^{N}(x_j - \overline{x})^2} \tag{B.3}$$

with N number of measured data points in the considered time series for the quantity X, consisting in the measured values x_j for that quantity in a given location.
The Fig. B.8a illustrates the actual behavior of the distribution of density fluctuations in the SOL in a given radial location, measured in various discharges of the TCV device for different values of line-averaged density [118]. As we can see, the normalized function is effectively non-gaussian (being strongly positively skewed, i.e. positively asymmetric, indicating the presence of large positive bursts to the time series of density fluctuations about their mean value) and, moreover, independent on the specific plasma conditions. This independence from the plasma conditions can be clearly seen also from the time trend of the *pulse shapes* of the measured density fluctuations resulting from the passing of a blob from a given radial location [118], as in the Fig. B.8b (in collecting these pulses, usually a conditional averaging of the measured data is carried out, meaning that only fluctuations with a peak in magnitude grated than 2,5 standard deviations above the mean are retained in the analysis).

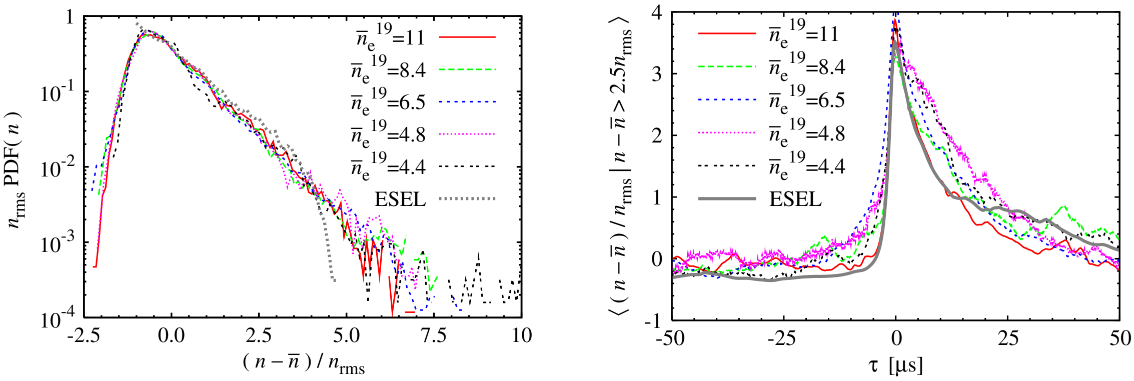

(a) Normalized probability distribution function.
(b) Conditionally averaged pulse shapes.

Figure B.8: Statistical analysis of density fluctuations in a given radial location in the SOL for different plasma conditions. Taken from [118].

This shows how the turbulent phenomena (i.e. the presence of interchange instabilities) which generate blobs are "universal" across different plasma parameters; what does actually change for different plasma parameters, determining then the resulting perpendicular transport regime, are the underlying forces driving the blob motion and the current closures determining the radial blob velocity, which ultimately determine the fraction of blobs which get to reach the wall, as it was pointed out in the Section 3.3.

What we got is that, in addition to the measurements of physical blob parameters, also the statistical observation of turbulence-driven fluctuations in the scrape-off layer seem to be common in toroidal plasma devices [54], in terms of highly skewed probability distribution functions for density fluctuations and characteristic pulse shape due to blob detection.

B.2 Mathematical model of radial blob propagation

In the Section 2.4.1 a brief overview to the mechanism through which blobs get to radially propagate in the SOL, once they are formed in the vicinity of the separatrix, was given. It was shown that it was due to the net charge separation occurring in their cross section as a consequence of an internal charge polarization due to the toroidicity (namely, resulting from an effective gravity force produced by curvature and ∇B effects), and the subsequent creation of an internal electric field $\boldsymbol{E}$; the resulting $\boldsymbol{E} \times \boldsymbol{B}$ drift motion, radially outward directed, propels these structures in a net convective motion, with some velocity $\boldsymbol{v}_b$.

In this section, a simple 2D mathematical model for radial blob propagation is derived, making some realistic assumptions, in order to estimate some figures of merits for the convective motion of blobs, such as their radial velocity, as a function of the global plasma parameters, with the goal of better characterizing their impact of global perpendicular transport regime for different plasma conditions.
For doing this, in literature it is common to use an exact definition of blob-filaments as structures characterized by a *size* δ_b in the poloidal plane and an *elongation* L_b along the field lines, which satisfy the following properties [14][15][119]:

- In their 2D cross-section on a poloidal plane, they have a monopole density distribution n_b, with a peak value much higher than the surrounding fluctuations of the background plasma.
- In a full 3D geometry, they are aligned parallel to the magnetic field, and their density variation along it is much weaker than in transverse direction, meaning that $\delta_b/L_b \ll 1$.
- They are characterized by a dominant convective $\boldsymbol{E}\times\boldsymbol{B}$ velocity component in the direction of the charge-polarizing force, and an associated electric potential and vorticity with dipole structures in the direction transverse to their propagation.

All these assumptions are coherent with the experimental features which were illustrated in the Section B.1.2.

B.2.1 Blob conservation relations

A simplified model for blob dynamics simply arises from the statement of some *conservation relations*. The forthcoming treatment follows [14][15][119].

First of all, regarding the electric currents naturally arising inside their structure due to the internal dipole potential structure, *charge conservation*

$$\nabla\cdot\boldsymbol{J} \equiv \nabla\cdot\boldsymbol{J}_\perp + \nabla_\parallel J_\parallel = 0 \tag{B.4}$$

must hold, in which $J_\parallel$ is the current in the direction of the magnetic field and $\boldsymbol{J}_\perp$ is the current in the poloidal plane.
Here, the perpendicular current can be written as a sum of the current induced by the charged-particle drifts due to an arbitrary force density $\boldsymbol{F}$ and the polarization current, that is

$$\boldsymbol{J}_\perp = \frac{\boldsymbol{F}\times\boldsymbol{B}}{B^2} + \frac{d}{dt}\left(\frac{n_b m_i}{B^2}\nabla_\perp\Phi\right) \tag{B.5}$$

where $\boldsymbol{F}$ is the charge-polarizing force and Φ is the resulting internal electric potential. Therefore, the charge conservation (B.4) will read

$$\nabla\cdot\frac{d}{dt}\left(\frac{n_b m_i}{B^2}\nabla_\perp\Phi\right) = \frac{\boldsymbol{B}}{B^2}\cdot\nabla\times\boldsymbol{F} + \nabla_\parallel J_\parallel \tag{B.6}$$

This basically states that polarization (left-hand side of (B.6)) results from the equilibration of a drive term plus a "parallel closure term" (right-hand side of (B.6)).

Then, an internal particle balance can also be formulated for the particles constituting a blob, following from the competition between the processes which tend remove particles from it (namely, radial transport towards all the surrounding low-density regions, at a background density n_0 much smaller than its internal density n_b, and losses due to parallel transport) and the processes which tend to create particles in it (namely, eventual ionization sources). Therefore, a *continuity equation* can be written as

$$\frac{dn_b}{dt} = D_n \nabla^2 n_b - \alpha n_b + \xi n_b \tag{B.7}$$

with D_n local anomalous particle diffusivity, $\alpha \equiv \frac{1}{\tau_\parallel}$, where $\tau_\parallel \approx \frac{L_\parallel}{c_s}$ is the usual characteristic loss time (which can be considered the time during which the blob can propagate radially before disappearing due to the parallel plasma flow), and $\xi \equiv n_n \langle \sigma v \rangle_i$ is the ionization source term, where n_n is the background neutral density.

Since we are interested to the evolution of some fields (density and electric potential field) which are actually moving as seen in a fixed reference frame, because of the radial propagation of the blob structure with a velocity $\boldsymbol{v}_b$, in the equations (B.6), (B.7) the time derivatives must be treated as *convective derivatives*, meaning that they consider both the absolute variation of the fields, i.e. the variation in a reference frame convecting with the blob, and the variation resulting from the convective motion of the blob frame with velocity $\boldsymbol{v}_b$, i.e.

$$\frac{d}{dt} \equiv \frac{\partial}{\partial t} + \boldsymbol{v}_b \cdot \nabla \tag{B.8}$$

in which $\boldsymbol{v}_b$ results as the $\boldsymbol{E} \times \boldsymbol{B}$ drift velocity, that is as

$$\boldsymbol{v}_b = \frac{\boldsymbol{B} \times \nabla \Phi}{B^2} \tag{B.9}$$

Once that an adequate assumption for $\nabla_\parallel J_\parallel$ has been done (cfr. next section), the equation (B.6) can be analytically solved, leading to a solution for the electric potential Φ as a function of the blob density field n_b. After that, substituting the obtained expression in (B.9), a proper expression for the radial propagation velocity as a function of the blob density field can be derived as well.
Finally, for converting this to an absolute expression, function of the plasma conditions, we have to couple this with the continuity equation (B.7), which can be written as

$$\begin{gathered} \frac{dn_b}{dt} + \gamma n_b = \\ \frac{\partial n_b}{\partial t} + \boldsymbol{v}_b \cdot \nabla n_b + \gamma n_b = \\ \frac{\partial n_b}{\partial t} + \frac{\boldsymbol{B} \times \nabla \Phi}{B^2} \cdot \nabla n_b + \gamma n_b \approx 0 \end{gathered} \tag{B.10}$$

assuming, for simplicity, to neglect the dissolution of the blob structure due to the radial transport (which is reasonable, since background diffusive fluxes are actually negligible with respect to he rate of convective radial transport of particles with blob propagation), and where the term $\gamma \equiv \alpha - \xi$ regulates the competition between parallel losses and ionization sources.

The equation (B.10) could be analytically solved, substituting into it the adequate expression for $\nabla \Phi$ and assuming, for simplicity, no background plasma, blobs as isolated coherently propagating objects with constant temperature.
It is also necessary to assume a prototype solution form for the blob density field: for simplicity, we can assume a local cylindrical symmetry about the field lines, that is $n_b \equiv n_{b,0} n_b(x, y, t) = n_{b,0} n_b(\rho, t)$, with ρ radial coordinate in the local blob geometry, defined in such a way that $\rho^2 = x^2 + y^2$, with x, y coordinates in the poloidal plane, x representing the radial direction and y the binormal direction with respect to the field lines (see Fig. B.9).

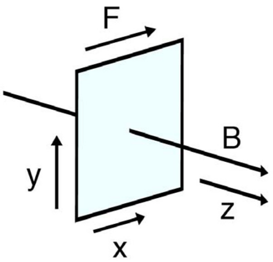

Figure B.9: Geometrical coordinates considered in this section. Taken from [15].

The most simple ansatz is a gaussian density profile in the convecting frame, with magnitude which increases or decreases in time due to the source/sink factor γ, which translates into the form

$$n_b(\rho,t) \equiv n_{b,0} \exp\left(-\frac{\rho^2}{2\delta_b^2}\right) \exp(-\gamma t) \tag{B.11}$$

This represents a separable solution on the poloidal plane, being writable as $n_b(\rho,t) = n_b^x(x,t)n_b^y(y)$, in which only the "radial" component is time-dependent, because x is, by definition, the direction in which the blob propagates.
Substituting this prototype solution in (B.10), it will be finally possible to transform it into a *ballistic equation* for $n_b^x(x,t) \equiv \exp\left(-\frac{x^2}{2\delta_b^2}\right) \exp(-\gamma t)$, that is

$$\frac{\partial n_b^x}{\partial t} + v_b \frac{\partial n_b^x}{\partial x} = 0 \tag{B.12}$$

describing the propagation of such isolated cylindrical blob in the x direction with a velocity v_b. Once this transformation is complete, from the resulting form of this equation it will be immediately possible to deduce the value of v_b.

B.2.2 Scaling of radial convective motion

Now, in order to solve the equations and calculate the resulting radial propagation velocity $\boldsymbol{v}_b$, a model for the parallel current is needed, for substituting $\nabla_\parallel J_\parallel$ in (B.6) with an expression acting on the poloidal plane, and thus achieving an expression for $\nabla\Phi$ to be substituted in (B.10). For doing this, we consider the Fig. B.10, which schematically illustrates the so-called *blob-equivalent electric circuit*, formed by the blob-filament structure itself and the axial bounding surface (in this case, the divertor target).

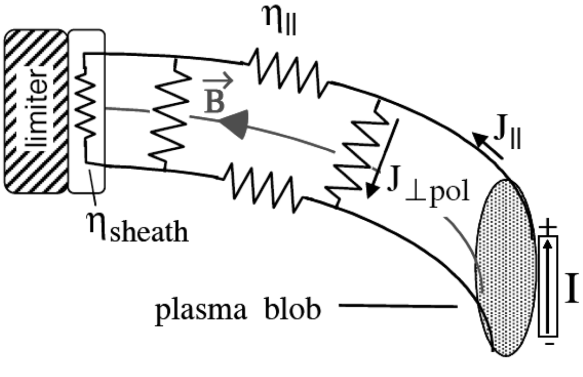

Figure B.10: Equivalent electric circuit and possible current paths in the 3D filamentary structure of blobs. Taken from [119].

The charge polarization acts as a constant current source I on the poloidal plane, producing a parallel circuit in the full 3D filamentary structure with a dipole configuration; the magnitude of the various resistivities will then control the distribution of currents, determining the parallel closure term and thus, ultimately, the radial propagation velocity of the whole structure. In this way, this velocity will get to mostly depend on the features characterizing the equivalent circuit, namely its length (related to the magnetic geometry), the parallel plasma resistivity $\eta_{\parallel}$, acting on the parallel length of the circuit, and the sheath resistivity η_{sheath}, acting on the "left" part of the circuit.

In particular, the effective resistivity characterizing the circuit will ultimately determine the vertical potential difference within the blob, and then the resulting radial $\boldsymbol{E} \times \boldsymbol{B}$ velocity as $v_b \propto \frac{d\Phi}{dy}$. Such an effective resistivity will obviously depend on the particular loop followed by the electric current in the circuit, that is, in particular, on whether the current gets to flow unimpeded from the midplane up to the sheath at the target or not [120]. In fact, in divertor configurations, this latter possibility could occur because of the presence of the X-point, which could actually disconnect the current flow from the divertor region. Such disconnection could occur because the blob circular cross section is actually stretched into a thin elliptical shape near the X-point, following the magnetic flux expansion this region (cfr. Section 2.1.1), resulting to be more radially extended and less extended in the binormal direction here (see Fig. B.11). Therefore, a perpendicular current will easily flow across the thin binormal size of the blob here, thus effectively closing the current loop in this region disconnecting it from the divertor region.

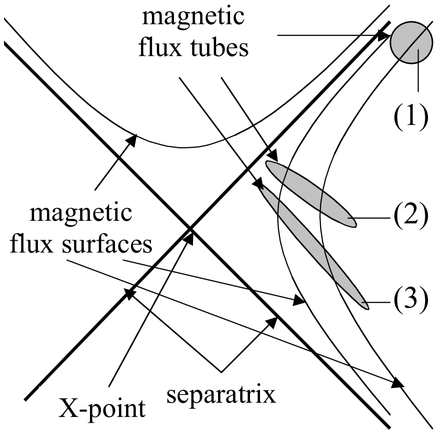

Figure B.11: Stretching of the blob cross section near the X-point in divertor configurations. Taken from [119].

So, for each current loop which could be followed, blob theory will allow different estimates for the resulting radial blob velocity v_b, with, in particular, different scalings with the blob size δ_b.

The eventual disconnection along magnetic field lines, including the X-point effects, has been analyzed in [120], in which a full analytic model predicting the radial blob transport regime in function of the blob size, for different plasma conditions and magnetic geometries, has been developed.

The model covers a wide range of possible *blob sizes*, *plasma conditions* and *magnetic geometries*: here we summarize its features which mostly concern radially propagating blobs in the scrape-off layer of diverted plasmas, namely limiting to blob sizes as usually measured in the SOL (of the order of cm) and to X-point magnetic geometries typical of current and future devices. Therefore, the only aspect remaining for characterizing the blob transport regime is given by the plasma conditions; according to the model developed in [120], this dependence can be explained by means of the so-called *collisionality parameter*

$$\Lambda = \frac{\Omega_i}{\Omega_e} \frac{\nu_{ei}}{c_s} L_{\parallel} \tag{B.13}$$

where $L_{\|}$ is a characteristic parallel length, ν_{ei} is the electron-ion collision frequency (inverse of eq. (A.12)), c_s is the plasma sound speed (eq. (2.17)) and $\Omega_{e,i}$ are the electron/ion gyrofrequencies (eq. (A.6)). In particular, this parameter gets to represent a measure of the ratio of the parallel plasma resistivity, impeding the parallel current flow to the divertor region, to the sheath resistivity; then, because of its direct proportionality to ν_{ei}, such parameter will be also directly proportional to the global density regime in the scrape-off layer.

A number of different *blob transport regimes* have been identified within the model developed in [120], in function of the just mentioned parameters; each regime is defined by different parallel closures of the electric current and thus characterized by different ways for solving the blob conservation relations, and hence definitely by different scalings for the radial propagation velocity v_b. In the limit of blob sizes and magnetic geometries of interest for fusion applications, two separated regimes were identified:

- A *sheath-connected regime*, defined by $\Lambda \ll 1$, being this characterized by a sufficiently low parallel resistivity that the current can flow unimpeded up to the divertor region, and the circuit is closed in correspondence of the sheath. In this situation, the gravity-force-induced drive term in (B.6) is effectively balanced by the parallel current flowing to the sheath, limited here by the sheath resistivity. The application of the model proposed in [120] led to a scaling of the radial propagation velocity of blobs with their size as $v_{b_{SC}} \propto \delta_b^{-2}$.
- An *inertial regime*, defined by $\Lambda \gg 1$, being this characterized by a sufficiently high parallel resistivity that the current cannot flow up to the divertor region, so that the connection with the target is broken and the circuit is closed in correspondence of the X-point. In this situation, the gravity-force-induced drive term in (B.6) is balanced with the inertia in the midplane region. The application of the model proposed in [120] led to a scaling of the radial propagation velocity of blobs with their size as $v_{b_{IN}} \propto \delta_b^{1/2}$.

The complete expressions for the velocities in the two regimes, obtained by fully solving the blob conservation relations, resulted to be

$$v_{b_{SC}} = 2c_s \frac{L_{\|}}{R_b} \left(\frac{\rho_s}{\delta_b} \right)^2 \tag{B.14}$$

for the sheath-connected regime [119], and

$$v_{b_{IN}} = c_s \left(2 \frac{\delta_b}{R_b} \right)^{1/2} \tag{B.15}$$

for the inertial regime [121], where ρ_s is the ion gyroradius corresponding to the sound speed, and R_b is the curvature radius of the considered flux surface.
Later, the model has been furtherly refined by the inclusion of more realistic features, namely the effects of temperature given by ions being hotter than electrons [122] (a situation, neglected in the basic conservation relations (B.6), (B.7) which is instead usually fulfilled in the SOL), and finite plasma background density $\overline{n}$ [123], leading to improved versions for these scalings in the two regimes given respectively by

$$v_{b_{SC}} = c_s (1 + \tau_i) \frac{\delta n}{\overline{n} + \delta n} \frac{L_{\|}}{R_b} \left(\frac{\rho_s}{\delta_b} \right)^2 \tag{B.16}$$

$$v_{b_{IN}} = c_s \left[(1 + \tau_i) \frac{\delta n}{\overline{n} + \delta n} \frac{\delta_b}{R_b} \right]^{1/2} \tag{B.17}$$

where $\tau_i \equiv T_i / T_e$ and δn is the (positive) density fluctuation due to the high blob density over the background density $\overline{n}$. As we see, in both cases this increases the resulting radial propagation

velocity, with different proportionality factors.
Considering typical SOL plasma parameters ($c_s \approx 2{,}5 \cdot 10^4$ m/s, $\rho_s \approx 4 \cdot 10^{-4}$ m), the ASDEX Upgrade characteristics (curvature radius $R_b \approx 2{,}15$ m at the outer SOL midplane, and X-point-to-target parallel connection length $L_{\parallel} \approx 5$ m) and, taking the same experimental values discussed in the Section 3.3, density fluctuations of the order of $\delta n \approx 0{,}5\,\overline{n}$, the results of the two equations are shown in the Fig. B.12 for both $\tau_i = 0$, $\tau_i = 3$, where the different scalings of v_b with δ_b are evident.

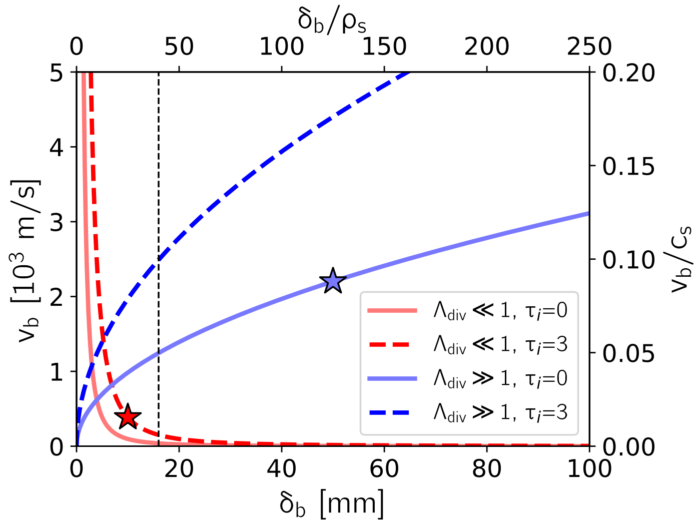

Figure B.12: Scaling of the radial propagation velocity of blobs for low and high collisionality regimes.

Experimentally, in L-mode discharges in ASDEX Upgrade with magnetic configurations equivalent as the ones considered in this work, it has been observed that, while for low densities ($\Lambda \ll 1$) the measured blob velocities nicely follow the scaling (B.16) with $\tau_i = 3$, for high density ($\Lambda \gg 1$), instead, the measured velocities are better explained by the scaling (B.17) with a cold ion approximation $\tau_i = 0$ [12]. So, assuming for example, as discussed in the Section 3.3 and suggested here by the Fig. 3.12, blob sizes of $\delta_{b,\,\Lambda_{div} \ll 1} \approx 10$ mm and $\delta_{b,\,\Lambda_{div} \gg 1} \approx 50$ mm for low/high collisionality, taking $\tau_i = 3\,/\,0$ for the two cases we could estimate, respectively,

$$v_{b_{SC}} \approx 0{,}4 \cdot 10^3 \text{ m/s} \tag{B.18}$$

$$v_{b_{IN}} \approx 2 \cdot 10^3 \text{ m/s} \tag{B.19}$$

which are represented as stars in the Fig. B.12. The values are roughly the same as experimentally measured (Fig. (d) in 3.11), at least in terms of order of magnitude.

From the analytic results presented in this section it can be concluded that increasing the SOL collisionality (i.e. the SOL density regime) effectively causes the blobs to disconnect the midplane region (where the curvature is strongest) from the divertor region, causing the transition between sheath-connected regime and inertial regime, and consequently a change in blob properties, such as their radial propagation velocity.
This is the reason why the increase of collisionality can be definitely invoked for explaining the experimental features presented in the Section 3.3 and numerically investigated in this thesis, such as the enhanced radial particle and heat transport and the formation of a density shoulder at the outer SOL midplane, as a consequence of an increased impact of radial blob propagation on the overall perpendicular transport regime.

Appendix C

Further aspects of plasma edge modelling

In this appendix, some aspects of plasma edge modelling in SOLPS-ITER will be presented with more detail. In particular, in the Section C.1 a detailed discussion about the derivation of global conservation relations for the plasma species, starting from the fundamental kinetic theory up to deduce an approximated fluid description, as resulting from collisional transport processes. Starting from this, a somehow more detailed presentation of the physics of SOLPS-ITER will be given, explicitly presenting the assumptions made and the equations which are solved; in particular, in the Section C.2 more details about the fluid module B2.5, for plasma particles modelling, will be given, while in the Section C.3 more details about the kinetic module EIRENE, for neutrals modelling, will follow.

C.1 Global conservation relations

As it was already mentioned in the Appendix A.3, the theory of transport processes in magnetized plasmas is still an incomplete field, because of the apparently insurmountable barrier of the lack of a complete turbulence theory. However, numerical codes for simulating the behavior of fusion plasmas, such as SOLPS-ITER, must be constructed at least on some analytical equations, which could be eventually improved by including some anomalous transport coefficient for the transport perpendicular to the magnetic field. For this reason, global *conservation relations* for the plasma must be deduced, after an adequate choice of assumptions and approximations, varying from case to case, so that to be implemented in numerical codes aimed to the modelling of fusion plasmas.

C.1.1 Kinetic theory

The aim of deducing conservation relations for the plasma must deal, as first thing, with the set up of the most complete description as possible for the plasma, namely the *kinetic theory* of gases [108]: according to this, the physical state of a gas can be totally specified by the knowledge of the *distribution function* $f_\alpha(\boldsymbol{x}, \boldsymbol{v}, t)$ characterizing each of its particles. In particular, these quantities describe the density of particles of the species α (where $\alpha = e$ for electrons and $\alpha = i$ for ions, in case of a simple plasma) at the time t in the point $(\boldsymbol{x}, \boldsymbol{v})$ of a six-dimensional *phase space*. In this way, the quantity $f_\alpha(\boldsymbol{x}, \boldsymbol{v}, t)\, d^3\boldsymbol{x}\, d^3\boldsymbol{v}$ will represent the number of particles of the species α in the six-dimensional volume element $d^3\boldsymbol{x}\, d^3\boldsymbol{v}$.
By performing a balance for the quantity f_α over the a six-dimensional volume element, it can be deduced that the behavior of each of these particles can be described by equations, describing

the time evolution of each distribution function in the phase space, written in the form [108]

$$\frac{\partial f_\alpha}{\partial t} + \boldsymbol{v}_\alpha \cdot \frac{\partial f_\alpha}{\partial \boldsymbol{x}} + \frac{\boldsymbol{F}_\alpha}{m_\alpha} \cdot \frac{\partial f_\alpha}{\partial \boldsymbol{v}} = C_\alpha \tag{C.1}$$

(where $\partial/\partial\boldsymbol{x}$ denotes a gradient in $\boldsymbol{x}$ and $\partial/\partial\boldsymbol{v}$ denotes a gradient in $\boldsymbol{v}$), and best known as *Boltzmann equations*. Here, m_α is the mass of particles of species α, and $\boldsymbol{F}_\alpha$ is the force exerted at the location $\boldsymbol{x}$ of a particle of species α having velocity $\boldsymbol{v}$. For the case of ionized gases, where the particles of species α have a charge q_α, the force field is simply written as

$$\boldsymbol{F_\alpha} = q_\alpha(\boldsymbol{E} + \boldsymbol{v}_\alpha \times \boldsymbol{B}) \tag{C.2}$$

if the particles move in external electric and magnetic fields. Finally, the quantity C_α takes into account the effects of collisions between particles, which tend to modify the trend of the distribution functions with respect to a simply conserved quantity in the phase space.

In particular, since particles of species α can collide both with each other and with particles of other species, the term C_α must be written in the form

$$C_\alpha = \sum_\beta C_{\alpha\beta}(f_\alpha, f_\beta) \tag{C.3}$$

where $C_{\alpha\beta}$, called *collision term*, gives the unit time variation of the distribution function of particles of species α due to collisions with particles of species β.
In case of only binary elastic collisions being present, this collision term can be shown be simply given by [108]

$$C_{\alpha\beta}(f_\alpha, f_\beta) = \int [f_\alpha(\boldsymbol{v}')f_\beta(\boldsymbol{v}'_\beta) - f_\alpha(\boldsymbol{v})f_\beta(\boldsymbol{v}_\beta)]|\boldsymbol{v} - \boldsymbol{v}_\beta|\, d\sigma\, d^3\boldsymbol{v}_\beta \tag{C.4}$$

where $d\sigma$ is the differential cross section of scattering between charged particles (i.e. the Rutherford cross section), deduced from the laws of electromagnetism, into the element of solid angle $\sin\theta d\theta d\varphi$ for collisions of particles with relative velocity $|\boldsymbol{v} - \boldsymbol{v}_\beta|$. The variation on the distribution function carried out by each of the terms $C_{\alpha\beta}$ arises from the modification of the velocities of two colliding particles: this is taken into account in (C.4), considering that, before the collision, the particle α has velocity $\boldsymbol{v}$ and the particle β has velocity $\boldsymbol{v}_\beta$, while, after the collision, their velocities becomes respectively $\boldsymbol{v}'$, $\boldsymbol{v}'_\beta$, related to the initial velocities by the conservation of momentum and energy. In particular, the term $f_\alpha(\boldsymbol{v}')f_\beta(\boldsymbol{v}'_\beta)$ quantifies the particles entering into a volume element in the velocity space around $\boldsymbol{v}$, while the term $f_\alpha(\boldsymbol{v})f_\beta(\boldsymbol{v}_\beta)$ quantifies the loss of particles out of this volume resulting from collisions with particles β. Finally, the global effect is found by integrating over each possible initial velocity $\boldsymbol{v}_\beta$ and over each possible scattering direction.
Neglecting any processes eventually converting particles of one species into another species, the collision term must satisfy the conditions:

- $\int C_{\alpha\beta}\, d^3\boldsymbol{v}_\alpha = 0$, which states the conservation of the total number of particles in collisions.
- $\int m_\alpha \boldsymbol{v}_\alpha C_{\alpha\beta}\, d^3\boldsymbol{v}_\alpha + \int m_\beta \boldsymbol{v}_\beta C_{\beta\alpha}\, d^3\boldsymbol{v}_\beta = \boldsymbol{0}$, which states the conservation of total momentum in collisions (imposing that the momentum transferred from one particle to the other one is equal and opposite to the momentum gained by the other particle).
- $\int \frac{1}{2} m_\alpha v_\alpha^2 C_{\alpha\beta}\, d^3\boldsymbol{v}_\alpha + \int \frac{1}{2} m_\beta v_\beta^2 C_{\beta\alpha}\, d^3\boldsymbol{v}_\beta = 0$, which states the conservation of total energy in collisions (imposing that the energy transferred from one particle to the other one is equal and opposite to the energy gained by the other particle).

C.1.2 Braginskii equations

Solving the Boltzmann equations (C.1) for the distribution functions of each particle of the systems allows for the most complete and accurate description for the plasma. However, numerical modelling based on the kinetic description clearly results to be extremely heavy in computational requirements, and is then applied only to very specific problems.
Instead, a "simple" *fluid description* based on conservation relations for macroscopic plasma quantities (particles, momentum and energy) turns out to be valid if the characteristic length of the considered problem is much larger than the collisional mean free path of particles. This is because, in this case, the rate of collisions is sufficiently high to bring all the populations of particles in *thermal equilibrium*, with distribution functions depending only on their velocity, namely to a *maxwellian velocity distribution*

$$f(\boldsymbol{v}) = n\left(\frac{m}{2\pi T}\right)^{3/2} e^{-\frac{mv^2}{2T}} \tag{C.5}$$

In fact, it can be shown that, if the distribution function is supposed to change only by virtue of collisions, than any initial condition for the system will tend to approach a maxwellian distribution in the course of time, in a time scale of the order of the mean time between collisions, in a process usually called *relaxation* [108].

So, in describing a process whose characteristic time scales are sufficiently long to make relaxation occur, the system will be for sure in thermal equilibrium, and then the knowledge of quantities which are macroscopically averaged over the whole velocity space is sufficient to properly describe any populations of particles.
In this way, for each population α of particles, it is possible to define a *density*, that is the mean number of particles per unit volume, as

$$n_\alpha(\boldsymbol{x},t) \equiv \int f_\alpha(\boldsymbol{x},\boldsymbol{v},t)\, d^3\boldsymbol{v} \tag{C.6}$$

an *average velocity* of these, as

$$\boldsymbol{v}_\alpha(\boldsymbol{x},t) \equiv \langle \boldsymbol{v}_\alpha \rangle = \frac{1}{n_\alpha}\int \boldsymbol{v} f_\alpha(\boldsymbol{x},\boldsymbol{v},t)\, d^3\boldsymbol{v} \tag{C.7}$$

and a *temperature*, that is the mean thermal energy of these, as

$$T_\alpha(\boldsymbol{x},t) \equiv \frac{m_\alpha}{3}\langle(\boldsymbol{v}-\boldsymbol{v}_\alpha)^2\rangle = \frac{1}{n_\alpha}\int \frac{m_\alpha}{3}(\boldsymbol{v}-\boldsymbol{v}_\alpha)^2 f_\alpha(\boldsymbol{x},\boldsymbol{v},t)\, d^3\boldsymbol{v} \tag{C.8}$$

The equations describing the evolution of such macroscopic parameters can be then obtained from the Boltzmann equation (C.1) multiplying it by 1, $m_\alpha \boldsymbol{v}$ and $\frac{1}{2}m_\alpha v^2$, respectively, and integrating over the whole velocity space. What we obtain in this way are the so-called *transport equations*.
The derivation of the transport equations involves then considering a maxwellian distribution as (C.5) for the integration, and explicitating the collision term (C.4) for the case of coulomb collisions between charged particles. Finally, in order to take into account also the presence of external electric and magnetic fields $\boldsymbol{E}$, $\boldsymbol{B}$, the force field must be expressed as (C.2).
The whole calculations were firstly carried out by Braginskii in [109], for the simple case in which the plasma consists of only electrons and a single species of ions with charge state Z, and under the usual assumption of local quasineutrality (i.e. $n_e = Zn_i$) (for this reasons, the original transport equations for this case are also usually known as *Braginskii equations*). The resulting equations are:

- *Continuity equations*:

$$\frac{\partial n_e}{\partial t} + \nabla \cdot (n_e \boldsymbol{v}_e) = S_{n,e} \tag{C.9}$$

$$\frac{\partial n_i}{\partial t} + \nabla \cdot (n_i \boldsymbol{v}_i) = S_{n,i} \tag{C.10}$$

- *Momentum equations*:

$$\frac{\partial}{\partial t}(m_e n_e \boldsymbol{v}_e) + \nabla : (m_e n_e \boldsymbol{v}_e \boldsymbol{v}_e) = -\nabla p_e - \nabla : \underline{\underline{\boldsymbol{\Pi}}}_e - e n_e (\boldsymbol{E} + \boldsymbol{v}_e \times \boldsymbol{B}) + \boldsymbol{R} + \boldsymbol{S}_{\boldsymbol{v},e} \tag{C.11}$$

$$\frac{\partial}{\partial t}(m_i n_i \boldsymbol{v}_i) + \nabla : (m_i n_i \boldsymbol{v}_i \boldsymbol{v}_i) = -\nabla p_i - \nabla : \underline{\underline{\boldsymbol{\Pi}}}_i + Z e n_i (\boldsymbol{E} + \boldsymbol{v}_i \times \boldsymbol{B}) - \boldsymbol{R} + \boldsymbol{S}_{\boldsymbol{v},i} \tag{C.12}$$

- *Energy equations*:

$$\begin{aligned} &\frac{\partial}{\partial t}\left(\frac{3}{2} n_e T_e + \frac{1}{2} m_e n_e v_e^2\right) + \nabla \cdot \left[\left(\frac{5}{2} n_e T_e + \frac{1}{2} m_e n_e v_e^2\right) \boldsymbol{v}_e\right] = \\ &= -\nabla \cdot \boldsymbol{q}_e - \nabla \cdot (\underline{\underline{\boldsymbol{\Pi}}}_e \cdot \boldsymbol{v}_e) - e n_e \boldsymbol{E} \cdot \boldsymbol{v}_e + \boldsymbol{R} \cdot \boldsymbol{v}_i + Q + S_{E,e} \end{aligned} \tag{C.13}$$

$$\begin{aligned} &\frac{\partial}{\partial t}\left(\frac{3}{2} n_i T_i + \frac{1}{2} m_i n_i v_i^2\right) + \nabla \cdot \left[\left(\frac{5}{2} n_i T_i + \frac{1}{2} m_i n_i v_i^2\right) \boldsymbol{v}_i\right] = \\ &= -\nabla \cdot \boldsymbol{q}_i - \nabla \cdot (\underline{\underline{\boldsymbol{\Pi}}}_i \cdot \boldsymbol{v}_i) + Z e n_i \boldsymbol{E} \cdot \boldsymbol{v}_e - \boldsymbol{R} \cdot \boldsymbol{v}_i - Q + S_{E,i} \end{aligned} \tag{C.14}$$

In these equations, we find:

- A scalar *pressure* $p_\alpha = n_\alpha T_\alpha$, for each species.
- A *stress tensor* $\underline{\underline{\boldsymbol{\Pi}}}_\alpha$, for which it is necessary to assume some constitutive relation.
- A *heat flux density* $\boldsymbol{q}_\alpha$, for which it is necessary to assume some constitutive relation.
- A vector $\boldsymbol{R}$ describing the *collisional momentum transfer* from ions to electrons, given by a friction contribute due to the existence of an average relative velocity between the two populations, and a thermal contribute due to the temperature gradient.
- A quantity Q describing the *collisional heat transfer* from ions to electrons, due to the eventual difference in their temperature (i.e. ion-electron thermalization).
- Eventually, *volumetric source* terms for particles ($S_{n,\alpha}$), momentum ($S_{\boldsymbol{v},\alpha}$) and energy ($S_{E,\alpha}$).

C.1.3 Constitutive relations and transport coefficients

For completing the closure of the conservation equations will be then necessary to formulate some *constitutive relations* for the stress tensors and the heat flux densities, in order to express these quantities as functions of some physical characteristics of the systems by using some *transport coefficients* as proportionality coefficients. Such coefficients, which will definitely describe the collisional transport in the plasma, will clearly result to be functions of the electron/ion collision times τ_α (eqs. (A.9), (A.10)) and, since we are in the presence of a magnetic field, of the electron/ion gyrofrequencies Ω_α (eq. (A.6)).

In [109], Braginskii firstly performed a self-consistent closure of the conservation equations for the case of a fully ionized plasma in the presence of a magnetic field, under linearity assumptions for the stress tensors and the heat flux densities, obtaining then analytic expressions for the related transport coefficients.

The calculations were performed in the limit of $\Omega_e \tau_e \gg 1$, $\Omega_i \tau_i \gg 1$, meaning that consideration is given to a situation in which collisions take place so frequently that many collisions occur even during one gyration period. In other words, we are considering a situations in which transport is dominated by collisions, rather than by the collective motion of particles.

The actual expressions for the considered constitutive relations, and the related transport coefficients, are rather complicate. Here are reported, for simplicity, only the expressions derived for a simple plasma (i.e. $Z = 1$) in which, for each vector quantity, the component parallel to the magnetic field is indicated with the subscript $\|$, while the component perpendicular to the magnetic field is indicated with the subscript $\perp$.

The stress tensor $\underline{\underline{\mathbf{\Pi}}}_\alpha$ for each population is assumed to be defined by a linear constitutive relation

$$\underline{\underline{\mathbf{\Pi}}}_\alpha = -\eta_{0,\alpha} \underline{\underline{\boldsymbol{W}}}_\alpha \tag{C.15}$$

with $\underline{\underline{\boldsymbol{W}}}_\alpha$ strain tensor, with components

$$W_{jk} = \frac{\partial v_j}{\partial x_k} + \frac{\partial v_k}{\partial x_j} - \frac{2}{3}\delta_{jk} \nabla \cdot \boldsymbol{v} \tag{C.16}$$

The components of the stress tensor (which is then assumed to be symmetric) for both electrons and ions, in a coordinate system with magnetic field directed as the z axis, are then computed as

$$\begin{aligned}
\Pi_{xx} &= -\eta_0 \frac{1}{2}(W_{xx} + W_{yy}) - \eta_1 \frac{1}{2}(W_{xx} - W_{yy}) - \eta_3 W_{xy} \\
\Pi_{yy} &= -\eta_0 \frac{1}{2}(W_{xx} + W_{yy}) - \eta_1 \frac{1}{2}(W_{yy} - W_{xx}) + \eta_3 W_{xy} \\
\Pi_{zz} &= -\eta_0 W_{zz} \\
\Pi_{xy} &= -\eta_1 W_{xy} + \eta_3 \frac{1}{2}(W_{xx} - W_{yy}) \\
\Pi_{xz} &= -\eta_2 W_{xz} - \eta_4 W_{yz} \\
\Pi_{yz} &= -\eta_2 W_{yz} + \eta_4 W_{xz}
\end{aligned} \tag{C.17}$$

in which the coefficients η, stating a linear proportionality of the stress tensor with respect to the strain tensor, are called *viscosities*, and are given for the electrons by

$$\begin{aligned}
\eta_{0,e} &= 0{,}73\, n_e T_e \tau_e \\
\eta_{1,e} &= 0{,}51\, \frac{n_e T_e}{\Omega_e^2 \tau_e} \\
\eta_{2,e} &= 4\, \eta_{1,e} \\
\eta_{3,e} &= -\frac{1}{2} \frac{n_e T_e}{\Omega_e} \\
\eta_{4,e} &= 2\, \eta_{3,e}
\end{aligned} \tag{C.18}$$

and for the ions by

$$\begin{aligned}
\eta_{0,i} &= 0{,}96\, n_i T_i \tau_i \\
\eta_{1,i} &= 0{,}30\, \frac{n_i T_i}{\Omega_i^2 \tau_i} \\
\eta_{2,i} &= 4\, \eta_{1,i} \\
\eta_{3,i} &= \frac{1}{2} \frac{n_i T_i}{\Omega_i} \\
\eta_{4,i} &= 2\, \eta_{3,i}
\end{aligned} \tag{C.19}$$

Then, the heat flux density $\boldsymbol{q}_\alpha$ for each population is assumed to be constituted by a component linearly proportional to the local temperature gradient, for both electrons and ions, and by a friction component due to the existence of a net electric current $\boldsymbol{J}$, arising eventually in presence of a relative velocity $\boldsymbol{v}_e - \boldsymbol{v}_i$, that is $\boldsymbol{J} = -e(n_e\boldsymbol{v}_e - n_i\boldsymbol{v}_i)$ (the last component arising only for electrons).
With this assumption, the electron heat flux density is computed to be

$$\boldsymbol{q}_e = -\kappa_{\parallel,e}\nabla_\parallel T_e - \kappa_{\perp,e}\nabla_\perp T_e - \frac{5}{2}\frac{n_e T_e}{eB}\frac{\boldsymbol{B}}{B} \times \nabla T_e - 0{,}71\, T_e\frac{\boldsymbol{J}_\parallel}{e} - \frac{3}{2}\frac{T_e}{e\Omega_e\tau_e B}\boldsymbol{B} \times \boldsymbol{J}_\perp \tag{C.20}$$

and the ion flux density is computed to be

$$\boldsymbol{q}_i = -\kappa_{\parallel,i}\nabla_\parallel T_i - \kappa_{\perp,i}\nabla_\perp T_i + \frac{5}{2}\frac{n_i T_i}{eB}\frac{\boldsymbol{B}}{B} \times \nabla T_i \tag{C.21}$$

in which the coefficients κ, stating a linear proportionality of the components of the heat flux density with respect to the temperature gradient, in parallel and perpendicular direction, are called *thermal conductivities*, and are given for the electrons by

$$\begin{aligned} \kappa_{\parallel,e} &= 3{,}16\,\frac{n_e T_e \tau_e}{m_e} \\ \kappa_{\perp,e} &= 4{,}66\,\frac{n_e T_e}{m_e \Omega_e^2 \tau_e} \end{aligned} \tag{C.22}$$

and for the ions by

$$\begin{aligned} \kappa_{\parallel,i} &= 3{,}9\,\frac{n_i T_i \tau_i}{m_i} \\ \kappa_{\perp,i} &= 2\,\frac{n_i T_i}{m_i \Omega_i^2 \tau_i} \end{aligned} \tag{C.23}$$

The momentum transfer vector, sum of a friction force and a thermal force, is then computed as

$$\boldsymbol{R} = e n_e \left(\frac{\boldsymbol{J}_\parallel}{\sigma_\parallel} + \frac{\boldsymbol{J}_\perp}{\sigma_\perp}\right) - 0{,}71\, n_e \nabla_\parallel T_e - \frac{3}{2}\frac{e n_e^2}{\sigma_\perp B}\frac{\boldsymbol{B}}{B} \times \nabla T_e \tag{C.24}$$

where the coefficients σ, called *electrical conductivities*, are given by

$$\begin{aligned} \sigma_\parallel &= 1{,}96\,\frac{e^2 n_e \tau_e}{m_e} \\ \sigma_\perp &= \frac{e^2 n_e \tau_e}{m_e} \end{aligned} \tag{C.25}$$

Finally, the energy exchange term Q due to the collisions between electrons and ions is computed to be

$$Q = 3\,\frac{m_e}{m_i}\frac{n_e}{\tau_e}(T_i - T_e) \tag{C.26}$$

being the coefficient $3\,\frac{m_e}{m_i}\frac{n_e}{\tau_e}$ proportional to the inverse of the thermalization time τ_{th} (eq. (A.14)).

C.2 Physics of B2.5

As it was discussed in Chapter 2, a description for the plasma edge in magnetic fusion devices has to include both the cross-field *perpendicular transport*, which is dominant inside the separatrix, and the *parallel transport* along field lines, which basically controls the transport outside the separatrix up to the material boundaries. Therefore, at least a two-dimensional description of plasma edge modelling is required.
Although plasma particles move along field lines which are twisted around the toroidal flux surfaces in current fusion devices, therefore in an inherently 3D motion, it is actually possible to construct a pure 2D description of plasma parameters because of the axial symmetry of tokamak geometry. Therefore, numerical plasma edge models are usually constructed as *two-dimensional models*, in which it is sufficient to model the evolution of plasma parameters as seen in an arbitrary *poloidal plane* of the torus.
This is true in particular also for B2.5, the program dedicated to the numerical modelling of plasma particles in SOLPS-ITER, whose physics will be discussed in this section. As it was already mentioned in the Chapter 4, B2.5 solves a set of modified Braginskii equations, obtained employing several simplifications and assumptions to the complete equations, describing the two-dimensional poloidal and radial transport of single- or multi-species plasmas in a poloidal plane, assuming toroidal symmetry. The aim of this section is just to explore more in depth the physics on which B2.5 is constructed.

C.2.1 Validity of the fluid approximation

The evolution of electrons and ions as computed by B2.5 is considered within a *fluid approximation*. The reason for this is the achievement of enormously faster computation times with respect to the case of a full kinetic treatment, with the results still being in good agreement with experimental results [67]. Here we see why a fluid description of plasma particles in the framework of plasma edge modelling turns out to be, indeed, valid within acceptable approximation.

As it was already pointed out in the Section C.1.2, the derivation of some fluid equations, as it was performed by Braginskii, involves a computation of the collision term in the Boltzmann equation (eq. (C.1)) involves an expansion of the distribution function around a maxwellian form (eq. (C.5)); therefore, the system is implicitly assumed to be in thermal equilibrium. For this to be true, a maxwellian distribution for particles must be achieved faster than how it is perturbed again from the macroscopic evolution of the system; this means that he relaxation process must be completed in a time shorter than the time scale for the evolution of the eventual fluid quantities, so that the system can be effectively described by equations controlling the evolution of these quantities [22]. In other words, the processes leading to the relaxation (that is the collisions between particles) must take place faster than the macroscopic time scales of the system, i.e. the time variation of the fluid quantities must be slow with respect to the collision times for both electrons and ions, that is

$$\frac{\partial}{\partial t} \ll \frac{1}{\tau_\alpha} \tag{C.27}$$

and the spatial variation of the same must be larger than the average distances travelled by particles between collisions, that is

$$L_{\parallel} \gg \lambda_\alpha \tag{C.28}$$

where $L_{\parallel}$ is a characteristic parallel length for the system and λ_α is the collisional mean free path. For the case of the plasma edge, $L_{\parallel}$ can be safely defined with respect to the scale length for the parallel variation of the magnetic field intensity, that is $L_\parallel \equiv \left|\frac{\nabla_\parallel B}{B}\right|^{-1}$, which approximately equates the parallel connection length at the separatrix $L_\parallel \approx \pi R q_{sep}$.

Taking ASDEX Upgrade as an example, for which $L_\parallel \approx 16$ m, considering average SOL densities about 10^{19} m^{-3} and average SOL temperatures about 10 eV, and taking $\ln\Lambda \approx 15$, the electron/ion collision times (eqs. (A.9), (A.10)) can be estimates as

$$\begin{aligned} \tau_e &\approx 7{,}3 \cdot 10^{-8}\ \mathrm{s} \\ \tau_i &\approx 4{,}4 \cdot 10^{-6}\ \mathrm{s} \end{aligned} \tag{C.29}$$

which are evidently shorter than any time scale of interest for macroscopic plasma edge modelling. Then, writing the collisional mean free paths as $\lambda_\alpha \equiv v_{th,\alpha}\tau_\alpha$, with $v_{th,\alpha} = \left(\frac{T_\alpha}{m_\alpha}\right)^{1/2}$ thermal velocities of particles, these can be estimated as

$$\begin{aligned} \lambda_e &\approx 0{,}17\ \mathrm{m} \\ \lambda_i &\approx 0{,}09\ \mathrm{m} \end{aligned} \tag{C.30}$$

which are evidently shorter than the characteristic parallel length scaled in the edge plasma. From this we can conclude that the plasma edge in ASDEX Upgrade is likely to be collisional enough for the fluid approximation to be valid.

However, strictly speaking, the condition (C.28) turns out to be not fulfilled in the thin plasma-material interface layer, the sheath, since this is a region where steep gradients of density and temperature exist, so that the fluid approximation cannot be expected to properly describe the physics of this region [22]. For this reason, as it will described better in the Section C.2.5, in fluid codes for plasma edge modelling it is customary to take the sheath entrance as the boundary of the computational domain, rather than the actual plasma-material interaction, and to impose appropriate boundary conditions here.

C.2.2 Curvilinear coordinates in toroidal geometry

The previous section basically told us that a fluid model for the plasma edge, based then on the Braginskii equations, is valid. However, in order to be able to properly model the plasma edge in toroidal devices, it is necessary to convert these equations, given for a general reference system, in a reference system set up for a *toroidal geometry*. We must then implement a mathematical treatment of these in curvilinear coordinates, which can be derived from a general orthogonal system through appropriate coordinate transformations.

In detail, the position

$$\boldsymbol{x} = x\boldsymbol{e}_x + y\boldsymbol{e}_y + z\boldsymbol{e}_e \tag{C.31}$$

of a given point in a cartesian reference frame, with $\boldsymbol{e}_x$, $\boldsymbol{e}_y$, $\boldsymbol{e}_z$, the three cartesian orthonormal basis vectors, can also be specified by a triplet of *orthogonal curvilinear coordinates* (q_1, q_2, q_3) whose coordinate axes are generally no fixed in direction, whose local basis vectors will be

$$\boldsymbol{h}_i = \frac{\partial \boldsymbol{x}}{\partial q_i} \tag{C.32}$$

This will be a local basis, meaning that its vectors change their length and direction from point to point. Therefore, it is not the most convenient basis for dealing with physical problems, since the description of a physical vector in terms of this basis will not generally have the correct physical dimensions.

For obtaining the corresponding curvilinear orthonormal basis vectors $\boldsymbol{e}_i$, it is possible to introduce the so-called *metric coefficients*

$$h_i \equiv |\boldsymbol{h}_i| = \left|\frac{\partial \boldsymbol{x}}{\partial q_i}\right| \tag{C.33}$$

from which the basis vectors can be finally normalized as

$$\boldsymbol{e}_i = \frac{\boldsymbol{h}_i}{h_i} \tag{C.34}$$

In this way, writing a generic physical vector $\boldsymbol{A}$ in terms of these, i.e. as $\boldsymbol{A} = A_i \boldsymbol{e}_i$, its components A_i will have for sure the correct physical dimensions, for which reasons they are called *physical components*.

Now, in order to shift from a cartesian system (x, y, z), with orthonormal basis $(\boldsymbol{e}_x, \boldsymbol{e}_y, \boldsymbol{e}_z)$, to an arbitrary curvilinear orthogonal system (q_1, q_2, q_3), with orthonormal basis $(\boldsymbol{e}_1, \boldsymbol{e}_2, \boldsymbol{e}_3)$, it will be necessary to set up the *coordinate transformation*

$$\begin{aligned}
\boldsymbol{e}_1 &= \frac{\partial x}{\partial q_1}\boldsymbol{e}_x + \frac{\partial y}{\partial q_1}\boldsymbol{e}_y + \frac{\partial z}{\partial q_1}\boldsymbol{e}_z \\
\boldsymbol{e}_2 &= \frac{\partial x}{\partial q_2}\boldsymbol{e}_x + \frac{\partial y}{\partial q_2}\boldsymbol{e}_y + \frac{\partial z}{\partial q_2}\boldsymbol{e}_z \\
\boldsymbol{e}_3 &= \frac{\partial x}{\partial q_3}\boldsymbol{e}_x + \frac{\partial y}{\partial q_3}\boldsymbol{e}_y + \frac{\partial z}{\partial q_3}\boldsymbol{e}_z
\end{aligned} \tag{C.35}$$

which defines the *jacobian matrix* $\underline{\underline{\boldsymbol{J}}}$ of the transformation, with components

$$J_{\alpha\beta} \equiv \frac{\partial x_\alpha}{\partial q_\beta} \tag{C.36}$$

The metric of the space, written as

$$d\boldsymbol{x} \cdot d\boldsymbol{x} = \frac{\partial x_k}{\partial q_i}\frac{\partial x_k}{\partial q_j} dq_i dq_j \tag{C.37}$$

can be used to define the so-called *metric tensor* of the considered curvilinear coordinates as having components

$$g_{ij} \equiv \frac{\partial x_k}{\partial q_i}\frac{\partial x_k}{\partial q_j} \tag{C.38}$$

The metric tensor will then fully describe the geometry of the curvilinear system with respect to the one of a fixed cartesian system, since it describes the transformation of a generic line elements between these.
So, since it turns out that $g_{ij} = h_i h_j$, the metric coefficients can be redefined as

$$h_i = \sqrt{g_{ii}} \tag{C.39}$$

Finally, one can define the quantity $\sqrt{g}$ as

$$\sqrt{g} \equiv \sqrt{g_{ii} g_{jj} g_{kk}} = h_i h_j h_k \;\Rightarrow\; \sqrt{g} = \det \underline{\underline{\boldsymbol{J}}} \tag{C.40}$$

which is then shown to relate the metric coefficients with the jacobian of the transformation.

These concepts allows to fully describe a toroidal geometry in the most adequate curvilinear coordinates. The forthcoming discussion of this follows [22].

In particular, as the three components of the plasma motion are directed parallel to the magnetic field (parallel direction $\|$), perpendicular to it in the magnetic flux surface (diamagnetic direction $\perp$) and perpendicular to it normal the flux surfaces (radial direction r), this is in principle best resolved in such an orthogonal system $(\|, \perp, r)$. On the other hand, the toroidal symmetry of tokamaks more easily allows to describe the plasma in another orthogonal system making use of toroidal direction φ and poloidal direction θ for describing the parallel + diamagnetic motion; in this way, the toroidal coordinate φ becomes de facto ignorable, making possible a simpler two-dimensional description rather than the full three-dimensional one. This is description adopted in B2.5, with plasma particles motion being then resolved in a so-called *poloidal coordinate system* (φ, θ, r).

In this sense, we could consider the system $(\|, \perp, r)$ as a "dynamic" frame, since it follows in each point the actual motion of plasma particles, and the system (φ, θ, r) as a "geometric frame", since it follows the topology of the magnetic field lines. In each case, the two systems will turn out to differ only the orientation of the two basis vectors which are tangent to the flux surfaces, as we can see in the Fig. C.1.

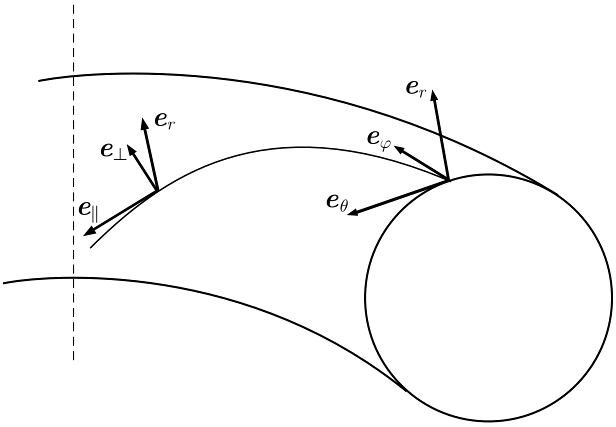

Figure C.1: Coordinate axes of parallel system $(\|, \perp, r)$ and poloidal system (φ, θ, r).

Using the definitions for the two systems of basis vectors, it is possible to deduce mutual relations between then. In particular, considering the physical components of the magnetic field $\boldsymbol{B}$, the two systems are definitely related by

$$\boldsymbol{B} \equiv B\boldsymbol{e}_\| = B_\varphi \boldsymbol{e}_\varphi + B_\theta \boldsymbol{e}_\theta \tag{C.41}$$

since the parallel direction is, by definition, the direction of $\boldsymbol{B}$, so that

$$\boldsymbol{e}_\| = \frac{B_\varphi}{B}\boldsymbol{e}_\varphi + \frac{B_\theta}{B}\boldsymbol{e}_\theta \tag{C.42}$$

Then, the diamagnetic basis vector is perpendicular to the parallel basis vector and directed tangent to the flux surface, which means that is can be also expressed as a linear combination of the toroidal and poloidal basis vectors; after a choice for the direction of $\boldsymbol{e}_\perp$ (for example as in the Fig. C.1) we would find

$$\boldsymbol{e}_\perp = -\frac{B_\theta}{B}\boldsymbol{e}_\varphi + \frac{B_\varphi}{B}\boldsymbol{e}_\theta \tag{C.43}$$

In this way, considering that a generic vector $\boldsymbol{A}$ can be written in both the coordinate systems, leading to $A_\varphi \boldsymbol{e}_\varphi + A_\theta \boldsymbol{e}_\theta + A_r \boldsymbol{e}_r = A_\| \boldsymbol{e}_\| + A_\perp \boldsymbol{e}_\perp + A_r \boldsymbol{e}_r$, using the just defined coordinate transformations (eqs. (C.42),(C.43)) the physical components for a vector will transform as

$$\begin{aligned} A_\varphi &= \frac{B_\varphi}{B} A_\| \\ A_\theta &= \frac{B_\theta}{B} A_\| \end{aligned} \tag{C.44}$$

C.2.3 Computational domain of B2.5

As it was also widely discussed in the Chapter 4, the physical region of interest for plasma edge modelling, on which the plasma evolution is computed by B2.5, consists in a thin annulus of the outer core plasma and entire scrape-off layer, fully including private flux region and divertor region [18].
The computational grid consists in quadrilaterals, with two of the sides aligned along the magnetic flux surfaces, with high-resolution regions defined by the expected presence of steep gradients for physical quantities (which mostly occur close to the divertor targets and near the separatrix) [18]. For the case of ASDEX Upgrade it can consist of 48 cells in poloidal direction and 18 cells in radial direction (as it was for this work) or, if a generally higher resolution is required, of 96 cells in poloidal direction and 36 cells in radial direction. In each case, since the grid is generated after the knowledge of magnetic equilibrium configuration of the scenario to be modelled, the strict alignment of this with the flux surfaces will make the radial stepping of cells follow the flux expansion (cfr. Section 2.1.1). In this way, cells are more radially distanced near the targets with respect to the upstream region, and, moreover, the radial stepping will follow the expansion/compression of the flux surfaces at the inner/outer sides of the torus respectively, as resulting from the Shafranov shift (cfr. Appendix A.2.3).

The physical domain is translated in a (x, y) orthogonal coordinate system, where x, y are uniformly distanced *cell coordinates*, with x representing the orthogonalized *poloidal coordinate* θ and y representing the orthogonalized *radial coordinate* r. The equations are then solved through finite-difference calculations in such a curvilinear orthogonal system after the employment of adequate metric coefficients describing the coordinate transformation $(\theta, r) \rightarrow (x, y)$ of the physical domain into the computational domain, obtained by the grid generator code itself by conformal mapping [18]. The advantage of the orthogonality of the coordinate system in which the equations are actually solved is that it ensured that all the fluxes out of a volume element can be specified between the cell itself and those neighboring its faces, rather than involving other cells adjoining just its edges, simplifying then the discretized equations [18].
For obtaining the computational domain as it is actually mapped in B2.5, the physical domain is cut along a vertical line passing through the X-point and reformed into the topologically equivalent rectangular domain, so that such fictitious line appears now as two internal boundaries (Fig. C.2).

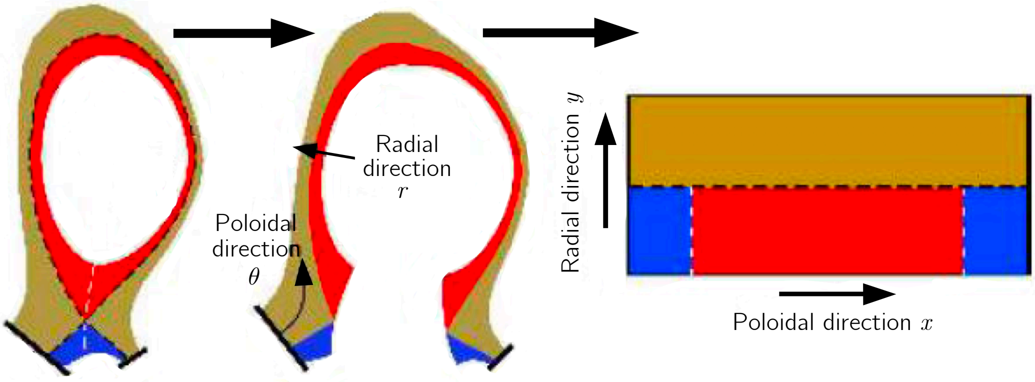

Figure C.2: Transformation of the physical domain into the topologically rectangular computational domain.

In each case, in order to extend the computations over the whole toroidal length of the torus, each cell is supposed to have a third spatial dimension z, representing the toroidal direction φ, along which each of these has length $2\pi R$, with R local major radius.

C.2.4 Equations in B2.5

For obtaining the equations which are practically solved by B2.5, it is then necessary to adapt the Braginskii equations, presented in the Section C.1.2, to the curvilinear coordinates (θ, r), and then perform a transformation to the orthogonal cell coordinates (x, y).
For doing this, the metric coefficients h_x, h_y, h_z have to be defined for each cell of the rectangular mesh, in such a way for resulting in a jacobian $\sqrt{g} = h_x h_y h_z$. While $h_z = 2\pi R$, the other two coefficients will vary from cell to cell, according to the local geometry. Following their definition (eq. (C.33)), the coefficients h_x, h_y for each cell must be such that any line element ds in the physical geometry can be described, with the same length, also in the orthogonalized geometry, i.e. by imposing that

$$ds^2 = h_x^2 (dx)^2 + h_y^2 (dy)^2 \tag{C.45}$$

Applying this, it is possible to adapt the vector operations and the differentiation operators present in the Braginskii equations for giving results in the cell coordinates (x, y). In particular, it $\boldsymbol{e}_x$, $\boldsymbol{e}_y$ are the unit vectors defining the directions of the computational domain, with straightforward calculations it is possible to show that, given a generic scalar function $\Phi(\theta, r) \to \Phi(x, y)$, its gradient can be computed as

$$\nabla \Phi = \frac{1}{h_x} \frac{\partial \Phi}{\partial x} \boldsymbol{e}_x + \frac{1}{h_y} \frac{\partial \Phi}{\partial y} \boldsymbol{e}_y \tag{C.46}$$

while, given a generic vector function $\boldsymbol{A}(\theta, r) \to \boldsymbol{A}(x, y)$, its divergence can be computed as

$$\nabla \cdot \boldsymbol{A} = \frac{1}{\sqrt{g}} \left[\frac{\partial}{\partial x} \left(\frac{\sqrt{g}}{h_x} A_x \right) + \frac{\partial}{\partial y} \left(\frac{\sqrt{g}}{h_y} A_y \right) \right] \tag{C.47}$$

According to what just defined, in the equations implemented in B2.5 the following notation for indicating the various component of the particles motion is adopted [18]:

- v_x denotes the physical component of the velocity in the poloidal direction.
- v_y denotes the physical component of the velocity in the radial direction.
- v_z denotes the physical component of the velocity in the toroidal direction.
- $v_\parallel \equiv \frac{B}{B_\theta} v_x$ denotes the physical component of the velocity in the parallel direction.
- $v_\perp \equiv \frac{B}{B_\varphi} v_z$ denotes the physical component of the velocity in the diamagnetic direction.

Assuming a static and given magnetic field, in describing a *pure hydrogenic plasma* (as it is considered in this work), supposed as quasi-neutral (so that $n_e = n_i$), we have in general ten unknowns: the density, the three components of the flow velocity, the electron and ion temperatures, the three components of the electric current density and the electrostatic potential. The full derivation of the corresponding ten equations, obtained transforming the Braginskii equations in a poloidal coordinate system (φ, θ, r), and their successive transformation into the cell coordinates system (x, y, z), can be found in [22]; here we just summarize the results, reporting not the full equations but only as they were considered in this work.

In particular, the equations which are effectively solved by B2.5 are usually a reduced set of full equations, since extra simplifications are employed in order to greatly reduce the computation time without losing much accuracy in the results. The additional assumptions that are usually done are [18]:

- All drift motions of the charged plasma particles are totally neglected, so that each component of the flow velocity derives only from the transport processes acting in that particular direction. This yields a general simplification of all the equations, allowing to neglect several terms in these.

- A pure ambipolar flow is assumed, so that no electric current is considered in the entire domain. This allows to consider a single momentum conservation equation, for both electrons and ions, to remove other several terms from the fluid equations, and, in addition, it makes not necessary anymore to solve a conservation equation for the electrostatic potential.
- The stress tensor in the momentum conservation equation is simplified, neglecting cross-field derivative terms, and the flow velocity in diamagnetic direction is neglected.

Then, the following assumptions are generally done for the transport processes:

- Transport in parallel direction, along the magnetic field lines, is supposed to be purely (neo)classical, after the assumption of the plasma being in a highly collisional regime [18]. In this way, in the equations we consider a viscosity and electron/ion thermal conductivities in the x direction as simply scaled by the parallel transport coefficients in the Braginskii formulation. So, firstly, the ion viscosity is taken as

  $$\eta_{x,i} \propto \frac{B_\theta^2}{B^2}\eta_{\parallel,i} \tag{C.48}$$

  where $\eta_{\parallel,i} = 0{,}96\, n_e T_i \tau_i$ (first eq. of (C.19)). Then, the electron thermal conductivity is

  $$\kappa_{x,e} \propto \frac{B_\theta^2}{B^2}\kappa_{\parallel,e} \tag{C.49}$$

  where $\kappa_{\parallel,e} = 3{,}16\, \frac{n_e T_e \tau_e}{m_e}$ (first eq. of (C.22)), while the ion thermal conductivity is

  $$\kappa_{x,i} \propto \frac{B_\theta^2}{B^2}\kappa_{\parallel,i} \tag{C.50}$$

  where $\kappa_{\parallel,e} = 3{,}9\, \frac{n_e T_i \tau_i}{m_i}$ (first eq. of (C.23)).
  While the functional dependence of the classical transport coefficients is the same as found by Braginskii, in the last versions of the code improved numerical prefactors, which take into account the neoclassical effects of toroidicity, are implemented. In particular, in the version included in SOLPS-ITER, the implemented numerical prefactors follow the computations performed in [124].
  However, it is customary to implement so-called flux limiters, through which one can impose limits for the classical viscosity and thermal conductivities to become relevant in case of large parallel fluxes (for taking into account the lack of validity that the linear constitutive relations for parallel momentum and heat transport could suffer in case of large parallel gradients, which could likely occur near sheath entrance) [18].
- The cross-field perpendicular transport is assumed to be purely anomalous, following the experimental evidence of anomalous contribution due to to turbulence effects being much stronger than the classical contribution (cfr. Appendix A.3.4). Therefore, in the radial transport equations, all classical terms for radial fluxes are neglected, and the classical values of radial velocities are replaced by simple diffusive expressions (as eq. (A.31)). In the most basic version of the code, it has then to be defined an anomalous *particle diffusivity* D_n, which drives a radial particle flux proportionally to the radial density gradient, and anomalous electron/ion *thermal diffusivities* χ_e, χ_i, which drive radial electron/ion heat fluxes proportionally to the relative temperature gradients [18].
  These can be specified as uniform in the whole domain, or it can be implemented some radial variation (for fitting better the experimental radial plasma profiles) as well as some poloidal variation (for considering an eventual ballooning nature of some phenomena).
  No anomalous ion viscosity was instead imposed in the performed simulations, so that for $\eta_{y,i}$ its (neo)classical expression was simply used.

With the just considered simplifications and assumptions, what keeps to be necessary is a reduced set of six equations, governing the evolution of (electron) density n_e, parallel $v_\parallel$, radial v_y and toroidal v_z flow velocity components, and electron T_e and ion T_i temperatures. The resulting form of the equations is [18]:

- *Continuity equation*:

$$\frac{\partial n_e}{\partial t} + \frac{1}{\sqrt{g}}\frac{\partial}{\partial x}\left[\frac{\sqrt{g}}{h_x} n_e (v_x + v_z)\right] + \frac{1}{\sqrt{g}}\frac{\partial}{\partial y}\left(\frac{\sqrt{g}}{h_y} n_e v_y\right) = S_n \tag{C.51}$$

- *Parallel momentum balance*:

$$\begin{gathered}\frac{\partial}{\partial t}(m_i n_e v_\parallel) + \\ \frac{1}{\sqrt{g}}\frac{\partial}{\partial x}\left[\frac{\sqrt{g}}{h_x} m_i n_e (v_x + v_z) v_\parallel - \frac{\sqrt{g}}{h_x^2}\eta_{x,i}\frac{\partial v_\parallel}{\partial x}\right] + \frac{1}{\sqrt{g}}\frac{\partial}{\partial y}\left[\frac{\sqrt{g}}{h_y} m_i n_e v_y v_\parallel - \frac{\sqrt{g}}{h_y^2}\eta_{y,i}\frac{\partial v_\parallel}{\partial y}\right] = \\ = \frac{B_\theta}{B}\frac{1}{h_x}\left(-\frac{\partial p_i}{\partial x} - \frac{\partial p_e}{\partial x}\right) + F + S_{m_i v_\parallel}\end{gathered} \tag{C.52}$$

- *Diffusion equations*:

$$v_y = -\frac{1}{h_y}\frac{D_n}{n_e}\frac{\partial n_e}{\partial y} \tag{C.53}$$

$$v_z = -\frac{1}{h_x}\frac{D_n}{n_e}\frac{\partial n_e}{\partial x} \tag{C.54}$$

- *Electron energy balance*:

$$\begin{gathered}\frac{\partial}{\partial t}\left(\frac{3}{2} n_e T_e\right) + \\ \frac{1}{\sqrt{g}}\frac{\partial}{\partial x}\left(\frac{\sqrt{g}}{h_x}\frac{5}{2} n_e v_x T_e - \frac{\sqrt{g}}{h_x^2}\kappa_{x,e}\frac{\partial T_e}{\partial x}\right) + \frac{1}{\sqrt{g}}\frac{\partial}{\partial y}\left(\frac{\sqrt{g}}{h_y}\frac{5}{2} n_e v_y T_e - \frac{\sqrt{g}}{h_y^2} n_e \chi_e \frac{\partial T_e}{\partial y}\right) = \\ = \frac{v_x}{h_x}\frac{\partial p_e}{\partial x} + \frac{v_y}{h_y}\frac{\partial p_e}{\partial y} - k(T_e - T_i) + S_{E,e}\end{gathered} \tag{C.55}$$

- *Ion energy balance*:

$$\begin{gathered}\frac{\partial}{\partial t}\left(\frac{3}{2} n_e T_i + \frac{1}{2} m_i n_e v_\parallel^2\right) + \\ + \frac{1}{\sqrt{g}}\frac{\partial}{\partial x}\left[\frac{\sqrt{g}}{h_x}\left(\frac{5}{2} n_e (v_x + v_z) T_i + \frac{1}{2} m_i n_e (v_x + v_z) v_\parallel^2\right) - \frac{\sqrt{g}}{h_x^2}\left(\kappa_{x,i}\frac{\partial T_i}{\partial x} + \frac{1}{2}\eta_{x,i}\frac{\partial v_\parallel^2}{\partial x}\right)\right] + \\ + \frac{1}{\sqrt{g}}\frac{\partial}{\partial y}\left[\frac{\sqrt{g}}{h_y}\left(\frac{5}{2} n_e v_y T_i + \frac{1}{2} m_i n_e v_y v_\parallel^2\right) - \frac{\sqrt{g}}{h_y^2}\left(n_e \chi_i \frac{\partial T_i}{\partial y} + \frac{1}{2}\eta_{y,i}\frac{\partial v_\parallel^2}{\partial y}\right)\right] = \\ = -\frac{v_x}{h_x}\frac{\partial p_e}{\partial x} - \frac{v_y}{h_y}\frac{\partial p_e}{\partial y} + k(T_e - T_i) + S_{E,i}\end{gathered} \tag{C.56}$$

where the terms with m_e have been neglected anywhere, $p_e \equiv n_e T_e$, $p_i \equiv n_e T_i$ are the electron/ion static pressures, S_n, $S_{m_i v_\parallel}$, $S_{E,e}$, $S_{E,i}$ are the volumetric source terms of particles, parallel momentum, electron energy and ion energy respectively, and $k(T_e - T_i)$ is the rate of energy transfer from electron to ions through collisions (i.e. ion-electron thermalization mechanism), where $k \equiv 3\,\frac{m_e}{m_i}\frac{n_e}{\tau_e}$.

In particular, such model equations will yield the following definitions for the various flux densities in the computational domain [18]:

- *Poloidal particle flux density*, given by classical flux plus anomalous contribution:

$$\Gamma_x \equiv n_e v_x - D_n \frac{1}{h_x}\frac{\partial n_e}{\partial x} \tag{C.57}$$

- *Radial particle flux density*, given by purely anomalous contribution:

$$\Gamma_y \equiv -D_n \frac{1}{h_y}\frac{\partial n_e}{\partial y} \tag{C.58}$$

- *Poloidal momentum flux density*, associated to the poloidal particle transport:

$$\pi_x \equiv m_i \Gamma_x v_\parallel - \eta_{x,i}\frac{1}{h_x}\frac{\partial v_\parallel}{\partial x} \tag{C.59}$$

- *Radial momentum flux density*, associated to the radial particle transport:

$$\pi_y \equiv m_i \Gamma_y v_\parallel - \eta_{y,i}\frac{1}{h_y}\frac{\partial v_\parallel}{\partial y} \tag{C.60}$$

- *Poloidal energy flux density*, given by a convection heat flux and a kinetic energy flow (associated to the poloidal particle transport), a conduction heat flux (associated to the poloidal temperature gradient) and a term associated to the work of the viscous forces:

$$q_x \equiv \frac{5}{2}\Gamma_x (T_e + T_i) + \frac{1}{2} m_i \Gamma_x v_\parallel^2 - \frac{1}{h_x}\left(\kappa_{x,e}\frac{\partial T_e}{\partial x} + \kappa_{x,i}\frac{\partial T_i}{\partial x}\right) - \frac{1}{2}\eta_{x,i}\frac{1}{h_x}\frac{\partial v_\parallel^2}{\partial x} \tag{C.61}$$

- *Radial energy flux density*, given by a convection heat flux and a kinetic energy flow (associated to the radial particle transport) and a conduction heat flux (associated to the radial temperature gradient) and a term associated to the work of the viscous forces:

$$q_y \equiv \frac{5}{2}\Gamma_y (T_e + T_i) + \frac{1}{2} m_i \Gamma_y v_\parallel^2 - \frac{1}{h_y} n_e \left(\chi_e \frac{\partial T_e}{\partial y} + \chi_i \frac{\partial T_i}{\partial x}\right) - \frac{1}{2}\eta_{y,i}\frac{1}{h_y}\frac{\partial v_\parallel^2}{\partial y} \tag{C.62}$$

C.2.5 Boundary conditions in B2.5

The numerical implementation of *boundary conditions* in B2.5 is obtained by introducing additional small volume elements along the boundaries, called *guard cells*, which are just used for setting arbitrary physical parameters at the boundary without performing any actual calculations on them [22]. So, for example, in case of a 48×18 grid, the actual number of cells will be 50×20, with the bottom/top rows and the leftmost/rightmost columns reserved for specification of the boundary conditions.

Various different plasma parameters can be prescribed as boundary conditions, i.e. [22]:

- A *constant flux density* Γ_Φ of a quantity Φ through the interface between a boundary cell and the neighboring guard cell. This is done by putting a source/sink

$$S = -\Gamma_\Phi A \tag{C.63}$$

  which can be constant or function of the local parameters, in the guard cell, otherwise isolated, with A physical area of the boundary.

- A *constant quantity* Φ on a boundary cell. This is done by putting a constant source/sink S in the neighboring guard cell, and defining here the same quantity Φ_g; in this way, using a very high transport coefficient h between the two cells, the definition of the sink as
$$S = -h(\Phi - \Phi_g) \tag{C.64}$$
will lead to $\Phi \approx \Phi_g$, so that in the boundary cell the considered quantity assumes the same value as in the neighboring guard cell.
- A *constant gradient* $\frac{\partial \Phi}{\partial s}$ of a quantity Φ at the boundary. This, which in discretized form is written as $\frac{\partial \Phi}{\partial s} \approx \frac{\Phi_b - \Phi_g}{\Delta s} = C$, where Δs is the physical distance between the boundary cell and the guard cell, is imposed by putting on the guard cell a value Φ_g for the quantity given by
$$\Phi_g = \Phi_b - C\Delta s \tag{C.65}$$
in function of its value Φ_b on the boundary cell.

The typical boundary conditions for B2.5, most commonly used in the SOLPS-ITER runs are [22]:

- *Core plasma boundary* (middle part of the south boundary of the computational domain): usually here given values of radial particle and heat fluxes are prescribed, for imposing an input of particles and heat from the inner core plasma, in combination with a zero parallel velocity; alternatively, it is also possible to prescribe given values of density and temperature.
- *First wall boundary* (north boundary of the computational domain): usually here a given values of temperature or radial temperature gradient are imposed, together with a zero radial gradient for density and for parallel velocity.
- *Divertor targets* (west and east boundaries of the computational domain): these are considered as the sheath entrances, so that, according to the Bohm criterion, the parallel velocity is set to be equal to the local plasma sound speed. Therefore, the poloidal particle flux onto divertor targets is set as $\Gamma_{x,div} \equiv n_e v_{x,div} \equiv n_e \frac{B_\theta}{B} c_s$, and accordingly the poloidal heat fluxes are set as $q_{x,div} \equiv \gamma \Gamma_{x,div}(T_e + T_i)$, where the sheath heat transmission factor is usually considered as $\gamma \equiv 7$.

C.2.6 Numerical aspects of B2.5

Finally, here we give some brief references to the *numerical implementation* of the equations considered in the Section C.2.4. The procedure which is implemented consists in a *finite-volume spatial discretization* of a non-uniform staggered mesh, and a *fully implicit time discretization.* This method employs separate relaxation of the differential equations in cyclic order [22].

Each balance equation is considered in the general form
$$\mathcal{D}(\Phi) = 0 \tag{C.66}$$
describing the evolution of the plasma quantity Φ (density, temperature, etc.), which is solved iteratively over the two-dimensional mesh. Here $\mathcal{D}$ represents a generic non-linear differential operator describing one particular equation in the conduction-convection conservation form
$$\mathcal{D}(\Phi) \equiv \nabla \cdot (\rho \boldsymbol{v} \Phi - \underline{\underline{\boldsymbol{\kappa}}} \cdot \nabla \Phi) - S \tag{C.67}$$
where $\boldsymbol{v}$ is the eventual convective velocity of the field Φ, the scalar ρ and the tensor $\underline{\underline{\boldsymbol{\kappa}}}$ are coefficients (which could in turn depend on Φ, $\boldsymbol{v}$, and S is the source/sink. Its expanded form is
$$\mathcal{D}(\Phi) = \frac{1}{\sqrt{g}} \sum_\alpha \frac{\partial}{\partial x_\alpha} \left[\frac{\sqrt{g}}{h_\alpha} \left(\rho v_\alpha \Phi - \frac{1}{h_\alpha} \kappa_\alpha \frac{\partial \Phi}{\partial x_\alpha} \right) \right] - S \tag{C.68}$$

Each equation is used to improve the initial trial value for the corresponding plasma quantity: in this way, starting from a trial value $\overline{\Phi}$, the *residual* R of each equation (which quantifies the discrepancy from the exact solution), after an iteration, is evaluated as

$$\mathcal{D}(\overline{\Phi}) = -R \tag{C.69}$$

Subsequently, a linearized correction equation $\mathcal{D}'(\Delta\Phi) = R$, with $\Delta\Phi \equiv \Phi - \overline{\Phi}$ is discretized, leading to a set of equations of the kind

$$[\underline{\underline{\boldsymbol{D}}}][\Delta\Phi] = [R] \tag{C.70}$$

where $[\underline{\underline{\boldsymbol{D}}}]$ is a matrix with plasma-state-dependent coefficients. This is then inverted to find all the quantities in the vector $[\Delta\Phi]$, from which all the quantities Φ are calculated, which are differently different from the initial trial values.

These just calculated plasma quantities are then used as new trial quantities for the next step, and the procedure is repeated until convergence is reached, i.e. the final quantities are as similar as possible to the trial quantities. In this way, a criterion for establishing the achievement of the convergence is to check the trend of the residuals of each balance equation: if they have a constant trend over many successive steps, with sufficiently small values, then convergence is reached, and the final values of the quantities Φ for each cell will constitute the actual final solution.

C.3 Physics of EIRENE

Now, after having focused on the aspects of plasma particles modelling in SOLPS-ITER, we turn to the topic of *neutrals transport modelling.* The crucial importance of this aspect for plasma edge studies is given by the fact that, as widely discussed in the Chapter 2, neutral sources (such as the ones coming from atomic processes and recycling processes) have a role in all the SOL balances.

So, since such source distribution and the consequent neutral particles transport are essentially determined by the plasma background, it is necessary that plasma and neutrals transport are considered in a self-consistent way for an accurate plasma edge modelling. This is the reason why it was necessary to couple a fluid code such as B2.5 with a code for neutrals transport modelling such as EIRENE, whose physics will be discussed in this section.

C.3.1 Necessity of a kinetic transport model

As already discussed in the Chapter 4, a full kinetic description, as the one implemented in EIRENE, is implemented for modelling the transport of neutrals in SOLPS-ITER.

A full kinetic description is, indeed, a complete model, and easily incorporates detailed geometric considerations and complex atomic, molecular and surface physics aspects; however, such approach is very costly in terms of computation time, and unavoidably introduces some statistical noise in the results, meaning additional care needed to ensure convergence to a stationary solution [18]. It is then evident that some essential reasons have to exist for the choice of implementing a kinetic description of neutrals, with respect to the case of a standalone run of B2.5 in which neutrals are, instead, treated with a fluid description.

This need is easily understood considering the collisionality of neutral particles with plasma particles for characteristic SOL plasma conditions. This can be done by comparing their charge-exchange mean free path

$$\lambda_{CX} = \frac{v_{th,n}}{n_i \langle \sigma v \rangle_{CX}} \tag{C.71}$$

which defines the average distance travelled before suffering a collision with an ion, and their ionization mean free path

$$\lambda_i = \frac{v_{th,n}}{n_e\langle\sigma v\rangle_i} \tag{C.72}$$

which defines the average distance travelled before being ionized through the impact with an electron, where $v_{th,n}$ is the thermal velocity of neutrals and $\langle\sigma v\rangle$ are the atomic rate coefficients. Whereas for low plasma temperatures ($<$ 10 eV) the collisionality of neutrals with plasma particles is relatively high, being in this case $\lambda_{CX} \ll \lambda_i$, for higher temperatures ($>$ 10 eV), which are characteristic of the entire scrape-off layer apart from the near-targets regions, the collisionality is quite low, being in this case $\lambda_{CX} \approx \lambda_i$. So, since in the almost entire edge plasma ionization processes occur at a rate similar as collisions, a kinetic description is indeed strictly required in order to model these in the most possible accurate way. [18].

Such a description will then require a way for solving the full 3D *Boltzmann equations*

$$\frac{\partial f_n}{\partial t} + \boldsymbol{v}\cdot\frac{\partial f_n}{\partial \boldsymbol{x}} = C_n \tag{C.73}$$

for the neutrals distribution function f_n, where the collision term C_n includes all kinds of neutral-plasma interactions and neutral-neutral collisions, creating then a strongly non-linear problem because of the dependence on density and temperature of the cross sections of all the processes considered in C_n [23].

C.3.2 Equations in EIRENE

As it was also discussed in the Chapter 4, the way in which the high degree of stochasticity in the processes involving the neutrals, describable only via cross sections, is taken into account in EIRENE is through a *Monte Carlo method*, that is simulating the behavior of so-called *test particles* in a prescribed background medium (which, in case of coupling with B2.5, is just the plasma as computed after each time step of this), with external databases for atomic, molecular and surface processes providing the cross sections for each considered process and their dependence on plasma parameters [23].

In detail, the quantity which is computed by EIRENE is the one-particle distribution function $f(\boldsymbol{x},\boldsymbol{v},i,t)$, specifying the probability density in the six-dimensional phase space $(\boldsymbol{x},\boldsymbol{v})$ of the neutral species i around the point $(\boldsymbol{x},\boldsymbol{v})$ at the time t [23]. The full form of the considered Boltzmann equations for these functions, including the expanded form of the collision term, is

$$\begin{aligned} \frac{\partial f(\boldsymbol{x},\boldsymbol{v},t)}{\partial t} + \boldsymbol{v}\cdot\frac{\partial f(\boldsymbol{x},\boldsymbol{v},t)}{\partial \boldsymbol{x}} &= \\ = \iiint \sigma(\boldsymbol{v}',\boldsymbol{V}';\boldsymbol{v},\boldsymbol{V})|\boldsymbol{v}'-\boldsymbol{V}'|f(\boldsymbol{v}')f_b(\boldsymbol{V}')\,d^3\boldsymbol{v}'d^3\boldsymbol{V}'d^3\boldsymbol{V} &- \\ - \iiint \sigma(\boldsymbol{v},\boldsymbol{V};\boldsymbol{v}',\boldsymbol{V}')|\boldsymbol{v}-\boldsymbol{V}|f(\boldsymbol{v})f_b(\boldsymbol{V})\,d^3\boldsymbol{v}'d^3\boldsymbol{V}'d^3\boldsymbol{V} & \end{aligned} \tag{C.74}$$

where $f(\boldsymbol{v})$ is the distribution function for the test particles, denoted by the velocity variable $\boldsymbol{v}$, and $f_b(\boldsymbol{V})$ is the distribution function for the background particles, denoted by the velocity variable $\boldsymbol{V}$. In this form, it is written for the simple case of only one test particle species i interacting with the background species b, so that the species index was omitted. The Boltzmann equation written in this way does not take into account any external force field: the particle motion between the interaction events is governed only by inertia, as it is true for neutrals since they do not feel the effects of electric and magnetic fields.

In particular, $\sigma(\boldsymbol{v}', \boldsymbol{V}'; \boldsymbol{v}, \boldsymbol{V})$ is the cross section for a binary particle interaction; the first two arguments, that is the velocities $\boldsymbol{v}', \boldsymbol{V}'$ of the first integral, correspond to the velocity of the species i, b before the interaction, which are turned into the post-interaction velocities $\boldsymbol{v}, \boldsymbol{V}$. In this way, $\sigma(\boldsymbol{v}', \boldsymbol{V}'; \boldsymbol{v}, \boldsymbol{V})$ is defined in such a way that $\sigma(\boldsymbol{v}', \boldsymbol{V}'; \boldsymbol{v}, \boldsymbol{V})\, d^3\boldsymbol{v} d^3\boldsymbol{V}$ is the number of particles per unit time (per unit flux of test particles incident on a background particle) emerging after an interaction with velocity in the interval $[\boldsymbol{v}, \boldsymbol{v} + d\boldsymbol{v}]$. Therefore:

- The first integral in (C.74) describes the transition $(\boldsymbol{v}', \boldsymbol{V}' \to \boldsymbol{v}, \boldsymbol{V})$ into the velocity space interval $[\boldsymbol{v}, \boldsymbol{v} + d\boldsymbol{v}]$ for the test particles, resulting into a source term for the population of particles with velocity $\boldsymbol{v}$ following an interaction, starting from any other velocity $\boldsymbol{v}'$.
- The second integral in (C.74) describes the transition $(\boldsymbol{v}, \boldsymbol{V} \to \boldsymbol{v}', \boldsymbol{V}')$ into the velocity space interval $[\boldsymbol{v}', \boldsymbol{v}' + d\boldsymbol{v}']$ for the test particles, resulting into a loss term for the population of particles with velocity $\boldsymbol{v}$ following an interaction, turning to any other velocity $\boldsymbol{v}'$.

Since, when EIRENE is coupled with B2.5, the distribution function $f_b(\boldsymbol{V})$ of background particles is given by the latter, the distribution function $f_b(\boldsymbol{v})$ of test particles can be taken out of the second integral in the equations (C.74), allowing then to write this as

$$\begin{aligned} &\frac{\partial f(\boldsymbol{x}, \boldsymbol{v}, i, t)}{\partial t} + \boldsymbol{v} \cdot \frac{\partial f(\boldsymbol{x}, \boldsymbol{v}, i, t)}{\partial \boldsymbol{x}} + \nu(\boldsymbol{x}, \boldsymbol{v}, i) f(\boldsymbol{x}, \boldsymbol{v}, i, t) = \\ &= \int C(\boldsymbol{x}; \boldsymbol{v}', i' \to \boldsymbol{v}, i) |\boldsymbol{v}' - \boldsymbol{V}'| f(\boldsymbol{x}, \boldsymbol{v}, i, t)\, d^3\boldsymbol{v}' + Q(\boldsymbol{x}, \boldsymbol{v}, i, t) \end{aligned} \tag{C.75}$$

where $\nu(\boldsymbol{x}, \boldsymbol{v}, i)$ is the total *collision frequency*, $C(\boldsymbol{x}; \boldsymbol{v}', i' \to \boldsymbol{v}, i)$ is the *collision kernel* and $Q(\boldsymbol{x}, \boldsymbol{v}, i, t)$ is a source term [23].
In particular, the total collision frequency is defined as the number of collisions which a test particle experiences during a unit time interval while travelling through the background particles, that is as

$$\nu(\boldsymbol{x}, \boldsymbol{v}, i) \equiv \sum_k \nu_k(\boldsymbol{x}, \boldsymbol{v}, i) \tag{C.76}$$

where

$$\nu_k(\boldsymbol{x}, \boldsymbol{v}, i) = \iiint \sigma_k(\boldsymbol{v}, \boldsymbol{V}, i; \boldsymbol{v}', \boldsymbol{V}', i') |\boldsymbol{v} - \boldsymbol{V}| f_b(\boldsymbol{V})\, d^3\boldsymbol{v}' d^3\boldsymbol{V}' d^3\boldsymbol{V} \tag{C.77}$$

is the collision frequency for the specific process k.
Then, the collision kernel is defined as the number of particles of species i' with velocity $\boldsymbol{v}'$ which emerge from the collisions as particles of species i with velocity $\boldsymbol{v}$, that is as

$$C(\boldsymbol{x}; \boldsymbol{v}', i' \to \boldsymbol{v}, i) \equiv \sum_k \nu_k(\boldsymbol{x}, \boldsymbol{v}, i) C_k(\boldsymbol{x}; \boldsymbol{v}', i' \to \boldsymbol{v}, i) \tag{C.78}$$

where

$$C_k(\boldsymbol{x}; \boldsymbol{v}', i' \to \boldsymbol{v}, i) = \frac{\iint \sigma_k(\boldsymbol{v}', \boldsymbol{V}', i'; \boldsymbol{v}, \boldsymbol{V}, i) |\boldsymbol{v}' - \boldsymbol{V}'| f_b(\boldsymbol{V}')\, d^3\boldsymbol{V}' d^3\boldsymbol{V}}{\iiint \sigma_k(\boldsymbol{v}', \boldsymbol{V}', i'; \boldsymbol{v}, \boldsymbol{V}, i) |\boldsymbol{v}' - \boldsymbol{V}'| f_b(\boldsymbol{V}')\, d^3\boldsymbol{v}' d^3\boldsymbol{V}' d^3\boldsymbol{V}} \tag{C.79}$$

is the conditional probability distribution for the post-collision i, $\boldsymbol{v}$ for the specific process k.
In EIRENE, the collision frequency and the collision kernel can include not only volumetric processes but also surface processes, such as absorption and reflection at the material boundaries.

The Monte Carlo approach which is used for solving the equations (C.74) in EIRENE can be derived straight from its physical meaning. In fact, these equations describe the distribution functions of the particles, which are "created" from the source $Q(\boldsymbol{x}, \boldsymbol{v}, i, t)$. Since they are not subject to any force field, they will travel along straight lines until they undergo collisions with other test particles, background particles or material boundaries, each kind of which occurring with frequencies $\nu_k(\boldsymbol{x}, \boldsymbol{v}, i)$. In each collision, the particles change their velocity and, eventually, species, according to the distributions $C_k(\boldsymbol{x}; \boldsymbol{v}', i' \to \boldsymbol{v}, i)$. This "path" for each test particle continues until it ultimately disappears due to some kind of absorption or ionization [23].

Practically, the equations are solved by reproducing such processes numerically for a finite number of trajectories, using machine-generated pseudo-random numbers. For a test particles emerging from the primary source or from a former collision, the distance λ to the next collision, i.e. its mean free path, is sampled from its inverse cumulative distrbution function $F(\lambda)$, defined as

$$F(\lambda) \equiv 1 - \exp\left(\int_0^\lambda \frac{\nu}{|\boldsymbol{v}|} dl\right) \tag{C.80}$$

where

$$\int_0^\lambda \frac{\nu}{|\boldsymbol{v}|} dl = -\ln u \tag{C.81}$$

in which u is generated as a random number uniformly distributed between 0 and 1; in this way, the cumulative distribution function of lengths travelled from a collision to the successive one is really randomly evaluated, starting however from a physical basis since the integral (C.81) is proportional to the actual total collision frequency ν [23].

Finally, at the point of the collision, the type of processes which the particles undergoes is sampled from the discrete probability distribution

$$p_k = \frac{\nu_k}{\nu} \tag{C.82}$$

After that, the post-collision velocity is sampled from the distribution C_k or, if the sampled process was an absorption or a ionization, the particles disappears [23].

In SOLPS-ITER, several types of sources for test particles are available. The most important are [23]:

- *Surface sources*, used for describing the recycling sources of neutrals at the material boundaries after the impact of ions.
- *Volumetric sources*, used for describing the volumetric recombination of plasma particles.

In addition to these, it is also possible to specify surface sources of neutrals to model the fuelling through gas puff.

Regarding the surface processes, after the sampling of the velocity of the ion impacting the surface, a surface interaction model is applied; in particular, three different processes can be modelled: *reflection*, *thermal desorption* and *sputtering*.

Instead, regarding the volumetric processes, these can be divided in two groups:

- *Electron-impact collisions*, modelling the processes which electrons cause while travelling in a "sea" of ions and neutrals; this group includes *ionization*, *dissociation* and *recombination* processes, whose rates depend on electron density and electron temperature, but are assumed to be independent of the test particle velocity.
- *Heavy particles collisions*, modelling the interaction processes between ions and neutrals; this group includes *elastic scattering* and *charge-exchange collisions*, whose rates depend on ion temperature and test particle velocity.

Bibliography

[1] J.P. Freidberg. *Plasma physics and fusion energy.* Cambridge University Press, 2008.

[2] J. Wesson. *Tokamaks.* Oxford University Press, 2011.

[3] ITER website.
https://www.iter.org/.

[4] The demonstration power plant: DEMO.
https://www.euro-fusion.org/programme/demo/.

[5] M. Wischmeier. "The physics basis for a solution to the power and particle exhaust problem of a next step device". *27th IAEA Fusion Energy Conference*, 2018.

[6] M. Wischmeier. "High density operation for reactor-relevant power exhaust". *Journal of Nuclear Materials*, 463, 2015.

[7] P.C. Stangeby. *The plasma boundary of magnetic fusion devices.* CRC Press, 2000.

[8] C.S. Pitcher and P.C. Stangeby. "Experimental divertor physics". *Plasma Phys. Control. Fusion*, 39, 1997.

[9] R. Parker et al. "Plasma-wall interactions in ITER". *Journal of Nuclear Materials*, 241, 1997.

[10] J. Gunn et al. "Surface heat loads on the ITER divertor vertical targets". *Nucl. Fusion*, 57, 2017.

[11] D. Carralero et al. "An experimental investigation of the high density transition of the scrape-off layer transport in ASDEX Upgrade". *Nucl. Fusion*, 54, 2014.

[12] D. Carralero et al. "Experimental validation of a filament transport model in turbulent magnetized plasmas". *Physical Review Letters*, 115, 2015.

[13] D. Carralero et al. "Recent progress towards a quantitative description of filamentary SOL transport". *Nucl. Fusion*, 57, 2017.

[14] S.I. Krasheninnikov. "On scrape off layer plasma transport". *Physics Letters A*, 283, 2001.

[15] D.A. D'Ippolito et al. "Cross-field blob transport in tokamak scrape-off layer plasmas". *Phys. Plasmas*, 9, 2002.

[16] D. Carralero et al. "On the role of filaments in perpendicular heat transport at the scrape-off layer". *Nucl. Fusion*, 58, 2018.

[17] D. Carralero et al. "A quantitative description of thermal transport in the SOL of ASDEX Upgrade". *44th EPS Conference on Plasma Physics*, 2018.

[18] R. Schneider et al. "Plasma edge physics with B2-EIRENE". *Contrib. Plasma Phys.*, 46, 2006.

[19] S. Wiesen et al. "The new SOLPS-ITER code package". *Journal of Nuclear Materials*, 463, 2015.

[20] X. Bonnin et al. "Presentation of the new SOLPS-ITER code package for tokamak plasma edge modelling". *Plasma and Fusion Research*, 11, 2016.

[21] B.J. Braams. *Computational studies in tokamak equilibrium and transport.* Ph.D. thesis, 1986.

[22] M. Baelmans. *Code improvements and applications of a two-dimensional edge plasma model for toroidal fusion devices.* Ph.D. thesis, 1993.

[23] D. Reiter et al. "The EIRENE and B2-EIRENE codes". *Fusion Science and Technology*, 47, 2005.

[24] A. Herrmann et al. "ASDEX Upgrade - Introduction and overview". *Fusion Science and Technology*, 44, 2003.

[25] G. Miley et al. "Fusion cross sections and reactivities". *Technical report, Illinois University*, 1974.

[26] L. Spitzer. *Physics of fully ionized gases.* John Wiley and Sons, 1962.

[27] J.D. Lawson. "Some criteria for a power producing thermonuclear reactor". *Proc. Phys. Soc.*, B70, 1957.

[28] Courtesy of D. Brida.

[29] R. Pitts et al. "Fusion: The way ahead". *Phys. World*, 19, 2006.

[30] D. Naujoks. *Plasma-material interaction in controlled fusion.* Springer, 2010.

[31] M. Shimada et al. "Helium ash exhaust with single-null poloidal divertor in Doublet III". *Phys. Rev. Lett.*, 47, 1981.

[32] F. Wagner et al. "Regime of Improved Confinement and High Beta in Neutral-Beam-Heated Divertor Discharges of the ASDEX Tokamak". *Phys. Rev. Lett.*, 49, 1982.

[33] G.F. Matthews. "Plasma detachment from divertor targets and limiters". *Journal of Nuclear Materials*, 220, 1995.

[34] J. Bohdansky. "A universal relation for the sputtering yield of monoatomic solids at normal ion incidence". *Nucl. Instrum. Methods Phys. Res. B*, 2, 1984.

[35] W. Eckstein et al. "IPP Garching report 9/82". 1993.

[36] M. Bernert at al. "Power exhaust by SOL and pedestal radiation at ASDEX Upgrade and JET". *Nuclear Materials and Energy*, 12, 2017.

[37] A. Kallenbach et al. "Impurity seeding for tokamak power exhaust: from present devices via ITER to DEMO". *Plasma Phys. Control. Fusion*, 55, 2013.

[38] R. Chodura. *Plasma flow in the sheath and the presheath of a scrape-off layer, in "Physics of plasma-wall interactions in controlled fusion".* Plenum, 1986.

[39] P.C. Stangeby. *The plasma sheath, in "Physics of plasma-wall interactions in controlled fusion"*. Plenum, 1986.

[40] A. Scarabosio et al. "Outer target heat fluxes and power decay length scaling in L-mode plasmas at JET and AUG". *Journal of Nuclear Materials*, 438, 2013.

[41] T. Eich et al. "Empirical scaling of inter-ELM power widths in ASDEX Upgrade and JET". *Journal of Nuclear Materials*, 438, 2013.

[42] I. Paradela Pérez. *Power spreading in tokamak divertor using SOLPS code.* Master thesis, 2014.

[43] F. Wagner. "A study of the perpendicular particle transport properties in the scrape-off layer of ASDEX". *Nucl. Fusion*, 25, 1985.

[44] R. Schneider. *Plasma edge physics for tokamaks.* Lecture notes, 1997.

[45] Y. Shimomura et al. "Characteristics of the divertor plasma in neutral-beam-heated ASDEX discharges". *Nucl. Fusion*, 23, 1983.

[46] M. Wischmeier. *Simulating divertor detachment in the TCV and JET tokamaks.* Ph.D. thesis, 2005.

[47] I. Paradela Pérez et al. "SOL parallel momentum loss in ASDEX Upgrade and comparison with SOLPS". *Nuclear Materials and Energy*, 12, 2017.

[48] P.C. Stangeby. "Basic physical processes and reduced models for plasma detachment". *Plasma Phys. Control. Fusion*, 60, 2018.

[49] B. Lipschultz et al. "Divertor Physics Research on Alcator C-Mod". *Fusion Science and Technology*, 51, 2007.

[50] Y. Hayashi. "Plasma detachment study of high density helium plasmas in the Pilot-PSI device". *Nucl. Fusion*, 56, 2016.

[51] B. LaBombard et al. "Cross-field plasma transport and main-chamber recycling in diverted plasmas on Alcator C-Mod". *Nucl. Fusion*, 40, 2000.

[52] J.L. Terry et al. "Observations of the turbulence in the scrape-off layer of Alcator C-Mod and comparisons with simulation". *Phys. Plasmas*, 10, 2003.

[53] S.J. Zweben et al. "Edge turbulence measurements in toroidal fusion devices". *Plasma Phys. Control. Fusion*, 49, 2007.

[54] D.A. D'Ippolito et al. "Convective transport by intermittent blob-filaments: Comparison of theory and experiment". *Phys. Plasmas*, 18, 2011.

[55] A. Wynn et al. "Investigation into the formation of the scrape-off layer density shoulder in JET ITER-like wall L-mode and H-mode plasmas". *Nucl. Fusion*, 58, 2018.

[56] P.C. Stangeby. "Modeling plasma contact with the main vessel walls of a divertor tokamak". *Phys. Plasmas*, 9, 2002.

[57] D. Carralero et al. "On the effect of shoulder formation on thermal transport in the SOL of ASDEX Upgrade". *23rd International Conference on PSI in Controlled Fusion Devices*, 2018.

[58] ASDEX Upgrade Design Team & Tokamak Theory Group. "ASDEX Upgrade. Definition of a tokamak experiment with a reactor compatible poloidal divertor". *IPP Garching report 1/197)*, 1982.

[59] ASDEX Upgrade documentation. https://www.aug.ipp.mpg.de/wwwaug/documentation/physics/physics.shtml.

[60] B. Streibl et al. "Machine design, fueling and heating in ASDEX Upgrade". *Fusion Science and Technology*, 44, 2003.

[61] R. Neu et al. "Plasma-wall interaction and first-wall materials in ASDEX Upgrade". *Fusion Science and Technology*, 44, 2003.

[62] R. Neu et al. "Plasma wall interaction and its implication in an all tungsten divertor tokamak". *Plasma Phys. Control. Fusion*, 49, 2007.

[63] J. Neuhauser et al. "Edge and divertor physics in ASDEX Upgrade". *Fusion Science and Technology*, 44, 2003.

[64] A. Herrmann et al. "Solid tungsten divertor-III for ASDEX Upgrade and contributions to ITER". *Nucl. Fusion*, 55, 2015.

[65] E. Wolfrum et al. "Fast lithium-beam spectroscopy of tokamak edge plasmas". *Rev. Sci. Instrum.*, 64, 1993.

[66] I.H. Hutchinson. *Principles of plasma diagnostics.* Cambridge University Press, 2002.

[67] J. Schweinzer et al. "Reconstruction of plasma edge density profiles from LiI(2s-2p) emission profiles". *Plasma Phys. Control. Fusion*, 34, 1992.

[68] R. Fischer et al. "Probabilistic lithium beam data analysis". *Plasma Phys. Control. Fusion*, 50, 2008.

[69] M. Willensdorfer et al. "Characterization of the Li-BES at ASDEX Upgrade". *Plasma Phys. Control. Fusion*, 56, 2014.

[70] H. Murmann et al. "The Thomson scattering systems of the ASDEX Upgrade tokamak". *Rev. Sci. Instrum.*, 63, 1992.

[71] B. Kurzan et al. "Signal processing of Thomson scattering data in a noisy environment in ASDEX Upgrade". *Plasma Phys. Control. Fusion*, 46, 2004.

[72] B. Kurzan et al. "Edge and core Thomson scattering systems and their calibration on the ASDEX Upgrade tokamak". *Rev. Sci. Instrum.*, 82, 2011.

[73] M. Weinlich et al. "Flush mounted probes in ASDEX Upgrade". *Contrib. Plasma Phys.*, 36, 1996.

[74] M. Weinlich et al. "Flush mounted Langmuir probes in an oblique magnetic field". *Phys. Plasmas*, 4, 1997.

[75] G. Birkenmeier et al. "Filament transport, warm ions and erosion in ASDEX Upgrade L-modes". *Nucl. Fusion*, 55, 2015.

[76] M. Greenwald. "Density limits in toroidal plasmas". *Plasma Phys. Control. Fusion*, 44, 2002.

[77] D. Carralero et al. "Implications of high density operation on SOL transport: A multimachine investigation". *Journal of Nuclear Materials*, 463, 2015.

[78] D.P. Coster et al. *SOLPS-ITER manual.* 2019.

[79] V. Kotov and D. Reiter. "Two-point analysis of the numerical modelling of detached divertor plasmas". *Plasma Phys. Control. Fusion*, 51, 2009.

[80] A.V. Chankin et al. "SOLPS modelling of ASDEX Upgrade H-mode plasma". *Plasma Phys. Control. Fusion*, 48, 2006.

[81] L. Aho-Mantila et al. "Assessment of SOLPS5.0 divertor solutions with drifts and currents against L-mode experiments in ASDEX Upgrade and JET". *Plasma Phys. Control. Fusion*, 59, 2017.

[82] M. Wischmeier et al. "Simulating the role of intrinsic carbon impurities in the divertor detachment of ASDEX Upgrade". *Contrib. Plasma Phys.*, 48, 2008.

[83] B. Gulejová et al. "SOLPS5 simulations of Type I ELMing H-mode at JET". *Journal of Nuclear Materials*, 390, 2009.

[84] W. Dekeyser et al. "SOLPS-ITER modeling of the Alcator C-Mod divertor plasma". *Plasma and Fusion Research*, 11, 2016.

[85] E.T. Meier et al. "Drifts, currents, and power scrape-off width in SOLPS-ITER modeling of DIII-D". *Nuclear Materials and Energy*, 12, 2017.

[86] V. Kotov et al. *Numerical study of the ITER divertor plasma with the B2-EIRENE code package.* 2007.

[87] D.P. Coster et al. "Integrated modelling of the edge plasma and plasma facing components". *Journal of Nuclear Materials*, 363, 2007.

[88] D.P. Coster et al. "Automatic evaluation of edge transport coefficients with B2-SOLPS5.0". *Contrib. Plasma Phys.*, 40, 2000.

[89] R. Schneider et al. "Extensions of B2 for the simulation of ASDEX Upgrade scrape-off layer plasmas". *Contrib. Plasma Phys.*, 32, 1992.

[90] R. Schneider et al. "B2-EIRENE simulation of ASDEX and ASDEX Upgrade scrape-off layer plasmas". *Journal of Nuclear Materials*, 196, 1992.

[91] D. Reiter. *EIRENE manual.* 2009.

[92] D. Reiter. *Randschicht-konfiguration von tokamaks: entwicklung und anwendung stochastischer modelle zur beschreibung des neutralgastransports.* Ph.D. thesis, 1984.

[93] AMJUEL database.
`http://www.eirene.de/amjuel.pdf`.

[94] HYDHEL database.
`http://www.eirene.de/hydhel.pdf`.

[95] T. Lunt et al. "EMC3-EIRENE simulations of particle- and energy fluxes to main chamber- and divertor plasma facing components in ASDEX Upgrade compared to experiments". *Journal of Nuclear Materials*, 463, 2015.

[96] F.A. D'Isa. *Evolution of the scrape-off layer plasma background at density shoulder formation.* Master thesis, 2016.

[97] R. Fischer et al. "Bayesian modelling of fusion diagnostics". *Plasma Phys. Control. Fusion*, 45, 2003.

[98] R. Fischer et al. "Integrated data analysis of profile diagnostics at ASDEX Upgrade". *Fusion Science and Technology*, 58, 2010.

[99] J.M. Canik et al. "Measurements and 2-D modeling of recycling and edge transport in discharges with lithium-coated PFCs in NSTX". *Journal of Nuclear Materials*, 415, 2011.

[100] M. Reich et al. "Lithium beam charge exchange diagnostic for edge ion temperature measurements at the ASDEX Upgrade tokamak". *Plasma Phys. Control. Fusion*, 46, 2004.

[101] U.S. Naval Research Laboratory. *NRL plasma formulary.* 2018.

[102] P. Manz et al. "The diffusion limit of ballistic transport in the scrape-off layer" (draft). 2019.

[103] S.A. Self and H.N. Ewald. "Static theory of a discharge column at intermediate pressures". *Phys. Fluids*, 9, 1966.

[104] J.D. Jackson. *Classical electrodynamics.* John Wiley and Sons, 1999.

[105] J.P. Freidberg. *Ideal MHD.* Cambridge University Press, 2014.

[106] F. Wagner. *Magnetic confinement, in "Plasma physics".* Springer, 2005.

[107] V.D. Shafranov. "Equilibrium of a toroidal plasma in a magnetic field". *J. Nucl. Energy, Part C Plasma Phys.*, 5, 1963.

[108] S. Chapman, T.G. Cowling. *The mathematical theory of non-uniform gases.* Cambridge University Press, 1939.

[109] S.I. Braginskii. "Transport processes in a plasma". *Reviews of Plasma Physics*, 1, 1965.

[110] R. Balescu. *Transport processes in plasmas, vol. 1 - Classical transport.* North Holland, 1988.

[111] R. Balescu. *Transport processes in plasmas, vol. 2 - Neoclassical transport.* North Holland, 1988.

[112] R. Balescu. *Aspects of anomalous transport in plasmas.* CRC Press, 2005.

[113] U. Stroth. *Transport in toroidal plasmas, in "Plasma physics".* Springer, 2005.

[114] D. Bohm. *The characteristics of electrical discharges in magnetic fields.* McGraw-Hill, 1949.

[115] O.G. Bakunin. *Turbulence and diffusion.* Springer, 2008.

[116] F.F. Chen. "Resistive overstabilities and anomalous "diffusion"". *Phys. Fluids*, 8, 1965.

[117] O.E. Garcia et al. "Mechanism and scaling for convection of isolated structures in nonuniformly magnetized plasmas". *Phys. Plasmas*, 12, 2005.

[118] O.E. Garcia et al. "Fluctuations and transport in the TCV scrape-off layer". *Nucl. Fusion*, 47, 2007.

[119] S.I. Krasheninnikov et al. "Recent theoretical progress in understanding coherent structures in edge and SOL turbulence". *J. Plasma Physics*, 74, 2008.

[120] J.R. Myra et al. "Collisionality and magnetic geometry effects on tokamak edge turbulent transport I: A two-region model with application to blobs". *Phys. Plasmas*, 13, 2006.

[121] O.E. Garcia et al. "Radial interchange motions of plasma filaments". *Phys. Plasmas*, 13, 2006.

[122] P. Manz et al. "Filament velocity scaling laws for warm ions". *Phys. Plasmas*, 20, 2013.

[123] M. Wiesenberger et al. "Radial convection of finite ion temperature, high amplitude plasma blobs". *Phys. Plasmas*, 21, 2014.

[124] V. Zhdanov. *Transport processes in multicomponent plasma.* Taylor and Francis, 2002.